Use of High-Density Surface-Electromyography of the Forearm as a Method for Predicting Thumb Rotation in Myoelectric Transradial Prosthetics

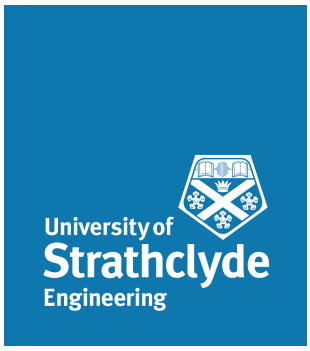

Alejandra Aranceta-Garza

Biomedical Engineering Department

University of Strathclyde

Supervisor: Prof. Bernard A. Conway

A thesis submitted for the degree of

PhilosophiæDoctor (PhD)

2015 February

1. Reviewer: Dr. Uma Shahani, Glasgow Caledonian University.

2. Reviewer: Mrs. Sarah Day, University of Strathclyde.

To my reviewers: Thank you for accepting being my examiners; I hope you enjoy reading it as much as I enjoyed writing it.

Day of the defence: 26/02/2015

Signature from head of PhD committee:

Declaration

I herewith declare that I have produced this paper without the prohibited assistance of third parties and without making use of aids other than those specified; notions taken over directly or indirectly from other sources have been identified as such. This paper has not previously been presented in identical or similar form to any other Scottish or foreign examination board.

The thesis work was conducted from October 2010 to October 2014 under the supervision of Prof. Bernard A. Conway and Dr. Heba Lakany.

Glasgow, Scotland, United Kingdom.

It's been quite a roller-coaster ride, but I've grown and learned a lot about myself. Here's to all of you...

A mis padres y hermanos, quienes me han apoyado de manera incondicional no sólo durante mi doctorado sino toda mi vida. Sin ustedes, sin su ejemplo, sin sus regaños y enseñanzas yo no sería lo que soy hoy. Ésta, por mucho, ha sido una de las pruebas más difíciles que he tenido en mi vida, y como todas las pruebas con las cuales me he topado, disfruté cada momento, los buenos y los malos. Esta forma de ver la vida se las debo a ustedes, gracias, gracias, gracias.

A mi más grande fuente de inspiración, Ro. Gracias por ser un ejemplo en vida y recordarme lo hermoso que es vivir, aún teniendo que enfrentar adversidades. Quiero decirte que teniéndote a mi lado me siento invencible y no hay nada que juntos no podamos hacer o lograr.

A todos los que se fueron dejándome aprendizajes invaluables que atesoro.

A quienes llegaron en el momento que debían hacerlo, en especial a Lore, por ayudarme a enfocar mi energía en terminar y hacer las cosas bien. Gracias por traer tanta motivación y felicidad a mi vida. A mi hermoso trío, Sonia, Marcia y Mariana, por siempre responder mis mensajes de llantos o risas de manera elocuente, reiterandome que todo saldría bien.

To all my friends and colleagues that have given some time of their life to read my thesis, or hear me moan about it. Specially to Cat, you've proven to me that friendship has no barriers and that it's always appropriate to have a glass of wine and chillax.

To Colette and all the Infinity team for keeping myself grounded and reminding me on how to breath through things.

To my supervisor, Bernie, thank you for all your knowledge, guidance and patience. I really enjoyed working with you and hope we can team up in the future. Thanks for teaching me how to look outside the box, and more importantly, thank you for caring.

Finally, I would like to thank Helen and Val, who I strongly believe helped me the most even before arriving to Glasgow. I really do see you as part of my family. Thank you for always be aware of me, not only in the academic sense, but in a personal way too. I will always be thankful with you.

Thank you all so very much, without you, I don't know where I'd be standing today.

Ale

Acknowledgements

I would like to acknowledge my sponsor The National Council on Science and Technology of Mexico (CONACyT) which has made this research possible by financing me under no. 214157.

I would also like to acknowledge and thank John Maclean and Stephen Murray for helping me out building the load sensor resistors and the testing rig. Thank you for your patience.

Abstract

Until now, natural thumb control mechanisms are lacking in the upper limb prosthetic development. This lag is due to the complex anatomy of the musculature of the hand making the upper limb prosthetic research a very complicated area.

Several studies have attempted to better our understanding of the neural control of the hand. With applications including clinical rehabilitation, surface-Electromyography (sEMG) has been steadily improving the knowledge in this area, albeit still very limited. The development of high-density sEMG (HD-sEMG) has drastically increased the sensitivity of EMG techniques. Despite this research effort, there are significant gaps in the field. Furthermore, current data analysis is almost exclusively performed off-line and so, neurally controlled prostheses are limited to research labs and are not a clinically viable technology. Therefore, it is evident that new technologies are required to understand the dexterity of the human hand for prosthetic control.

A common theme across the different hand-prosthetic developers is not to have mechanisms to drive the thumb based on muscular contractions. Due to the lack of intuitiveness for an amputee to operate the prosthetic device, it requires several highly demanding training sessions between the patient and the prosthetist. These sessions are oriented for the amputee to be able to control in duration and magnitude, the contractions of the chosen muscles to drive the motors of the prosthesis.

In this research, the muscle activity from the forearm is identified and correlated with specific hand movements leading to improve the commercially available myoelectric transradial prosthetics. This was achieved through the understanding of sEMG patterns related to differentiation of thumb opposition to different fingers. The acquired signals were investigated based on time-domain analyses (i.e. amplitude signal analysis, root-mean square values, statistical analyses), followed by a joint time and frequency-domain analyses (i.e. coherence estimate and cumulant analysis). Finally, unsupervised machine learning techniques were applied aiming to differentiate the different sEMG patterns during the different thumb opposition. This differentiation leads to a better understanding with regards to prospective controller mechanisms aiming to develop new prosthetic devices enhancing the experience of transradial amputees with the use of their prosthetic.

Contents

List of Figures

List of Tables

List of Abbreviations

$AbDm$	Abductor Digiti minimi
$AbPb$	Abductor Pollicis brevis
AdP	Adductor Pollicis
AP	Action potential
APl	Abductor Pollicis longus
BMU	Best-matching unit
$CMRR$	Common mode rejection ratio
CNS	Central Nervous System
CWT	Continuous Wavelet Transform
DOI	Dorsal Interossei
DWT	Discrete Wavelet Transform
$ECRb$	Extensor Carpi Radialis brevis
$ECRl$	Extensor Carpi Radialis longus
ECU	Extensor Carpi Ulnaris
ED	Extensor Digitorum
EDm	Extensor Digiti minimi
EEG	Electroencephalography
EI	Extensor Indicis
EKG	Electrocardiography
EMD	Empirical Mode Decomposition
EMG	Electromyography
EPb	Extensor Pollicis brevis
EPl	Extensor Pollicis longus
FCR	Flexor Carpi Radialis
FCU	Flexor Carpi Ulnaris
$FDmb$	Flexor Digiti minimi brevis
FDp	Flexor Digitorum profundus
FDs	Flexor Digitorium superficialis
FPb	Flexor Pollicis brevis
FPl	Flexor Pollicis longus
$FSRs$	Force sensor resistors
FV	Feature Vector
GUI	Graphical User Interface
$HD-sEMG$	High-Density Surface Electromyography
HOS	High Order Statistics
IED	inter-electrode distance
IVC	Isometric voluntary contraction
LM	Levenberg-Marquardt
LSR	Load sensor resistor
MDF	Median Frequency
MNF	Mean or Centroid Frequency
MSE	Mean square error
$MUAP$	Motor Unit Action Potential
MUs	Motor units
MVC	Maximum voluntary contraction
NN	Neural network
OP	Opponens Pollicis
Pb	Palmaris brevis
PCA	Principal component analysis
PCs	Principal component space
PDm	Opponens Digiti minimi
PI	Palmar Interossei
PL	Palmaris longus
PQ	Pronator Quadratus

PSD Power Spectrum Density

PT Pronator teres

RMS Root-Mean Square

RTI Noise referred to the input

SD Standard deviation

$sEMG$ Surface Electromyography

$SENIAM$ Surface ElectroMyoGraphy for the Non-Invasive Assessment of Muscles

$SOFM$ Self-Organising Feature Map

$SS(B)$ Sum of Square Between groups

$STFT$ Short Time Fourier Transform

SVD Single value decomposition

TMR Target Muscle Re-innervation

$UNIPOD$ United National Institute for Prosthetics & Orthotics Development

1

Introduction

After the brain, the hands are the most impressive and powerful tool of the human body. We tend to take our hands for granted, yet they form one of the most extraordinary features separating humans from animals. Hands are used to shape the brain as active parts of our thoughts, emotions, language, etc. no other part of the human body is so intimately related to the human behaviour as the hands are.

As a perceptual organ, hands have some advantages over the eyes, our hands can effectively see around corners, allowing us to explore all sides of an object: weight, compliance, slipperiness, amongst many others. The high number of degrees of freedom and the highly developed neural control, provides the hand with tremendous dexterity, allowing delicate and versatile manipulation.

The loss of an upper limb due to trauma, disease or congenital deficiency resulting in sudden loss of function, sensation and cosmesis is a far greater catastrophe for the individual than the loss of their lower limb. Research into upper limb prosthesis aims to develop a device that has functionality almost similar to the natural hand in terms of control, stability, dexterity, coordination and sensory feedback as well as good wearability, e.g. light weight, long-term usability and cosmesis.

The development of high-density sEMG (HD-sEMG) has drastically increased the sensitivity of EMG techniques and the chances of detecting single motor unit characteristics. Despite a zealous research effort, there are significant gaps in the field - specifically with regard to knowledge of motor unit recruitment during various hand movements. Furthermore, currently data analysis is almost exclusively performed off-line and so neurally controlled prostheses are limited to research labs and are not a

clinically viable technology. It is clear that new technologies are required to understand the dexterity of the human hand.

In this research, we attempt to identify and correlate the muscle activity with hand movements leading to improve the commercially available myoelectric upper limb prosthetics. This will be achieved through the understanding of EMG patterns related to differentiation of thumb opposition to different fingers. The acquired signals will be investigated based on time-domain analysis (i.e. amplitude signal analysis; root-mean square values; statistical analysis), followed by a joint time and frequency domain analysis (i.e. coherence estimate and cumulant analysis), as well as unsupervised machine learning aiming to cluster the different EMG patterns during the different thumb oppositions.

1.1 Research Context

It is important, given the multidisciplinary nature of this research, to provide the reader with enough tools to understand the mechanisms applied throughout: i) the motor neuroscience of large-scale electromyographic recordings; ii) upper limb amputations; iii) rehabilitation research, more specifically, mechanisms applied for interfacing myoelectric prosthesis and amputees. This will lead to comprehensive results and their critical appraisal and discussion.

1.1.1 Anatomy of the Hand and Forearm

All mammals and most vertebrates possess four limbs. These four limbs allow them to walk and interact with the world around, regardless the different morphology. In Figure 1.1, differences and similarities amongst mammals and vertebrates are depicted in order to illustrate limb diversity.

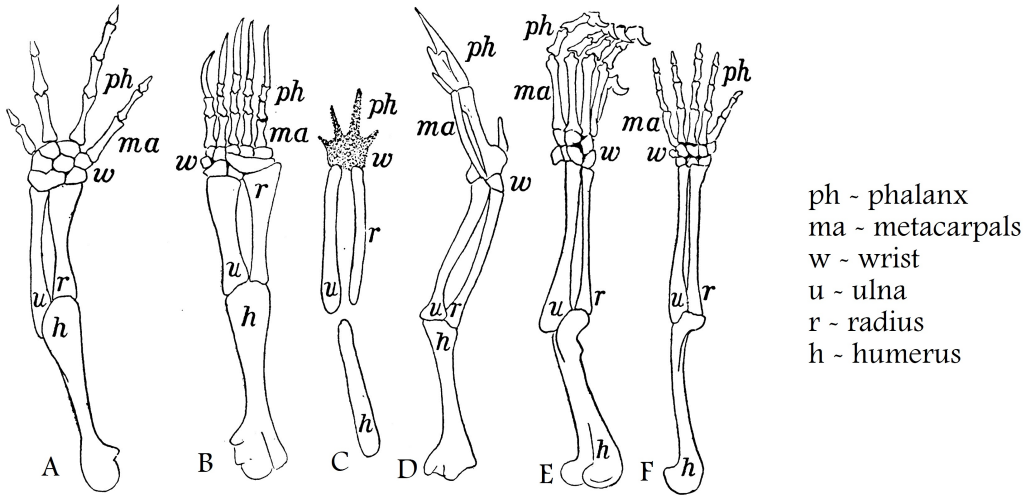

Figure 1.1: Comparison between the hands of some vertebrates - Fore limbs of vertebrates showing similarity of structure . A, salamander; B, turtle; C, very young turtle; D, adult bird; E, dog; F, man. -Davison, 1906.

The human hand has an apparent simple structure on the outside, but the amount of nerves (∼ 48); ligaments (∼ 123); muscles (∼ 34); bones (∼ 29)(Figure 1.2); joints (∼ 29); and arteries (∼ 30) make it a very complex structure .

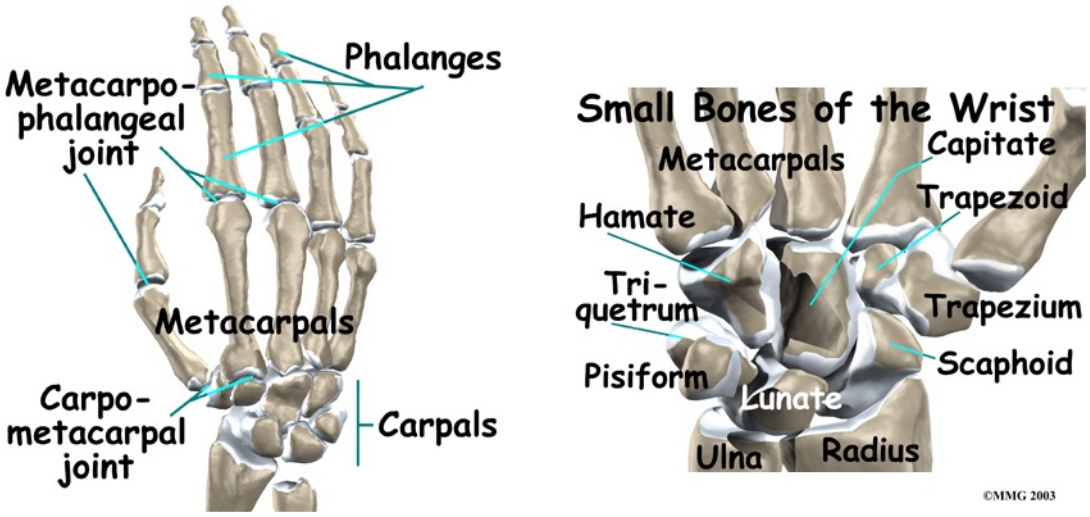

Figure 1.2: Bones in the hand and wrist - Left - Bones in the palm of the hand. Right - Bones in the forearm and small bones of the wrist. -Copyright Active Motion Physiotherapy. All rights reserved

The hand is able to make broad, smooth movements as well as small and fine movements. These are achieved with thanks to its anatomy (Figure 1.3), and the large amount of muscles in the hand (palm and forearm). The combination of the different muscles allow the hand to perform detailed tasks .

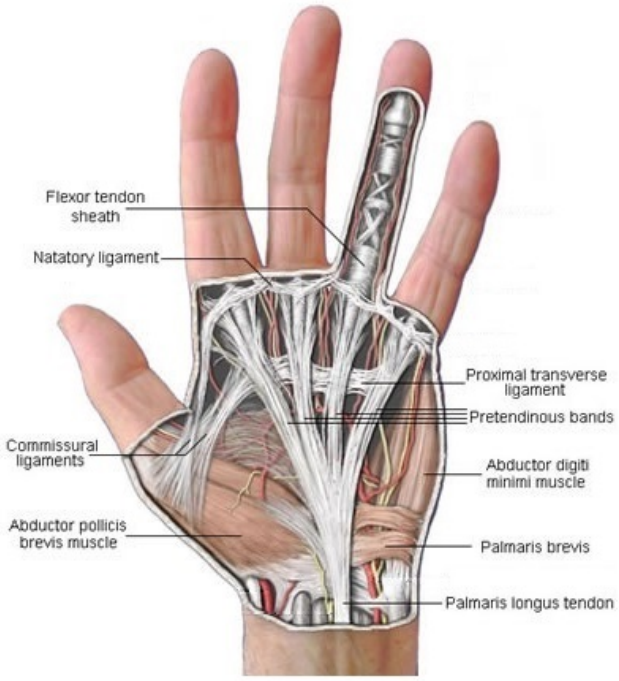

Figure 1.3: Anatomy of the human hand - Anatomy of the human hand. Muscles, ligaments and tendons located in the palm of the hand that are in charge of finger movement. From: Hertfordshire Orthopaedic Centre.

The secundus digitus manus (index), digitus medius (middle finger), digitus annularis (ring finger), and digitus minimus manus (pinky finger), have 4 different movements; whereas the thumb has an extra gesture. The range of movement is also referred as degrees of freedom, and this implies the amount of different movements that an object (a finger in this case) has when seen from one reference point. The four degrees of freedom that the 4 aforementioned fingers have are flexion, extension, abduction and adduction. On the other hand, the thumb has the same four motions plus opposition to the rest of the fingers, as is shown in Figure 1.4.

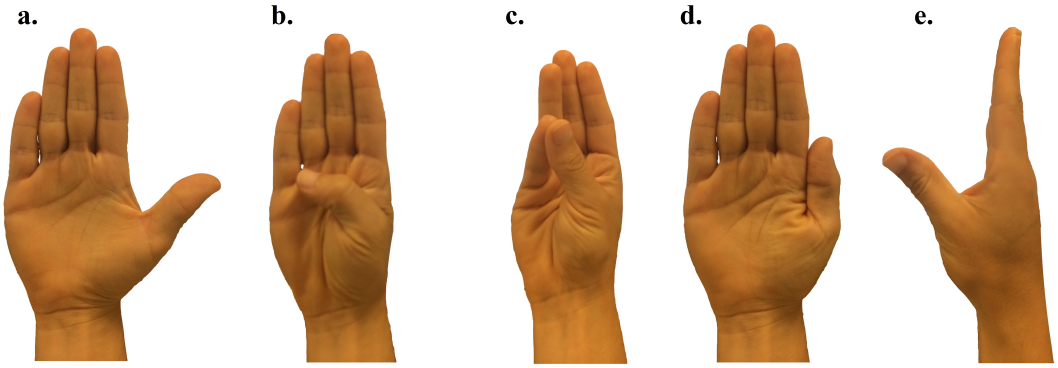

Figure 1.4: Degrees of Freedom of the Thumb - a. Extension; b. Flexion; c. Opposition of little finger; d. Adduction; e. Abduction

There are no muscles in the fingers, instead, the muscles that control them are located in the palm and in the forearm. With approximately 34 muscles in the palm of the hand and forearm, they work together to achieve wide variety of movements. These muscles provide the hands and fingers with flexibility, precise control, and gripping strength necessary for a range of activities from drawing and a gentle touch, to gripping a ball or using them as tools.

The muscles of the forearm most common separation is by compartments:

- Anterior Compartment of the Forearm [Figure 1.5]:

  Superficial Muscles. Table 1.1

  Deep Muscles. Table 1.2

- Posterior Compartment of the Forearm[Figure 1.6]:

  Superficial Muscles Table 1.3

Deep Muscles. Table 1.4

- Intrinsic muscles of the hand (palm):

  Snuff box Table 1.5

  Thenar lateral Table 1.6

  Hypothenar medial Table 1.7

  Intermediate area Table 1.8

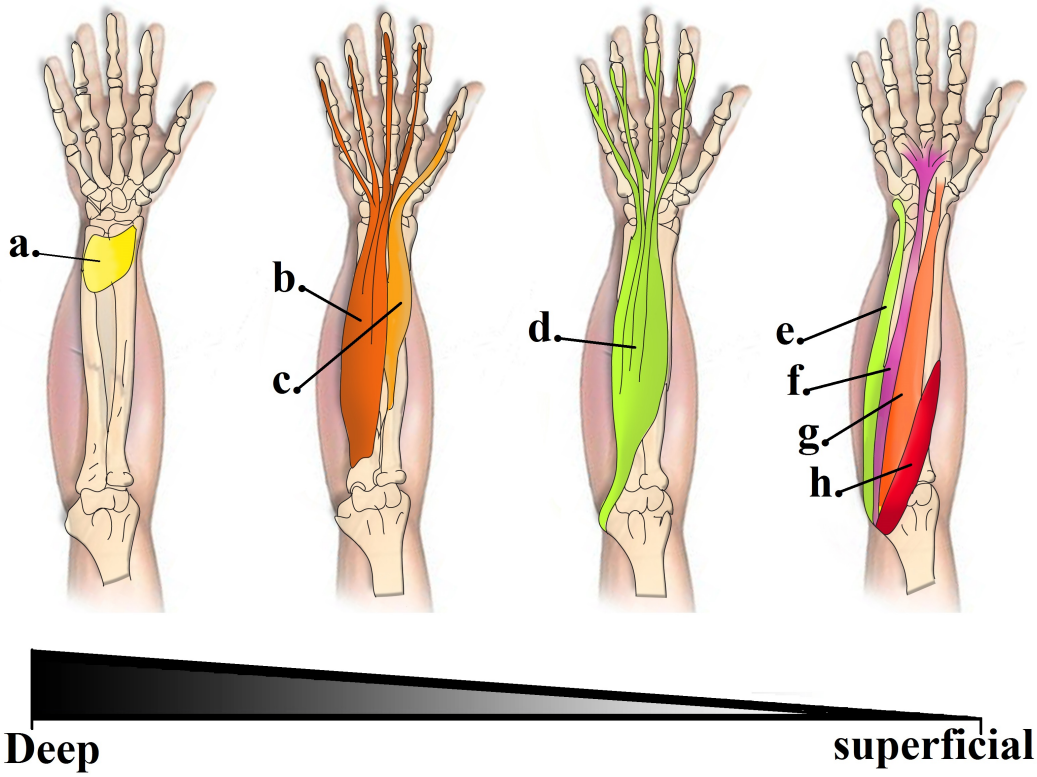

Figure 1.5: Muscles in the Anterior Compartment of the Forearm - Flexor Muscles - The muscles of the anterior compartment of the forearm are depicted in this image from the deepest layer to the most superficial one: a. Pronator quadratus (PQ) b. Flexor digitorium profundus (FDP) c.Flexor pollicis longus (FPL) d. Flexor digitorium superficialis (FDS) e. Flexor carpi ulnaris (FCU) f. Palmaris longus (PL) g. Flexor carpi radialis (FCR) h. Pronator teres (PT)

Table 1.1: Superficial Muscles in the Anterior Compartment of the Forearm

Muscle	Origin	Insertion	Artery	Nerve	Action	Antagonist
Pronator teres	Humeral head: medial epicondyle of humerus (common flexor tendon). Ulnar head: coronoid process of the ulna	Radius	Ulnar and radial artery	Median nerve	Pronation of forearm, flexes elbow	Supinator muscle
Palmaris longus	Medial epicondyle of humerus (common flexor tendon)	Palmar aponeurosis	Ulnar artery	Median nerve	Wrist flexor	Extensor carpi radialis brevis, Extensor carpi radialis longus, and Extensor carpi ulnaris
Flexor carpi radialis	Medial epicondyle of humerus (common flexor tendon)	Bases of second and third metacarpal bones	Ulnar artery	Median nerve	Flexion and abduction at wrist	Extensor carpi radialis brevis, Extensor carpi radialis longus
Flexor carpi ulnaris	Medial epicondyle of humerus (common flexor tendon)	Pisiform	Ulnar artery	Muscular branches of ulnar nerve	Flexion of wrist	Extensor carpi ulnaris
Flexor digitorum superficialis	Medial epicondyle of humerus (common flexor tendon), as well as parts of the radius and ulna.	phalanges	Ulnar artery	Median nerve	flexor of fingers (primarily at proximal interphalangeal joints)	Extensor digitorum muscle

Table 1.2: Deep Muscles in the Anterior Compartment of the Forearm

Muscle	Origin	Insertion	Artery	Nerve	Action	Antagonist
Pronator quadratus	Medial, anterior surface of the ulna	Lateral, anterior surface of the radius	Anterior interosseous artery	Median nerve (anterior interosseous nerve)	Pronates the forearm	Supinator muscle
Flexor digitorum profundus	Ulna	Distal phalanges	Anterior interosseous artery	Median nerve (anterior interosseous nerve), muscular branches of ulnar muscle	flexes hand and interphalangeal joints	Extensor digitorum muscle
Flexor pollicis longus	The middle 2/4 of the volar surface of the radius and the adjacent interosseous membrane. (Also occasionally a small origin slightly on the medial epicondyle of the ulna.)	The base of the distal phalanx of the thumb	Anterior interosseous artery		Anterior interosseous nerve (branch of median nerve) (C8, T1) Flexion of the thumb	Extensor pollicis longus muscle, Extensor pollicis brevis muscle

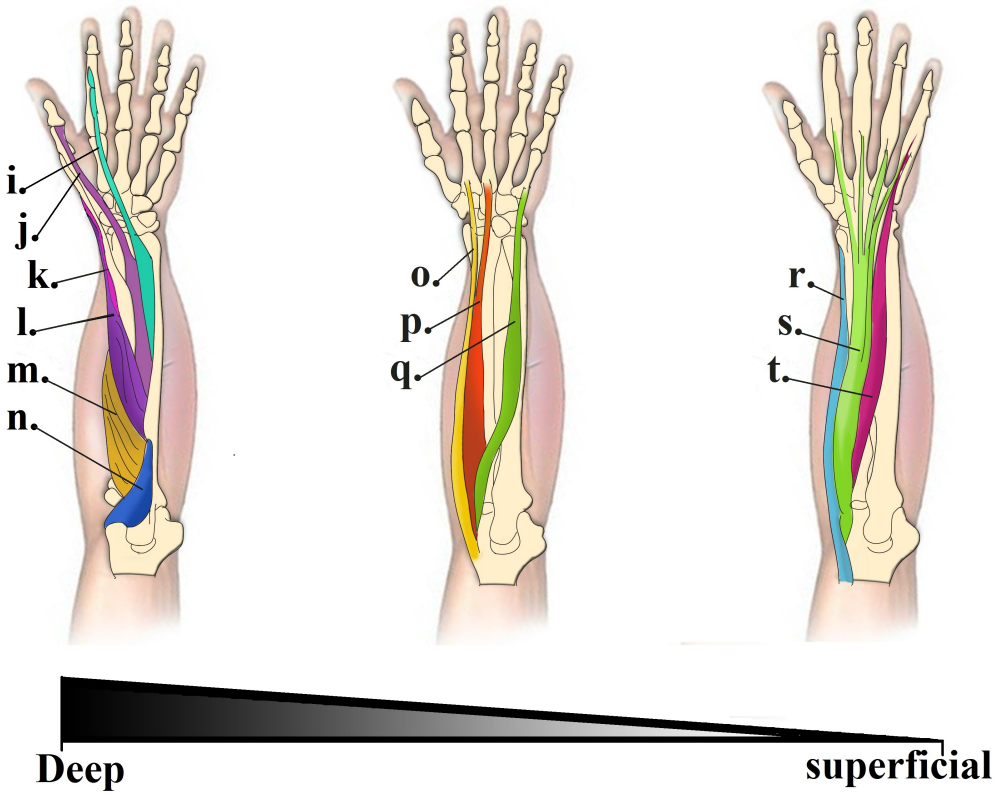

Figure 1.6: Muscles in the Posterior Compartment of the Forearm - The muscles of the posterior compartment of the forearm are depicted in this image moving from the deepest to the most superficial layer: i.Extensor indicis (EI) j. Extensor pollicis longus (EPL) k. Extensor pollicis brevis (EPB) l. Abductor pollicis longus (APL) m. Supinator (S) n. Anconeous (A) o. Extensor carpi radialis longus (ECRl) p. Extensor carpi radialis brevis (ECRb) q. Extensor carpi ulnaris r. Brachioradialis (B) s. Extensor digitorium (ED) t. Extensor digiti minimi (EDM)

Table 1.3: Superficial Muscles in the Posterior Compartment of the Forearm

Muscle	Origin	Insertion	Artery	Nerve	Action	Antagonist
Brachioradialis	Lateral supracondylar ridge of the humerus	Distal radius (Radial styloid process)	Radial recurrent artery	Radial nerve	Flexion of the forearm	-
Extensor carpi radialis longus	Lateral supracondylar ridge	Second metacarpal	Radial artery	Radial nerve	Extensor at the wrist joint, abducts the hand at the wrist	Flexor carpi radialis muscle
Extensor carpi radialis brevis	Humerus at the anterior of lateral epicondyle(common extensor tendon)	Base of the 3rd metacarpal	Radial artery	Deep branch of the radial nerve	Extensor and abductor of the hand at the wrist joint	Flexor carpi radialis muscle
Extensor digitorum	Lateral epicondyle (common extensor tendon)	2nd and 3rd phalanges	Interosseous recurrent artery and posterior interosseous artery	Posterior interosseous nerve (C7, C8)	Extension of hand and fingers	Flexor digitorum superficialis muscle, Flexor digitorum profundus muscle
Extensor digiti minimi	The anterior portion of the lateral epicondyle of the humerus(common extensor tendon)	Extensor expansion, located at the base of the proximal phalanx of the finger on the dorsal side	Posterior interosseous artery which originates from the common interosseous artery and more proximally, the ulnar artery	Posterior interosseous nerve (C7, C8)	Extends the little finger at all joints	Flexor digiti minimi brevis
Extensor carpi ulnaris	Common extensor tendon (lateral epicondyle), ulna	5th metacarpal	Ulnar artery	Posterior interosseous nerve (C7, C8)	Extends and adducts the wrist	Flexor carpi ulnaris

Table 1.4: Deep Muscles in the Posterior Compartment of the Forearm

Muscle	Origin	Insertion	Artery	Nerve	Action	Antagonist
Supinator	Lateral epicondyle of the humerus, supinator crest of ulna, radial collateral ligament, annular ligament	Lateral proximal radial shaft	Radial recurrent artery	Posterior interosseous nerve (C7,C8)	Extension of hand and fingers	Flexor digitorum superficialis muscle, Flexor digitorum profundus muscle

Table 1.5: Muscles in the Anatomical Snuff Box in the Deep Posterior Part of the Forearm

Muscle	Origin	Insertion	Artery	Nerve	Action	Antagonist
Abductor pollicis longus	Ulna, radial styloid process	First metacarpal	Posterior interosseous artery	Posterior interosseous nerve (C7,C8)	Abduction and extension of the thumb	Adductor pollicis muscle
Extensor pollicis brevis	Radius	Thumb, proximal phalanx	Posterior interosseous artery	Posterior interosseous nerve (C7, C8)	Extension of thumb at metacarpophalangeal joint	Flexor pollicis longus muscle, Flexor pollicis brevis muscle
Extensor pollicis longus	Ulna	Thumb, distal phalanx		Posterior interosseous nerve (C7, C8)	Extension of the thumb (metacarpophalangeal and interphalangeal)	Flexor pollicis longus muscle, Flexor pollicis brevis muscle
Extensor indicis	Ulna	Index finger (extensor hood)		Posterior interosseous nerve (C7, C8)	Extends index finger, wrist	

The intrinsic muscles of the hand can be broken down into three main parts: the thenar, which is the lateral or thumb side of the palm and are essential to the hand's flexibility and its ability to grip; the hypothenar, which is the medial or little finger side of the palm and they help spreading the fingers apart, flex the pinky finger, and rotate the fifth metacarpal pulling it anteriorly whilst opposition with the thumb; and the intermediate or middle section of the hand, moves collectively from the second through the fifth metacarpals and the second through fifth phalanges in a wide range of ways.

Table 1.6: Muscles in the thenar lateral volar area of the hand

Muscle	Origin	Insertion	Artery	Nerve	Action	Antagonist
Opponens pollicis	Trapezium and transverse carpal ligament	Metacarpal bone of the thumb on its radial side		Median nerve	Opposition of the thumb	
Flexor pollicis brevis	Trapezoid, flexor retinaculum	Thumb, proximal phalanx		Median nerve, deep branch of ulnar nerve(medial head)	Flexion of thumb	Extensor pollicis longus muscle, Extensor pollicis brevis muscle
Abductor pollicis brevis	Transverse carpal ligament, the scaphoid and trapezium	Radial base of proximal phalanx of thumb and the thumb extensor		Median nerve	Abduction of thumb	Adductor pollicis muscle
Adductor pollicis	Transverse head: anterior body of the third metacarpal. Oblique head: bases of the second and the third metacarpals and the adjacent trapezoid and capitate bones	Medial side of the base of the proximal phalanx of the thumb and the ulnar sesamoid		Deep branch of ulnar nerve (T1)	Adducts the thumb at the carpometacarpal joint	Abductor pollicis longus muscle, Abductor pollicis brevis muscle

Table 1.7: Muscles in the Hypothenar Medial Volar Area of the Hand

Muscle	Action	Antagonist
Palmaris brevis	wrinkle skin of palm	None
Abductor digiti minimi	Abduction of little finger	None
Flexor digiti minimi brevis	Flexes little finger	Extensor digiti minimi
Opponens digiti minimi	Brings little finger into opposition with thumb	None

Table 1.8: Muscles in the Intermediate Area of the Hand

Muscle	Action	Antagonist
Lumbrical	flex metacarpophalangeal and extendinterphalangeal joints	None
Dorsal interosseous	Abducts finger	Palmar interossei
Palmar interosseous	Adducts finger	Dorsal interossei

The various skeletal and muscular degrees of freedom of the hand, orchestrated by highly developed neural control systems, allow for tremendous dexterity and variety of movement synergies that allows for both sensitive exploration and flexible manipulation and use of objects.

1.1.2 Human Motor System

The human motor system can be consider as a system composed by several different sub-systems. These structures are highly interconnected and work together to achieve function guaranteeing proper motor control (4). Voluntary movements are dominated by the motor cortex which acts on the spinal and brain stem motor neurones as well as extrapyramidal pathways in order to orchestrate voluntary movements. The primary motor cortex is an important source of the descending signals to execute these movements. The brain stem and spinal cord are often viewed as regions of the central nervous system (CNS) containing interneuronal-motoneuronal networks in charge of the production of reflexive and rhythmic motor behaviours and supporting postural non volitional movements (5). In Figure 1.7 a diagram of the general organisation of the motor system in humans from the cortex and its different pathways is depicted.

As shown in Figure 1.7, the motor cortex acts on the spinal and brain stem motor neurones to produce action upon the muscles. The motor pathways could be differentiated as: i) Descending pathways - in charge of distributing the signals for the actual movement; ii) re-entrant circuits modulating the ongoing activation, like a feedback control loop; and iii) cortico-cortical pathways which determine the interactions amongst the cortical regions in the brain (5) and most likely aid in motor learning and skill acquisition. Communication between the CNS pathways and the target muscles or sensory receptors is the peripheral nervous system (PNS). The PNS is the link between the CNS and the limbs and organs.

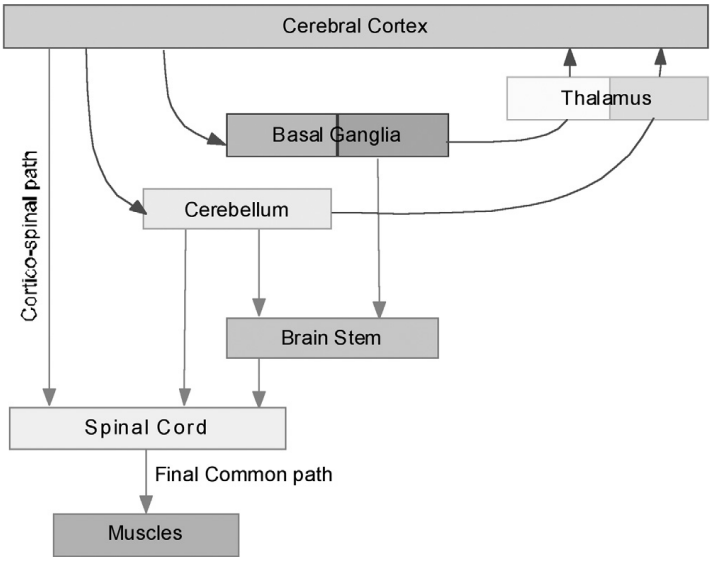

Figure 1.7: Diagram of the General Organisation of the Motor System in Humans - Simplified organisation of the motor system in humans. All the descending tracks originate from the cerebral cortex. The basal ganglia and the cerebellum play the role of coordination of movement through a modulatory influence of the cortex. Movement impulse make its way all through the spinal cord finalizing in the muscles.*From (5).*

The skeletal muscle fibres in mammals are innervated each, by a single motor neurone (6). In Figure 1.8, a diagram of the connection between the PNS towards the muscular activation is shown.

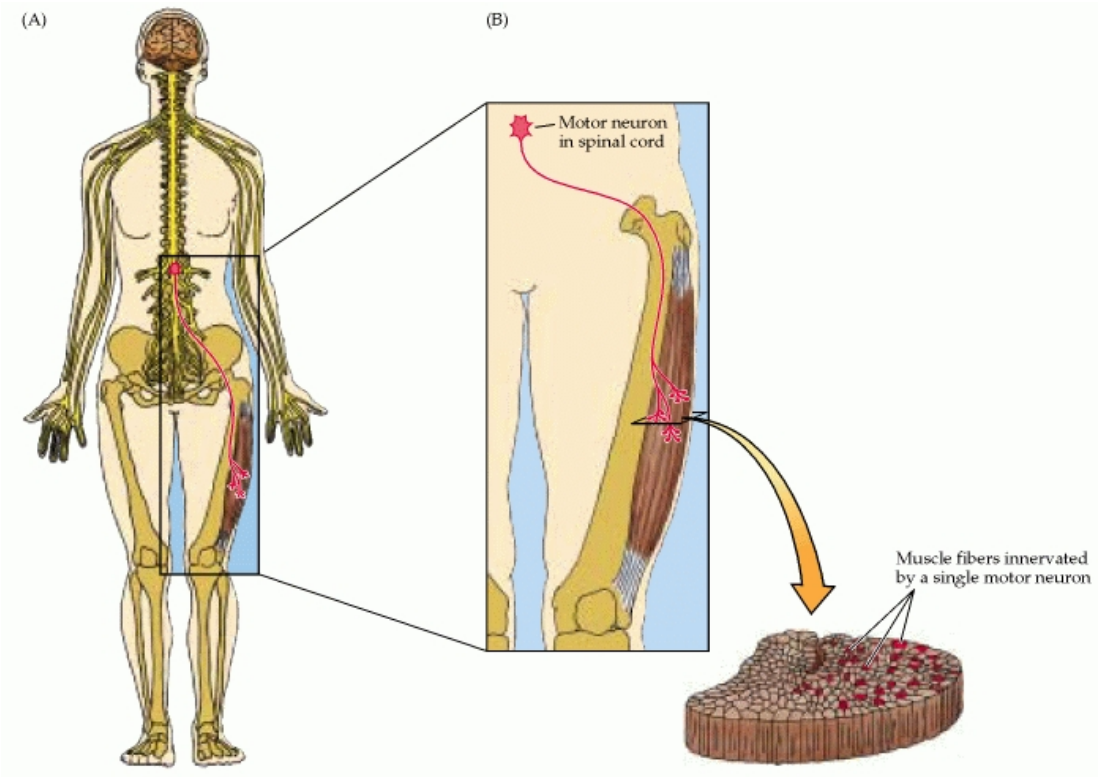

Figure 1.8: Motor Unit Activation Diagram - A) PNS connecting from a ventral horn in the spinal cord and the course of its connecting axon to the actuator (muscle); B) Each motor neurone found in the ventral horn connects to a several muscle fibres. The motor neurone and its connecting muscle fibres is known as motor unit. On the far right of this figure, a cross section of the muscle and the muscle fibre distribution is shown. From (6) - Copyright ©Sinauer Associates, Inc.

In the motor neurone, an action potential (also referred as a nerve impulse), is produced. This potential produces a contraction in the muscle cell which is perceived as movement (7). The stimulation produces a wave of electrical excitation propagated across the muscle fibre, as shown in Figure 1.9. The generation of this impulse is given by the opening/closing of ionic channels in the membrane.

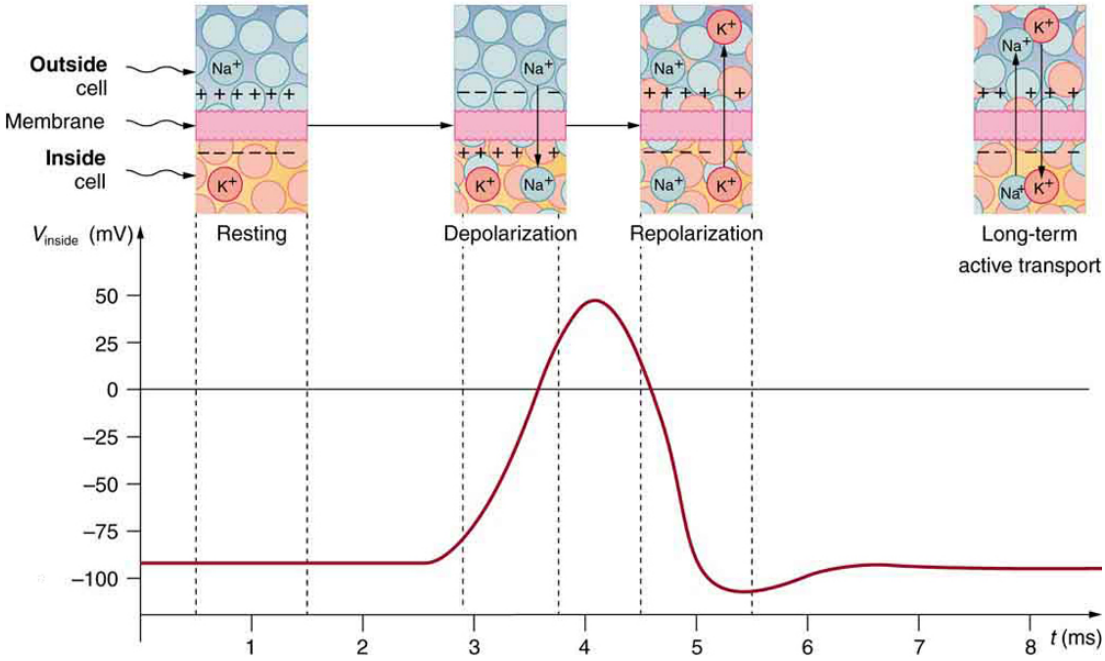

Figure 1.9: Propagation of Action Potential Across a Muscle Fibre - The impulse generated inside the nerve cell and the ionic movement across its membrane is depicted in this figure. Depolarization occurs when a stimulus causes the ionic channels to open causing sodium ions to permeate into the membrane causing a depolarisation. As a reaction, the ionic channels permeable to potassium open repolarising the cell causing the movement of this ions to propagate along the fibre causing an AP. From (8)

The ionic fluctuations in the membrane are classified in different ways [as shown in Figure 1.10]: resting potentials, and potential changes due to activity. The latter can be classified into different types of APs, e.g., transducer potential (produced across the membrane from an external impulse caused by synapses); and the ones arising from the previous (further response may arise if whether the magnitude exceeds the cell threshold). If the threshold is not exceeded a non-propagating response occurs, on the other side, an AP is produced obeying the 'all or nothing' law (9).

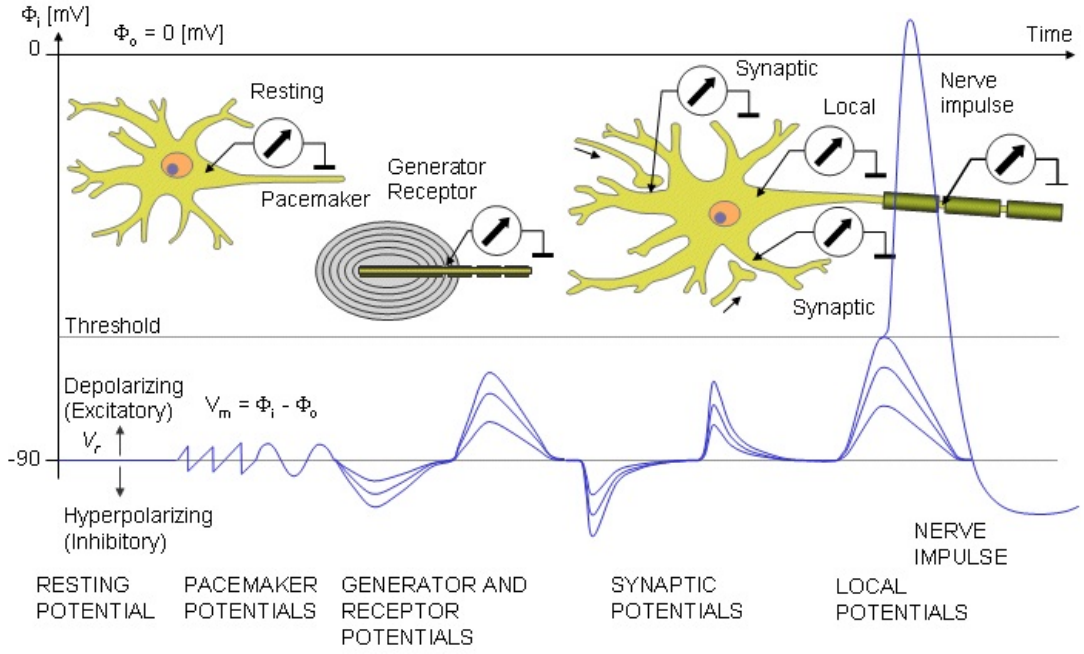

Figure 1.10: Transmembrane potentials according to Theodore H. Bullock - Transmembrane potential can be classified into different types: 1) Pacemaker potentials, 2) Transducer potentials, and 3)APs. For purpose of this research the only relevant potentials are resting potentials, neuromuscular synaptic potentials, and APs. *From (9)*

The resting membrane potential normally lies between -70mV and -100mV. The negative value refers to the cell being negatively polarised on the inside compared to the outside. AP propagation occurs rapidly when the threshold is reached resulting in a sharp spike. Once the membrane is depolarised more commonly by the action of acetylcholine in normal neuromuscular transmission, typically peaking at +30 mV (10), the extracellular fields generated by the AP waveform and its propagation along the muscle can be measured by placing a pair of electrodes within the volume conductor containing the muscle. This is the basics of electromyography.

1.1.3 Electromyography

The study of human motor function has progressed greatly as science has evolved throughout the years. Advances in anatomy and physiology started in late 18th century, with sophisticated techniques of brain tissue fixation and sectioning (5), providing more information on the structures of the brain. All muscle activity is controlled by the nervous system, and activity generated in neural, motor and sensory structures can be measured electrophysiologically by detecting the transient electrical signals. Electromyography (EMG) is the method used to study and monitor the spontaneous and voluntary activity of muscles throughout the body. The motor unit AP (MUAP) is a spatio temporal summation of individual muscle APs. Hence, the EMG is an algebraic summation of the MUAP and is influenced by distance from the signal source and separation from the source. This signal as well as being a function of time, is generally described in terms of its amplitude, frequency and phase (11). Moreover, the EMG signal is directly dependent on the anatomical (e.g., diameter of muscle fibre) and physiological properties of the muscles (e.g., distance between active muscle fibres and detection site). As the signal travels through the body, it is distorted and it acquires noise as it propagates through different tissues (i.e. adipose tissue thickness).

In general, EMG as a method can be categorised into two main types and two main approaches: clinical and research, and surface non-invasive recordings or invasive methods using intramuscular wires or needles. Clinically diagnostic EMG, is usually performed by a trained specialist with focus on features related to the duration and the amplitude of the MUAP, or the size and latency of evoked motor responses. In research studies, not only are parameters of MUAP waveforms of interest, but so are activation patterns across different muscle groups. This type of information form the basis for

much of the literature about analysis of movement. This type of EMG attempts to understand the relation between muscular functionality and the movement of parts of the body. The EMG method is subdivided by the type of electrode used for acquisition: surface or needle/inserted wire. Surface electrodes are also divided into two categories. The first is active electrodes, which have built-in amplifiers at the electrode site to overcome problems of amplitude impedance matching over long cables thereby reduced artefact picked up, and also allowing gel free electrodes to be used. A common application for this type of electrodes is their incorporation into commercial upper limb myoelectric prosthetics. The other type of electrodes are passive electrodes, that rely on low impedance interfacing between skin and electrode materials. This type of electrode normally is connected by long shielded cables of the amplifier system in order to detect the muscular activity. With this form of EMG, it is critically important to reduce the skin-electrode impedance by skin preparation and use of electro-conductive gels.

Table 1.9: Pros and Cons of the Different Type of Electrodes

Type of Electrodes	Pros	Cons
Surface Electrodes	∗ pain free ∗ easy to apply ∗ good for movement applications	∗ large pick-up area, therefore: ∗ susceptible to cross-talk ∗ tissue acts as filter ∗ prone to interference
Inserted /Needle Wire Electrodes	∗ increased bandwidth and signal amplitude ∗ localised pick-up area ∗ potential ability to track deep muscles ∗ isolation of specific muscles ∗ ability to test small muscles otherwise impossible to detect due to cross-talk	∗ requires specialised training ∗ can be painful ∗ electrical position can change during contractions ∗ less repeatable ∗ difficult to use in strong contractions

For purpose of this research, needle/inserted electrode acquisition will be put to a side and sEMG will be discussed further.

The sEMG signal varies from μV to mV . When sEMG is acquired, there are things

to be considered that have a direct impact on the quality of the recordings, i.e. distance from the active muscle area; the size of the electrodes; positioning of the electrodes; timing and intensity of muscular contraction; tissue in between the actuator and the electrode; and the quality of contact between the electrode and the skin (12).

Furthermore, factors such as: electrode properties (dimension, material, etc.); their interaction with the skin; and the amplifier design are relevant in the measurement and representation of the sEMG signal accurately. To remove common mode components (e.g., power line) and to compensate for the filtering effect of the tissue separating the muscle and the electrodes, the signals are commonly detected as a linear combination of different electrodes. The most common recording is the bipolar montage, where a pair of electrodes are used in addition to a common reference point. The aim of this is to maximise the amplitude of the signal while minimising the noise and rejecting commonly detected signals such as electrocardiography (EKG) and external fields.

The common sources of noise found while sEMG acquisition are:

- Ambient noise - Interference generated by electromagnetic devices. The type of devices considered within this category are mostly the ones that are plugged into the wall A/C current. The frequency ranges widely, however the most common frequency is that of 50Hz (Europe) or 60Hz (America) related to the power line.

- Transducer noise - This is generated from the electrode-skin connection. The electrodes pick up the ionic currents underlying the skin from the APs converting it into an electronic current easy to manipulate in the following stages with electronic circuits (allowing the A/D conversion).

The skin separating the muscles from the electrodes acts as a low-pass filtering of the actuator. Nowadays pre-amplifier design, incorporating high input impedance has reduced the importance of measuring sEMG with a low impedance in between sources.

A common problem with sEMG, specially when targeting small muscles is that the electrodes will not only record the activity belonging to the desired actuator, but of all the other muscles that might be active while doing a certain task. This phenomenon is known as cross-talk. Cross-talk can be reduced and sometimes avoided by choosing the right size of electrode, orienting it relevant to the muscle under study, and choosing an appropriate inter electrode distance depending on the application.

There are three main factors (Figure 1.11) that affect the sEMG signal:

1. Causative Factors - direct impact on signal. Could be extrinsic or intrinsic,
2. Intermediate Factors - physical and physiological phenomena caused by one or several causative factors, and
3. Deterministic Factors - caused by intermediate factors.

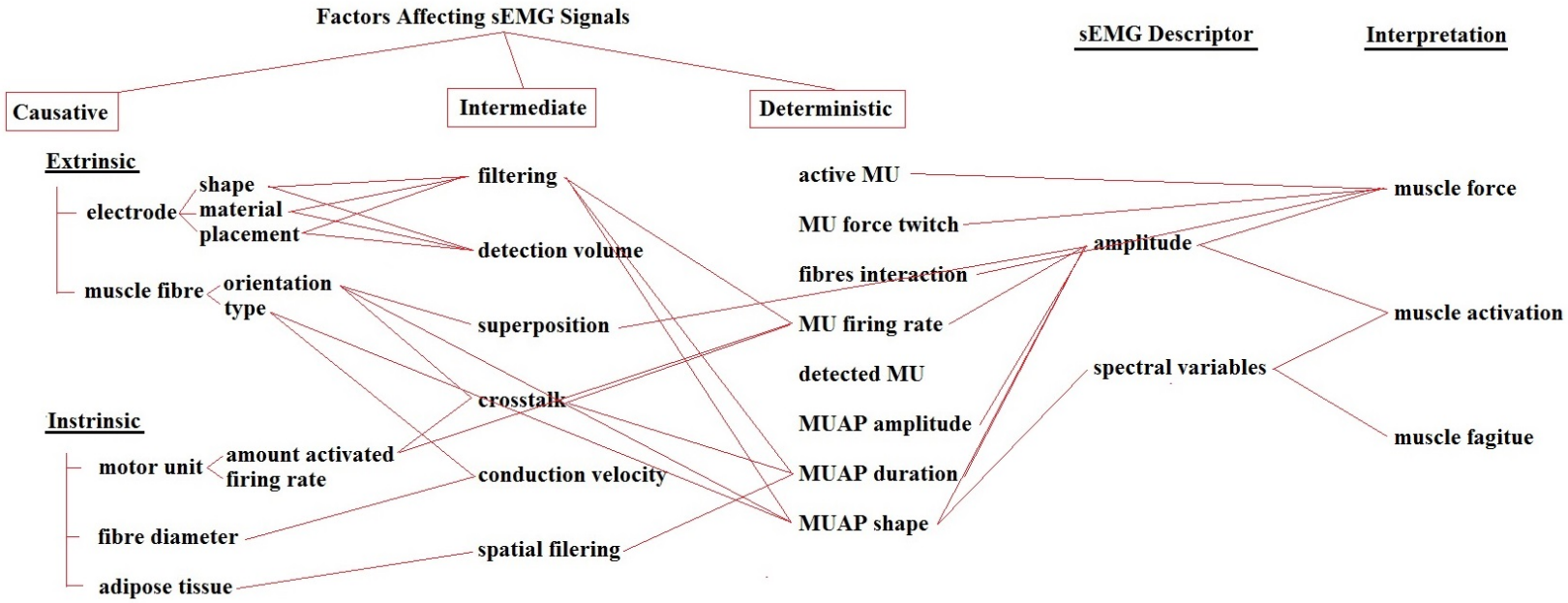

Figure 1.11: Factors Affecting the sEMG Signal - In this figure, causative factors are shown, this factors induce the intermediate factors that at the same time, induce some deterministic factors. Furthermore, it is depicted the descriptor that the sEMG has for each factor as well as its interpretation.

In recent years, work performed by one of the leading figures in developing EMG, Carlo De Luca and his research group has focused around spectral analysis of the EMG, motor unit recruitment and muscle fatigue. This has created a wealth of information relating to the properties of individual MUAPs and how they sum to create sEMG signal (13).

In the next section, sEMG instrumentation will be explained to gain a better understanding of the available systems for acquisition and to introduce to high-density sEMG.

1.1.3.1 sEMG Instrumentation

The acquired sEMG signal characteristics are dependent on the performance of the amplifier used to record them and the conditioning of the signal by filters or software algorithms. EMG distortion propagates as the field travels from the muscle within the volume conductor enclosed by the shin from where it is measured and visualised. A block diagram of this distortion is shown in Figure 1.12.

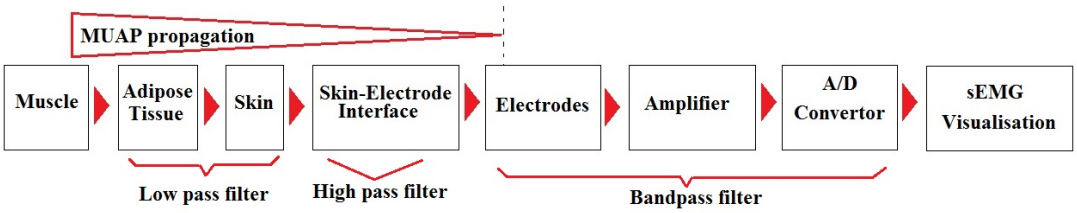

Figure 1.12: Block Diagram of the Distortion of the sEMG Signal During Acquisition - Block diagram of the general aspects during signal acquisition distortion. The muscle generates a signal that is acquired with a pair of electrodes. In between this two blocks we find passive filters that modify the sEMG visualization.

For an appropriate signal detection, a few factors have to be considered:

i) electrode configuration - detecting the electrical potential with respect to an isoelectric reference point situated in an electrically unrelated and inactive tissue. When a single electrode is used for detection it is called a monopolar configuration. When a pair of electrodes are used in addition to a common reference point, the term bipolar configuration is used;

ii) spatial filtering - As the signal travels throughout the biological layers (tissue), the amplitude attenuates with distance. The electrode placement with respect to the

length of the muscle fibres is crucial (14);

iii) electrode-electrolyte interface - the contact layer between the skin and the electrode forms an electrochemical bridge that behaves as a high pass filter. The amplitude and bandwidth of the acquired signal will be affected by this junction;

iv) amplifier characteristics - it has to be designed ideally with such a configuration that will have a minimal distortion over the acquired sEMG signal. The connecting cables should be shielded and ideally as short as possible preventing any electromagnetic field and avoiding any movement that might cause a change in the signal morphology travelling through them. As it was shown by De Luca (14), these phenomena might be reduced by applying a pre-amplifier located no more than 10cm away.

The vast majority of sEMG amplifiers have either a low gain avoiding signal saturation or incorporate a high pass filter to remove it. Another important feature for these type of amplifiers is their common mode rejection ratio (CMRR) (15). The CMRR describes the capability of the device to reject the power line voltage (mainly) and other conveying signals detected at the sensor sites.

Although the classic sEMG electrode configuration is bipolar, recent trends are moving towards a high-dimensionality in the electrode array. The main reason for this is that of accurate movement tracking. When a movement is being tracked by a bipolar recording any movement may cause the muscles under the skin (where the electrodes are fixed) to move in relation to the electrode. For this reason, using a matrix of electrodes results to be more effective in tracking of MUAP propagation.

1.1.3.2 High-Density Surface Electromyography

The possibilities of having different montages is one of the main features of the high-density sEMG (HD-sEMG) and this approach follows the introduction of high density electromyography over the past 20 years. Moreover, increasing the number of EMG electrodes has a direct impact on the number of recording positions, providing topographical information about the distribution of the activity of the muscle(s).

Multi-channel recordings allow a more intensive study of the muscles of interest and signal propagation shape through the muscle. By assessing the signal, one can be able to determine muscular regions, e.g,. endplate zone, belly muscle, tendons, etc. In Figure 1.13 some of the aforementioned regions are shown.

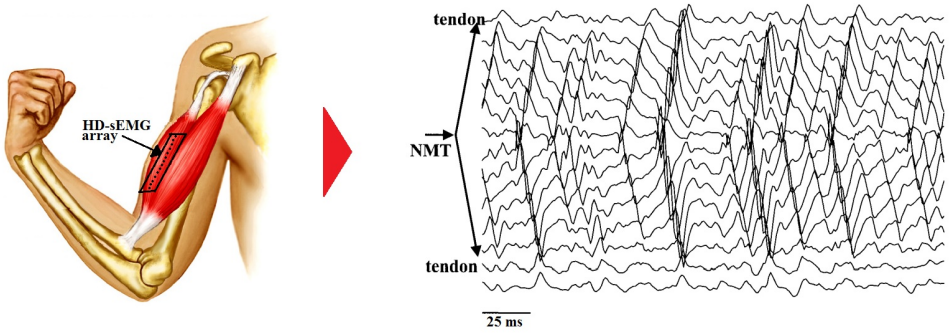

Figure 1.13: Example of an Acquired Signal from a HD-sEMG Array - Bipolar HD-sEMG montage over the biceps brachii. These signals represent 70% of MVC during an isometric contraction, with an i.e.d. of 10cm. The end plate zone (NMT) is shown and the propagation of the MUs is visible ('V' shape). It becomes clear that when an electrode sits on top of a tendon, the amplitude of the signal changes, as it was referred to in Figure 1.11. Adapted from Farina et al. 2002 (16).

Some of the HD-sEMG applications to date are related to i) movement (dynamic conditions); ii) ergonomics (muscles involved in joint stabilisation during working tasks); iii) exercise and sports; iv) obstetrics (locating IZ before epistonomy) (17). With this new technology, applications are expected to emerge specifically in the field of rehabilitation. In this research, HD-sEMG is applied to assess the activity patterns of the forearm to identify EMG patterns that can infer changed thumb positions from synergistic activation of muscles with no direct action on this digit. This has interest for the creation of ways to control robotic thumb as part of a myoelectric hand.

1.1.4 EMG-EMG Coherence

Coherence between different neurophysiological signals, including EMG, is reported to be related to factors of interest to motor control researchers and clinicians. Coherence is a frequency domain measure of coupling that is useful in the study of co-modulation of muscle activity, and the synchronisation of motor output directed to different muscle groups. It is mathematically obtained by dividing the cross-spectrum between two time series (input signals) by the root of the two spectra (similar to a correlation (18)). The cross-power spectrum is the fast-Fourier transform (FFT) of one of the input signals multiplied by the complex conjugate of the other input signal. The coherence estimate

ranges from 0 (absence of synchrony) to 1 (maximum synchrony). These values are irrespective of their amplitudes (19).

The coherence method is also a useful tool to study the presence of common rhythmic drive arising from the CNS during voluntary or involuntary movements. Farmer (20) showed in his synchronisation studies that coherent oscillations arising from common presynaptic connections to motor neurones generate a modulation of their discharges. This highlights that part of the motor drive is oscillatory in nature and produces a certain form of motor unit coupling. Further studies on muscle synergy by De Luca and Erim (21) introduced the concept of common drive, linking populations of motor-units within single and co-contracted muscles. The principle of common drive is that for co-contracting muscles, there must be a shared synaptic drive that brings a group of muscles to activate simultaneously. This common drive can be studied using frequency domain measures such as coherence, and time domain measures based on cross-correlation analysis.

If the activity showed by sEMG acquisition, belongs to a group of motor units, then the coherence or cross-correlation measures must show significant coupling between its muscles providing detail on the timing of the co-contracting drives(22).

Coherence coupling provides information on any rhythmic features in this coupling (shared drive) with the cross-correlation. The common drive concept also links to Henneman's size principle: 'A relationship exists between the susceptibility of a motoneurone to discharge and its size: the smaller the motoneurone, the higher the susceptibility to discharge' (23). In other words, a common drive from the CNS affects motor unit recruitment patterns in different muscles in a similar way depending on the individual motor unit propagation. An example of coherence analysis between simulated EMG-EMG synaptic inputs is shown in Figure 1.14.

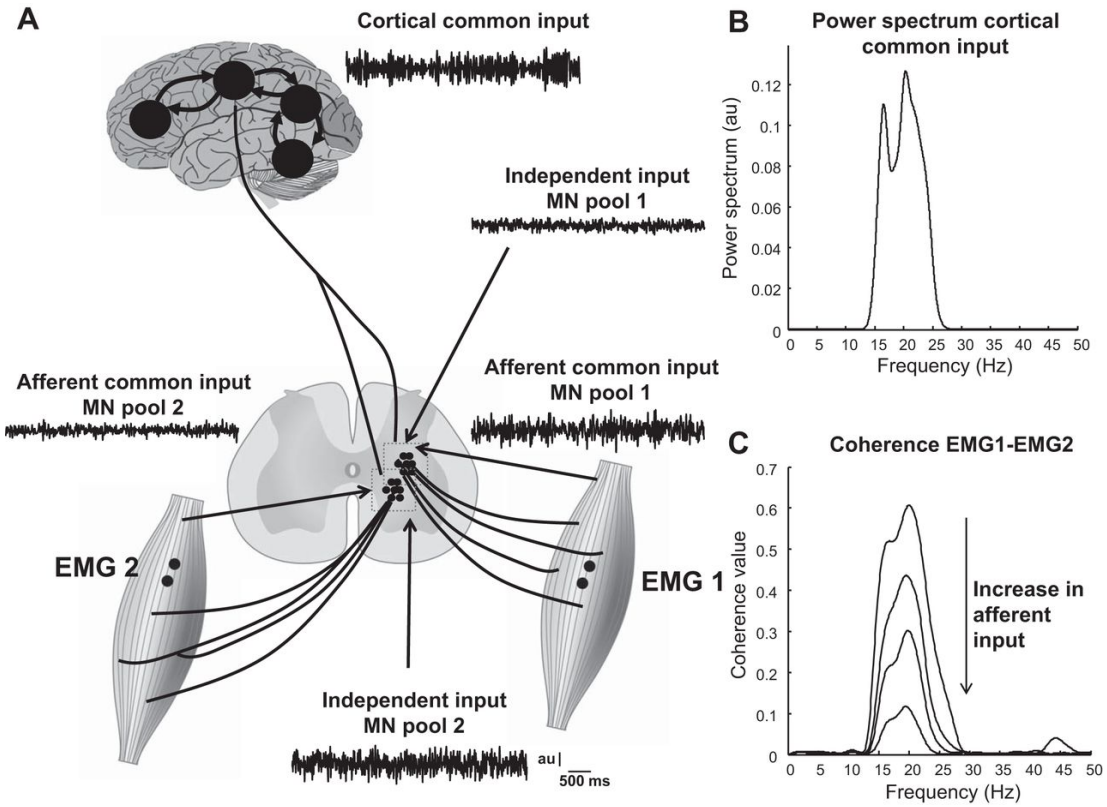

Figure 1.14: Example of Coherence Analysis Amongst Simulated Synaptic Input - Influence of a secondary common synaptic input on EMG-EMG coherence. A: 2 simulated pools of motor neurones receive 3 sources of synaptic input. The 1st is common to all motor neurones in both pools and is a cortical input, whose power spectrum is shown in B. The 2nd source simulates an afferent input to each motor neurone pool. This input is assumed to be independent for the 2 motor neurone pools but common to all motor neurones within each pool. The 3rd source of input is an input independent for each neurone. The common afferent inputs and the independent inputs were simulated as coloured noise processes with bandwidth 0100 Hz. Each motor neurone was simulated as a perfect integrate-and-fire system. Each motor neurone pool innervates a different muscle. The EMG-EMG coherence between the 2 sEMG signals of the 2 muscles was computed in 4 levels of common afferent input to 1 muscle (0, 10, 20, and 30% of total power). The total power of the 3 sources of input to each motor neurone pool was constant for all simulations and was normalized to 100%. The relative power of the cortical input was constant across all conditions and was set equal to 70% by altering the power of the independent inputs. For example, the 1st condition corresponded to 70% cortical input, 0% afferent input, and 30% independent input, whereas in the 2nd condition the powers were 70, 10, and 20%, and so on. Therefore, the strength of the common cortical input to the 2 muscles was identical for all conditions. Despite the invariance of the common cortical input, peak coherence ranged from 0.1 (30% afferent input) to 0.6 (0% afferent input) (C). Variation in the afferent input to the other muscle would have similar effects and concurrent variation of both afferent inputs would have additive effects. From Farina et al. (2014) (24).

Coherence and cross-correlation methods are powerful tools to use in studies on trying to understand the central drive muscle groups that co-activate during movements. It is therefore a potentially useful method to use in investigating coupling of forearm and thus muscle activation in this study.

Leading to comprehensive results in order to classify the HD-sEMG patterns, and the synergistic behaviour between the muscles of the hand aiming to improve the control in the myoelectric-upper limb prosthetics, machine learning must be brought into context. This method is applied in this research in means of unsupervised learning with aims to cluster the different EMG patterns for prosthetic control.

1.1.5 Machine Learning

Learning is a distinctive feature of human intelligence and the principal way to obtain knowledge. Over the last years, there has been a growth in artificial intelligence capability and its applications. In parallel, an increasing interest in machine learning has emerged. Machine learning is a field involved with the development of computational theories around learning processes and interconnected with building learning machines.

Learning is an activity with others like memory; thinking; perception; feeling; amongst others, closely related (25).

In recent years, machine learning has focused on how to use computers to simulate human learning activities. Computational resources have one advantage over the humans: they do not get bored or lose attention when repeating the same task many times; therefore, they are also used to study self-improvement methods. These self-improvement methods are where artificial intelligence obtains new knowledge and new skills, and with that, improve in their performance and achievements.

Arthur Samuel (1959) (26) defined machine learning as a field of study that would give computers the capacity to learn without being programmed for a particular task. Samuel created the checkers playing programme and ran it for over a 10,000,000 times. After these iterations, the programme was able to learn over time, learning the prediction of movements, and becoming an expert, by the end of many games, the machine was able to beat him.

Tom Mitchell (1998) refers to machine learning as

> "a computer program that learns from experience E with respect to some task T and some performance measure P, if its performance on T, as measured by P, improves with experience E " (27)

In Figure 1.15, the basic model of machine learning is shown. In the process of machine learning, the quality of the information is obtained from the surroundings, providing the system with the primary factor (27). This information is then passed and transferred into knowledge (by the learning process); this knowledge is passed and stored where general principles guide the implementation action.

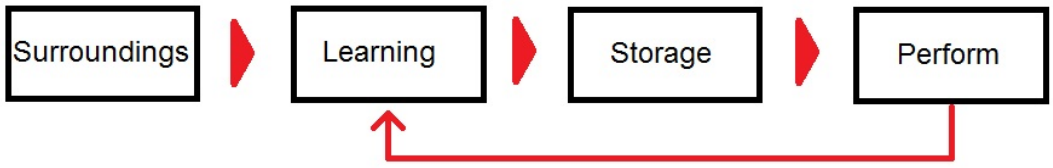

Figure 1.15: Basic Flow Diagram of Machine Learning - Basic model of machine learning process. In general, 4 stages can be consider: surroundings - the quality of information is provided; Learning - the outside information is processed to knowledge; storage - general principles are stored that guide the implementation of action; and perform - implements the knowledge from the storage to complete a determined task, and feed back the information obtained to the learning stage.

Algorithms used for this type of learning are based on mathematical and computational methods to acquire knowledge and to learn directly from the input data without a predetermined equation as model. Having the ability to adapt and improve their performance as the number of samples available for learning increases. This is particularly relevant in this research that aims for a natural control in a myoelectric prosthetic device to be able to direct the movement desired by means of the sEMG patterns.

Machine learning algorithms are extensively used in applications such as computational finance [(28) and (29)], energy production [(30), (31)], computational biology [(32), (33) and (34)], natural language processing [(35) and (36)], amongst many more.

There are some inherent challenges when this algorithm is used, there is no 'one size fits all' solution, on the contrary, it is an iterative approach which, depending on the methodology applied, may becomes time consuming.

The importance of this methodology in this research, lies in the ability to clearly identify different movements from sEMG patterns. With this patterns clearly defined,

this is particularly of interest as a way to control and improve the communication between man and machine (patient-myoelectric upper limb prosthetic).

Machine learning can be branched into two types of learning methodologies: i) unsupervised learning, and ii) supervised learning. For the first one, the data are grouped (based on some similarities or characteristics) and interpreted based only on input data. For the latter, a predictive model is created based on both input and output data (response variable).

1.1.5.1 Supervised Learning

For this machine learning methodology, a predictive model is developed based on both input and output data (response variable). Expectation of factors will have an impact on the response without much understanding between the relation in between the input and the factors. If the response is discrete in nature, it becomes a classification process, on the other hand, if it is continuous in nature, it is a regression process. In Figure 1.16 a generic block diagram is shown.

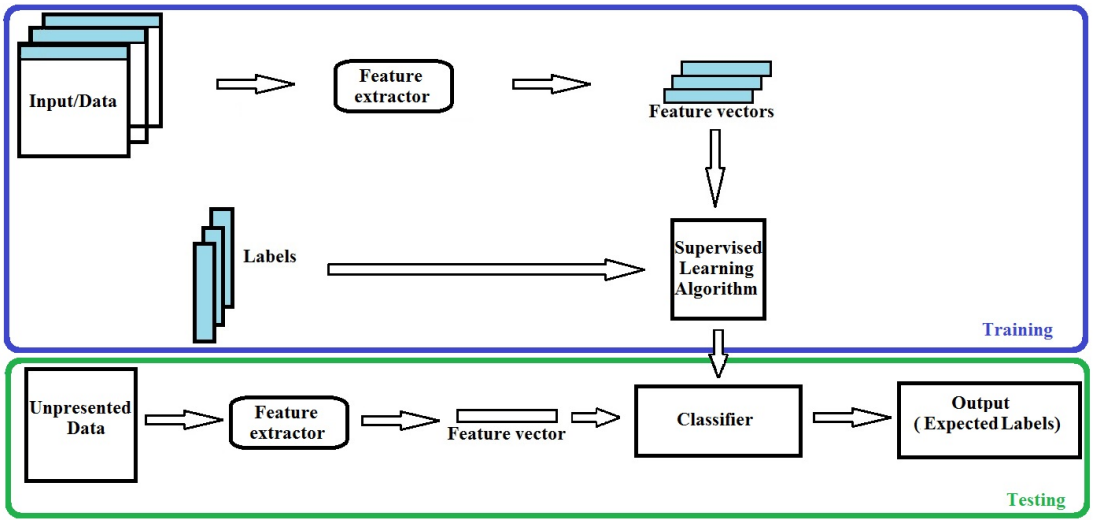

Figure 1.16: Generic Block Diagram for a Supervised Machine Training Algorithm - In this figure two stages are depict: training and testing. For a supervised algorithm, during the first stage, labels are introduced with the data into the machine-learning algorithm. During the testing stage, new data is introduced into the classifier and an output is presented.

For the purpose of this research, the supervised algorithms will not be reviewed

but they are available from the following references: regression algorithms [(37) and (38)], neural networks [(39) and (40)], decision trees [(41) and (42)], ensemble methods [(43) and (44)], non-linear regression [(45) and (46)], classification algorithms [(47) and (48)], support vector machines [(49) and (50)], discriminant analysis [(51) and (52)], naive bayes [(53) and (54)] and nearest neighbours [(55) and (56)].

1.1.5.2 Unsupervised Learning

This machine learning methodology groups the data based on some similarity or characteristic, without a priori knowledge about the grouping. The unsupervised learning uses clustering techniques to help group data.

In an unsupervised procedure, unlabelled input data is used to estimate the parameter values for clustering. In Figure 1.17 a generic block diagram for an unsupervised machine learning training algorithm is depicted. In the following sections, some clustering algorithms relevant to this research will be discussed.

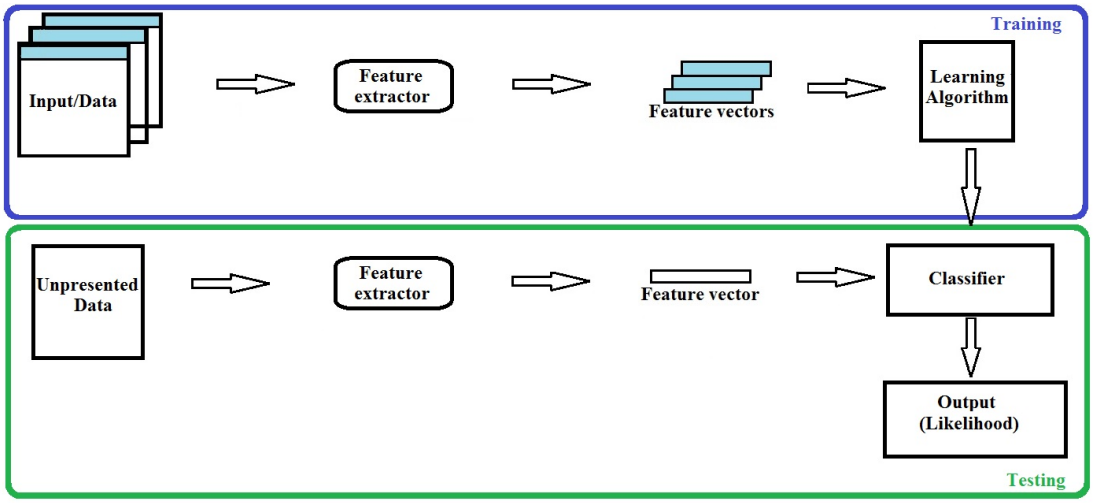

Figure 1.17: Generic Block Diagram for an Unsupervised Machine Training Algorithm - Two stages can be appreciated in this figure. The first one, training, data is presented to a machine learning algorithm and this classifies the data according to differences in between their feature vectors. The second one, is the training, where new data is presented and the each new feature vector is classified depending on the likelihood found amongst the trained data and the new data.

Clustering Algorithms

K-Means - This is an algorithm that estimates the unknown cluster centres (a.k.a. means) $M = \{\mu_1, ..., \mu_K\}$ based on the input data $D = \{x_1, ..., x_N\}$. Aiming to minimize

$$J(M) = \sum_{i=1}^{N} \|X_i - \mu i\|^2 \tag{1.1}$$

where μ_i is the closest cluster centre to x_i.

The K-means algorithm is simple and has a local optimization algorithm; although the cost function of $J(M)$ may not be suitable since the different size of clusters cannot be separated. In Figure 1.18 a random classification example of this algorithm is used.

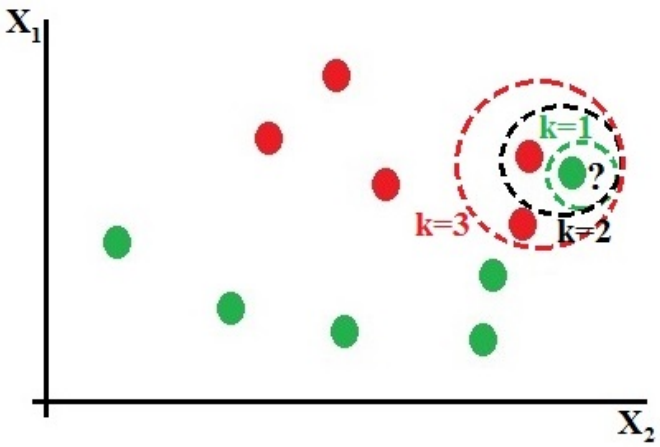

Figure 1.18: Random KNN Classification Example - This example consists in two variables: X1 and X2, and two classes: red and green circles. The question mark represents a new instance in need to be classified. a 1-nearest neighbour classifies an unlabelled instance as a green circle. A 2-nearest neighbour looks at the two closest examples these being a red and a green circle bringing it to a tie, having to go for a 3-nearest neighbour which would classify our unknown instance into a red circle (two reds vs. one green). Setting k at an odd value avoids ties in the class assignment.

Principal Component Analysis - Principal component analysis (PCA) (Jolliffe, 2002) (57) is a method that can be used to reduce data with high dimensionality. To decrease it, PCA uses a lower dimensional presentation computed in such a way that

a minimum amount of information is lost. The task is to find an alternative mapping from the original d-dimensional space to a k-dimensional subspace where $k < d$. In addition to dimensionality reduction, PCA is widely used for other applications such as feature extraction, data visualization, image processing, pattern recognition and time-series prediction, as it will be seen throughout the machine learning results of this thesis.

The most common formulation of PCA, the maximum variance formulation, defines PCA as an orthogonal projection of the data onto a lower dimensional linear space (a.k.a. principal subspace), in which the variance of the data is maximized, that is, the maximum amount of information is preserved (58).

Self-Organising Feature Maps - The self-organising feature map is an unsupervised artificial neural network algorithm which aims to discover underlying structure in the input data. The SOFMs preserve topology by having an explicit neighbourhood function that preserves its relations between neurones. They quantize the feature vectors (FV) from the input by defining the neighbourhood relations of the codebook vectors.

Neurones of the SOFMs are called map units or prototypes. These map units are seen to be a representative sample of the data (codebook vectors in vector quantisation). Each map unit is associated with a reference vector m_i. The reference vectors m_i are weighted local averages of the data associated with the given map unit in the original data space. A graphical example is shown in Figure 1.19.

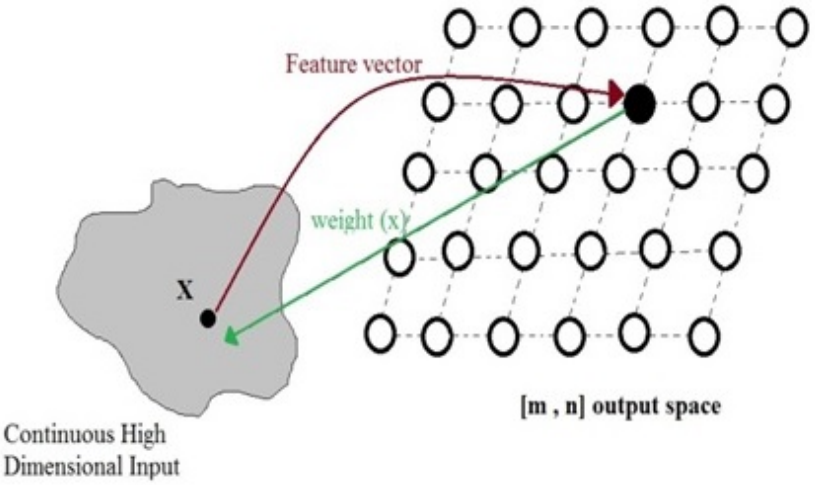

Figure 1.19: Self-Organizing Feature Map Scheme - Organizational maps of a continuous high dimensional input. The weight in between each point of the output space is given by de Euclidean distance in between an output point and the input space.

In this research, a two-dimensional SOFM will be used; therefore, the SOFM will define a mapping from the input data space onto a two-dimensional plane. Every map unit i is referenced to a parametric vector (a.k.a. model vector) $m_i \in \Re^d$, where d is the dimension of the data.

Two different types of lattices can be used for the array of units in the neighbourhood, hexagonal and rectangular. To avoid any preference on the training regarding the direction it moves in the map, an hexagonal lattice is generally preferred. In Figure 1.20, an example of an hexagonal and rectangular lattices are depicted.

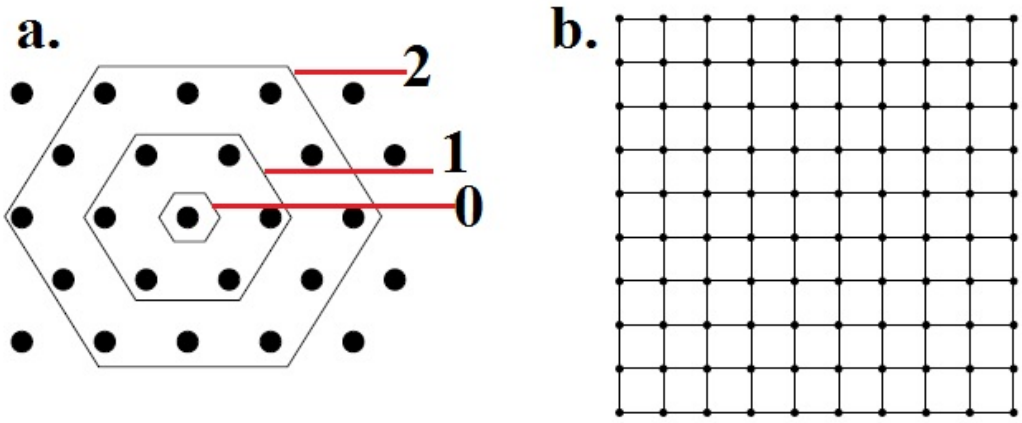

Figure 1.20: Type of Neighbourhoods for a Self-Organizing Feature Maps Training - Discrete neighbourhood of three different sizes (0,1,and 2) and map shape. a. Hexagonal grid, the innermost polygon corresponds to a topological neighbourhood N(t) where t = 0,1,2., where N(2) less than N(1) less than N(0) b. Sheet map shape, each vertex represents one feature vector

Defining a training data matrix as $\mathbf{X} \in \Re^{N \times d}$ where N is the sample number and d is its dimensionality; the model vector (m_i) is used to refer to the units and their vector in the same way.

The Euclidean distance is the core of this method (equation 1.2). The unit with the smallest Euclidean distance is referred to as the best-matching unit (BMU) of the data vector x_n (equation 1.3).

$$d_e(x, y) = \sqrt{(\xi_1 - \eta_1)^2 + (\xi_2 - \eta_2)^2 + \cdots + (\xi_n - \eta_n)^2} \tag{1.2}$$

$$m_{c(x_n)} = argmin_i \, \|x_n - m_i\| \tag{1.3}$$

Figure 1.21 depicts how the BMU is updated towards the input x.

The SOFM updates the weight of the vector i through equation 1.4 as described by Vesanto (2000) (59).

$$m_i(t+1) = m_i(t) + \alpha(t) h_{ci}(t) \, [x(t) - m_i(t)] \tag{1.4}$$

where,

t denotes time;

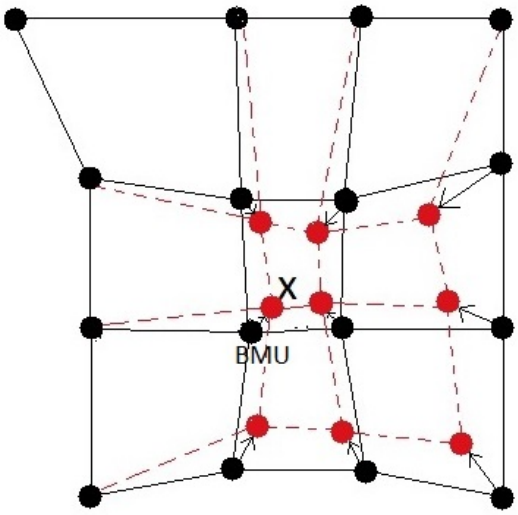

Figure 1.21: Updating The Best-Matching Unit - The BMU and its neighbours are updated towards the input x. The black solid line corresponds to the instant before training and the red dashed line to the instant after being updated.

$x(t)$ is an input vector randomly drawn from the input data set at time t;
$h_{ci}(t)$ is the neighbourhood kernel around the winner unit c,
and $\alpha(t)$ the learning rate at time t.

The neighbourhood kernel is a non-increasing function of time and of the distance of unit i from the winner unit c.

The neighbourhood function is defined by the Gaussian function described in equation 1.5, where $\|r_c - r_i\|$ is defined as the distance between the BMU: r_c, and unit i in the array; the learning-rate factor is $0 < \alpha(t) < 1$, and $\sigma(t)$ is the width of the neighbourhood kernel.

$$h_{ci} = \alpha(t) \cdot exp\left\{\frac{\|r_c - r_i\|^2}{2\sigma^2(t)}\right\} \tag{1.5}$$

During the training, each input vector is chosen randomly, and the training updates on each iteration using the equation 1.6:

$$m_i = \frac{\sum_n h_{ni} x_n}{\sum_j h_{ni}} \tag{1.6}$$

where,
j and n run over the vectors of data whose BMU satisfy $h_{ni} > 0$.

The size of the map to be trained is a crucial part of this method. Choosing a size randomly could have an impact in the quality of the map, as well as its accuracy. The size of the map is indirectly proportional to the quantization error and directly proportional to the topological error, that is, the bigger the map the quantization error decreases but the topological error tends to increase (60). The determination of the map size can obtained through the equation 1.7

$$map\ units = 5 \times dlen^{0.54321} \tag{1.7}$$

where, dlen is the number of repetitions.

After choosing all the parameters and type of training, this information is fed into the system and the SOFMs trains the data. Unified matrixes (Figure 1.22), also known as U-matrix, are used as assistive visual tools to understand how the different clusterings occur. Parameters such as sensitivity and specificity are used to asses the quality and reliability of the training. Sensitivity gives the positive rate, i.e. the test's ability to identify positive results, and the specificity provided the true negative rate, i.e. the proportion of negatives that were correctly identified as such.

For the purpose of this research, other unsupervised clustering algorithms will not be reviewed but they are available from the following references: fuzzy c-means [(62), and (63)], hierarchical (64), Gaussian mixture model (65), and hidden Markov model [(66), and (67)].

Unsupervised learning, more specifically SOFMs, are effective tools to use in studies on trying to categorise and cluster different inputs without a prior knowledge about them. Then, in all likelihood, it is a useful method to use in investigating the different sEMG patterns in relation to different thumb positions, relevant to this study.

The importance of machine learning algorithms in this research, is to improve the available myoelectric upper limb prosthetics. The unsupervised nature of the method, aims to provide dexterous control using the EMG propagation signals as input vectors. This dexterity is expected to be achieved through the extraction of sEMG features without giving any prior knowledge leading to improve the quality of life of an amputee.

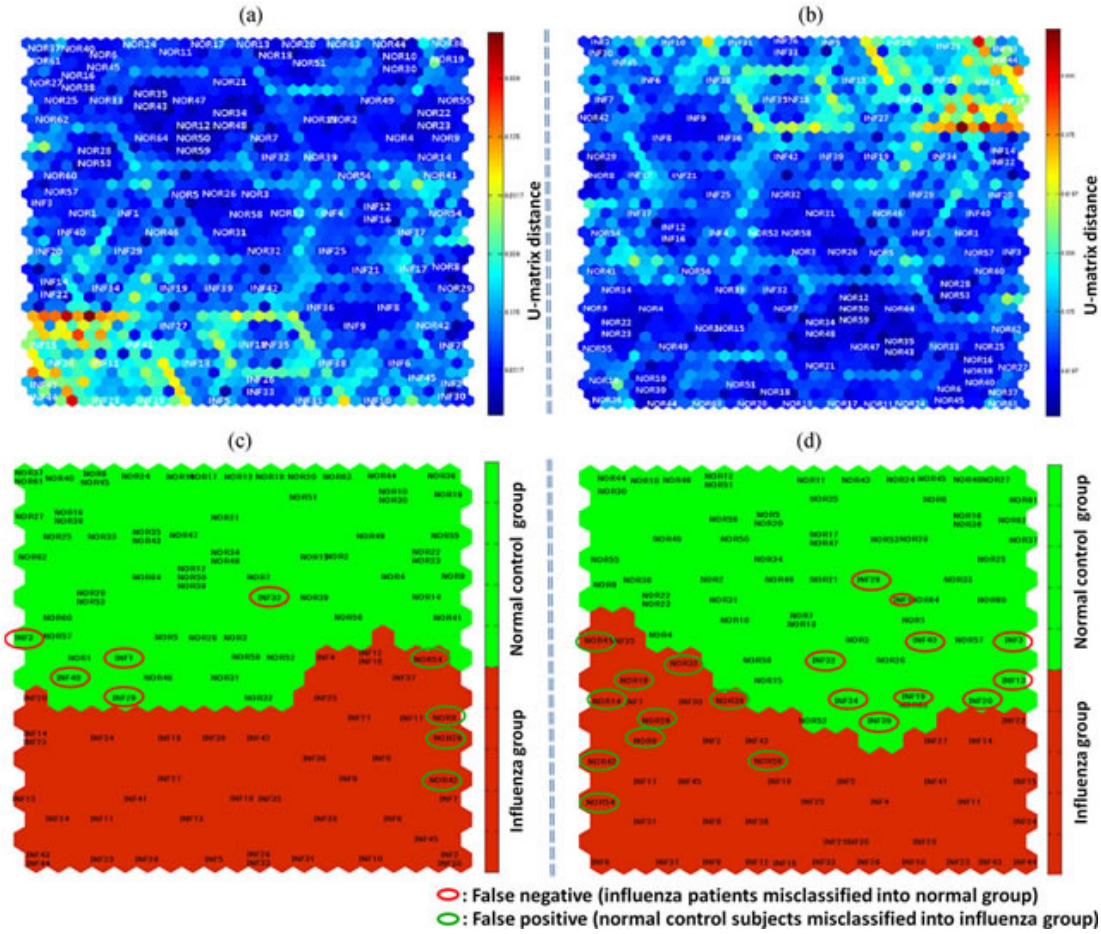

Figure 1.22: Generic Example of an Unified Distance Matrix - Generic example of the unified distance matrix (U-matrix) based on an infection screening system that uses vital signs and percutaneous oxygen saturation for influenza screening. (a) and (b) The SOM clustering result is visualized on a 2-dimensional map using U-matrix. (c) The SOM map created from the data obtained from a total of 109 subjects on the basis of 4 parameters including SpO2. Normal control subjects were included in the normal group (green cluster). Five patients with influenza (circled in red) were misdiagnosed as normal and 4 normal control subjects (circled in green) were misdiagnosed as infected. (d) The SOM map developed on the basis of the data from the same subjects, but by using only 3 parameters, excluding SpO2. Herein, 35/45 patients with influenza were included in the influenza group (red cluster), and 54/64 normal control subjects were included in the normal group (green cluster). Ten patients with influenza (circled in red) were misdiagnosed as normal and 10 normal control subjects (circled in green) were misdiagnosed as infected. From (61)

In the following Section, upper limb amputations will be reviewed. Furthermore, details regarding the device abandonment, the type of prosthetics commonly used in UK, and a brief history regarding upper limb prosthetics will be provided.

1.2 Upper Limb Amputations

The loss of an upper limb due to trauma or disease results in sudden loss of function, sensation, and is a far greater catastrophe for the individual than the loss of their lower limb. Furthermore, children born with congenital limb loss also suffer from loss of function compared to normal able bodied people. Research into upper limb prosthesis aims to develop devices that have functionality similar to the natural hand in terms of control, stability, dexterity, coordination and sensory feedback as being comfortable, light weight, realistic in appearance.

When an upper limb is seriously compromised due to trauma, there are various ways that amputations can be carried out. These amputations depend on the specific part of the limb that needs to be removed and how much of it can be saved.

According to the NHS (68) the main type of upper limb amputations performed are finger or digit amputation; transhumeral amputation; transradial amputation; wrist disarticulation; and elbow disarticulation. The aforementioned levels of amputation are schematically shown in Figure 1.23. There are many factors that can determine how much or how little of the limb is amputated. In general terms, the more remaining limb and the more joints that are kept intact, the easier it is to be fit with and use of a prosthetic device.

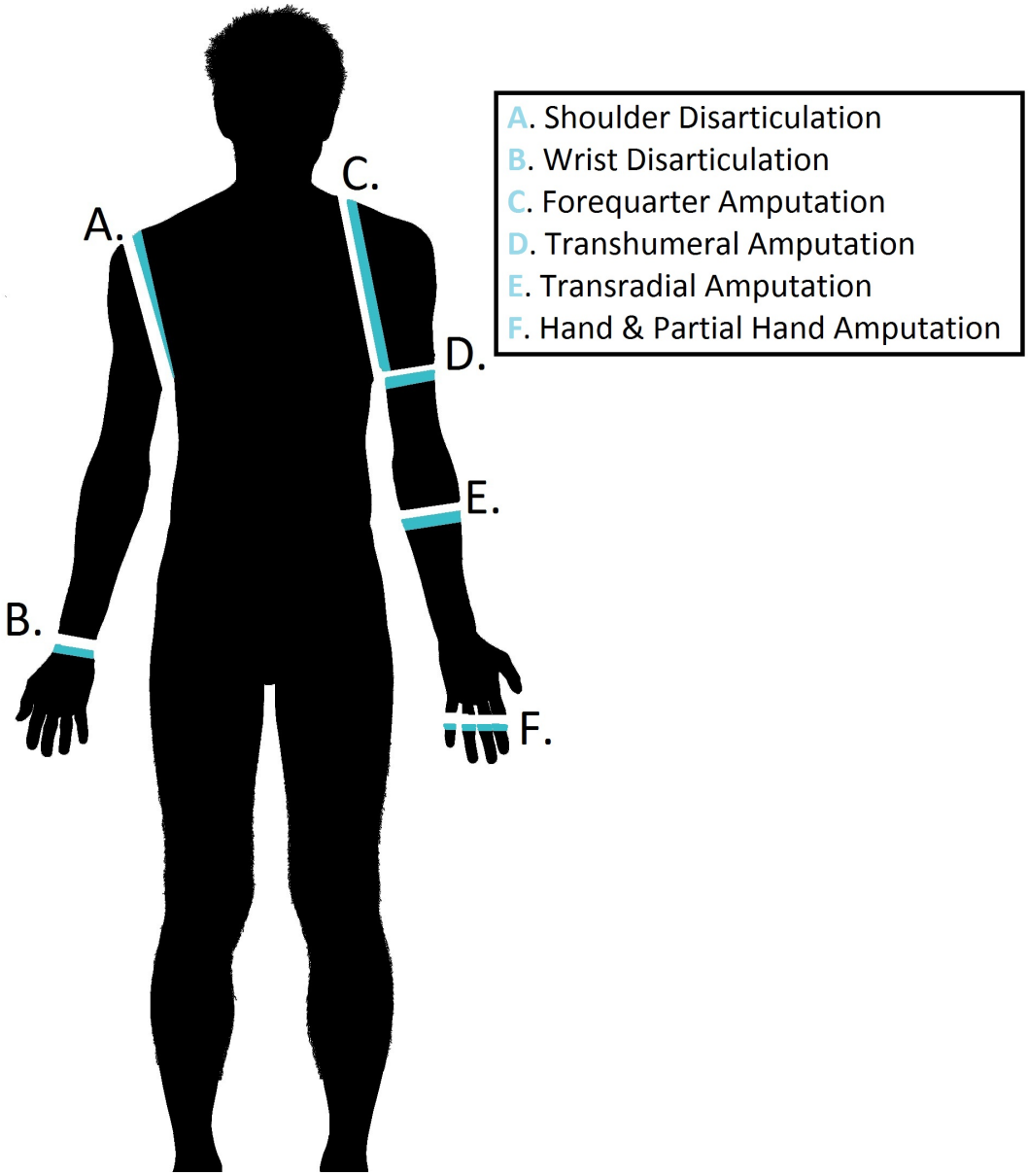

Figure 1.23: Upper-Limb Amputation Levels - Six main levels are consider for the upper-limb amputations: A. Shoulder Disarticulation - The shoulder blade is kept, the collarbone may or not may be removed; B. Wrist Disarticulation- The limb is amputated at the level of the wrist bones; C. Forequarter Amputation-Amputation where the shoulder blade and the collarbone are removed; D. Transhumeral Amputation - Limb is amputated somewhere in between elbow and shoulder; E. Transradial Amputation - Limb is amputated from the elbow to the wrist; F. Partial & Partial-Hand Amputations - Finger(s), thumb or portion of the hand below the wrist.

1.2.1 Current Types of Upper Limb Prosthetics

With a great number of upper limb amputees all over the world each of them with different needs, there has been a variety of prosthetic options available in the market. The different types available are: body powered; myoelectric; passive (also known as cosmetic); and hybrid.

Body Powered - The body powered prosthesis is operated by a harness system. This system is controlled by a specific body movement which triggers the prosthesis to move in a certain way. This type of device is lighter and less expensive that myoelectric devices with adhered reduced costs and maintenance.

Myoelectric - This device is powered by a rechargeable battery system and is controlled by EMG signals acquired from muscle contractions. This prosthetic offers cosmesis restoration as well as functionality.

Passive / Cosmetic - This type of device aims to give the same appearance as the non-affected arm. The cosmetic prosthetic aims to provide aid in balancing.

Hybrid - The hybrid prosthetic combines both myoelectric and body powered. The only advantage that this type of device has is the greater functionality and the costs of maintenance are reduced.

1.2.2 Statistics about Amputation

In the UK, there is a high risk of trauma resulting in limb amputations. Deformity or illnesses such as diabetes, gangrene, also are major causes of amputation. Approximately 5-6,000 major limb amputations are carried out in England every year (69).

Not all the amputees are suitable for a prosthetic limb and those that are, get assessed and treated by a prosthetist, who will determine the state of the body and the type of prosthesis that is suitable for a patient.

The United National Institute for Prosthetics & Orthotics Development (UNIPOD) is in charge of producing a repository for the quantitative information on the UK limbless population who are referred for prosthetic treatment. This repository includes

data for demographic and clinical quantitative, anonymised information grouped by cause; level; site; and side of limb absence.

In the following Sections, the demographic and clinical quantitative data will be presented according to the last available report from UNIPOD accessible online (Limbless-statistics.org) for UK limbless population dated from 2010-2011.

1.2.2.1 Amputees registered and referred for prosthetics treatment in 2010-2011

A total of 473 upper limb amputees were referred between 2010-2011 for prosthetic treatment. This population varies in widely in demographics (gender and age) and in side, level of amputation and prosthesis assigned. In Figure 1.24 the data is shown by side (left/right) according to each level of amputation registered (also depicted in the previous Figure 1.23). From this graph, we can appreciate that the transhumeral, transradial and hand digit are the most common levels of amputation and the spread between sides is, in general, 50-50.

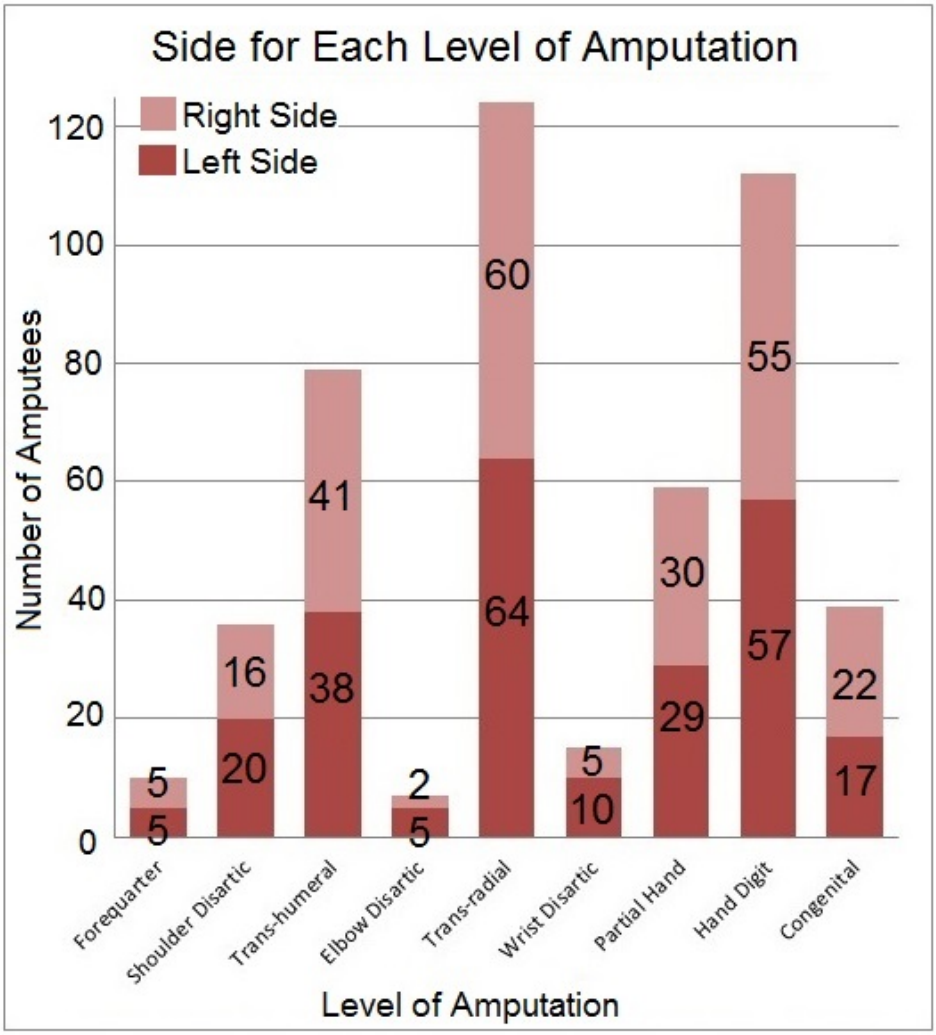

Figure 1.24: Side Spread by Level of Amputation. Registered from 2010-2011 in the UK - Correlation in between the side of amputation, i.e. left or right, and the level of amputation registered. A total of 473 amputees was examined. Data Source: UNIPOD (70). Table 14(3-4), p.77. Version 29-04-2013.

In Figure 1.25 the data is shown by gender (male/female) according to the aforementioned levels of amputation registered. As the previous case, the transhumeral, transradial and hand digit are the most common occurring levels of amputation and the spread between them has a slight tendency to the male population. This tendency might be due to the job that some males have over the female population that might impact in the usage of heavy tools or machinery or to participating in high risk past-times such as motorcycling.

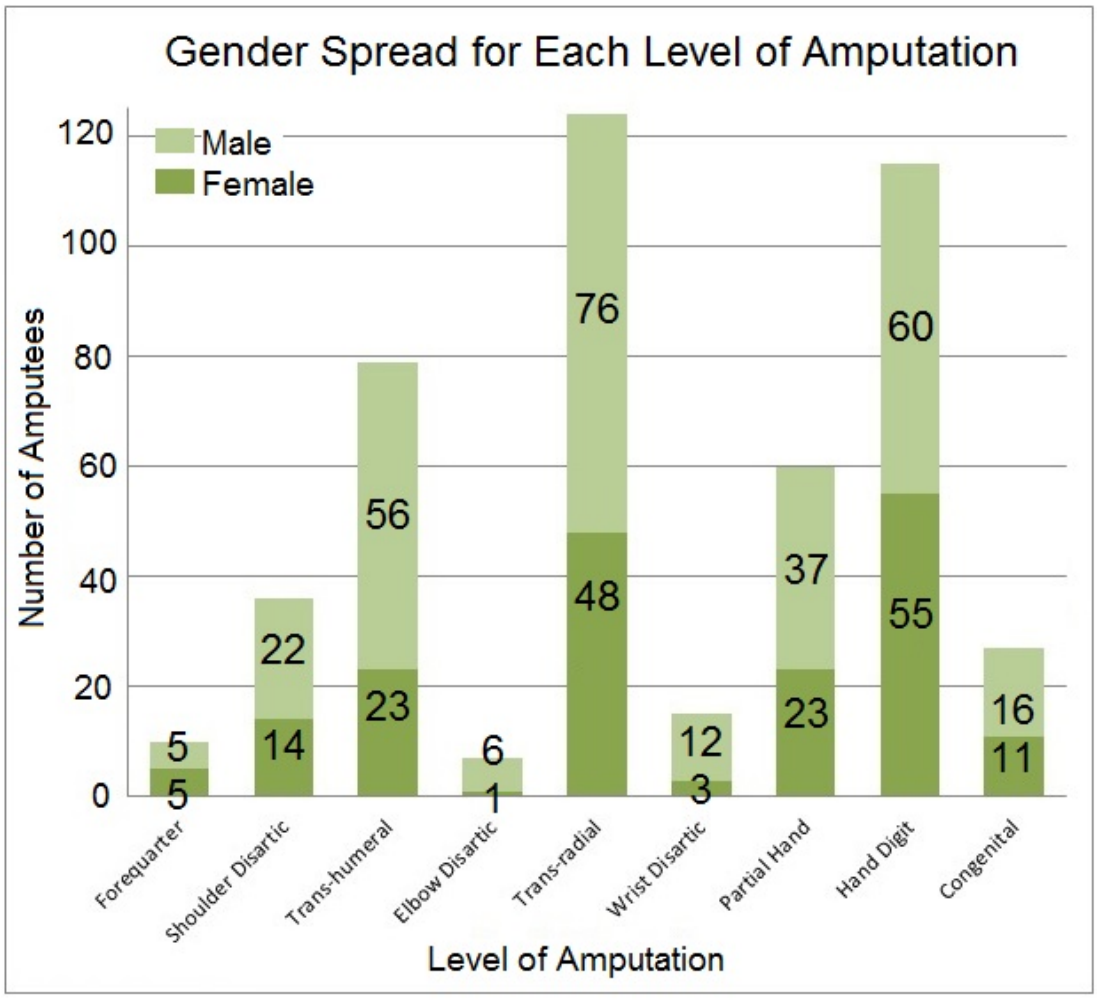

Figure 1.25: Gender Spread by Level of Amputation. Registered from 2010-2011 in the UK - Correlation in between the gender of the amputee, i.e., male or female, and the level of amputation registered. A total of 473 amputees was examined. Data Source: UNIPOD (70). Table 14(3-4), p.78. Version 29-04-2013.

From all amputees that were recorded (473), 29% patients referred to prosthetic treatment did not record the cause of amputation, from the remaining 71% amputations due to trauma and congenital are almost the same (28% and 27%, respectively), the remaining 16% is split between different pathologies i.e. dysvascularity, infection, neoplasia, neurological disorders and infection. This is better understood in Figure 1.26.

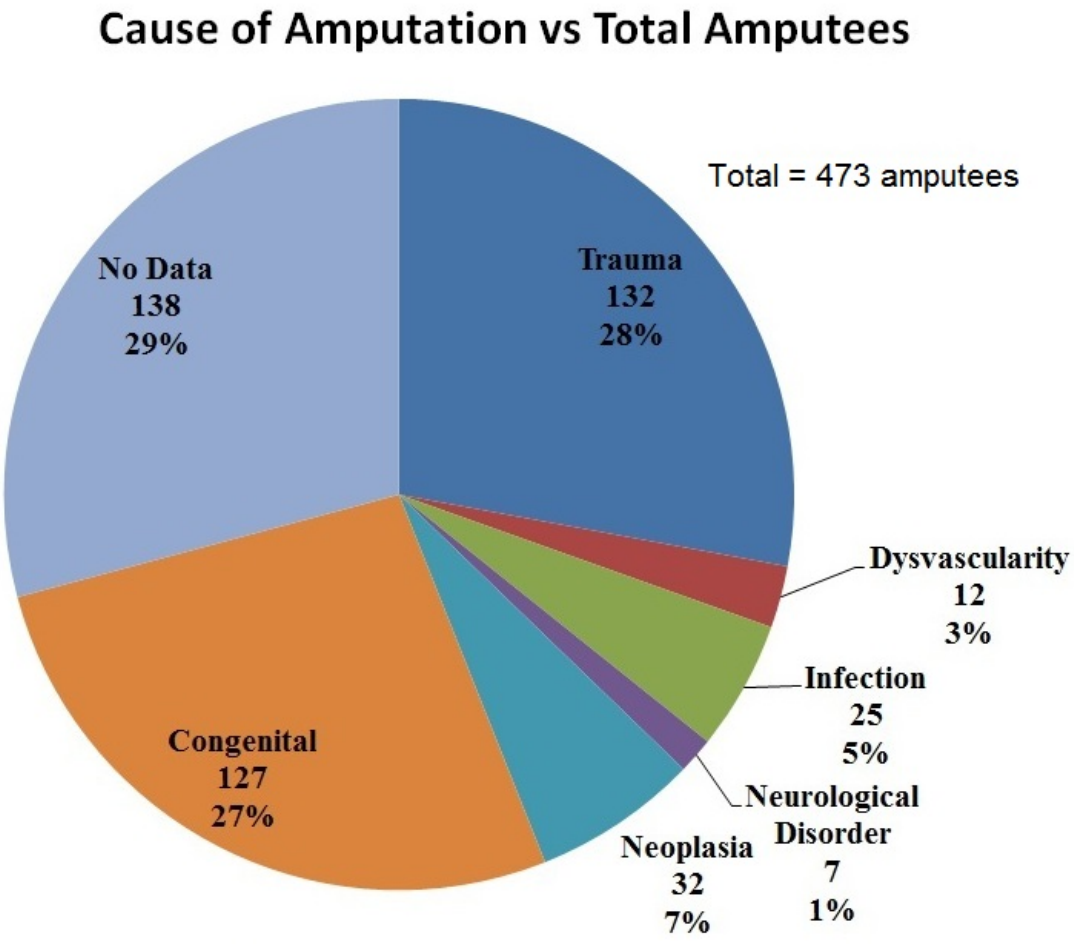

Figure 1.26: Cause of Amputation vs Total Number of Amputees registered from 2010-2011 in the UK. - From a total of 473 amputees registered across the United Kingdom, the causes of amputation tracked were: Trauma, Dysvascularity, Infection, Neurological Disorder, Neoplasia, Congenital and a last group with no data registered. The no data is given by the absence of information in the records for those patients. Data Source: (70) Table 21(1), p.112. Version 29-04-2013.

The information gathered by the previous graph is better explained in Figure 1.27. In this Figure, the spread of the cause of amputation is further detailed by level of amputation. As stated before, the transradial, transhumeral and partial hand amputations are the most common levels of amputations. The spread of the level becomes particularly interesting for each of the three cases. From the total of patients with a transradial amputation, the 41% of them are congenital, 23% have no data, and 19% are due to trauma. For the hand digit amputation, a large amount of patients have no information detailed in their record regarding the cause (43%), the other large percentage is that of trauma (39%). In contrast, for transhumeral amputees, the major spread is due to trauma (40%), and 27% have no data.

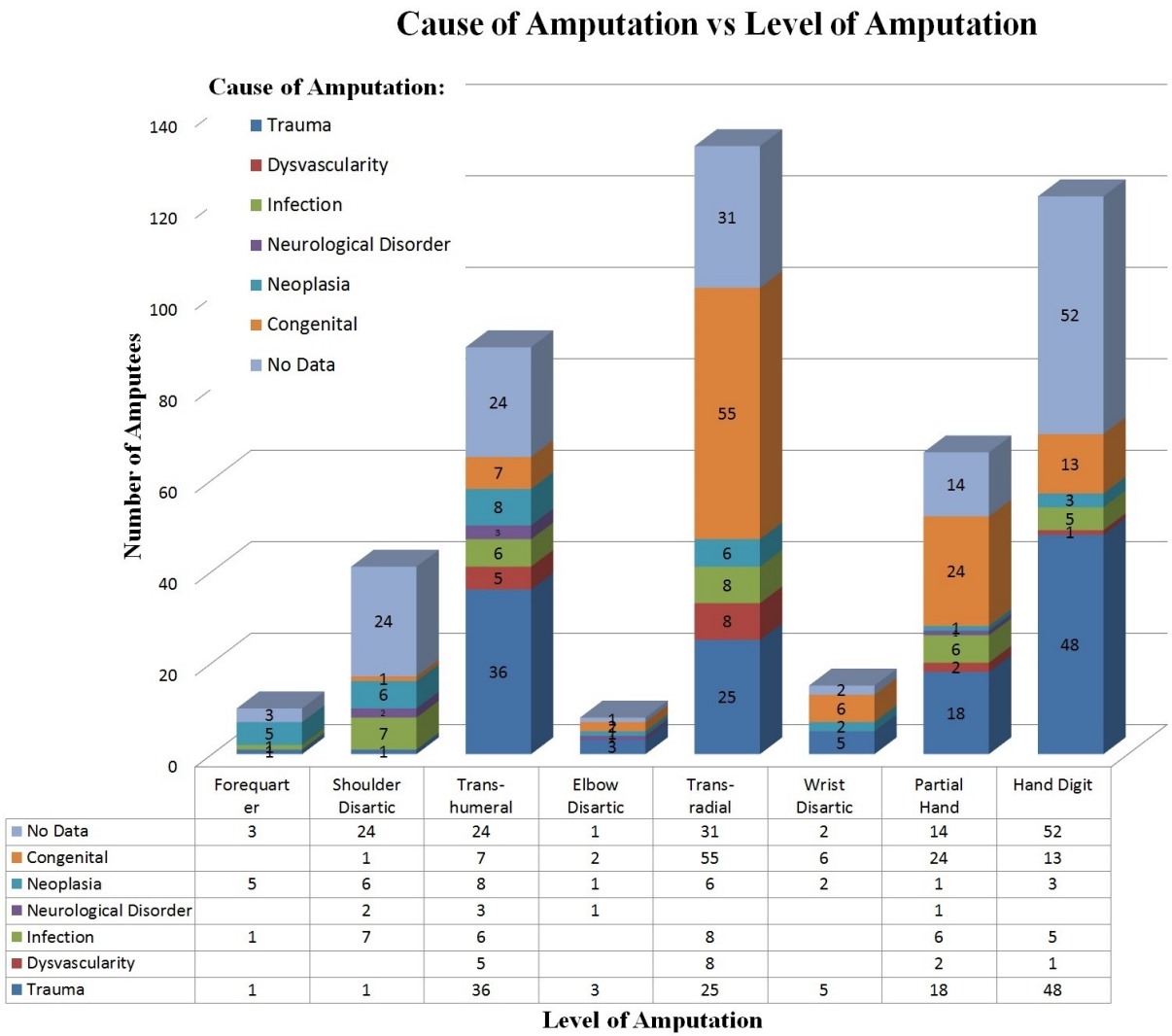

	Forequarter	Shoulder Disartic	Trans-humeral	Elbow Disartic	Trans-radial	Wrist Disartic	Partial Hand	Hand Digit
No Data	3	24	24	1	31	2	14	52
Congenital		1	7	2	55	6	24	13
Neoplasia	5	6	8	1	6	2	1	3
Neurological Disorder		2	3	1			1	
Infection	1	7	6		8		6	5
Dysvascularity			5		8		2	1
Trauma	1	1	36	3	25	5	18	48

Figure 1.27: Cause of Amputation vs Level of Amputation registered from 2010-2011 in the UK. - From a total of 473 amputees registered across the United Kingdom, The correlation in between level of amputation and cause of amputation was tracked. The possible level of amputations were: Forequarter, Shoulder Disarticulation, Transhumeral, Elbow Disarticulation, Transradial, Wrist Disarticulation, Partial Hand, Hand Digit. Data Source: (70). Table 21(1), p.112. Version 29-04-2013.

When the cause of amputation is other than congenital, the time that elapses between amputation and referral becomes important particularly when a myoelectric prosthetic is to be fitted. This relates to memory of actions that activate residual muscles of the stump and ease in training patients to use a myoelectric device. In Figure 1.28 the time elapsed (in weeks) between referral and amputation are depicted.

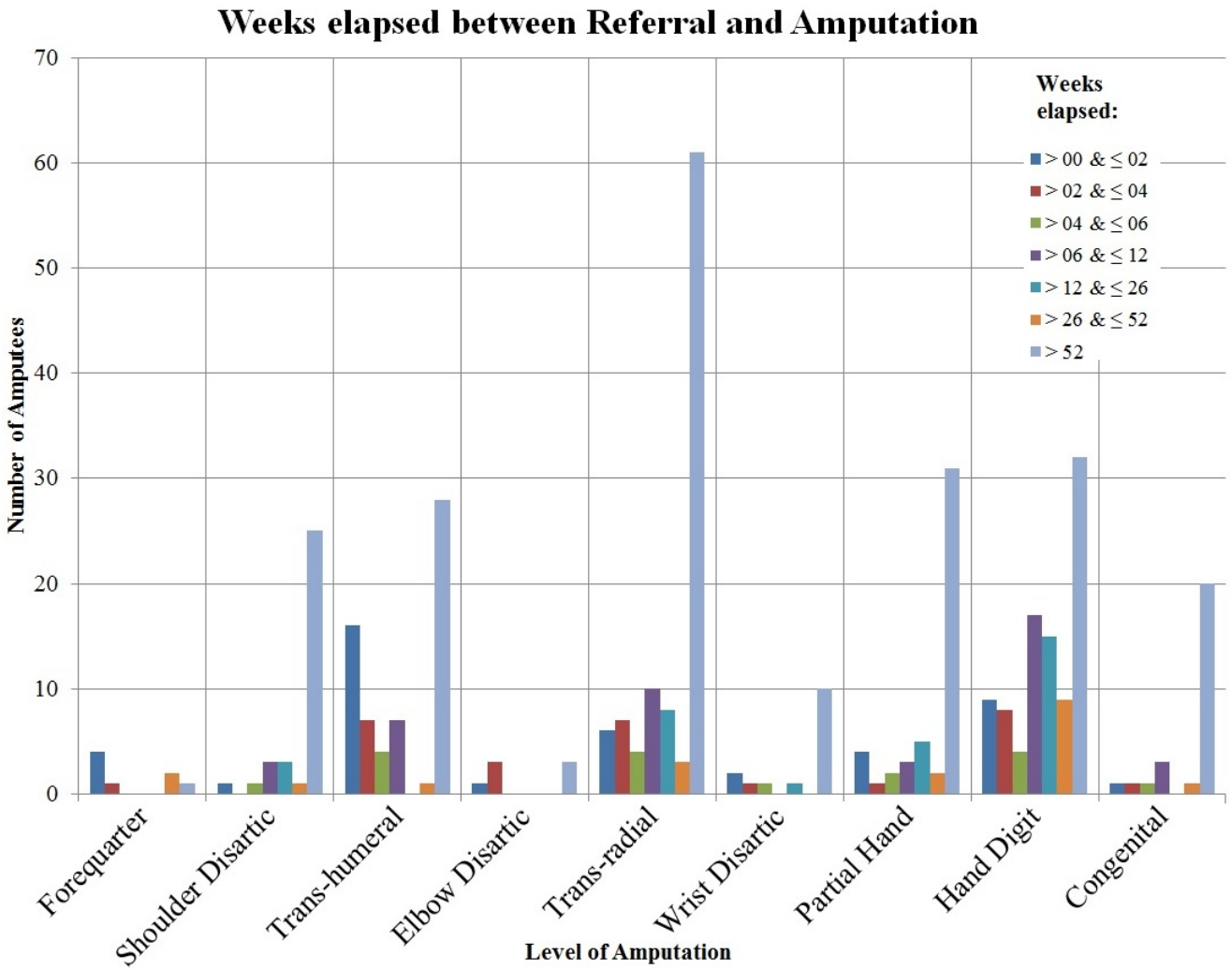

Figure 1.28: Weeks elapsed between Referral and Amputation - This graph states the weeks passed once the patients were referred for an amputation and further prosthetic use and the actual day they had the surgical procedure. It is separated in the level of amputation for a detailed analysis. Data Source: (70). Table 14(1), p.75. Version 29-04-2013.

From 1.28 is clearly seen that a great proportion of the amputees referred for a prosthetic only do so after more than 52 weeks across all the different levels of amputation.

Another important thing to take into consideration, is the age of the patient when they are referred. The prosthetic devices are chosen depending on the type of activity that the amputee need to perform and his ability to learn how to use it. A child might be easier to train on a myoelectric prosthetic hand than someone in later life; therefore, the age must be taken into consideration as it represents an important factor. In Figure 1.29, the age of the 473 patients referred by level of amputation is depicted. Common across amputation levels, is the age group ranging from 16 to 64 years old. This age group represents more than 50% for the overall data. The age group that is least referred ranges between 55 an 64 years old.

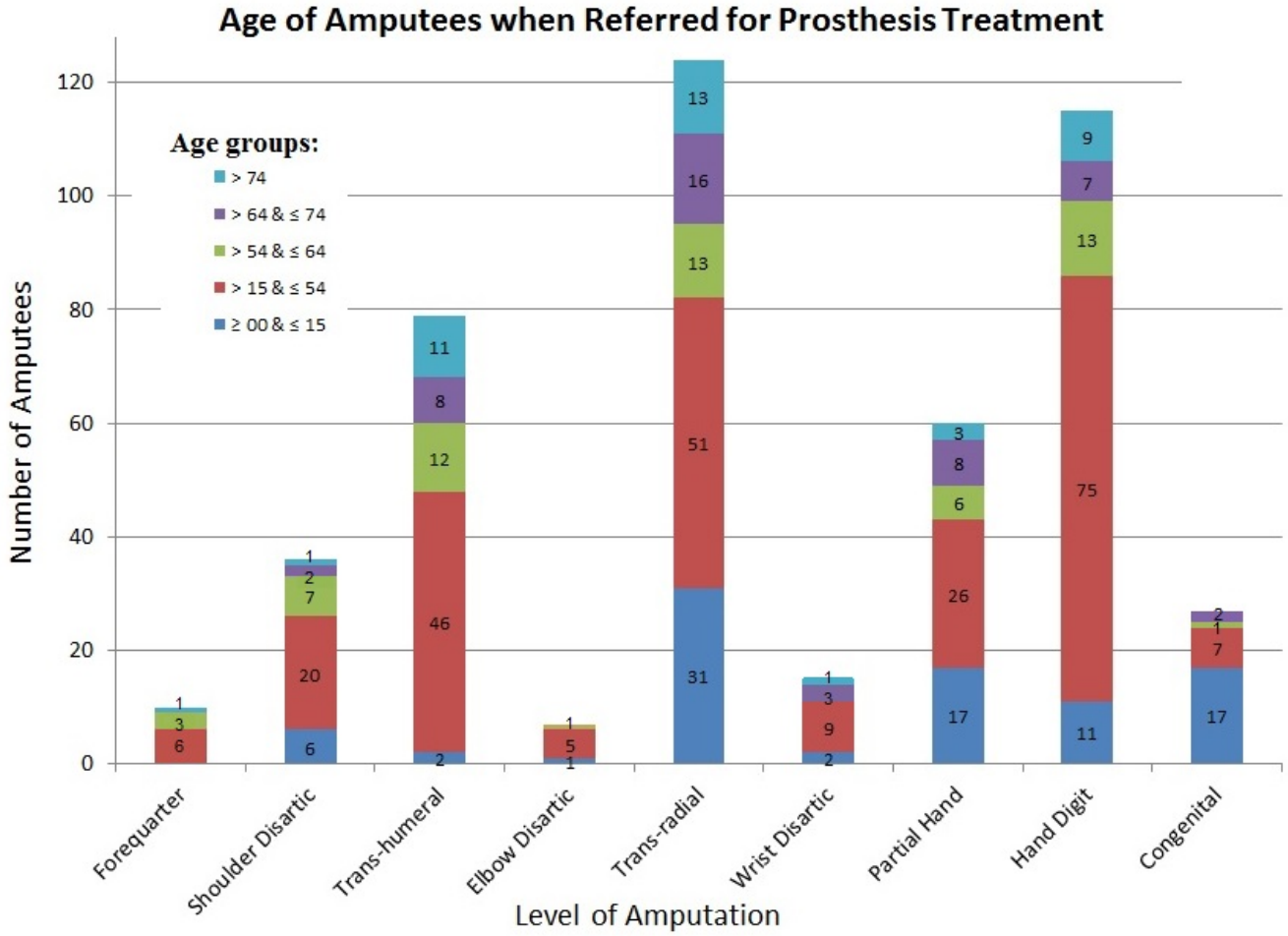

Figure 1.29: Age of the Patient when Referred for Prosthesis Treatment. - In this graph the age group can be found by level of amputation. Common across each level is the age group from 16 to 64 years old as more than 50% for each case. The age group that is least referred in this graph is between 55 an 64 years old. Data Source: (70) Table 15(1), p.79. Version 29-04-2013.

These data in itself helps us understand why different prostheses are referred to different patients according to their gender, age, side of limb absence, level of amputation, and type of work (although this last one has not been reviewed in this report). In the next section, a study case will be presented. This research was performed by Biddiss and Chau in 2007 (71), their aim was to investigate the roles of predisposing characteristics, need, and enabling resources in upper-limb prosthesis use and abandonment.

1.2.2.2 A Study Case on Device Abandonment

A study carried out by Biddiss and Chau (2007) (72), aimed to understand the critical factors for hand prosthesis abandonment. An anonymous, completed survey was designed to explore these factors. This questionnaire was available online and distributed throughout prosthesis providers, community support groups, and one prosthetic manufacturer. A total of 244 participants of a variety of and levels of upper-limb absence completed the survey. More, no details about the geographical location distribution of the survey was provided in this study.

In Figure 1.30 the distribution of adult and paediatric populations are shown. Furthermore, these groups are separated into amputation due to trauma or congenital. Finally, the level of amputation throughout these populations is displayed. The survey can be seen to sample predominantly patients with transradial amputation and therefore is highly relevant to the myoelectric user community.

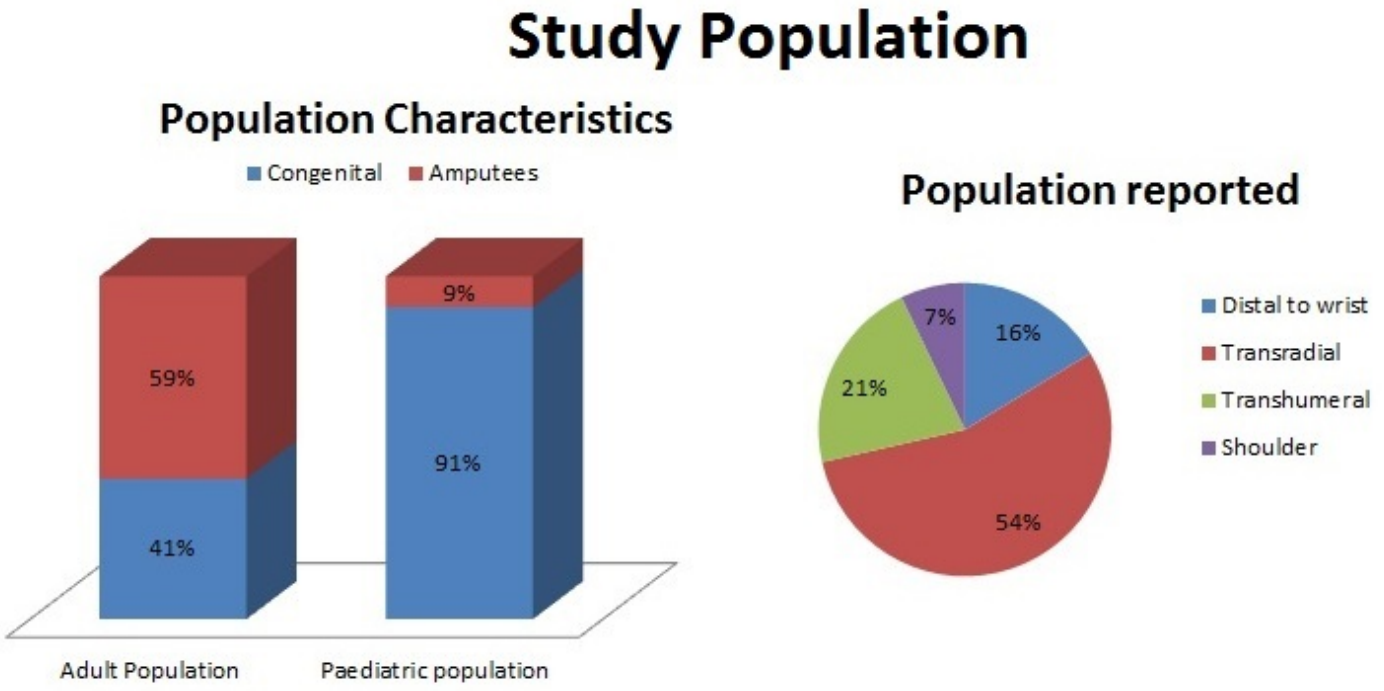

Figure 1.30: A Study Case on Device Abandonment Population Characteristics - A study population characteristics made by Biddiss and Chau. On the left chart we find the spread of the adult and paediatric population and the partition of them amongst congenital and amputees. A similar partition is appreciated for the adult population between congenital and trauma amputation, on the other side, the majority of the paediatric population is due to congenital occurrence. On the right chart, the level of amputation across the entire population are displayed. It is immediately seen that more than half of them resulted in transradial amputation. Data source: (72).

From the previously described population, the rejection rates (Figure 1.31) revealed that the largest group rejecting prosthetic devices are those with congenital limb loss. In the trauma and other groups, abandonment is greatest for high level amputees and absent for partial low level hand amputations. The high abandonment in people with congenital limb loss may demonstrate that they adapt to a life without a limb for better than those who lose a limb later in life.

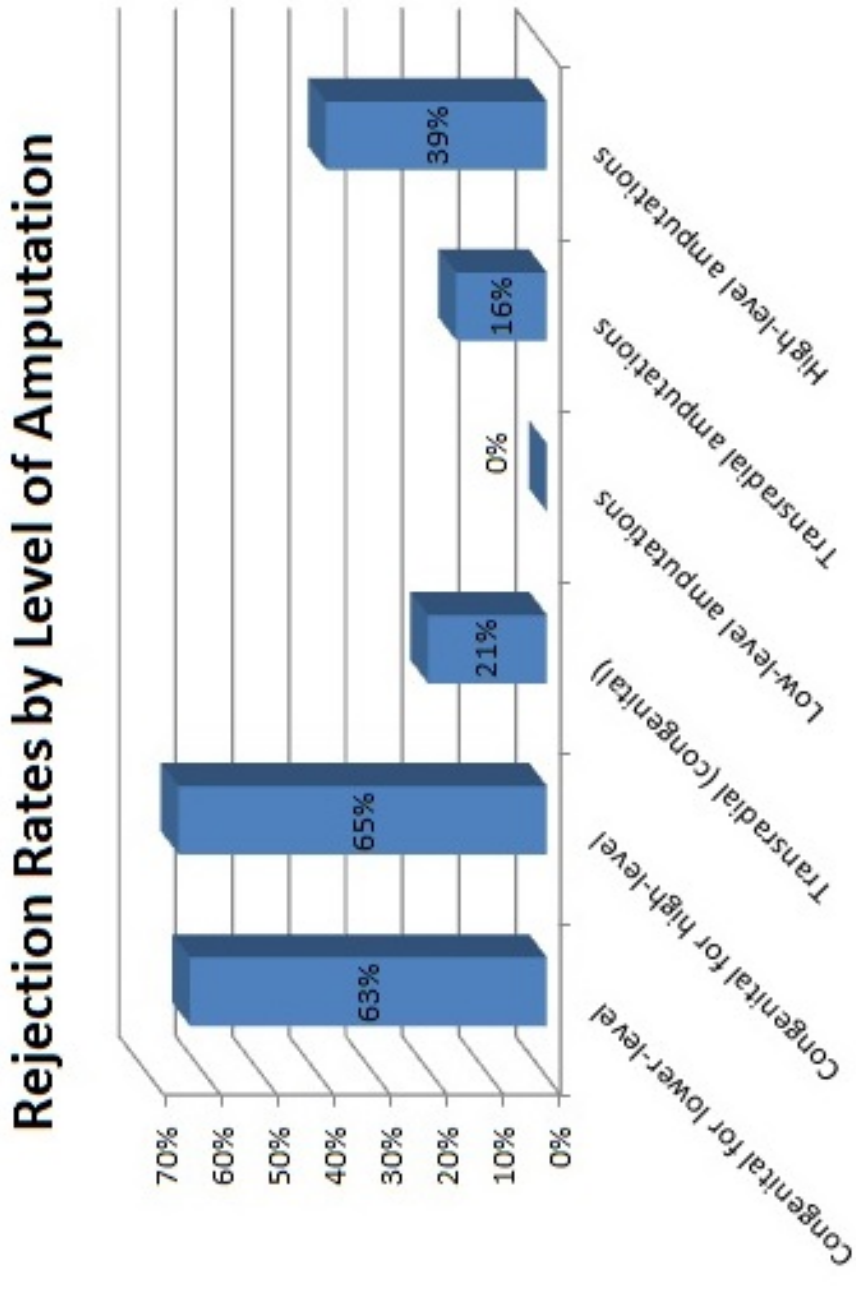

Figure 1.31: A Study Case on Device Abandonment Rejection Rates - Rejection rates found for the different type of limb loss. Data source: Biddis and Chau (2007) (71)

A summary of their findings has been summarised in Figure 1.32. The rejection rates are categorised by prosthesis type (passive/comsetic, body-powered, electric and no prosthetic), type of population (paediatric and adult) and their mean rejection rate. From the paediatric population, 45% abandoned their body-powered prosthetic, where from the adult population, 39% rejected their passive (cosmetic) hand. From the whole population, only 16% and 20% for paediatric and adult population, respectively, decided not to wear any type of prosthetic.

Rejection rates for the current active prosthetic devices are difficult to interpret as no controlled trial data of any significant size exist to know whether a particular prosthetic has a better or worse abandonment than another. Nevertheless, given the capital and clinical support costs in providing such prosthetics abandonment rate close to 25% is poor.

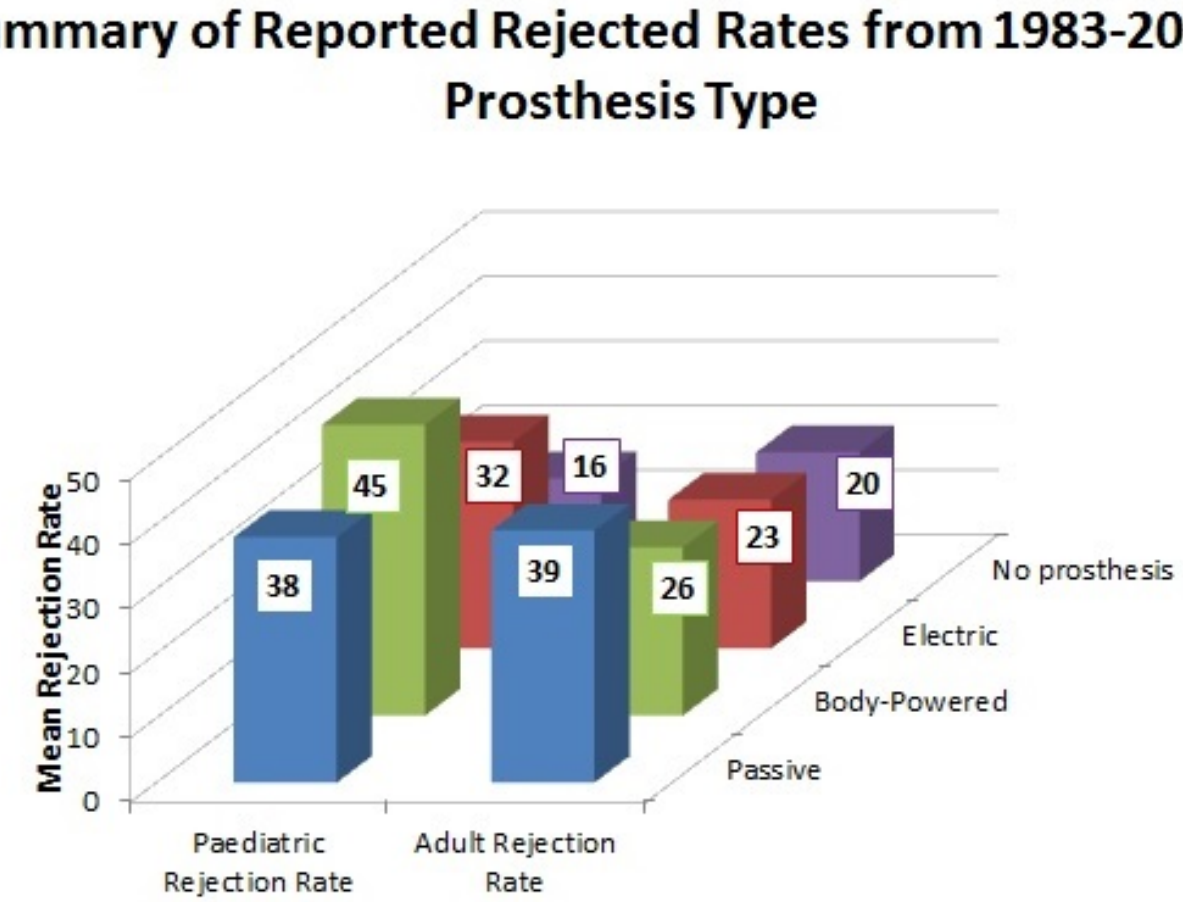

Figure 1.32: Summary of Reported Rejected Rates from 1983-2005 by Prosthesis Type - Summary of rejected rates found by Biddis and Chau in their study over 1983-2005. The mean rejection rates were calculated averaging the documented rejection rates and weighted by the sample size for each reviewed study over the specific sample groups: paediatric or adult, as well as the prosthesis samples:passive, body-powered, electric and no prosthesis. Data source: (71).

In the next section, the history of upper limb prosthetics will be provided as an understanding on where and how this research was originated, how it has evolved and where the field is moving to.

1.2.3 History of Upper Limb Prosthetics

From its primitive start to its highly-developed present, the evolution of upper limb prosthetics will be detailed to gain an up-to-date understanding of its progression.

Before ancient civilization such as Greek, Roman and Egyptian emerged, upper limb prostheses were made from materials such as wood and leather. This early devices were developed for purely aesthetic purposes. As seen in Figure 1.33, the first prosthetic hand found is dated to 1580. This rare hand was found in Germany, made entirely of iron. The functionality of this prosthetic was limited to an external button that moved the thumb and paired the fingers. In 1857, William Selvo patented a prosthetic arm which used muscular motion from the functional, opposite arm (body powered prosthesis). This motion activated the opening/closing of the hand. The influence of the Civil War, in the United States, from 1861 - 1865 was of high influence in the development of this field. With over 30,000 amputees (both upper and lower limbs), the need for limb replacement was evident (73).

The history of upper limb prosthetics can be tracked back to the XV century, when the first prosthetic device was found. Upper limb prosthetics can be traced back in early 1500.

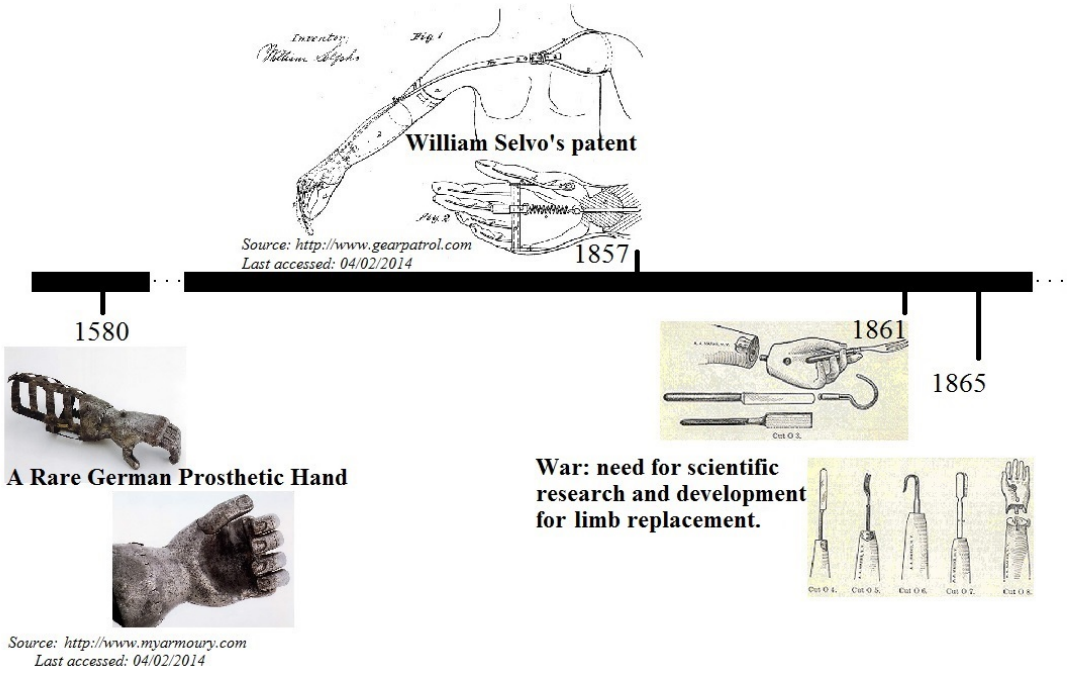

Figure 1.33: Timeline of the History of Upper Limb Prosthetics I: From 1580 - 1865 - The first found prosthetic hand is dated to 1580. The rare German hand, made entirely of iron, furnished with a movable thumb and paired fingers with an external button release. In 1857, William Selvo patented a prosthetic arm which used muscular motion from the functional, opposite arm, to activate the opening/closing of this device. In 1861 - 1865, the American Civil War took place, the need for scientific research and development for limb replacement was evident.

In 1915, the first powered prosthesis was patented in Germany. In Figure 1.34, the first sketches of the pneumatic hand published in Ersatzglider and Arbeitshilfen. In later years, the design that followed Becker's idea is shown. William McElroy patented his design in 1930 followed by the first Becker patent in 1933. The latter is probably one of the most common hands when talking about upper-limb prosthetics.

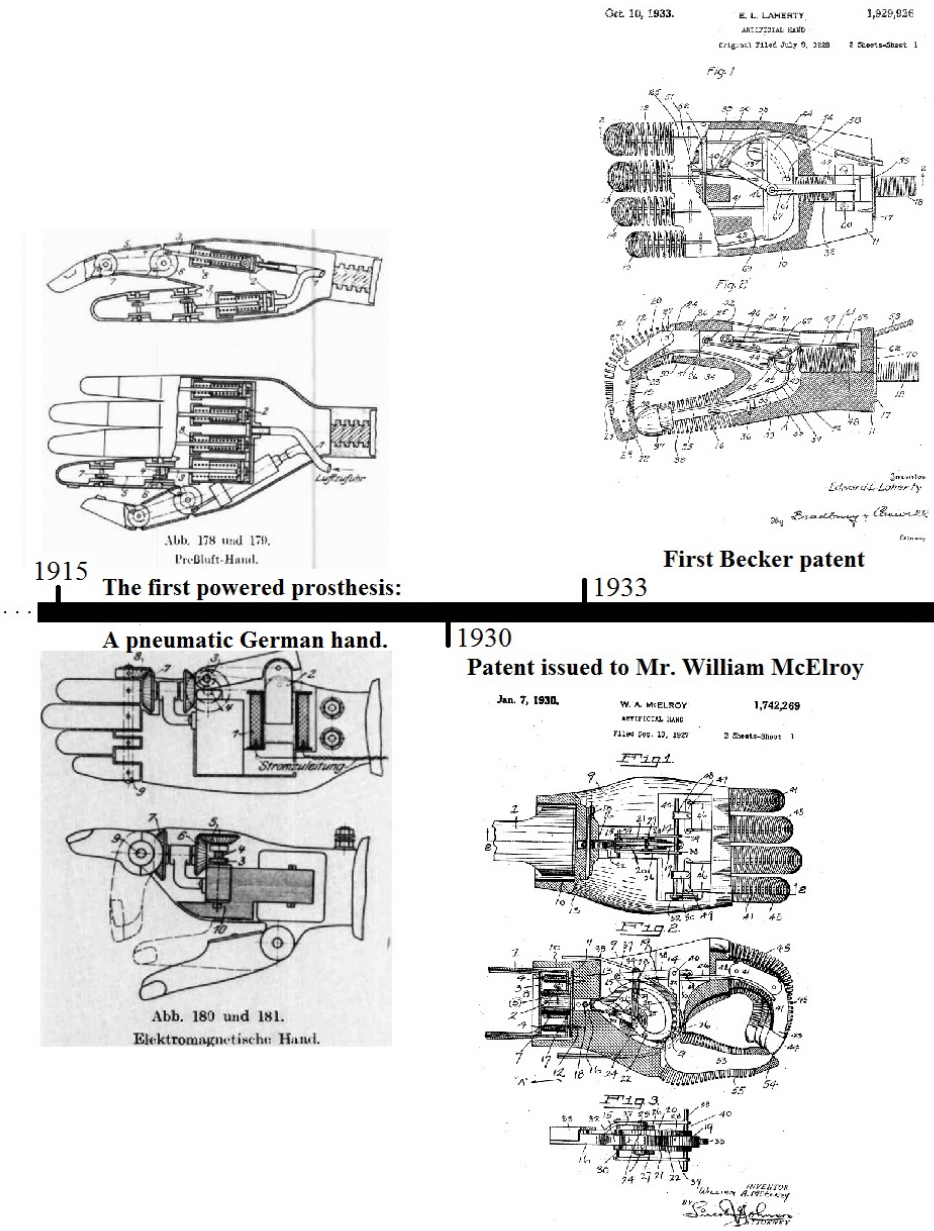

Figure 1.34: Timeline of the History of Upper Limb Prosthetics II: From 1915 - 1933 - The first powered prosthesis, a pneumatic hand patented in Germany. These drawings were published in 1919 in Ersatzglider und Arbeitshilfen (Substitute Limbs and Work Aids). The Becker hand is probably one of the most common hands when talking about upper limb prosthetics. In this image we can find what is probably what gave Becker his idea; Mr. William McElroy patented his hand in January 7th, 1930, followed by the first Becker patent, filed just six months after McElroy, issued to Edward Laherty three years after, Laherty assigned 49% of Intellectual Property to Becker.*Source: http://www.openprosthetics.ning.com/ - Last accessed: 04/02/2014.*

By 1938, Becker filed for his second patent. The mechanism involved in this later design is still used in many (if not all) the mechanical hands that are still commercially available today. The first known myoelectric prosthesis was developed during the 1940's by Reinhold Reiter, the system was controlled by a vacuum tube amplifier (74). After the World War II, the Vaduz hand was developed (Figure 1.35) in 1953. This hand was controlled by the muscles operated by a portable power source. This hand had a gear mechanism to enable it to obtain higher forces for gripping. The hands now-a-days manufactured by Otto Bock are based on this principle.

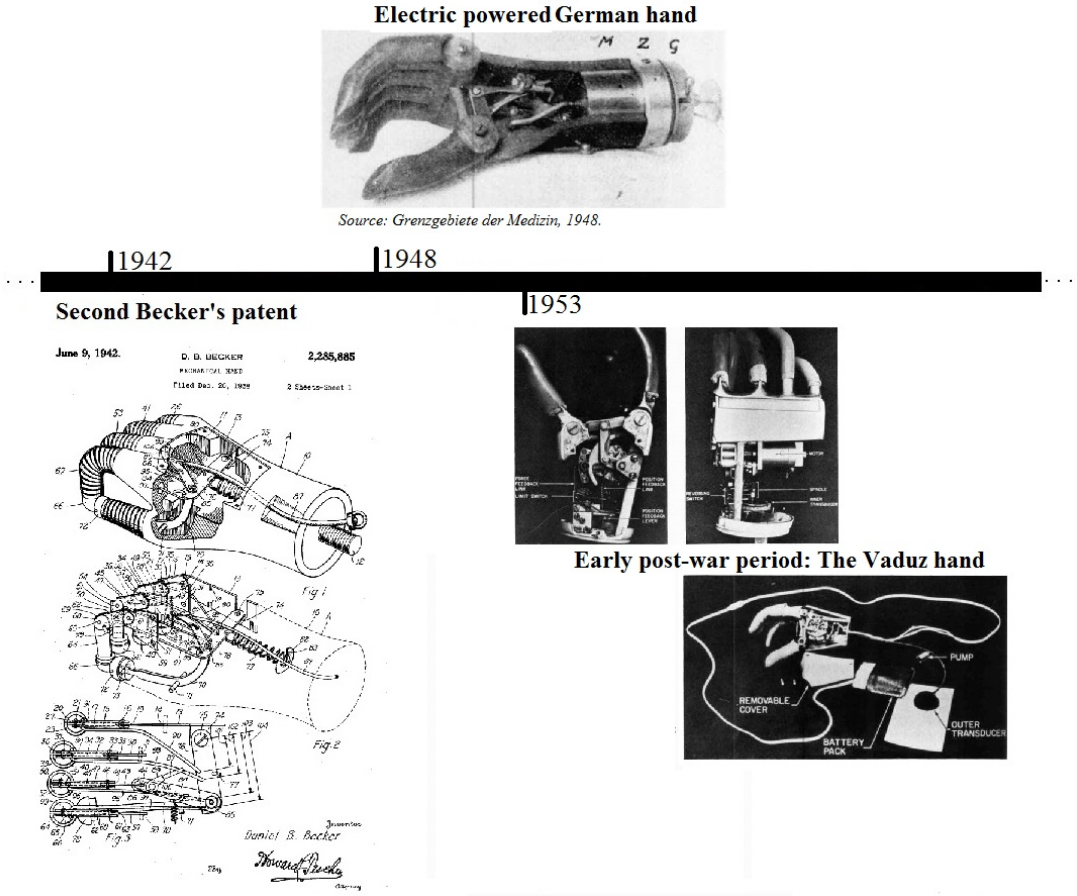

Figure 1.35: Timeline of the History of Upper Limb Prosthetics III: From 1942 - 1953 - By 1938, Becker filed for his second patent, for which hand are based the Becker Mechanical Hands that are still sold today. The first known myoelectric prosthesis was developed during the 1940's by Reinhold Reiter. This system was controlled by a vacuum tube amplifier, it was not portable. After the World War II, the Vaduz hand was developed. The hand was controlled by the muscles operating by a portable power source. This hand had a gear mechanism to enable it to obtain higher forces for gripping; this principle is currently used by Otto Bock hands. *Source: http://www.openprosthetics.ning.com/ and www.oandplibrary.org - Last accessed: 04/02/2014.*

In 1959, the Russian Hand was the first myoelectric with portable capabilities. This hand had an external battery back and charger, electrode wires and suspension straps (75). In 1965, a Swedish research group began their work on an electric hand more adaptive and with multiple functions. This hand was able to grasp, extend and flex the wrist, and pronate and supinate the hand. This Swedish hand was called SVEN-Hand, it is widely used in research, specially that of muscle control (76). In 1968, the Boston Arm became the first myoelectrically controlled elbow, later known as Boston Elbow. The Otto Bock Electric Greifer introduced in 1970, numerous advantages: voluntary opening and closing of the hand; wide opening; built-in wrist flexion; battery-powered; and myoelectric operated. Nevertheless, it was a very heavy device, it was not water resistant and there was no tension feedback (77). These devices are depicted in Figure 1.36.

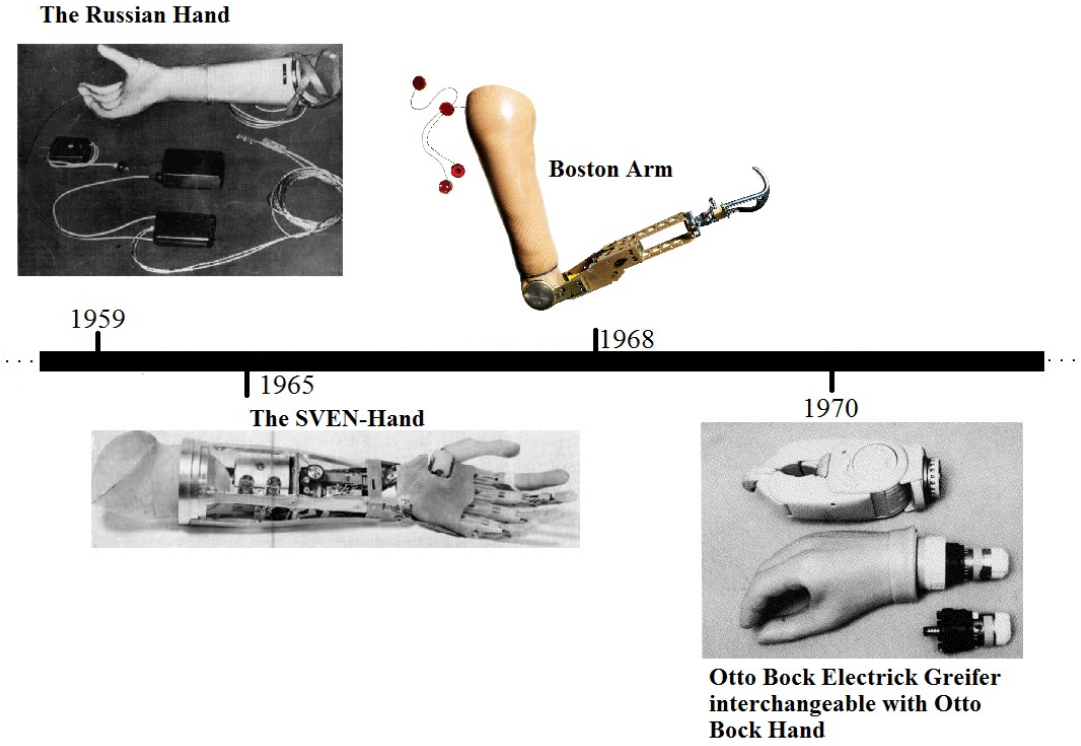

Figure 1.36: Timeline of the History of Upper Limb Prosthetics IV: From 1959 - 1970 - The Russian Hand was the first myoelectric portable hand. With an external battery back, a battery charger, electrode wires and suspension straps. *From Science Journal article by R.N. Scott, March 1966.* In 1965, a Swedish research group began their work on an electric hand more adaptive and with multiple functions, i.e. grasp, wrist flexion-extension and hand supination-pronation. This hand was known as SVEN-Hand, widely used in research, specifically regarding muscle control. The Boston Arm became the first myoelectrically controlled elbow, which designed was later known as Boston Elbow. The Otto Bock Electric Greifer introduces a number of additional advantages; voluntary opening/closing; wide opening; built-in wrist flexion; battery-powered; myoelectric. On the downside: heavy; cannot be immerse in water; no tension feedback. *Source: http://www.amputee-coalition.org - Last accessed 04/02/2014.*

In 1980, and inspired by Luke Skywalker from Starwars, Dean Kamen began a prosthetic arm called 'Luke arm'. In 1981, Motion controlled introduced the first Utah Arm, whose hand had opening and closing capabilities as well as flexion and extension of the elbow. Years later, this design was re-engineering an their electronics were made to be the most durable and dependable myoelectric arm available for a long arm. This device was named Utah Arm 2 (U2), in 1987. In 1993, David Gow developed a partial hand system, this invention is now attached to Touch Bionics (78). The developments from 1980 to 1993 are shown in Figure 1.37.

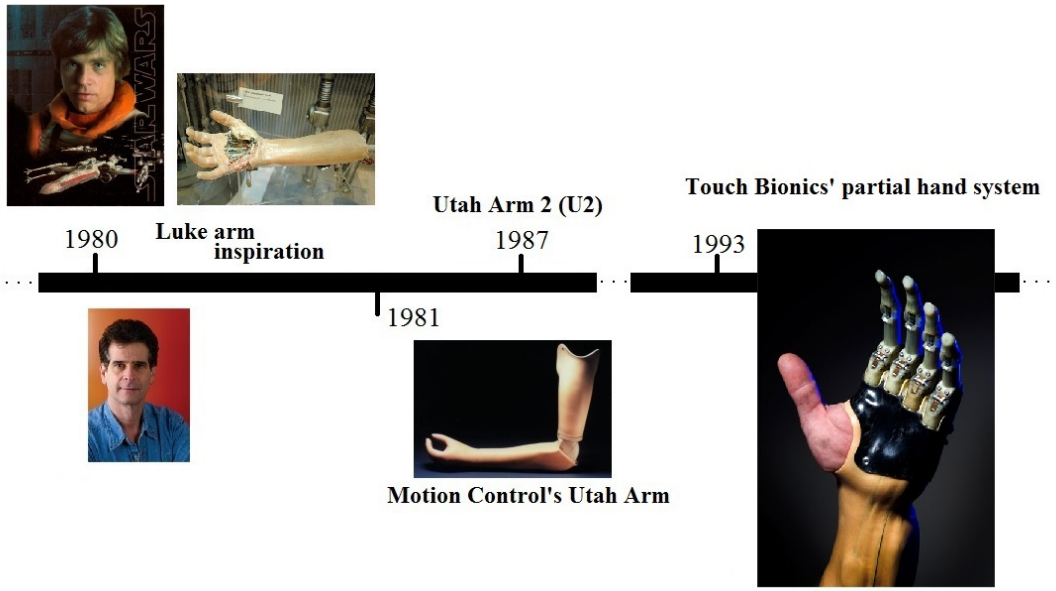

Figure 1.37: Timeline of the History of Upper Limb Prosthetics V: From 1980 - 1993 - Dean Kamen's "Luke arm" conception began by inspiration from Star Wars. In 1981 Motion Controlled introduced the Utah Arm. Years later, they re-engineered their electronics only to make it the most durable and dependable myoelectric arm available for a long time, Utah Arm 2 (U2). David Gow developed in 1993 (receiving international publicity until 1998) a partial hand system. *Source: http://www.utaharm.com/motion-control-company-profile.php and www.touchbionics.com/about/history-Last accessed: 04/02/2014.*

By 2004, Motion Controlled introduced the 3rd generation of their Utah Arm: The Utah Arm 3 (Figure 1.38). U3 had a computer interface that allowed the prosthetist to fine-tune the adjustments to achieve maximum performance. A year later, in Southampton, Paul Chappell developed the Southampton Remedi-Hand, controlled by muscles through a processing unit controlled by small contractions of the muscles which move the wrist. Thereafter, in 2006, Otto Bock introduced the first target muscle re-innervation (TMR) inducing the body's repair mechanisms.

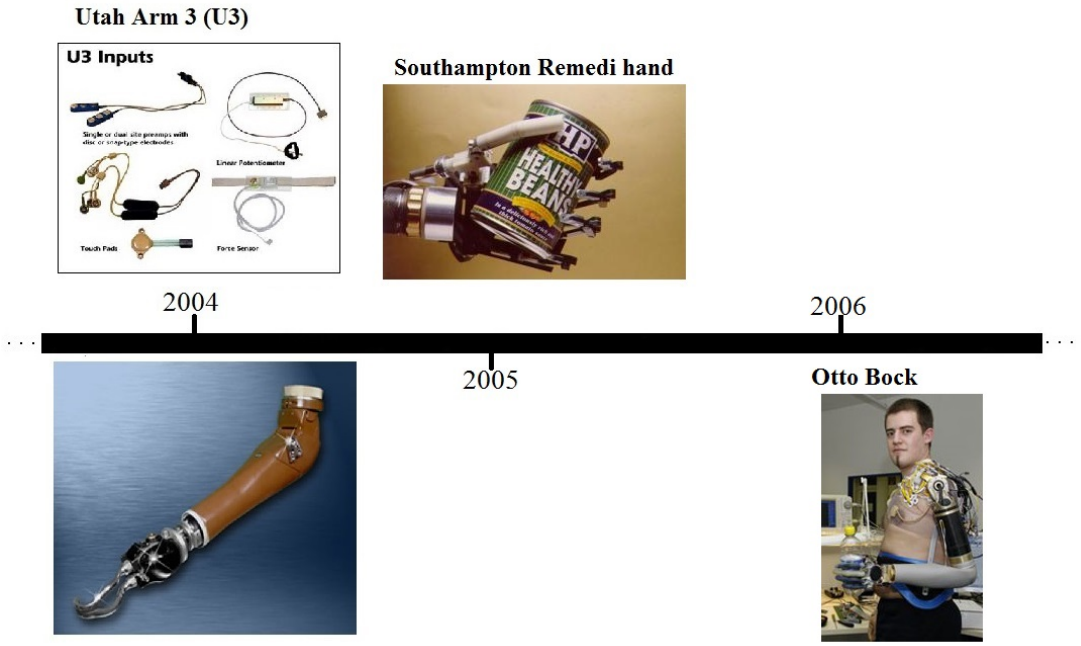

Figure 1.38: Timeline of the History of Upper Limb Prosthetics VI: From 2004 - 2006 - In 2004, Motion Controlled introduced the Utah Arm 3, with a computer interface that allowed the prosthetist to fine-tune the adjustments to achieve maximum performance. One year after, Paul Chappell developed the Southampton Remedi-Hand controlled by muscles through a processing unit controlled by small contraction of the muscles which move the wrist. In 2006, Otto Bock introduced the target muscle re-innervation inducing the body's repair mechanisms. *Source: www.ottobock.com/ - Last accessed: 05/02/2014.*

As it is shown in Figure 1.39, in 2007, Touch Bionics launched the i-LIMB hand, the first powered prosthetic hand incorporating articulate fingers, independently powered through independent motors. That same year, Dean Kamen's Luke arm was now a project left to The Defence Advanced Research Projects Agency (DARPA). A year later, Otto Bock released their Michelangelo hand with multiple grip functions, showing improves in their previous version regarding speed, strength and aesthetics. In parallel, a research center in Karlsruhe presented the Fluidhand, able to flex the joints of the fingers through hydraulics, having a better flexibility over the motorised fingers. In 2009, TMR research gave another step with Swedish researchers, introducing the sense of touch in their Smarthand. The sensors were surgically connected to the nerves in the arm allowing the amputee to 'feel' objects within their grasp. In that same year, Touch Bionics launched their partial hand solution for people for had partial hand amputation, ProDigits.

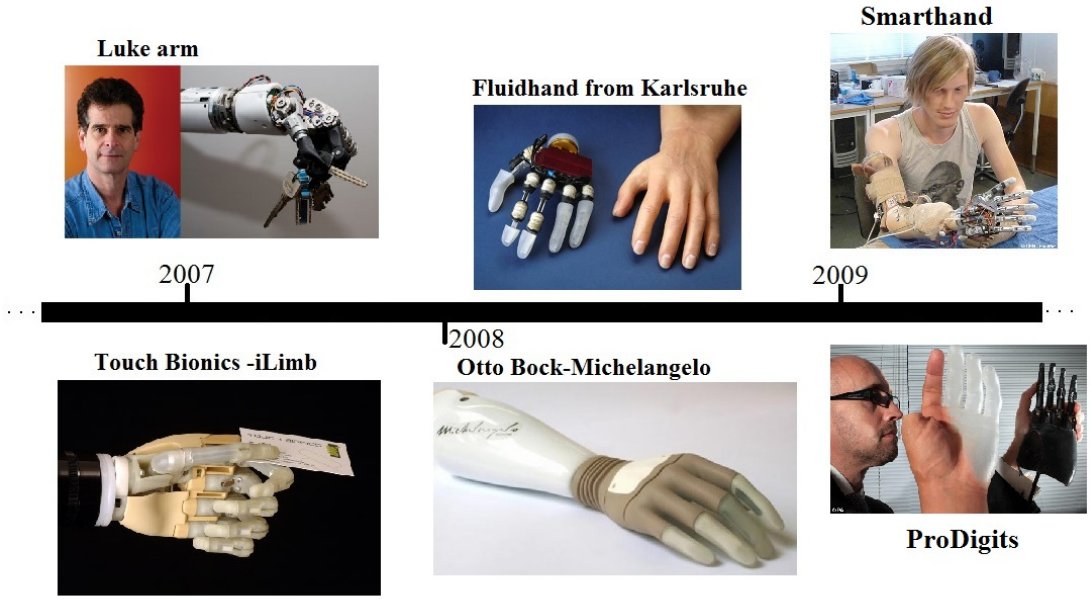

Figure 1.39: Timeline of the History of Upper Limb Prosthetics VII: From 2007 - 2009 - In 2007, Touch Bionics launched the i-LIMB hand, the first powered prosthetic hand incorporating articulate fingers, independently powered. That same year, Dean Kamen's Luke arm was now a project left to The Defence Advanced Research Projects Agency (DARPA). In 2008, Otto Bock released their Michelangelo hand with multiple grip functions, showing improves in speed, strength and aesthetics. The same year, a research center in Karlsruhe presented to the world their Fluidhand, which was able to flex the joints of the fingers through hydraulics, having better flexibility than the motorized fingers. In 2009, Swedish researchers introduced the sense of touch in their 'Smarthand'. The sensors were surgically connected to the nerves in the arm allowing the amputee to 'feel' objects within their grasp. That same 2009, Touch Bionics launched their partial hand solution for people who have lost some fingers: ProDigits. *Source:www.shil.co.uk/About-Us/touch-bionics.html, www.handresearch.com and www.living-with-michelangelo.com- Last accessed: 05/02/2014*

In recent years, the advances of the upper limb prosthetics have been with regards to the controller (microchip) instead of the motor control mechanisms. In 2010, i-Limb Pulse was introduced to the market and presented significant advantages within the same line of Touch Bionic's producs, additionally, this device came with BioSim, a software that allowed prosthetists and amputees to modify the device's configuration through a bluetooth connection. In 2011, Touch Bionics improved the Pulse version of their hand presenting the Ultra, with a virtual environment embedded in the software allowing an easier training stage for both prosthetists and amputees. In parallel, Motion Controlled upgraded their U3 arm to U3+, providing it with bluetooth communication protocol and improved performance. Finally, in 2013, Touch Bionics launched a mobile application for prosthetic control replacing the previous bluetooth protocol through their BioSim.

Until now, natural control mechanisms are lacking in the upper limb prosthetic development. This lag in its development is due to the complex anatomy of the hand. In this study, the question regarding the possibility for a myoelectric upper-limb prosthetic will be reviewed, specifically with regards to thumb opposition.

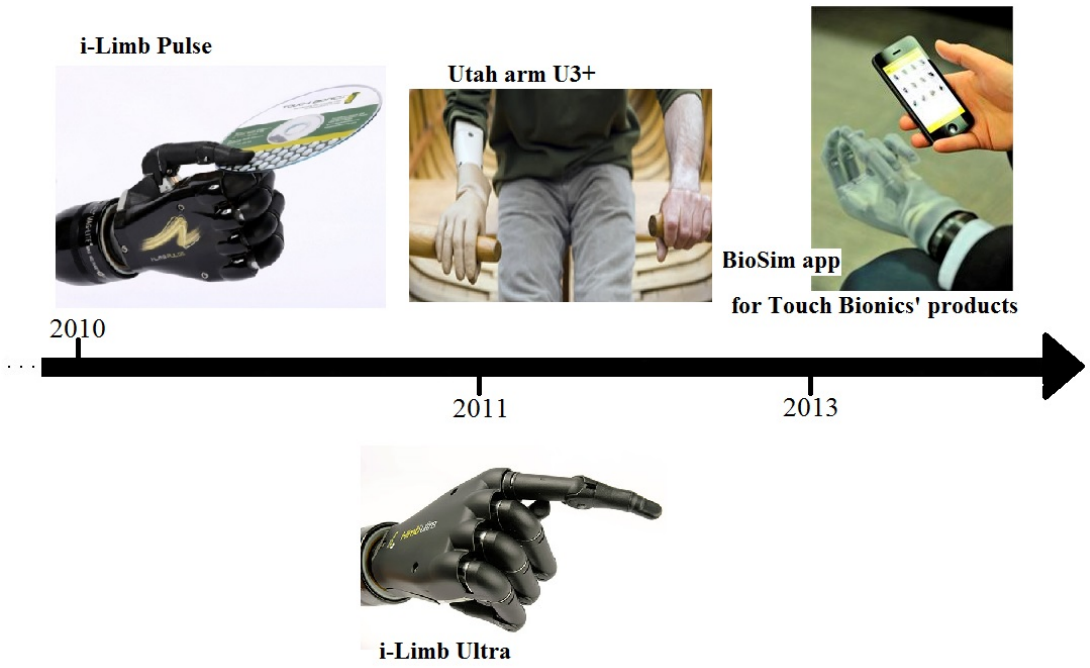

Figure 1.40: Timeline of the History of Upper Limb Prosthetics VIII: From 2010 - Present - In 2010 i-Limb Pulse introduction to the market presented a significant advance within the same line of Touch Bionics' products, additionally, this device came with BioSim, a software tool that allowed prosthetists and amputees to modify the hand through bluetooth connection. In 2011, Touch Bionics improved the 'pulse' creating a new device: i-Limb Ultra, with a virtual environment embedded in the software allowing training. In parallel, Motion Controlled upgraded their own U3 arm to U3+, providing it with bluetooth capability and improved performance. Finally, in 2013 Touch Bionics launched a mobile application for prosthetic control.*Sources: www.utaharm.com/ and www.touchbionics.com/ - Last accessed 05/02/2014.*

1.3 Thesis organisation

This thesis consists of 8 chapters. The appendices, found in chapter 8, contain important information and the reader is advised to refer to them when required. Chapter 2 contains the literature review in the related fields to the present research project. The research statement and hypothesis are stated in chapter 3. In chapter 4, the methodology of this study is presented analytically. In chapter 5 and 6 the reader can find the time and time-frequency results as well as the machine learning results, respectively. Finally, in chapter 7 the thesis conclusions and final discussions are presented.

2

Literature review

2.1 Summary

This review will focus mainly on how muscle synergies of the hand happen, providing an insight into how the research in this field has been evolving to date. A brief history behind current state of knowledge is provided to give insight into the methods, analyses of muscular signals, the different existing techniques applied in movement studies and a specific focus on applications for below-elbow prosthetic devices.

2.2 From Electrophysiology Principles to Electromyography Acquisition

2.2.1 Early History of Electrophysiology

Study and interpretation of electrophysiological signals leads to a better grasp of the mechanisms behind the control of muscle actions and their translation into movement behaviour. The history of surface electromyography (sEMG) involves the development of instruments and equipment necessary to be able to analyse electrical activity in the muscles that otherwise is unseen by the observer. The development of sEMG recordings can be traced back to 1650, when Francesco Redi experimented on electric ray fish energy(79), and by 1773, John Walsh demonstrated the eel's muscle tissue as an electricity generator. Bioelectricity as a feature of movement was first described by Luigi Galvani back in late 1700 (80) from his studies on the effects of electricity on frog muscle (Figure 2.1). His studies demonstrated some fundamental physiological

processes such as nerve conduction and muscular contraction. More details about Galvani's experiments can be found in (81).

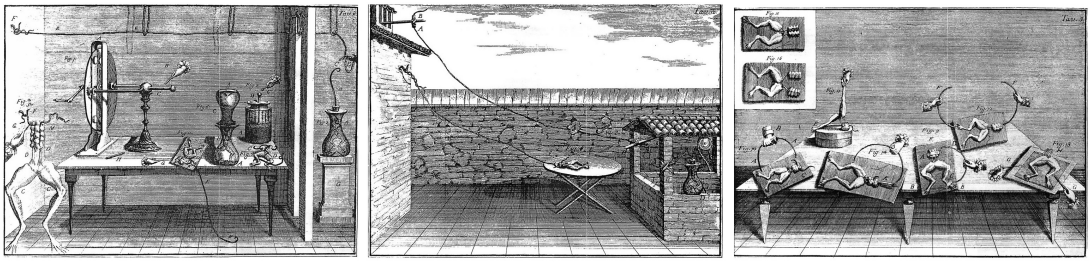

Figure 2.1: Galvani's Frog Electrical Machine - Luigi Galvani study on the effects of electricity on animals, particularly on a frog. Left - With the frog's lower limb nerves exposed in their course of the spinal cord, and a metal wire placed over the spine inducing electricity stimulating the nerves. Central - Galvani's Frog Electrical Machine with Stormy Atmospheric Electricity, same concept as the previous but the electricity induced was obtained from an electrical storm. Right - Galvani's Frog Electrical Machine with metallic arcs; Luigi Galvani study on the effects of electricity on animals. He made a frog preparation, with the lower limb nerves exposed in their course of the spinal cord, and a metal wire inserted across the vertebral canal. *Source: Piccolino, M. (1998) (82)* .

Galvani discovered a relationship between the intensity of the discharge and the strength of the contraction of the excited muscle. This realisation lead to an understanding of the event now referred to as the depolarisation threshold. This threshold represents the point at which increasing discharge beyond a certain magnitude would not lead to a greater contraction, and reducing it would result in the disappearance of the contraction (80). The concept of irritability was revisited back by Galvani -initially introduced by Glisson (83)- and developed by Albrecht von Haller (84) based on the idea that the frog's reaction was its way of responding to the application of an external stimulus, and the movement of the frog's legs was the expression of its internal functional organisation acting upon the irritation of the external excitatory stimulus.

The legacy of Galvani was soon picked up by his nephew, Giovani Aldini in early 1800 applying the Galvanic concepts on animal preparations. It was thanks to Aldini (85) that people started becoming interested about reanimation by the of stimulating corpses, believing that expired creatures could be revived, e.g., Mary Shelley's Frankenstein.

Soon after Galvani's first experiments on frogs, Alessandro Volta gave a different interpretation to the one hypothesised by Galvani. Volta's comments on Galvani's ex-

periments were that the frogs were capable of reacting due to intrinsic electricity. Further exploration of these arguments led Volta to various discoveries, i.e. the electrical battery, leading to a different type of development around electricity and conductivity (86). Volta and Galvani worked in parallel, where the first repeated some experiments of the latter without much frog preparation, leading to the examination of different body parts, e.g., eyes, tongue. Johannes M*ü*ller used Volta's findings stipulating the physiological effects of nerve stimulation applied in humans (stimulating the eyes would lead to sudden light appearance) (87).

After Galvani's experiments on 'animal electricity', scientists like Leopoldo Nobili and Carlo Matteucci looked into similar conduction mechanisms to elicit muscular contraction, with the latter subsequently proving to have interpreted the results correctly: current was of biological origin and it disappeared when the muscle was in a tetanic state (88). Matteucci recognised in his studies the need for connecting two different types of surfaces to be able to record what he called the 'muscular current' (from (82) referring to (89)). In this study, Matteucci piled several frog thighs (prepared using Galvani's method) and showed that with more thighs piled together, the galvanometer's needle increased in proportion. With this experiment he was able to prove Galvani's 'animal electricity' hypothesis, proving that the measured current was due to the muscular tissue and not the metals touching it. Furthermore, Mateucci used the galvanometer to demonstrate the electrical potential produced between a stimulated frog's nerve and its damaged muscle. At this point, the existence of muscle current was successfully demonstrated. It became clear that the muscle contraction was an expression of a difference in the potential between internal and external compartments of the muscular fibres.

Continuing the electrophysiological research of Matteucci, involving nerve and muscular contraction, was Emile du Bois-Reymond in the 1840s. Du Bois-Reymond was able to measure with a galvanometer, the electrical activity after the excitation of a nerve calling it 'the negative variation' ('Negative Schwanking'). Representing the first instrumental recording of an action current (from nerve) and action potential (from muscle) . Furthermore, he provided the first evidence of electrical activity in human muscles during voluntary contractions. His human work consisted of placing a cloth on the subject's hand immersing them in separate barrels of saline solution, while connecting electrodes to the galvanometer. The concept of skin impedance is also tracked

to him, when in this same study he removed a portion of the subject's skin, replacing the electrodes and noting a drastic increase in the magnitude of the signal during wrist flexion (From (90) original source (91)).

2.2.2 First Documented Electromyographic Recordings

In 1917, Pratt began demonstrations of the magnitude of the energy associated with a muscular contraction. This energy was linked to the recruitment of the individual fibres as opposed to the size of the neural impulse (92). In the coming years, Herbert S. Gasser and Newcomer used a cathode ray oscilloscope to show muscle propagation (93). This work led them to win the Nobel Prize in 1944.

During the next 30 years (leading up to the 1950s), there was continuous development to improve EMG instrumentation, using the newly developed equipment to study normal and abnormal muscular functionality. The studies performed in 1948 by JP Price, et al., (94) were found to be the first work to have studied clinical populations and noting that the sEMG patterns began to shift away from the original site of injury. Later, in 1955, Floyd and Silver were able to demonstrate through their research in the erector spine muscles, that muscles acted in synchrony, shutting on and off depending on the movement (flexion/extension) of the trunk (95).

In the 1960s, the technique of biofeedback emerged through John Basmajian's work on single motor unit training via fine-wire electrodes (rather than surface-EMG) (96). Subsequently, this technique was widely applied in a clinical environment [(97), (98)] .

In the following years, sEMG was used to teach (99), retrain patients with neuromuscular deficiencies (100), to assist restoration of function in hemiplegic patients (101), treatment of pain (102), etc.

In the early 1980s, Cram and Steger established databases to be used as clinical guides (103). Their scanned data led to the differentiation of three different characteristics: (i) site of activity; (ii) position; and (iii) degree of symmetry. Later, Will Taylor measured the synergy patterns in the trapezius introducing it as a new concept (104). With this work, other scientists like Lewis et al.(105), Middaugh et al. (106), were able to confirm the synergy between muscular dysfunction (hyper/hypo-activity) and pain.

After a meeting organised by Basmajian, in 1965 with the intention of collecting all the available EMG techniques and methodologies developed over the last decades, the

International Society of Electrophysiological Kinesiology (ISEK) was formed. This society is still active in promoting new techniques and applications of EMG (see www.isek-online.org)

2.2.3 Current Preferences and Techniques for EMG Recordings

As mentioned in the previous section, EMG can be detected by intramuscular electrodes and by surface electrodes attached onto the skin overlying the muscles of interest. When recording muscular activity with inserted (needle) electrodes, they are positioned as close as possible to the source of interest. The action potential deflection acquired through this invasive method is very different to the one recorded via non-invasive alternatives (sEMG).

Despite the fact that sEMG has been evolving significantly since Redi in late 1650, most methodological developments have been confined to research groups which follow their own protocol and hence, this varies between research groups. A big effort was put into this part of the field by Hermens et al., in 1996 (107) in a EU sponsored project called Surface ElectroMyoGraphy for the Non-Invasive Assessment of Muscles (SENIAM) . This project systematically reviewed ∼144 peer-reviewed papers with the purpose of standardising sEMG acquisition, recording and interpretation protocols. The main outcome of the SENIAM project was a set of European recommendations for sEMG. These recommendations cover the essential requirements for appropriate sEMG recordings, such as: (i) sensor placement; (ii) sensor location for 27 muscles; (iii) recording and processing sEMG; (iv) modelling tasks for problem solving; and (v) how to report sEMG assuring repeatability.

This project revealed the large variability in methodologies used in different European research facilities. The journals and literature scanned for this purpose are shown in Table 2.1.

From this systematic review, Hermens et al. (2000) (1) stated that 91.24% reported that bipolar configuration was the most frequently used, followed by the array/line configuration (4.76%) and lastly, the monopolar configuration (4%). Furthermore, the electrode shape and size information collected revealed that 78.7% used circular electrodes, 17.3% rectangular/bar, 2.7% squared and the rest used oval shape electrodes.

Table 2.1: Numbers and years of sEMG publications reviewed for the SENIAM project. Adapted from (1)

Journal	Scanned volumes	Number of publications
The Journal of Electromyography and Kinesiology	1991 - 1996	34
Electromyography in Clinical Neurophysiology	1993, 1995, 1996	20
Electroencephalography in Clinical Neurophysiology	1992 - 1996	38
The Journal of Biomechanics	1992 - 1997	13
Ergonomics	1994	6
Muscle and Nerve	1992, 1993, 1994, 1996	9
The European Journal of Applied Physiology	1995, 1996	24
	Total:	144

The sensor configuration has been an important part in the sEMG recordings, particularly related to this thesis as it will be reviewed when addressing the technology used. These numbers, as well as the accepted skin impedance, are represented on Figure 2.2.

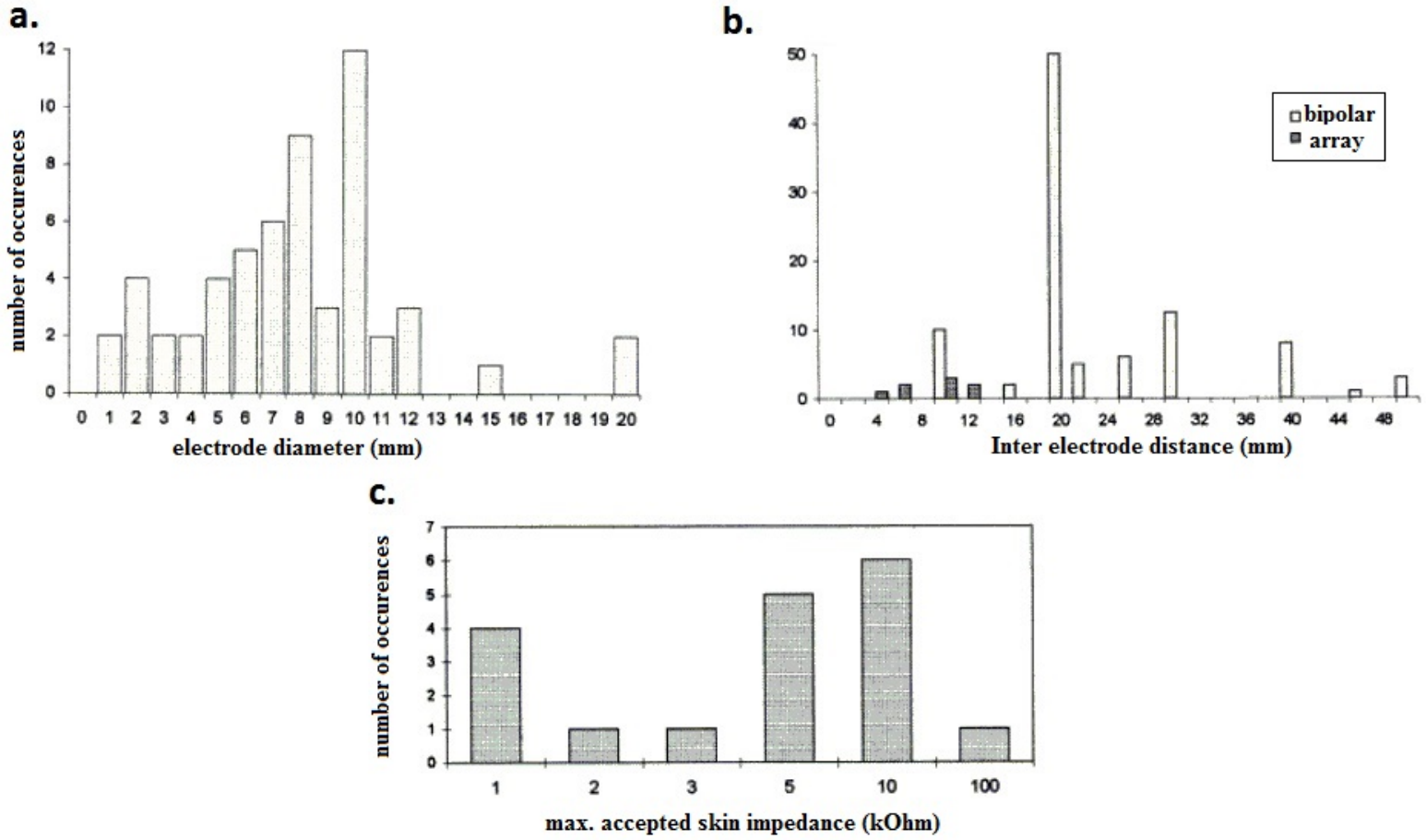

Figure 2.2: Recommendations for sEMG Electrodes from SENIAM project - Recommendations for sEMG electrodes and their placement based on literature found in between 1996-1999. a. Electrode diameter found in the literature; b. Accepted skin impedance for sEMG recordings; and c. Inter-electrode distance (IED) most frequently used reported in the literature. Adapted from (1).

Although the author recognises that these data are from pre-1996, the recent sEMG advances have been around the number of electrodes to be used. Developments since 1996 have focused on creating large electrode grids (of up to 64 electrodes) combined with the possibility of different recording configurations, e.g. monopolar, bipolar, hybrid. When multiple electrodes are arranged in close proximity, the electrode configuration is known as high-density sEMG (HD-sEMG) and given the state of this technology, these types of configuration are still confined to use in research groups.

2.2.4 Electromyography Signal Analysis

The sEMG signals acquire noise and attenuate while travelling through different tissues of the body and being picked up by the sEMG electrodes(11). The acquired surface electromyographic signals require advance processing methods for their correct classification (depending on the application).

Amplitude and spectral analysis (time and frequency, respectively) have been used for many years to assess muscle activation and muscular fatigue. Given the nature of sEMG, these analyses become particularly challenging when extracting information related to individual MUs, or to map their recruitment.

Over the years, there have been different methodologies to achieve all the previous. In this subsection, sEMG processing techniques will be explained and classification techniques will be described, leading to the sEMG application of interest in this research, i.e. the control of powered upper limb prosthesis.

2.2.4.1 EMG Signal Processing

Signal processing techniques are used to extract information from the sEMG. Many different approaches (some traditional, other emerging) will be discussed next.

In the time domain, the change in shape of the sEMG is related to the muscular effort or muscle fatigue. On the other hand, the dominant changes in the frequency domain are seen in the signal spectrum in lower frequencies, especially when an isometric voluntary contraction (IVC) is performed. Spectral changes can be evaluated in the time domain with zero crossing techniques of the signal (108). The current state of the art methods will be summarised next.

sEMG Filtering - Noise and interference contained in the sEMG signals have to be themselves attenuated. Failure in doing so may lead to erroneous interpretation of the signal. According to De Luca (2010) (109), the simplest and most direct way to increase the fidelity of the sEMG signal is to filter the maximum amount of noise and keep as much of the sEMG signal spectrum as possible. Often, a high-pass filter is applied to the signal (with cut-off frequency near 10-20Hz) and a low-pass filter (cut-off frequency near 400-450Hz). These filters are used to reduce the noise and artefacts, nevertheless, analogue notch filters are commonly used to reduce the 50 or 60Hz interference [(110),(111)], however this can be debated as there is significant EMG spectral power at 50 Hz. The band-pass determination of the filters results in a compromise between reducing the noise and preserving the desired information from the sEMG signal (2). Over the past three decades, several recommendations have been put in place, which can be found in Table 2.2.

Table 2.2: Recommendations and Standards Proposed for sEMG Filtering since 1980. Adapted from (2)

Proposed by	High-Pass Cut-off Recommendation
International Society of Electrophysiology and Kinesiology (1980) (112)	20Hz
Standards for Reporting EMG Data (1990) (113)	5Hz
Journal of Electromyography and Kinesiology	10Hz
sEMG for Non-invasive Assessment of Muscles (SENIAM) (107)	10-20Hz
van Boxtel (1998) (114) & van Boxtel (2001) (115) (only empirical recommendation)	15-28Hz

sEMG Amplitude Processing - For an amplitude estimation, the sEMG should ideally be noise-free and have zero mean, which is rarely the case. According to Merletti et al. (2005) (108), the sEMG has to undertake the following stages for an appropriate

amplitude estimation: i) Noise and interference attenuation (the goal is to eliminate additive noise, artefact noise and power line manifestation in the signal); ii) Whitening (increasing the signal to noise ratio of the EMG amplitude estimate); iii-v) After ii), the signal is assumed noise-less and uncorrelated, this stage raises the absolute value of each sample to a power (demodulation), then the signal is smoothed (by sliding a window forming averaging filter), and then relinearized.

This processing is of high importance when post-processing techniques are applied to further understand different sEMG patterns and characteristics.

sEMG Information in Frequency Domain - The first observations on in the spectrum of a sEMG signal were observed in 1912 by Piper (from (108) about (116)) when he detected a change in the oscillations of the signal during MVC recordings (led by muscular fatigue). In the coming years, research in the frequency domain of sEMG signals was made using spectral descriptors:

- Mean or centroid frequency (MNF) [(117), (118)]
- Median frequency (MDF) [(119), (120)]
- High and low frequency ratio (121)

MNF and MDF provide information regarding the change of the spectral signal versus time. Both values are found to be the same when the spectrum is symmetric with respect to the centre line and their difference is reflected in spectral skewness

In addition to the previous descriptors, parameters obtained from the time domain e.g., zero crossings [(122) and (123)] and spike properties (124), were proposed as other indicators of the changes found in the spectral content (108).

After considerable efforts to investigate factors influencing sEMG spectra [(125), (126), and (127)] underlining physiological events, conclusions were drawn by Lindstrom and Magnusson (125). These related mostly to the effect of the spacial filter on the power spectrum density (PSD), proving that the spectra vary as a direct consequence of the changes of MU conduction velocity. This concept was reinforced and further developed by Stulen et al. (128) emphasising the importance of the spectral analysis in studies of muscular fatigue.

The spectral analysis of sEMG signals detected during isometric voluntary contractions (IVCs) tasks is generally performed nowadays using the short-time Fourier transform (STFT) [(129), (130), (131), (132)].

The next overview will cover the latest advances in sEMG signal processing:

Wavelet Analysis - Wavelet analysis has been used as an alternative to the Fourier transform method. The ability to extract features in the spectrum analysis and then relating them to the relevant time points in the time domain is one of the most fundamental concepts in signal analysis. Wavelets can be analysed in both continuous and discrete forms (CWT-Continuous Wavelet Transform & DWT - Discrete Wavelet Transform). The computational time for DWT is low, nevertheless, CWT is more consistent and less time-consuming due to the lack of a down-sampling stage. The DWT method has been applied widely for non-stationary signals, such as sEMG but its output is a high-dimensional feature vector (133).

High Order Statistics (HOS) - Defined as spectral representations of high order cumulants. HOS can identify deviations from linearity, stationarity or Gaussianity in the signal (134). These methods have been found to be important for a high-quality neuromuscular diagnosis, to obtain information on innervation pulse trains and MUAP characteristics (135).

Empirical Mode Decomposition (EMD) - This is a data-driven adaptive technique introduced in 1998 by Huang et al. (136) aiming to decompose a multi-component signal into a number of virtually mono-component intrinsic mode functions (IMFs) plus a non-zero mean value of the residual component. For sEMG signals, EMD is sometimes used for background activity attenuation (137). This is found to be used occasionally in terms of high computational cost.

2.2.4.2 EMG Signal Classification

In recent years, classification (also commonly referred as machine learning) of algorithms of EMG signal patterns has been a research interest across research laboratories around the world. There are different type of classifiers and the choice of which one

to use depends manly on the application that will use their output. Most classification methods divide the signal into smaller segments (windows). A sliding window is often used for real-time applications due to the minimal pre-processing that has to be performed (138). From these windows we can extract features that will categorise the different features from the input data. An acceptable feature set, ideally, should have little variation between the same movement (intra-movement variability) but should vary significantly across the different movements (inter-movement variability). If applied to upper-limb prosthetic control, the variation of the muscle propagation feature set should ideally be different, providing a pre-defined output encouraging the device to move in a certain way.

The complexity of the input data will determine the ideal type of feature extraction methodology. It is important to identify the different features for effective classification (139). A variety of methods have been employed throughout the years to discriminate between movements, e.g., visual inspection and statistical analysis (140); correlation-based feature selection (141); forward-backward search of features (142); fast-Fourier transform coefficients (143). Further methods have been applied to the control of robotic arms and upper limb prosthesis, e.g., k-NN classifiers (144); multiple-window method (145); fuzzy classification (146); amplitude based classification (147).

Once the signal features have been derived, characterising the windows of input data, these features are used to feed into the classification algorithms. These types of algorithm should be able to recognise and relate the patterns in the features with each of the different activities. The extent of complexity varies from method to method. Regardless of the effort in the upper-limb prosthesis research, most of the classification methods have been used to analyse dynamic activities, e.g. walking; sitting-standing; standing-sitting; movement of the trunk compared to a limb. Some of these are:

i) Threshold-based classification - where an extracted feature is compared to a previously set threshold to determine if the feature is relevant (or significant) or not. This approach is mainly used to monitor day-to-day activities in conjunction with other type of sensors (i.e. accelerometers, gyroscopes). i.e. static postures, standing, sitting and lying [Makikawa and Iizumi (1995) (148), Busser et al (1997) (149), Bussmann et al (1998) (150), Uiterwaal et al (1998) (151), Aminian et al (1999) (152)].

Threshold-based classification has been mainly applied to the detection of falls (sudden postural transition).

ii) Hierarchical methods - this method is based upon binary decision constructed by consecutive nodes. At each node, a binary decision is made depending on the input features; this decision is made at each node is obtained through a manual inspection and analysis of the training data causing to be a highly time-consuming method. The classification schemes is based on threshold rules, probabilistic methods and signal morphology techniques [Fahrenberg et al (1996) (153), Fahrenberg et al (1997) (154), Lee et al (2003) (155)].

iii) Decision trees - similar to the aforementioned methods but instead of being a manual inspection of the data before its training, rigorous algorithms automate the process creating a set of rules. This method uses the time-domain features calculated through frequency-domain features using less computational resources [Bao and Intille (2004) (138), Maurer et al (2006) (141), Decision trees Parkka et al (2006)].

iv) K-nearest neighbour (kNN) - for this method, a multi-dimensional feature space is constructed, each dimension corresponds to a different feature. Classification is determined by the majority of k-nearest neighbours corresponding to a certain activity [Foerster et al (1999) (156), Foerster et al (2000) (157), Bao and Intille (2004) (138), Maurer et al (2006) (141),].

v) Artificial neural networks - often linked to mathematical functions to represent complex relationships between the input data. As decision trees, ANN are introduced with a set of training data, after the network is trained outputs are obtained for any set of inputs.

ANNs is commonly referred as multi-layer feedforward neural network. The information travels through the network controlled by the weighting of the links between the nodes, and their transfer function. This type of network is trained iteratively to optimise the distance between nodes [van Laerhoven et al (2004) (158), Baek et al (2004) (159), Zhang et al (2005) (139), Parkka et al (2006) (140)].

Alternatives to this method are the probabilistic neural network and the pulsed neural network, but unlike ANN, they require extensive training periods.

vi) Support vector machines - this algorithm finds the optimal decision separating hyperplanes between classes with the greatest boundary between the class features. This algorithm has been applied mainly to small number of classes [Huynh and Schiele (2006) (160), Zhang et al (2006)(161), Zhang et al (2006) (162), Doukas et al (2008) (163)].

vii) Naive Bayes and Gaussian mixture models - the first classifier is based on the estimated conditional likelihood of the signal features from each class. For the latter one, the centres and covariances of the mixture components are obtained through the expectation-maximization algorithm [Kern et al (2003) (164), Ravi et al (2005) (165), Huynh and Schiele (2006) (160)] .

viii) Fuzzy logic - this classifier maps from a set of inputs to one or more outputs through a set of if-then rules. The features are assigned as memberships through membership functions ranging from 0 (high) to 1 (low) [Lee and Mase (2002) (166), Salarian et al (2007) (167)].

ix) Self-organising maps (SOM) (Kohonen Maps) - patterns are identified and localised within a feature space from a number of time-domain features. The SOM is an array of neurones that store the projections of the inputs into a lower dimension. This classifier recognises and maintains the groupings proximity characteristics [van Laerhoven et al (2000) (168), Krause et al (2003) (169)].

At the beginning of 2001, Duda et al (170), categorised classification techniques into supervised and unsupervised; this was later revised by Webb (171) and Theodoridis et al (172). Although little has been done around unsupervised techniques to classify muscular activity, great efforts have been made by Preece et al (2009) (3) to review the different machine learning techniques in activity classification.

All the different methodologies produce different results depending on its application; under the same circumstances, some are more effective than others. A comparison between classification methods used across different literatures is shown in Table 2.3; although the data used for analysis comes from an accelerometer, it gives an idea of the differences between methods under the same application.

The accuracy of the methods and the computational resources used are of particular importance in upper-limb prosthetics research having a direct impact in the user-prosthetist training, the different device gestures available and how 'natural' a movement can be (human-machine interface).

Table 2.3: Literature comparing different machine learning methodologies when accelerometer data are used. Adapted from (3)

Publication (number of subjects)	Activities (number of activities)	Inter-subject classification accuracy placements
Bao and Intille (2004) (138)	Walking, sitting, cycling, running vacuuming, folding and more (20)	Decision tree (84%), kNN (83%) Naive Bayes (52%)
Parkka et al (2006) (140) (16 subjects)	Lying, sitting, walking, Nordic walking, rowing, cycling and more (8)	Decision tree (86%), Hierarchical (82%), Neural network (82%)
Maurer et al (2006) (141) (6 subjects)	Sitting, standing, walking, ascending/descending stairs and running (6)	Decision tree (87%), Naive Bayes (<87%), kNN (87%)
Prittikangas et al (2006) (142) (13 subjects)	Typing, watching TV, drinking walking upstairs, cycling and more (17)	Neural network (93%), kNN (90%)
Ermes et al (2008) (173) (12 subjects)	Lying, sitting, walking, Nordic walking, rowing, playing football and more (9)	Neural network (87%), Hierarchical (83%) Decision tree (60%)
Ravi et al (2005) (165) (2 subjects)	Standing, running, sit-ups vacuuming, brushing teeth walking and more (8)	Naive Bayes (64%) SVM (63%) Decision trees (57%), kNN (50%)
Lester et al (2005) (174) (2 subjects)	Walking, driving, jogging, ascending/descending in an escalator and more(10)	Naive Bayes (67%), HMM (47%) HMM and binary classifiers (95%)
Allen et al (2006) (175) (6 subjects)	Sitting, standing, lying, walking and four postural transitions (8)	Gaussian mixture model (91%) Hierarchical (71%)

The goal of using signal classifiers is to categorise the different types of activities into different groups to be used in different types of applications. In the next subsection, some applications will be detailed.

2.2.4.3 sEMG Applications

The specific properties that the sEMG provides can be used widely across different fields and for different applications. The main features that can be obtained and used, according to Stegeman et al. (2000) (176), are that of (i) source description; (ii) motor unit structure; (iii) volume conduction; (iv) recording configurations; and (v) recruitment and firing behaviour.

The most common sEMG applications are:

- Neurology - Disorders in the Central Nervous System (CNS) can be shown through abnormalities in the firing rate of the sEMG and are most commonly used with other sensors, e.g. accelerometers. The sEMG is often compared between natural patterns and affected ones. Some examples of this application can be found in (177) (Figure -a), (178) (Figure -b)

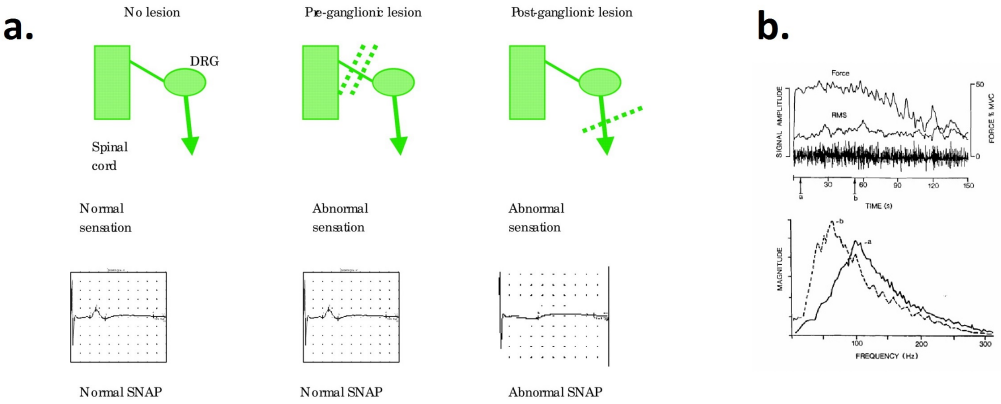

Figure 2.3: Examples of sEMG in Neurology - Examples for sEMG applied in Neurology. a. Normal and abnormal sensory responses in pre and post-ganglionic lesions, respectively. Adapted from (177), and b.Top - sEMG amplitude and force during an isometric voluntary contraction in the first dorsal interosseous muscle; b.Bottom - Power density spectra of the sEMG at the beginning and at the end of the contraction. Adapted from (178).

- Ergonomics - An increased sEMG reflects an augmentation of the muscular activity possibly related to bad postures. This type of sEMG application mainly use as a scope the muscle synergies between antagonists and agonists muscles. Some examples can be found in (179) and (180).

- Exercise Physiology - This is used to study the variation of the motor performance while a set of activities are carried out. It provides a description of normal muscle function during a selected routine of movements or postures. Recent applications in this field aim for the improvement of the performance during sports. Some examples can be found in (181), (182) and (183).

- Movement and Gait Analysis (Biomechanics) - The fields of human motor control and movement research analyses with sEMG acquisition. Investigations around the mechanical effect of muscular contraction while walking have been thoroughly studied in the past. Some examples of this application can be found in (184), (185), and (186).-

- Rehabilitation - One of the main applications of sEMG. The fields in within this application are vast and they focus on pain; pathologies; age-related effects; amongst others (187). Some examples of sEMG applied in rehabilitation can be found in (188) - Figure 2.4, and (189).

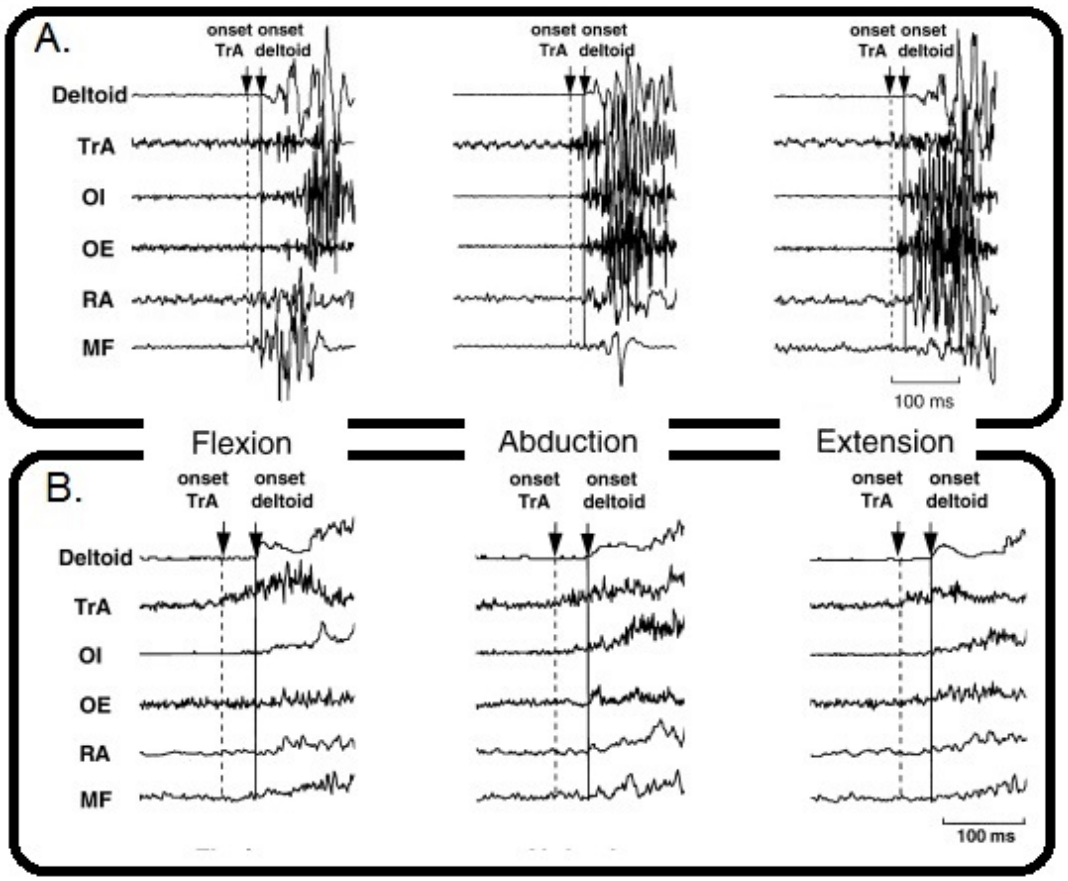

Figure 2.4: Example of sEMG applied in Rehabilitation - The sEMG is acquired from the muscles of the shoulder to assess if there are any changes in the firing patterns while three set of movements with the arm are performed, i.e. flexion, extension and abduction. A. sEMG acquired before fatigue, B. Fatigued shoulder muscles after a set of routine movements. Adapted from (188)

- Biofeedback - For this type of application, sEMG is used as a tool to show the user a desired output. This output is based on their performance which they will use to correct/maintain the activation levels required/exerted. According to Cram(187) the biofeedback applications are commonly found in clinical psychology and physical medicine. Some examples can be found in (190), (191).

- Control of Powered Upper Limb Prosthesis - For this application, the electrical impulses from the muscles of the arm are used as input for the control of hand prostheses. The variation of the muscular impulses collected from the amputees' hand becomes a challenge in itself. The different amputation procedures, remaining muscles, and the state of the skin in the arm come into play when a prosthetic device is diagnosed.

  To date, different methodologies have been used for upper-limb prosthetic control. The main algorithm that has had most success, and therefore, used across different myoelectric devices, are based on the estimates of the sEMG amplitude. These estimates are used to drive and control the myoelectric prosthesis. A flow diagram can be found in Figure 2.5 comparing the human physiological model paired with examples of the same model mimicked by some myoelectric hand prosthesis. This is part of a systematic review performed on myoelectric control from Fougner et al (2012) (192). Further to the aforementioned chart, a 3D representation of the myoelectric control for upper limb prosthesis can be found in Figure 2.6. In this figure, the different types of methodologies applied, as well as the stages where the commercially available prosthesis and the prosthesis confined to research laboratories sit are depicted.

  In Figure 2.7 the citation map of the last decades is shown from 1960-2010 with regards to machine learning techniques applied in myoelectric prosthesis. This map depicts the main contributors to the field as well as the review papers that have appeared throughout.

  Finally, in Figure 2.8, the number of papers produced in the last decades in this field is depicted. With that, a noticeable increment of research performed in upper limb myoelectric prostheses is shown.

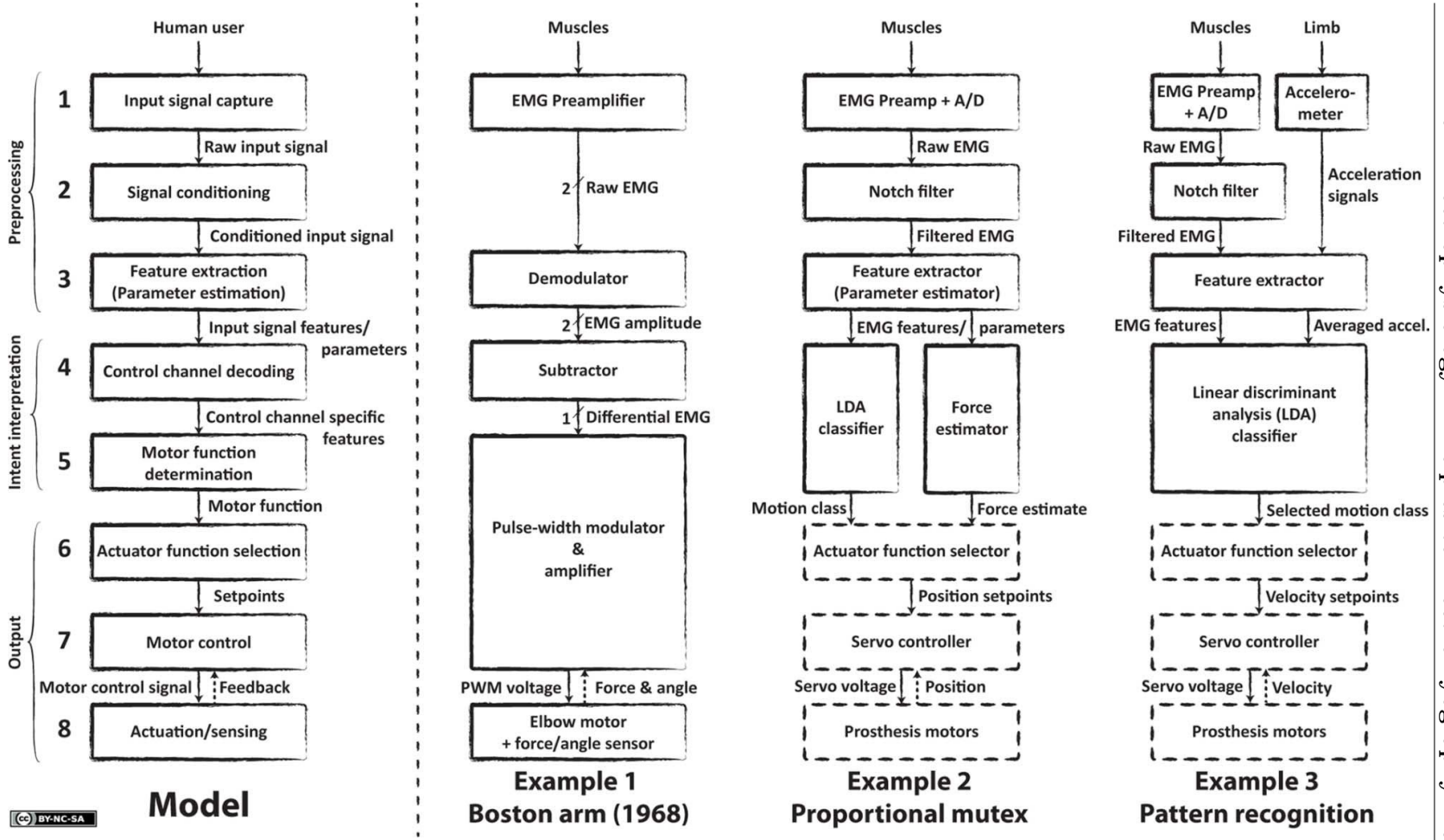

Figure 2.5: A Layered Functional Partitioned Model and Corresponding Taxonomy for Prosthesis Control Problem - Augmented version of the model based on Losier(193) proposed by Fougner (192). Three examples are given: 1) Control system for the Boston Arm in the year 1968 (194); 2) Proportional mutex control system, where level 1-5 correspond to the research by Hudgins (195) and levels 6-8 (dashed lines) represent a possible implementation in a prosthesis; 3) multi-modal pattern recognition approach, where levels 1-5 are described by Fougner(196) and the dashed lines represent a possible implementation of layers 6-8.

Figure 2.6: A 3-D Representation of Myoelectric Control for Upper Limb Prostheses - Some examples of commercial prostheses are indicated in the diagram, along with two examples limited to research laboratories. The 'Research state-of-the-art' label is that one that refers to a multi-modal pattern recognition system (defined by Fougner (196)), as well as the 'SVEN hand' example which refers to Almstrom's research (197). The intent interpretation axis corresponds to the complexity of the system to interpret the user's intention. This figure is licensed under a Creative Commons BY-NC-SA license. Adapted from Fougner et al (192).

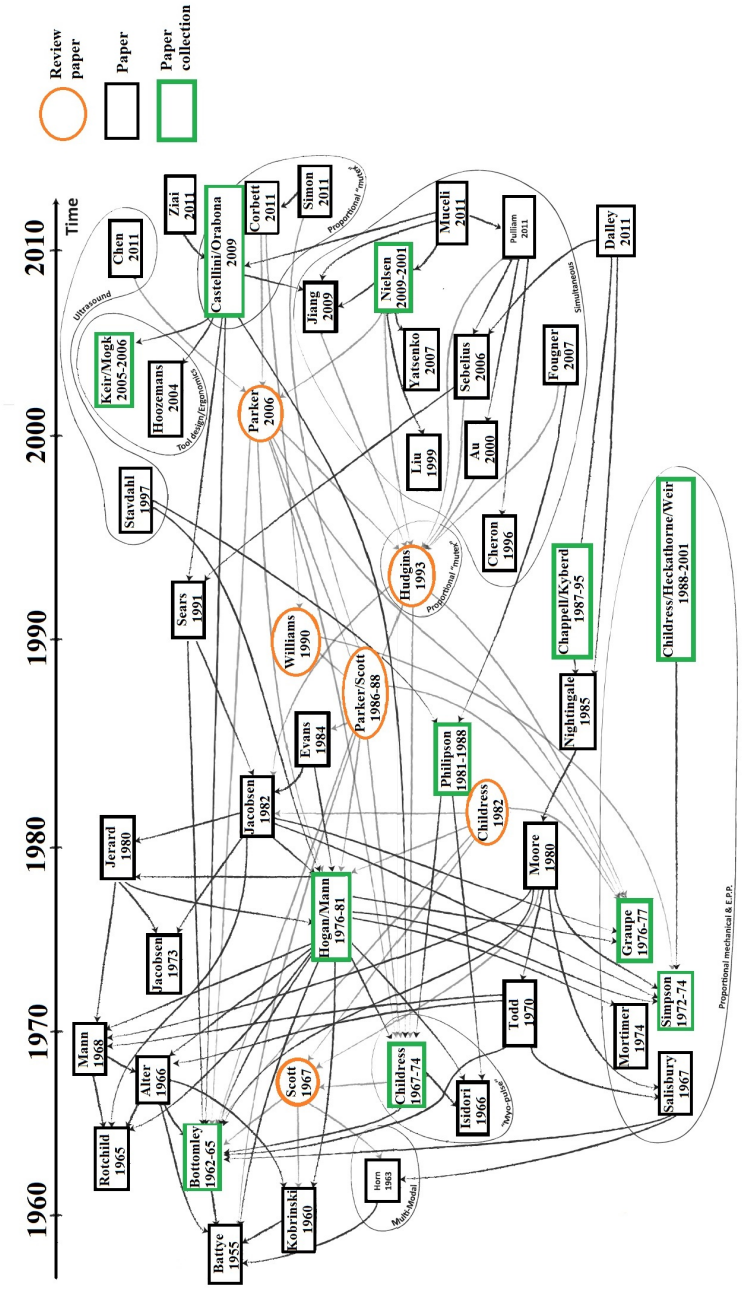

Figure 2.7: Citation map from 1960 - 2010 about Machine Learning applied in myoelectric prosthesis - Citation map of the last decades depicting the main contributors in the field, as well as the review papers that have appeared throughout. Adapted from Fougner et al (192)

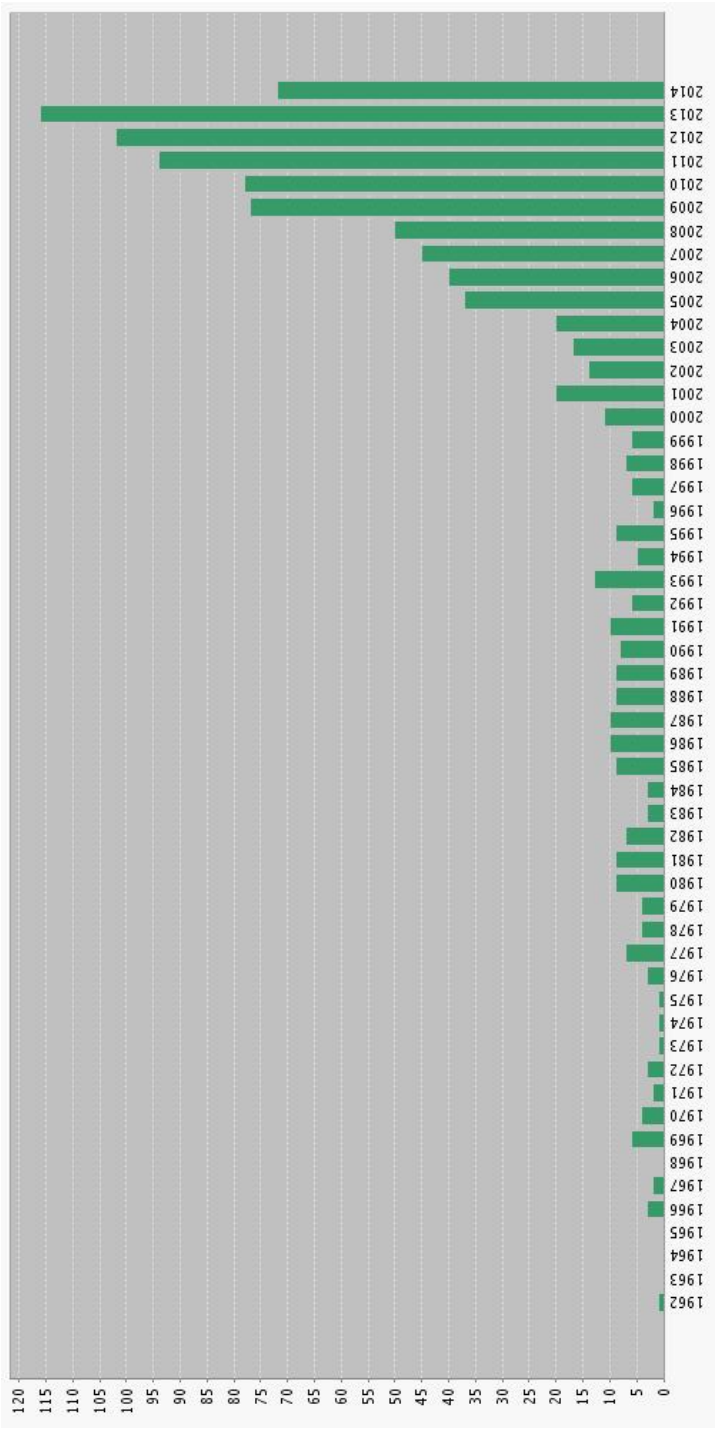

Figure 2.8: Papers produced about Myoelectric Prosthesis from 1962 to 2014 - The amount of papers produced in the last decades is clear in this chart. There is a noticeable increment of research performed in upper limb myoelectric prostheses and machine learning methods applied to them.

2.3 Coherence in sEMG

Coherence estimates quantify the range of frequencies of common rhythmic synaptic inputs across the motor neurone pool [Farmer et al. (1993) (198), Rosenberg (1998) (199)].

During experiments done by Barker et al. (22) Kilner et al. (200) and Semmier (201), dependence between specific motor tasks and the oscillatory synchronisation were repeated during maintained steady grip (contrary to his findings for movement phases).

Although EMG-EMG coherence has been experimentally found at 16-32 Hz [Halliday et al. (1998) (202), Barker et al. (1999) (22), Kilner et al. (1999) (200)], from neurophysiological signals (e.g. electroencephalograms (EEGs), magnetoencephalograms (MEGs), and cortical neurone and motor unit discharge times), the mechanism producing this oscillatory drive to the motoneurone pools of the synergistic muscles is still unknown and may involve closed loop pathways, supporting this is a lack of coherence during isotonic contribution against fixed leads resulting in no length change in the muscle. During isometric contractions, coherence has been found present during the beta band (15-30 Hz) (203). In a further study by Halliday et al. (1999) (204), the MU analysis revealed coherence in two distinct frequencies for motor-unit synchronization, 1-12 Hz and 15-30 Hz.

The sEMG is influenced by many different factors [as explained in Section 1.1.3] that are independent of muscle activity (Farina et al. (2004) (24)). These elements have influence in the quantity derived from the sEMG to deduce activity from the analysed motor units. Keenan et al. (2011) (205) found that coherence measures between hand muscles were sensitive to the electrode location (placing electrodes near the innervation zone decreased the magnitude of coherence). In addition to this, Beck et al. (2008) (206) and Rainoldi et al. (2004) (207), found that that these coherence differences were also due to the variation in the sEMG amplitude.

The sEMG rectification (prior to the coherence analysis) has been found to improve the coherence estimates [Yao (2007) (208), Halliday (2010) (209), Boonstra (2012) (210)].

An incremental in the oscillatory drive from EMG recordings has been associated with impaired performance. This was found during hand tasks in younger adults by

Halliday et al. (1999) (204) and Kakuda (1999) (211). Furthermore, Baker et al. (2001) (22) and Kilner et al. (1999) (212) showed that (for hand muscles) the coherence estimates are relative to isometric grip force task undertaken.

Current literature has shown a vast range of research done in coherence analysis regarding electrophysiological signals. As shown in Table 2.4, it has been reported in the literature that lower frequency ranges (below 50 Hz), have been associated with synchronous oscillatory drive to motor neurone pools.

Table 2.4: Coherence Estimates Found Across Literature Between Different Hand Muscles.

Publication	Methods	Coherence Frequency Range [Hz]	Coherence magnitude
Kilner et al (1999) (212)	Hold task from forearm muscles	15-30	0.5
Grosse et al (2004) (213)	Symptomatic and asymptomatic px with dystonia (EMG from tibialis anterior)	peaks at 5-10	0.8 & 0.9
Farmer et al (2007) (202)	Long and short thumb abductor muscles	1-12 & 16-32	0.1 & 0.05
Santos et al (2010) (214)	12 hand muscles during finger contraction tasks	5-15	0.05 & 0.1
Kisiel-Sajewicz (2011) (215)	Stroke and healthy patients muscles from shoulder flexor and elbow extensor	0 - 11	0-0.5

Regardless of the research efforts in this area, it is still unclear about the functional significance that the coherence estimate has.

3

Thesis Statement

In Section 1.1, a wide perspective on the motor neurophysiology at the actuators level (muscles) was explored. Based on the review regarding the human motor system and electromyographic mechanisms and processes (e.g., machine learning) to further our understanding in the motor neurophysiology and the upper limb amputations (techniques and descriptive statistics) presented in Section 1.2, it is concluded that understanding the electrophysiological mechanisms of the remaining muscles of the forearm is crucial to be able to drive myoelectric upper limb prosthetics in a natural way. The nowadays mechanisms adopted by the commercially available prosthesis were detailed in Section 2.2.4.

However, as described in Section 2.2.4.2, where signal classification techniques were discussed thoroughly, the aforementioned techniques are mainly focused in the pattern recognition analysis of the signal, provided a widely known set of movements (for prosthetic control). These movements are the ones that the commercially available prosthesis are able to achieve (driven by a single on/off muscular detection). These type of mechanisms, albeit improving amputees' quality of life, are still not driven by natural movements of the remaining muscles, hence, new mechanisms and new studies need to be performed to understand the electrophysiology of the muscles to be able to drive prostheses without computational cheats.

To date, there is no commercially available prosthesis able to drive the thumb from the muscles propagation nor muscles interaction acquired via sEMG. As it has already been explained, the thumb represents one of the most important fingers in the hand, making it hard for any amputee to be able to control their hand without proper

thumb-driving mechanisms. To the best of the author's understanding, techniques such as EMG-EMG coherence and unsupervised machine learning have not been applied to upper limb prostheses, therefore, nor studied different thumb opposition movements in the upper limb prosthesis context.

3.1 Research Statement

It is of interest to this research to:

1. Differentiate thumb opposition grips, based on muscle activation patterns.
2. Understand the motor drive controlling the extrinsic muscles of the hand providing meaningful contrasts through different type of analyses.
3. To understand the spectral composition variation that reflects changes in the muscle synergy while different thumb grips are executed.
4. To find a successful classification through machine learning techniques that would cluster the different thumb grips.
5. To implement the classification methods aiming for a dexterous prosthetic control.

3.2 Research Hypotheses

The Muscular Propagation while Thumb Opposition Tasks- It is of interest whether there are consistent signal features from the musculature of the hand associated with different thumb opposition movements. If this hypothesis is proved, then it opens a new possibility regarding the way upper limb prosthetics disseminate the muscular information acquired from the forearm.

The Cortical Activity Coherence in Two sets of Pools of Muscles - It is of interest whether there is coherence between the muscle pairs of the hand (extrinsic and intrinsic, respectively) while performing thumb opposition tasks. If this hypothesis is proved, by assessing the first pool of motor units it will be able to extract information about the position of the thumb, making it possible to create new programming mechanisms to drive upper limb prosthesis.

The Differentiation of Thumb Opposition Tasks - It is of interest to be able to classify different thumb opposition tasks through unsupervised machine learning algorithms, aiming for a new implementation through a controllable prosthetic thumb fro transradial amputees.

4

Materials and Methods

4.1 Summary

Control of high-end commercially available electric prostheses is driven by surface electromyographic (sEMG) signals. Such sEMG are a complex superposition of many different electrical signals that originate in the extrinsic hand muscles, i.e., the muscles of the forearm that act on the fingers of the hand. Due to the complexity of the resultant sEMG signals, intuitive user control of prostheses has remained elusive. A complete characterisation of the muscles' electrical activity is required if intuitive control is to be realised. To further understand sEMG signals during hand control, a routine of hand movements was established to isolate muscle activity during specific actions. The routine was comprised of a set of four movements, the thumb executed an opposition against the other fingers of the hand (Fig. 4.1): 1 - the secundus digitus manus (index finger); 2 - the digitus medius (middle finger); 3 - the digitus annularis (ring finger); and 4 - the digitus minimus manus (pinky finger). High-density sEMG (HD-sEMG) signals were collected using a multichannel amplifier, specifically designed for acquiring bioelectrical signals. Experiments were carried out in two stages: firstly a system calibration was performed, using maximum voluntary contraction (MVC); secondly, a suite of thumb opposition movements was performed while HD-sEMG signals were obtained.

To facilitate the experimental design, a custom built device was used to stabilise the subject's arm and hand to help identify non-relevant electrical activity originating in muscles controlling the wrist and elbow flexion and extension. The device contained

load sensor resistors (LSRs) acting as the opposing digits of the hand.

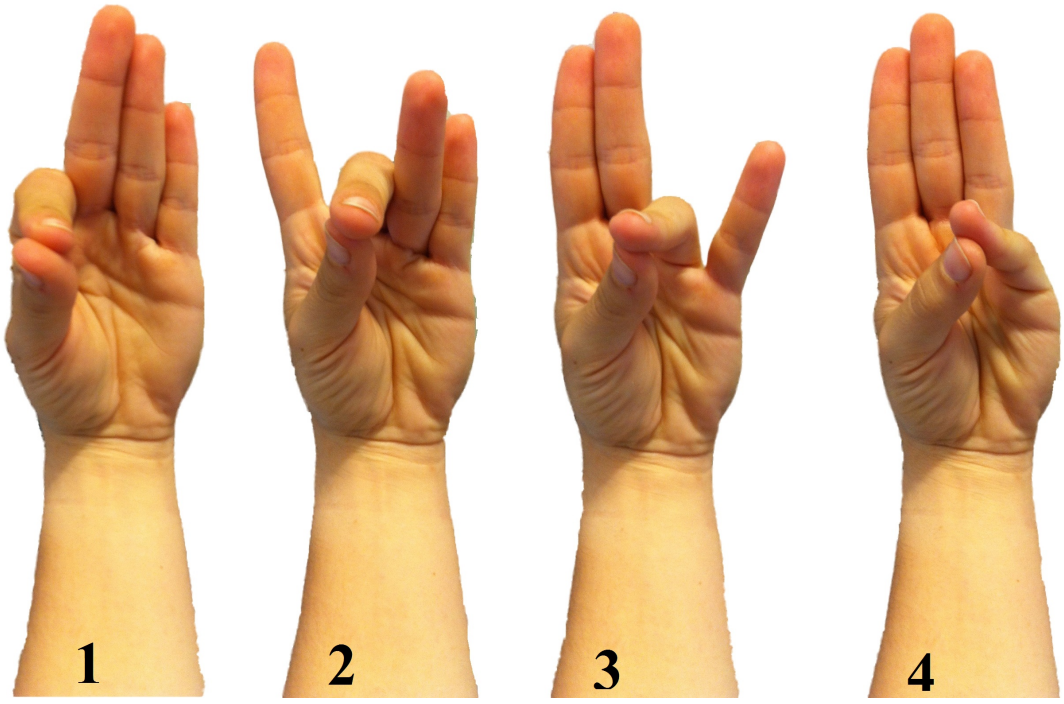

Figure 4.1: Thumb Opposition Against the Rest of the Digits - The 4 different positions described in this image represent the positions considered based on thumb opposition. The test rig was designed to mimic the positions. 1) Opposition to the index finger, 2) opposition to the middle finger, 3) opposition to the ring finger, and 4) opposition to the pinky finger. From: A. Aranceta-Garza(2013) (216)

4.2 Experimental Design

Subjects were asked to perform a set of four different thumb opposition tasks. Their right forearm was positioned on a test-rig that stabilised the wrist and the elbow. The fingers of the hand were fastened to the fingers holder (see Figure 4.2), whilst the thumb was left free to act as the main actuator. Experiments were carried out with the help of two graphical user interfaces (GUI). The first GUI was used to calibrate the system according to the subject's MVC in each of the oppositions; the second GUI was used to assist HD-sEMG signal acquisition from the muscles of the forearm during the thumb opposition movements, providing the subjects with instructions. The software

sequentially instructed the subjects to perform one of four randomly chosen thumb opposition exertions and repeated the process until a total of 30 trials per position was reached (a total of 120).

4.2.1 Research Subject/Participants

Surface-EMG data were acquired from seven healthy right-handed subjects [6 male, 1 female mean age 28.5 ± 3.7yr (mean $\pm$ SD)] with no prior history of nerve damage, hand surgery, existing neuromuscular pain, tremor, epilepsy or Parkinson's disease. All subjects were provided with an information sheet along with a consent form prior to the experiment. The experiments had been approved by the Departmental Ethics Committee of the Biomedical Engineering Department at the University of Strathclyde (a sample of the Ethics Consent Form can be found in Appendix 8.2). All the procedures complied with the Declaration of Helsinki.

4.2.2 Hardware development

To avoid any muscular contraction from the muscles responsible for flexion and extension of the wrist and elbow, a test apparatus was designed and built (Fig. 4.2). The built-in LSRs were used to time-stamp the signal when an opposition occurred, and acquired the force applied by the thumb in order to be able to control the amount of muscular contraction, and therefore avoid fatigue, during the experiment.

In preliminary experiments, force sensor resistors (FSRs) were found to be inadequate in normalising the sEMG data across experiments (for more information on the use of FSRs the reader is referred to Appendix 8.3). Instead, load sensor resistors (LSRs) were used for a further control in the force exerted by each subject. A simplified diagram of the system is shown in Figure 4.3 and its experimental use is demonstrated in Figure 4.4. The LSRs attached to the test rig's finger holder could be moved in the vertical axis to adapt their position to suit the different anatomical lengths of the subject's hand.

The LSRs were connected to a custom, electrically isolated, multichannel strain gauge amplifier (Fig. 4.5) with a gain of 500 V/V and were calibrated with a varying load: [0 - 581]g.

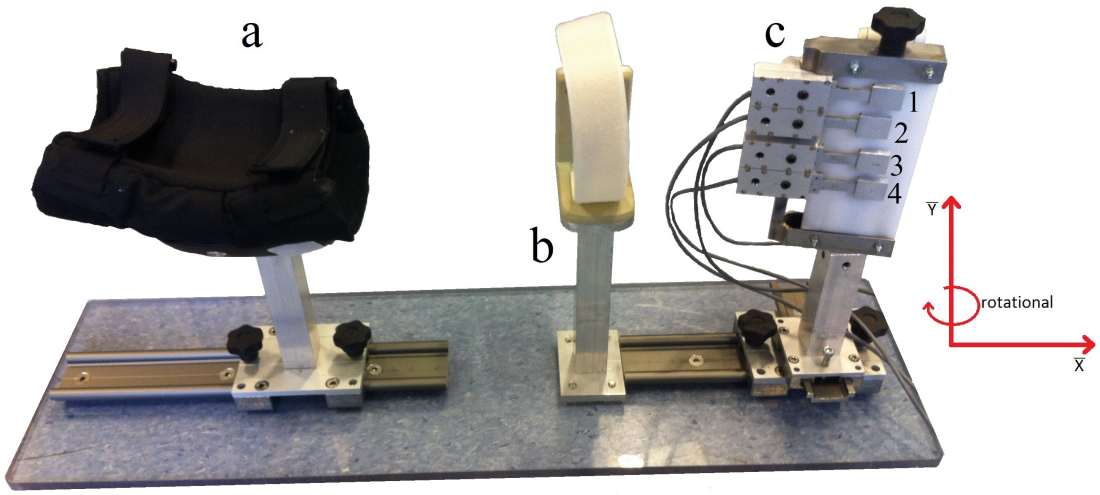

Figure 4.2: Built Test Rig - Final Design. - Test Rig used to examine thumb opposition; a) elbow holder: with movement in the X axis, to allow adjustment for subject comfort, minimising muscle contractions caused by pronation, supination, flexion or extension of the forearm; b) wrist holder: fixed padded holder that avoids any flexion or extension of the wrist, minimising the muscle activity in the forearm; and c) fingers holder: allows freedom of movement in the X and Y axis, as well as rotational movement. It has four load-sensor resistors (LSR) represented by the numbers 1, 2, 3 and 4, where each of them corresponds to the 4 digits: secundus digitus manus; digitus medius; digitus annularis and digitus minimus manus, respectively. Each LSR can be moved in the X and Y axis to allow adjustment to each subject's anatomical measurements.

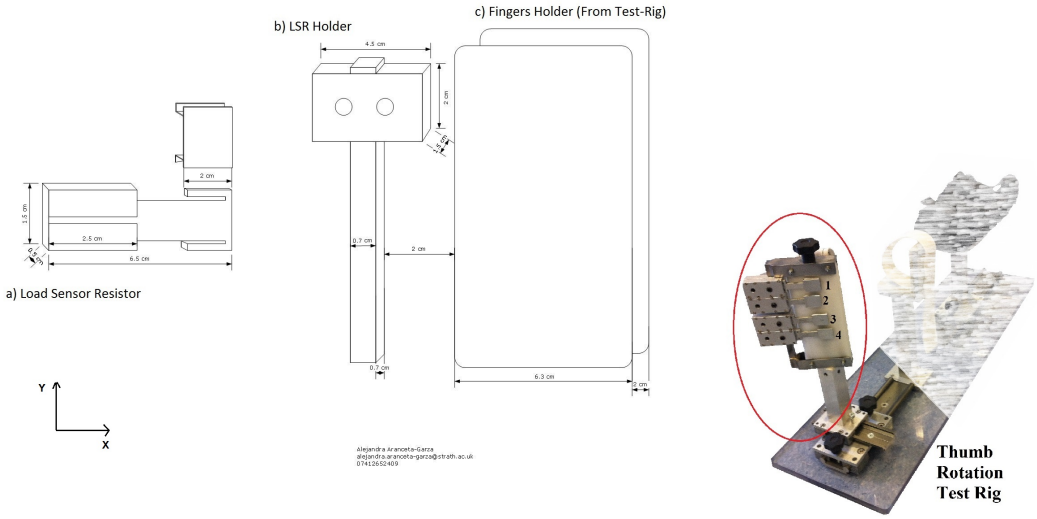

Figure 4.3: Dimensional Sketch Of The Construction of Load Sensor Resistors - Left: Sketch with dimensions of the developed load sensor resistors (LSRs) and the finger holder that was attached to the rig: a) one of the LSR with its lid (out of four built); b) rail where the LSRs were to be attached and supported, allowing freedom of movement in the Y axis; and c) the finger holder of the developed test-rig. Right- the test-rig apparatus with the fingers holder circled demonstrating the final result.

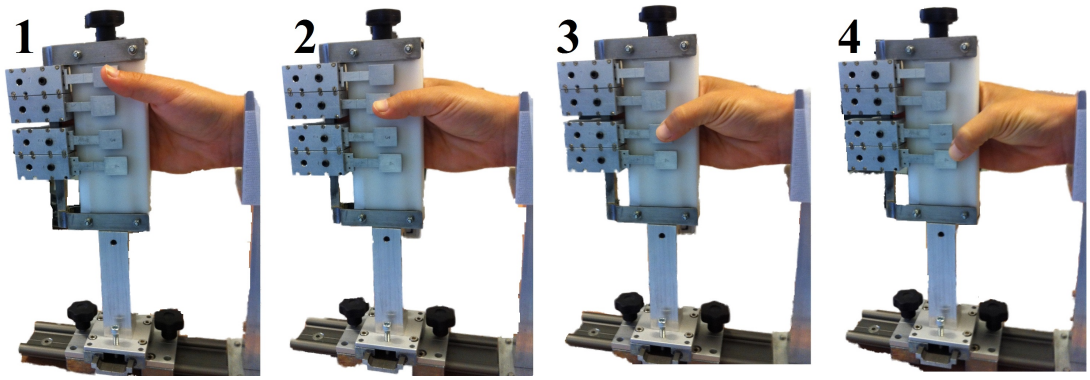

Figure 4.4: Finger Holder With LSRs - The image above shows the different movements that the volunteers were expected to perform. During each movement,the participant was instructed to press an LSR with a certain amount of force. 1- Opposition to index finger, 2- opposition to the middle finger, 3- opposition to ring finger, and 4- opposition to the pinky finger. From: Aranceta-Garza (2013)(216)

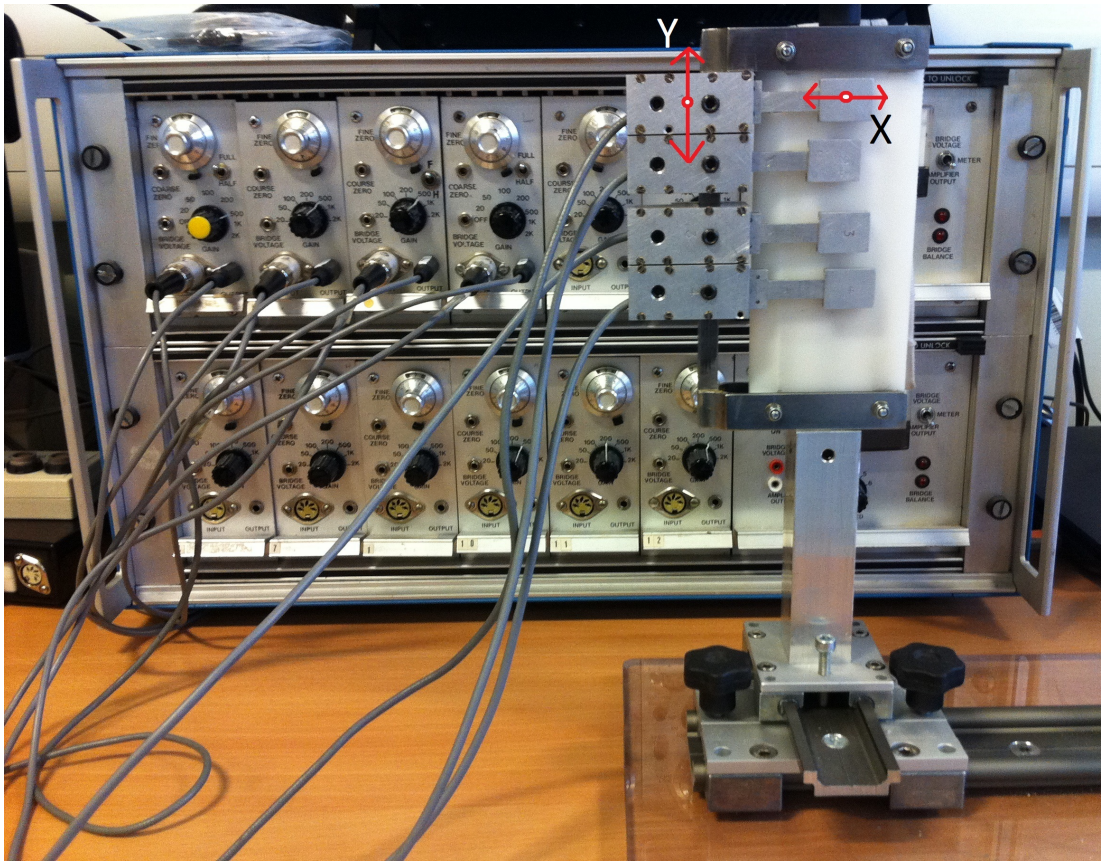

Figure 4.5: Custom-built Multichannel Strain Gauge Amplifier - In this image both the fingers holder with the LSRs and the multichannel strain gauge are shown. This amplifier was built in-house at the University of Strathclyde. The LSRs had movement in both X and Y axis as shown by the arrows. Adapted from: Aranceta-Garza (2013)(216)

4.2.3 Software development

To provide real-time visual feedback to the subjects, custom software was developed using LabVIEW (National Instruments, USA). Data from each of the LSRs (See Section 4.2.2) was acquired using a single analogue channel from a data acquisition card ([NI USB-6008], National Instruments, USA).

A separate graphical user interface (GUI) was developed for each of the two stages of experiment: 1, MVC calibration; and 2, task-opposition of the thumb. The two GUIs shared a common Main Menu (Fig. 4.6); the complete programming can be found in the supplementary material provided) which fed calibration data, obtained through MVC, to the task-opposition program. Each of the GUIs provided visual cues for the tasks required during the experiment and the main menu contained a demo program to allow the test subject to become familiar with the experimental tasks.

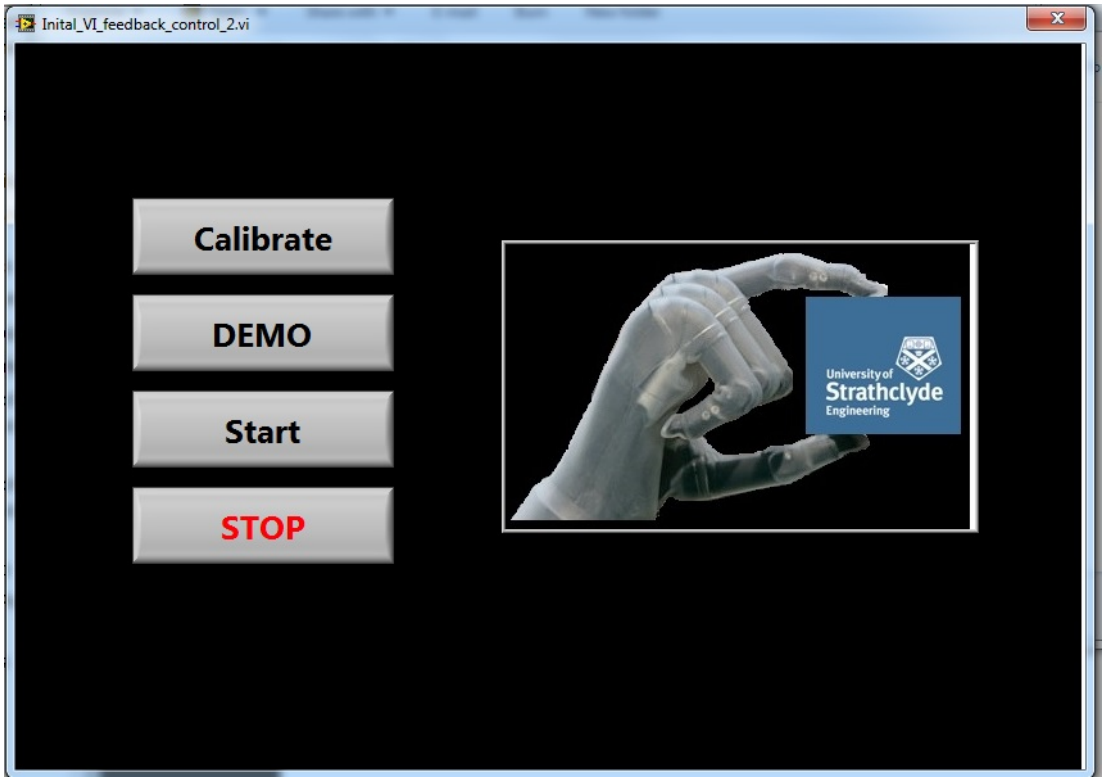

Figure 4.6: Main Menu for the Test Developed in LabVIEW - Front panel of the main menu developed for the test. This menu called up three interfaces: 1) Calibration, 2) Demo, and 3) Thumb opposition acquisition routine.

4.2.3.1 Calibration Graphic User Interface

To calibrate the task-opposition software, each subject was required to press each LSR in turn as hard as possible (isometric voluntary contraction, IVC). Contractions were maintained for three seconds and repeated three times, with a 60 second rest periods in between exertions. For each contraction, the maximum value of each IVC was calculated (also known as maximum voluntary contraction - MVC), and averaged across the 3 repetitions to provide a reference calibration for each finger (MVC). The force applied to each sensor was captured and displayed graphically on-screen, as shown in figure 4.7 (the LabVIEW source code can be found in the supplementary material provided, CD).

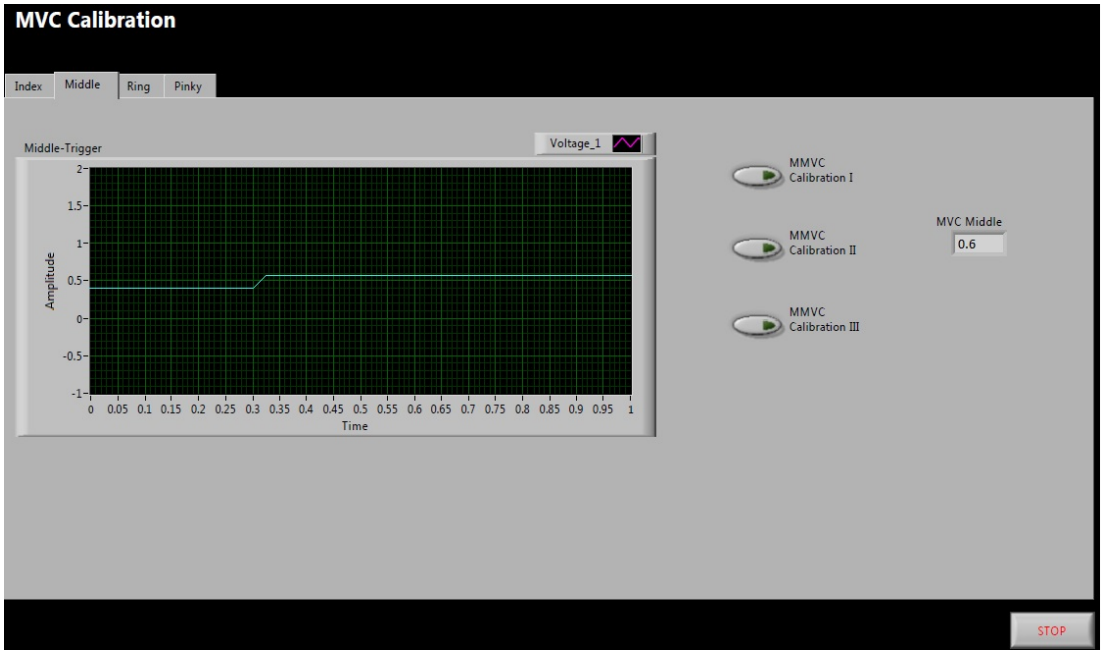

Figure 4.7: GUI For LSR Calibration According To The Subject's MVC - Front panel of the GUI programmed in LabVIEW. This interface calibrated the test rig's LSRs according to the subject's MVC. Three trials were recorded per finger, then the MVC values were average to give a maximum value. The subjects had a 60 seconds rest in between exertions.

4.2.3.2 Thumb Opposition Graphic User Interface

Following the MVC calibration, a separate GUI was developed to facilitate HD-sEMG data acquisition during thumb opposition tasks. The force exerted by the subject was required to be within 30-40% of their MVC obtained during calibration, with a five second duration, to avoid muscle fatigue during data acquisition. To facilitate this, the force exerted was displayed on screen using a coloured percentage indicator as shown in Figure 4.8-B. Furthermore, the software provided cues for the subject to rest in between exertions as well as providing information regarding which LSR was to be pressed within each iteration (Fig. 4.8-A). When a total of 120 thumb oppositions was reached (30 per position), the GUI automatically stopped. (For more details into the LabVIEW programming of this GUI, refer to the supplementary material provided, CD).

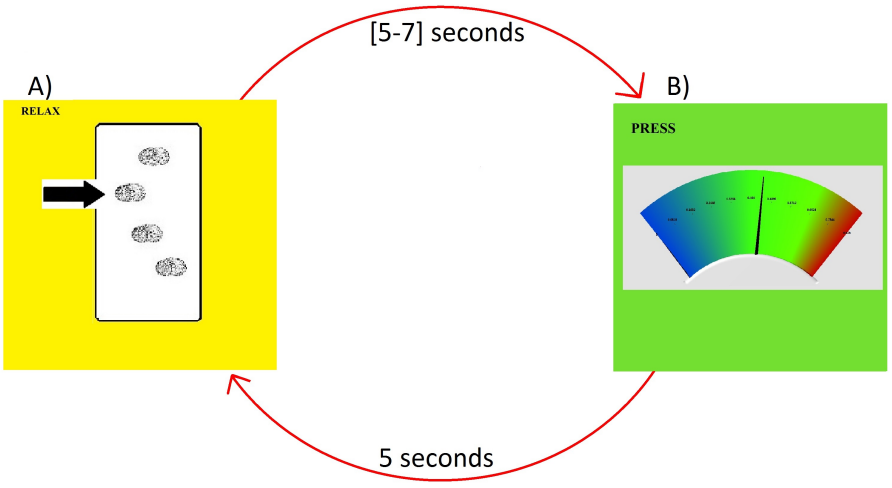

Figure 4.8: GUI For Thumb Opposition Using 30-40% of MVC - Graphical user interface showing the timing diagram and the visual cues that the subject was shown. A) Relax stage, varied from 5 - 7 seconds, the arrow indicating the LSR to be pressed changed between trials until a total of 120 was reached (30 for each position). B) Press stage, isometric contraction with a visual feedback prompt. The subject was asked to hold the hand position for 5 seconds keeping an approximate of 30-40% of their maximum voluntary contraction.

4.2.4 Electromyographic Data Acquisition

Monopolar HD-sEMG signals were acquired using 121 channels from a multichannel bioelectrical signal amplifier (EMG-USB2, OT-Bioelettronica, Italy). Samples were acquired at a rate of 2048 per second, with a fixed gain of 1000 V/V, and a bandwidth of 3-900Hz. A separate trigger input (from the LSRs) was used to time-stamp when each thumb-opposition occurred. The electrode configuration is depicted in Figure 4.9. Silver-electrode array matrixes (ELSCH004;ELSCH008 and ELSCH064R3S, OTBioelettronica, Italy) were used to extract information from different hand muscle groups. Each matrix had a different inter-electrode distance (IED). For the anterior and posterior compartments, two-64 electrode arrays (IED of 8mm) were used. Depending on the size of the volunteer's hand, a 4 or an 8-electrode array matrix (IED-10mm or IED-5mm, respectively), was placed on the first dorsal interosseous (FDI) muscle; a disposable electrode was used on the flexor pollicis brevis (FPb) muscle; and two disposable surface electrodes (N-00-S, Ambu, Denmark) were placed on the olecranon (as reference points).

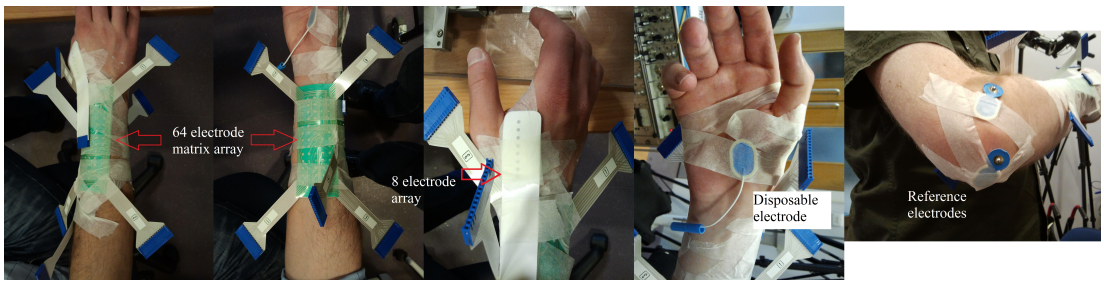

Figure 4.9: Electrode Array Configuration Setup - Electrode array configuration fixed onto the muscles. a) 64- electrode array on the extrinsic hand muscles, corresponding to the posterior compartment of the forearm. 8mm IED b) 64 - electrode array on the extrinsic hand muscles, anterior compartment of the forearm. 8mm IED c) 8-electrode array on the FDI muscle. 5mm IED d) Low-density electrode on FPB. e) surface electrodes used as grounding fixed onto the olecranon.

To increase electrode-skin contact and the quality of data recordings, the skin of the forearm and the palm of the hand were cleaned using conductive abrasive paste (A1, Spes Medica s.r.l., Italy). Electrodes were then prepared by attaching disposable pads with conductive adhesive paste (CC1, Spes Medica s.r.l., Italy). Electrode arrays were then positioned by palpation during thumb opposition exertion and relaxation and were

firmly secured in place with medical tape, to avoid any movement-induced artefacts. Once the electrodes were attached, the subject's arm was placed on the custom-built testing rig and the elbow, wrist and hand digits were positioned as described in Section 4.2.2 and in Figure 4.10. To ensure adequate adhesion, data were not collected until a period of 15-20 minutes had elapsed.

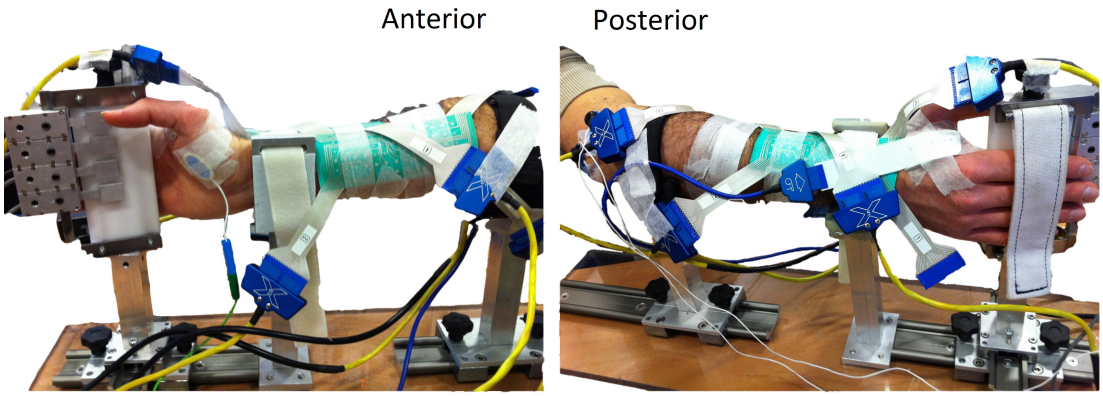

Figure 4.10: Volunteer Positioned In The Test Rig With Electrodes Attached Onto The Hand. - A volunteer positioned onto the test rig with the disposable electrodes attached to the hand. Left: Anterior view of the hand; Right: Posterior view of the hand.

To compare data acquired with different electrode placement, and in different environments, familiarisation trials were conducted. The HD-sEMG signals were acquired using medical grade isolators to remove interference. The performance of different reference points was assessed. Ideally, when sEMG is acquired from the forearm, the wrist would be the best possible place to position the reference electrodes. However, the wrist of upper arm amputees is absent and so, three alternative placements for the reference electrode were considered: 1, ankle; 2, biceps brachii; and 3, olecranon.

4.3 Data Analysis

121 channels of HD-sEMG plus an auxiliary (multiplexed from the LSRs) were recorded from each subject during the study. They were subsequently analysed using the processes described in this Section.

4.3.1 Data Inspection

The data were exported into MATLAB (Mathworks, Natick, Massachusetts, U.S.A.) for further analysis. MATLAB was chosen as an appropriate platform to further analyse the sEMG data given the possibility of developing algorithms, creating models and visualising results.

4.3.2 Importing *.otb Files into MATLAB

The software provided by the HD-sEMG manufacturer, OT BioLab, for analysis was basic and had little possibility for further development.

The manufacturer's software created a *.otb file containing the acquired HD-sEMG data and configuration information. A software to decode was created and then the data were imported into MATLAB.

4.3.2.1 Data Conditioning

The data were inspected for channels with clear noise and miss-contact, therefore the number of channels were reduced and segmented by muscle groups: flexor muscles - anterior compartment and extensor muscles - posterior compartment. The procedure applied was:

- Assessment of the quality of each electrode during the overall test with regards to noise and interference,
- Isometric voluntary contraction (IVC) separation for each position during each task repetition considering 500 ms before and after each IVC,
- Down-sampling of the signal.

4.3.3 Creating a sEMG visual toolbox in MATLAB

The HD-sEMG data acquired had a large file size and was required a considerable amount of computer processing power to analyse. Further techniques were required to develop an appropriate data visualisation and inspection method. Averaged amplitude windows of 300ms with a 50ms overlap were created. These windows allowed a better understanding of the signal propagation in time smoothing any spontaneous noise due to an electrode-skin false contact amongst others.

4.3.3.1 sEMG Propagation Visualisation

According to Barbero (2012)(13), each muscle produces a particular waveform, enabling the ability to track which muscle contributes to a particular movement. Based on this assumption, the sEMG propagation of the summation of different motor-units (MUs) was visualised. Propagation videos were produced in MATLAB to further the understanding of the recorded waveforms. Each frame corresponded to one sample (ratio 1:1) of the HD-sEMG recording. The signals were positioned in the same configuration as the electrode matrix arrays.

4.3.3.2 Colour Plots Visualisation

The processing of HD-sEMG signals as a topographical image was designed as an assistive tool for visualising muscles' propagation along the forearm. The averaged amplitude windows were used, allowing a better understanding of the contraction in the compartments of the forearm (i.e. flexor and extensor muscles), while sustaining the different thumb oppositions. In order to create a smooth sEMG pattern allowing to extract the important features in the muscle propagation, RMS values were estimated using 300ms windows with 50ms shift overlap during the isometric voluntary contraction (IVC) from each grid placed on the forearm.

Furthermore, in order to accentuate the differences seen in the colour plots, the resulting windows per grid of the forearm were averaged across each repeated movement to the four different thumb postures.

4.3.3.3 Root-Mean Square Analysis

The root-mean square (RMS) reflects the mean power of the signal, analysis is applied to the mean of each position that the thumb was opposed to. This value is known to be the equivalent to the amount of motor units activated and their firing rate (217). This method is widely applied for feature recognition/distribution, particularly that of fatigue. Changes in the motor units' central drive are estimated by the RMS value [Vitasalo et al (1977) (218)]. The RMS value is, therefore, a parameter frequently chosen because it reflects the level of the physiological activity during muscular contractions.

The quantification method recommended by Basmajian and DeLuca (12), consisted of an RMS value calculated by squaring each data point (over 300ms windows), sum-

ming the squares, dividing the sum by the number of observations, and taking the square root. Therefore, each position was plotted against the remaining 3 positions per grid of the forearm to assess the feature distribution of each thumb opposition.

4.3.4 Statistical Analysis

To evaluate the statistical significance of the distribution values for all trials throughout the tasks, data were used 500ms before movement initiation (contraction onset), sustained contraction, and 500ms after contraction (contraction offset).

New data windows were created based on the response time for myoelectric hands to operate without the user being aware of a delay, i.e. less than 350ms (Englehart, 2003 (219)). An average vector was used every 300ms and compared across the different hand movements. This average vector was also used to smooth any spontaneous artefact noise due to electrode-skin miss-contact. Finally, the results from the statistical analysis were used to assess the differences between the four thumb oppositions throughout the time course of each movement (contraction), i.e. contraction onset, sustained contraction, contraction offset. The signal was downsampled from 2048Hz to 1024Hz for this analysis.

4.3.4.1 One-way Analysis of Variance

To find significant statistical differences between the features of the four movements, represented by each finger the thumb was opposed to, a parametric method was used. A one-way ANOVA was applied to the data to compare the means of the four movements. P-values were obtained and compared; if $p < 0.05$, it suggested that at least one position of the thumb was significantly different from the others. The null hypothesis is that all population means are equal, the alternative hypothesis is that at least one mean is different. For a detailed description of the methodology used for ANOVA, reader is referred to the Appendix 8.7.

The signals were separated per position creating vectors. These vectors were so that we could perform the ANOVA analysis comparing along the profile of the movement across thumb oppositions.

4.3.5 Time-Frequency Analysis

Time-frequency signal analysis, i.e. inter-muscular (EMG-EMG) coherence, was used in this thesis as an important tool to understand the muscular signals with time-varying frequency content. The time-frequency analysis can show the variation of the frequency content during a certain time-span. This analysis can also be used to compared across subjects for the same set of tasks (thumb opposition).

4.3.5.1 Inter-muscular Coherence

The aim of this analysis was to investigate the effects of simultaneous activation of the muscles of the forearm in coordination with the hand muscles, while thumb opposition tasks were performed [as described in section 4.2]. These effects were assessed using the frequency content of the signal (coherence) and in the time domain (cross-intensity). The energy of the signal (power), phase and coherence were investigated and compared. The activation of the thenar muscles and the FDI muscle was studied while the previously described tasks were performed. The muscles of the palm of the hand were studied with the extrinsic muscles of the forearm.

Cross-correlation (time) and coherence (frequency) analyses were applied using the methodology thoroughly described by Halliday et. al. (199). The standard practice, which was applied to this analysis, is: i) full wave rectification, ii) hanning window to suppress the rippling introduced by the sampling process, iii) normalisation, iv) de-trend, and v) reduction of main frequency artefacts (50Hz).

The coherence analysis was performed between the electrode grids placed on the the intrinsic (thenar and FDI muscles) and the extrinsic (flexor and extensor muscle groups) hand muscles. Each available channel was cross-correlated in both time and frequency. The channels that had clear cross-talk were disregarded and not used for any further analysis.

The signal from the thenar muscles or FDI was used as the reference, or input, signal. In a study by Farmer (198), two analysis were performed, the first one being a steady condition test and a later one corresponding to a modulated condition test. The thumb opposition task used in this study corresponded to that of modulation (subjects would co-modulate their exertion level via the display described in section 4.2.3.2).

Therefore, a second stage of testing, corresponding to steady contractions, was later performed in one subject to assess the variability between conditions.

For the first testing, the modulated condition, the coherence analysis was performed separately between each intrinsic muscle (thenar and FDI) and every channel of the extrinsic muscles. Furthermore, each coupling was analysed per thumb opposition: i) to secundus digitus manus; ii) to digitus medius; iii) to digitus annularis; and iv) to digitus minimus manus.

A relation between the previously calculated RMS values of the sEMG and the area under the curve from the coherence analysis was used to further our understanding with regards to the amplitude of the sEMG feature distribution (different thumb oppositions) against the coherence estimate values, for each grid placed on the forearm.

As for the second test, the steady condition, the same analysis (as the modulated counterpart) was performed. To create a condition that corresponded to a steady-state contraction, the subject was not attached to the test rig, therefore there was no LSR to be pressed. The contractions were steady with a minimum exertion of force. The exertions lasted 10 seconds with a 5 second relaxation to avoid fatigue. The order of movement was set to 1 (secundus digitus manus), 2 (digitus medius), 3 (digitus annularis), and 4 (digitus minimus manus); repeating the cycle 10 times. The rest of the digits were kept in a natural relaxed position, the movements performed are depicted in Figure 4.11.

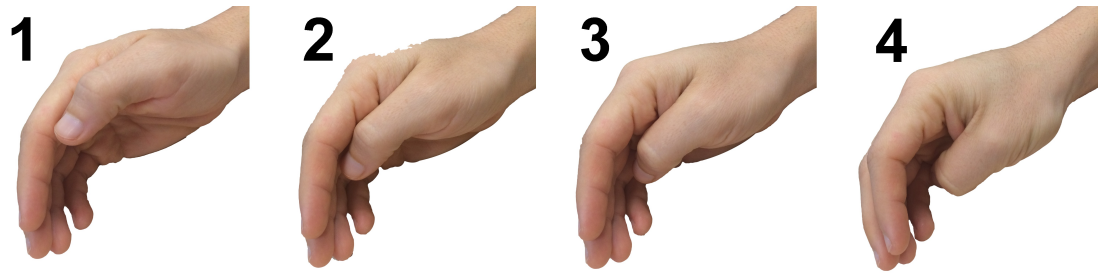

Figure 4.11: Movements Performed for the Second Testing - Steady Conditions - The four positions that the subject exerted are depict in this image. The positions are numbered from 1-4 and correspond to the opposition to index finger, middle finger, ring finger and pinky finger, respectively. Please note that Position 1 is very similar to that of hand rest.

4.3.6 Data Preprocessing for Machine Learning

In order to classify HD-sEMG patterns based on the thumb opposition tasks, the dimension of the time-domain signals had to be reduced and normalised in order to create classification vectors for feature extraction. A block diagram of the classification process is shown in Figure 4.12. The methods used for an unsupervised feature extraction were self-organising feature maps (SOFM) and principal component analysis (PCA). These methods were then validated through supervised methods such as the Levenberg-Marquardt and MATLAB's built-in neural network-pattern recognition toolbox.

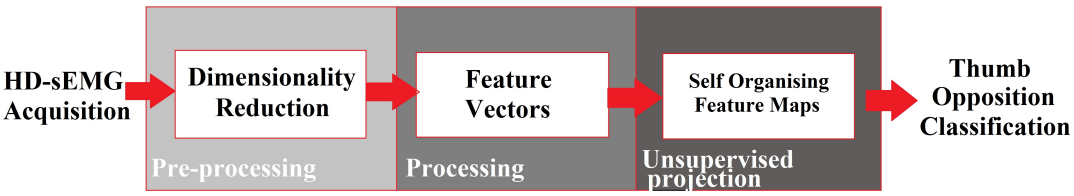

Figure 4.12: Block Diagram for HD-sEMG Feature Recognition - Block diagram representing the process for HD-sEMG thumb position classification.

4.3.6.1 Feature Vectors Extraction

Each of the feature vectors (FV) contained the IVC of a specific channel during a specific trial, e.g., $X_{position-channel}$ Y_{sample}. The new matrix arrangement can be found in Figure 4.13.

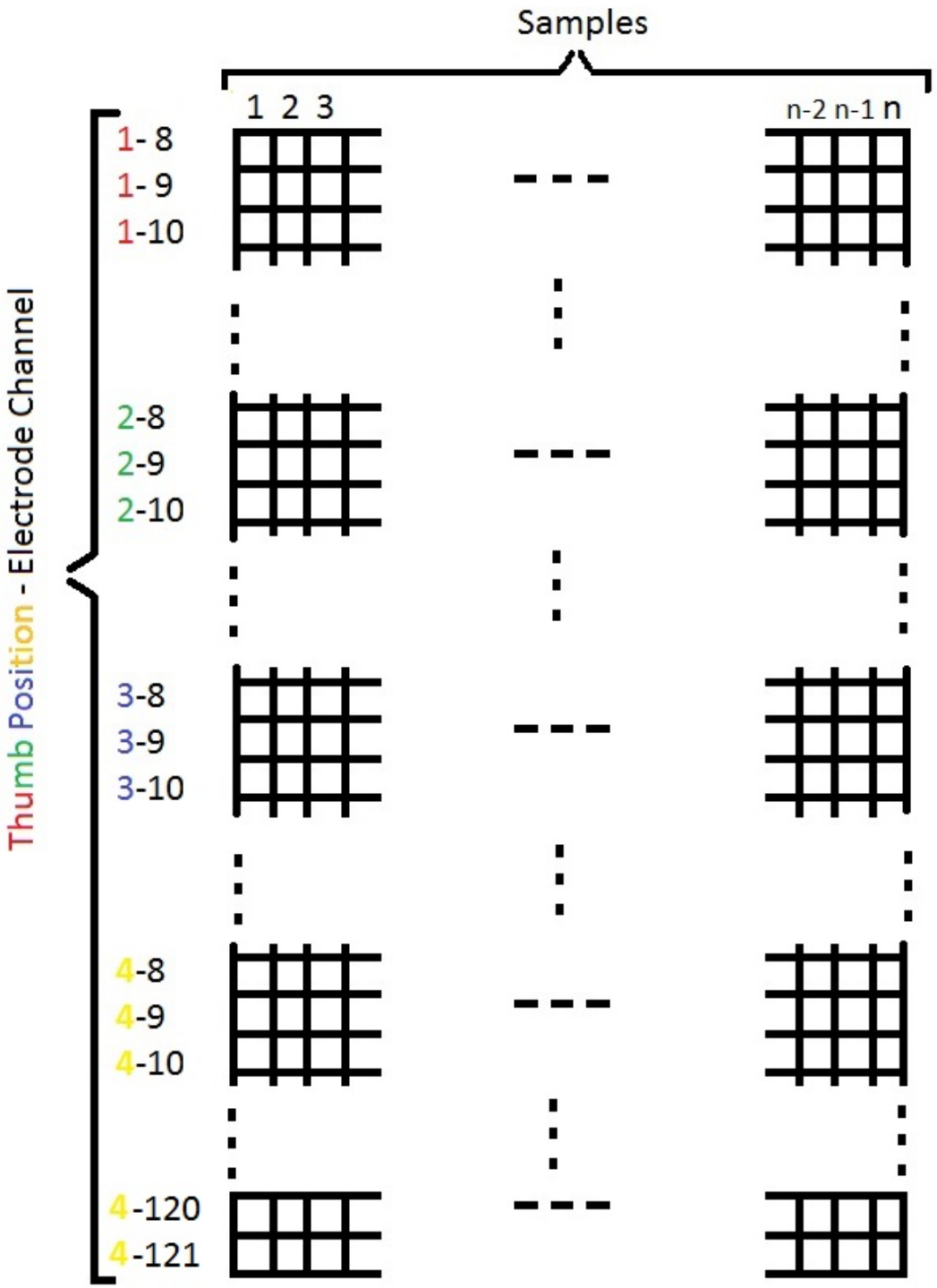

Figure 4.13: Example Of The 2D Matrix Array Obtained - Matrix-format data constructed from the feature vectors created, [$Position - ChannelxSamples$]. Position 1 refers to the opposition of the thumb against the index finger; position 2 refers to the opposition of the thumb against the middle finger; position 3 refers to the opposition of the thumb against the ring finger; and position 4 refers to the opposition of the thumb against the pinky finger.

4.3.6.2 Data Normalisation

A single-variable normalisation was used based on the algorithms developed by Kohonen 1982 (220). The variance was normalised to one, and its mean to zero through a linear transformation as shown on equation 4.1, guaranteeing that no electrode (channel) had a stronger influence over the others during the clustering analysis (also called machine learning training). For SOFMs, scaling is important because, as explained in section 1.1.5.2, the SOFMs algorithm is based on a Euclidean metric to measure the distances between vectors.

$$x' = (x - \bar{x})/\sigma_x \tag{4.1}$$

where,
$\bar{x}$ is the mean of the variable x
σ_x is its standard deviation

Once the data were suitable to be analysed an unsupervised machine learning approach was taken, as it will be explained next.

4.3.7 Unsupervised Machine Learning

4.3.7.1 Self-Organising Feature Maps

Self-organising feature maps (SOFM) were used as a clustering technique. The SOFM was applied using the SOM Toolbox for MATLAB 5 (free download in: www.cis.hut.fi) developed by The Helsinki University of Technology (59). The mathematical notation has been well defined by Vatanen (2012)(221) and was discussed in section 1.1.5.2. The data acquired from the subjects were split in two groups depending on the compartment of the forearm that was being inspected, i.e., anterior (flexor muscles) and posterior (extensor muscles) compartment . Therefore, the two sets of data considered per subject were analysed separately. Finally, these sets were further separated into two sets: 60% for training and 40% for testing.

The settings applied equally for all subjects were: i) hexagonal lattice; ii) sheet shape map; iii) random initialisation; iv) map size of [15,15]; v) batch algorithm training; and vi) a Gaussian neighbourhood.

The networks were trained, and a number of visualisation tools were used to assess the response. Performance measures such as sensitivity and specificity were obtained to test the 40% test data on the already trained data.

4.3.7.2 Principal Component Analysis

Principal component analysis (PCA) was used in this research to further reduce the dimensionality by merging similar features. Linear combinations are more likely to be used due to their easiness in computing and, as described by Duda (2000)(170), being "analytically tractable".

PCA is a linear transformation between the acquired data and a new space, also called PC space (PCs). The new PCs is based on the distribution of the original data. According to Jolliffe (2002)(57), a PCA transformation is considered to be the one that provides the largest variance for the first new variable and the largest variance for the next new variables independent from the previous new variables.

If n is the number of trials or observations and p is the number of variables or dimensions, then the raw data matrix is denoted by $\mathbf{X}_{n\times p}$ - Equation 4.2, where the rows correspond to trials or observations and the columns are variables. The transformation is formulated as stated in Equation :

$$Y_{n\times p} = X_{n\times p} C_{p\times p} \tag{4.2}$$

The transformed data $Y_{n\times p}$ should have maximum variance across observations, meanwhile the columns of the transformation matrix, $C_{p\times p}$ are orthogonally independent vectors in the new PCs representing the maximum variance directions from the original space. The transformation matrix used was calculated through single value decomposition (SVD), Jolliffe (2002)(57) and based on the values of n and p.

After applying the PCA on the HD-sEMG data, the resulting PCs were plotted to further understand the resultant clustering. Further methods were applied as a way assessing the performance of the classifiers by means of comparison. These methods will be explained in the following section.

4.3.7.3 Data Validation

It is essential to quantify the performance of the classifiers used. Common validation methods are known as the ones where results are compared given a known method. In this case, supervised algorithms were used, i.e. Levenberg-Marquardt and the Neural Network Pattern Recognition MATLAB built-in toolbox. The methodology used by these methods is as follows:

Levenberg-Marquardt Validation - The Levenberg-Marquardt (LM) provides a numerical solution to the problem of minimizing a function. Function fitting is the process of training a neural network on a set of inputs in order to produce an associated set of target outputs. Once the neural network has fit the data, it forms a generalisation of the input-output relationship and can be used to generate outputs for inputs it was not trained on.

$$(J^t J + \lambda I)\delta = J^t E \tag{4.3}$$

where,
J is the Jacobian matrix for the system;
λ is the Levenbergs damping factor;
δ is the weight update vector that we want to find, and
E is the error containing the output errors.

The δ tells by how much we should change our network weight to achieve a better solution.

The LM consists of solving equation 4.3 with a different λ values until the sum of squared error decreases. The steps followed to achieve are enlisted next:

1. Compute the Jacobian (by using finite differences or the chain rule)
2. Compute the error gradient
$$g = J^t E \tag{4.4}$$
3. Approximate the Hessian using the cross product Jacobian :
$$H = J^t J \tag{4.5}$$
4. Solve
$$(H + \lambda I)\delta = g \tag{4.6}$$
to find δ
5. Update the network weights w using δ
6. Recalculate the sum of squared errors using the updated weights.

7. If the sum of squared errors has not decreased, discard the new weights, increase λ using v and go to step 4.

8. Else decrease λ using v and stop.

For this method, the mean squared error value (MSE) was obtained between the outputs and the targets; lower values mean greater accuracy and zero means no error. Furthermore, the percent error was also obtained to indicate the fraction of samples which were misclassified.

Neural Network Pattern Recognition-MATLAB Built-in Toolbox - As mentioned previously, the Neural Network (NN) Pattern Recognition toolbox was used. First the data were split (30% training, 35% testing, and 35% validating); next, the dimension of the data map was obtained (according to its size); finally, the network was evaluated using mean squared error (MSE) and confusion matrices.

The NN Pattern Recognition toolbox is based on supervised learning with two-layer feed-forward training (as depicted on Figure 4.14). This training classified inputs according to target classes. The feed-forward networks consist of a series of two layers: the first one is related to the network's input, it consists of a hidden sigmoid of the weights and the bias; the second layer produces the network's output and is comprised of a layer of neurones. These layers were used to classify the vectors. Increasing the number of hidden neurones in the hidden layer is known to increase the power of the network, but it required more computational resources and it is more likely to produce over fitting.

The training function applied by this method is based on the update of the weight and the bias values according to the scaled conjugate gradient method explained by Moller (1993) (223). The performance function used was the MSE between the network outputs and the target outputs defined, as shown in equation 4.7:

$$F = MSE = \frac{1}{N}\sum_{i-1}^{N}(e_i)^2 = \frac{1}{N}\sum_{i-1}^{N}(t_i - a_i)^2 \tag{4.7}$$

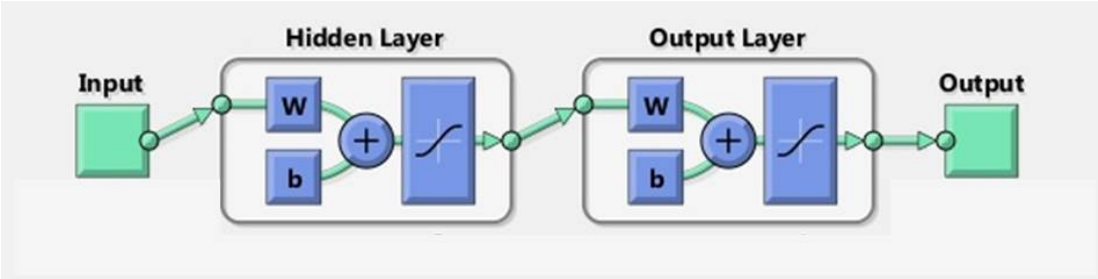

Figure 4.14: Neural Network For Pattern Recognition Diagram - Matlab Built-in Toolbox - A two-layers feed-forward network. The first layer is composed of a hidden sigmoid and the second layer is composed of output neurones. The network is trained with scaled conjugate gradient back-propagation. Source: Matlab NN Pattern Recognition Toolbox (222)

4.4 Chapter Conclusion

In this chapter, the methodology used in this research project was explained. Firstly, the hardware familiarisation and software development was explained in detail. Secondly, the sample population was explained. Thirdly and last, the machine learning algorithms applied to the acquired data was detailed and justified. In the next chapter, the results and output are presented.

5

Time and Time-Frequency Results

5.1 Summary

This chapter describes the performance of the volunteers participating in experiments designed to investigate sEMG patterns related to differentiation of thumb opposition to different fingers. The results presented initially based on time domain analysis and later on the basis of time and a joint frequency domain analysis.

5.2 Electromyographic Data Acquisition

As explained in section 4.2.4, HD-sEMG was acquired from 7 participants performing thumb opposition movements. Data were collected from 4 areas of interest: i) thenar muscles (single site); ii) FDI muscles (4 or 8-electrode grid); iii) anterior musculature of the forearm (64-electrode grid); and iv) posterior musculature of the forearm (64-electrode grid). In Figure 5.1, the electrode grids with the aforementioned configuration are shown (in shaded blue) as they were placed for each volunteer.

Figure 5.1: Electrodes Array Placement for Each Subject - Electrode matrix arrays were placed onto the hand of all subjects over the thenar and the first dorsal interosseous (FDI) muscles, and over the anterior and posterior muscle compartments of the forearm. As it is shown, four areas were of interest: 1) Flexors (anterior compartment of the forearm); 2) Extensors (posterior compartment of the forearm); 3) FDI muscle (intrinsic dorsal part of the hand); and 4) Thenar muscles (intrinsic palmar part of the hand). The electrode channels are also shown in a square next to each muscle group, indicating the arrangement taken for each test. Please note that for all but S6, the array placed onto the extensors muscle has 16 electrodes removed, this electrodes where used to acquire the intrinsic muscles.

In each experiment the participant opposed their thumb to each of the remaining 4 digits until a total of 120 repetitions had been completed (30 per position). As the subjects made each grip, the force applied between the thumb and the fingers was measured, and a target force level of 30% was set. Each contraction was timed to last 5 seconds. An example of the acquired sEMG with its corresponding force profile is shown in Figure 5.2, during a typical test for a random volunteer. A varying resting period (5-7 seconds) was introduced between each action. The amplifier sampling rate was set to 2048 samples per second, which produced a data matrix of size 121 channels x 689,000 samples per subject. The total file size (per volunteer) was between 2 and 3Gb.

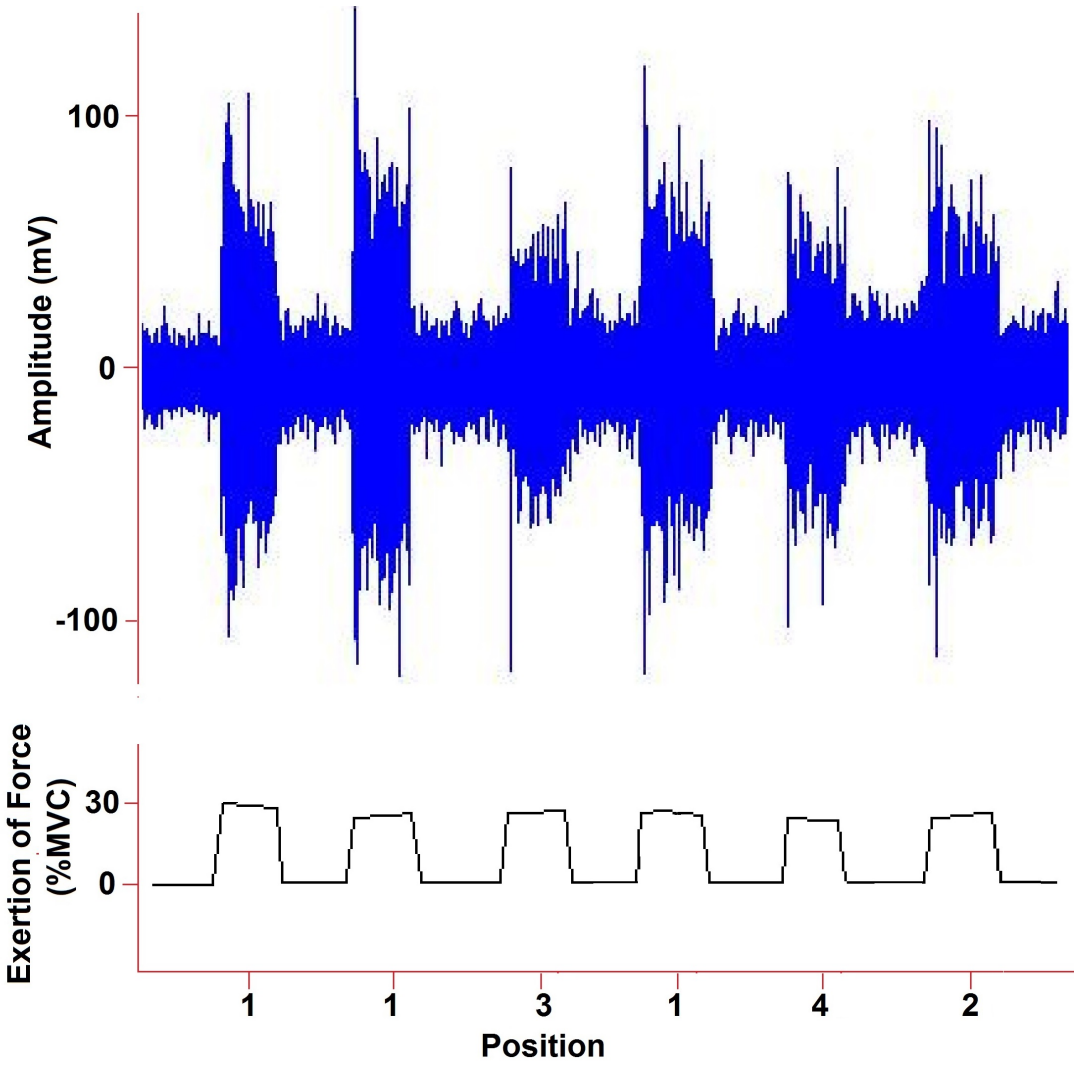

Figure 5.2: Example of EMG and Force Exerted During a Test - Example of the sEMG acquisition of a random sEMG channel showing 6 repetitions of an isometric thumb opposition. This example represents a typical subject during a typical test randomly chosen. Top: sEMG signal in time depicting 6 periods of thumb opposition. Bottom: Force profile exerted during each action.

As high density sEMG recording is a relatively new method, care was taken to assess the quality of the data and exclude channels contaminated by noise. Evidence of interference and noise were frequently encountered, and channels with noisy data were systematically discarded as described in Section 4.2.4. In Figure 5.3, typical examples of artefact contaminated sEMG signals in time and frequency are depicted. These interferences were present all throughout the testing, and therefore, these channels were discarded and not included for any further analysis.

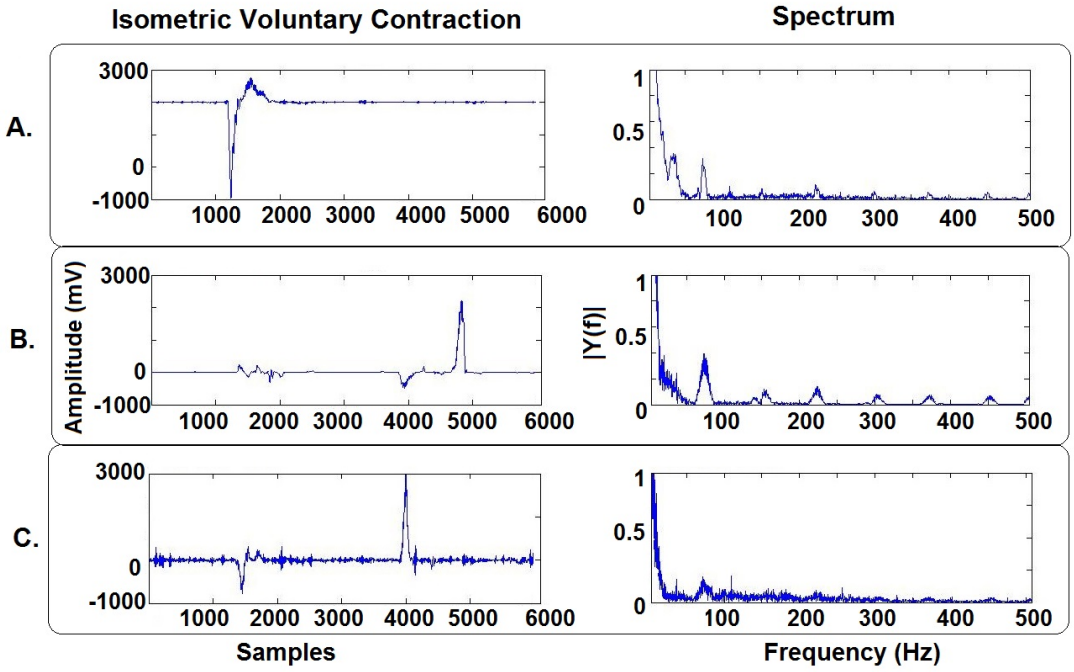

Figure 5.3: Examples of Contaminated sEMG Signals - Typical examples of artefact contaminated sEMG signal in time (left) and frequency content (right). In A. and C. the signals have DC offset; for these cases, high peaks of approximately 3000 mV amplitude are evident which can be associated with strong ambient noise, these is further inspected their corresponding spectrum, where a clear peak at 60Hz buries the muscle potential in the sEMG signal. For B., artefact contaminant noise is shown corresponding to a 60 Hz (highest amplitude peak in the spectrum) as well as its resonant frequencies. These interferences were present all throughout the testing, therefore no filtering was needed and hence, the channels were discarded and not considered for any further analysis.

The spectrum of the remaining channels was inspected, based on this, a notch filter was applied to reduce the 50Hz electromagnetic interference. A raw HD-sEMG channel randomly chosen is shown in Figure 5.4 - A; the raw sEMG spectrum shows a prominent

peak at 50Hz which can be filtered via the use of the noted filter (Figure 5.4-B) to allow a more effective data representation to be studied (Figure 5.4-C).

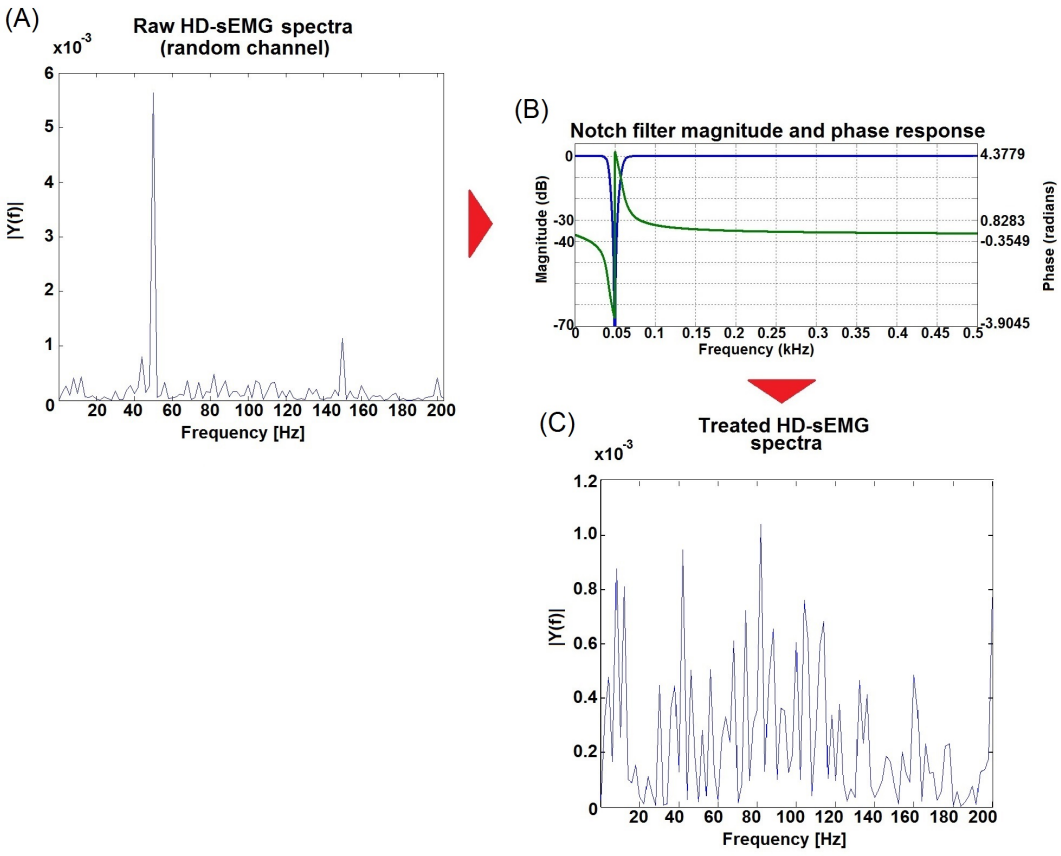

Figure 5.4: Resulting Filtered Signal Spectra After Notch Filtering - A random channel from the HD-sEMG was chosen for ease of demonstration. (A) Raw HD-sEMG randomly chosen with a clear peak at 50Hz; (B) Magnitude and phase response of the notch filter applied to the raw data; and (C) Data response after (B) was applied.

As mentioned previously, not all the acquired channels during the whole experiment were viable due to interference and artefact noise, the number of available channels per subject varied. This channel variation is summarised in Table 5.1 highlighting the number of available channels per subject by each of the 2 electrode grids placed on the forearm. This table shows that the channel yield ranged from 45% in Participant 6 to 100% in Participant 3 for the posterior grid, and from 48% in Participant 1 to 94% in Participant 5 for the anterior grid, as channels with appropriate sEMG signal.

Table 5.1: Available Channels for each Subject in the Compartments of the Forearm after Noise Inspection

Participant	Posterior Grid	Anterior Grid	Yield as % of maximum channels (Posterior - Anterior)
1	42	31	66 - 48
2	48	53	75 - 83
3	64	48	100 - 75
4	39	53	61 - 83
5	49	60	77 - 94
6	29	54	45 - 84
7	44	55	69 - 86

In Figure 5.5, the failure rate expressed as a % for each electrode grid is shown taking into account all the subjects. This information furthers our understanding regarding the variability of which area of the grids are most prone to electrode artefact problems when this type of flat film electrode grid is placed on a complex shape such as the forearm. Figure 5.5 shows that for the posterior grid the electrode sites numbered 52 to 55 have the greatest incidence of artefact when placed on the posterior aspect of the forearm. While for the anterior compartment grid no specific areas appear to be more problematic than others.

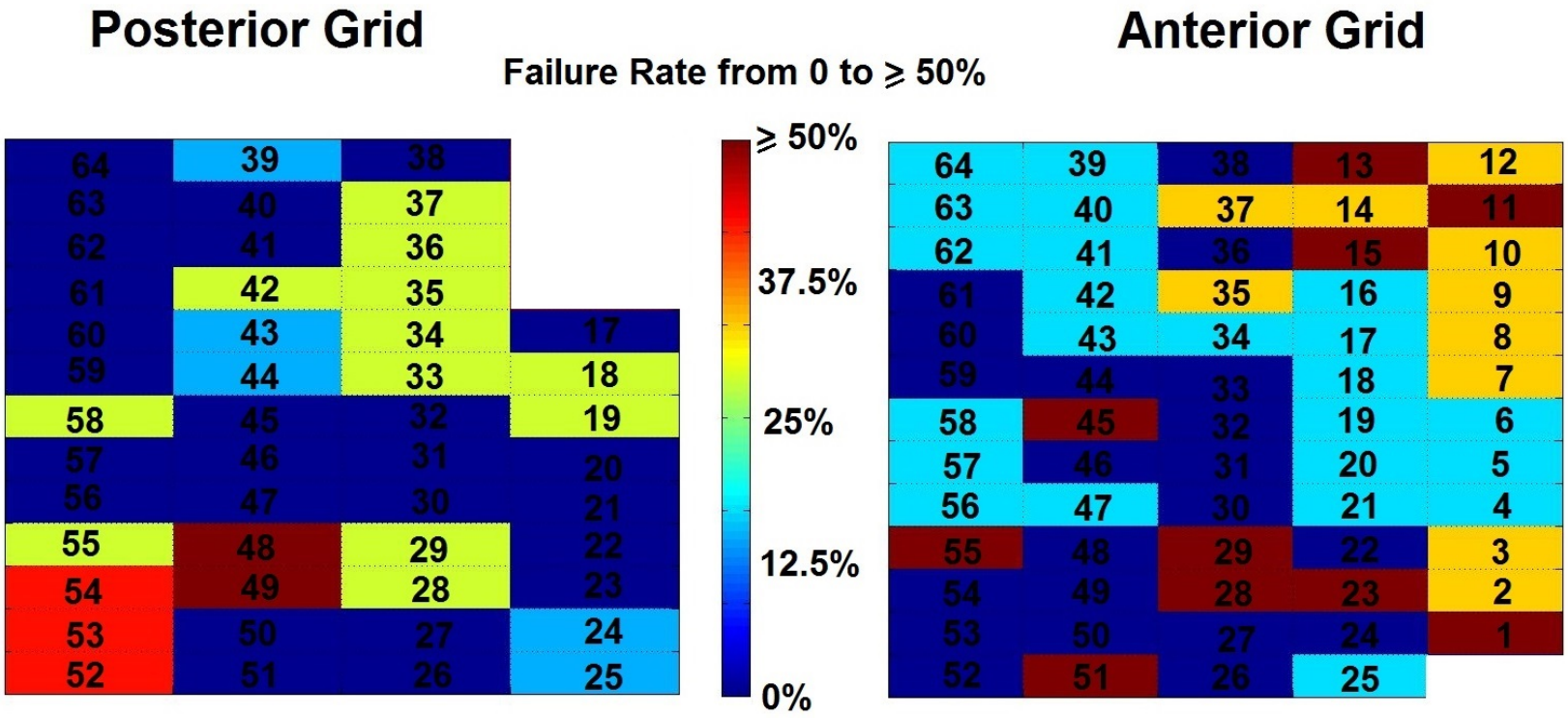

Figure 5.5: Electrode Failure Rate in Grid - The resulting electrode grids with the corresponding failure rate across subjects. The maximum failure percentage, shown in red, indicates that the electrode is not viable for further sEMG processing. These grids summarises the failing electrodes across all 7 subjects, allowing us to understand and identify areas of the forearm that would not be suitable to place electrodes allowing a simple dimensionality reduction.

Once the signal was treated, the data were inspected initially through the creation of sEMG activity propagation plots. These plots better our understanding about the interaction between the muscle groups underlying the compartments of the forearm while the thumb was opposed to the remaining 4 fingers. An example of these plots is shown in Figure 5.6, during a contraction period of 400ms, for channels 13-25 of an electrode grid placed on the forearm. This Figure shows that each electrode will pick up local EMG signal differently in relation to the underlying activity patterns.

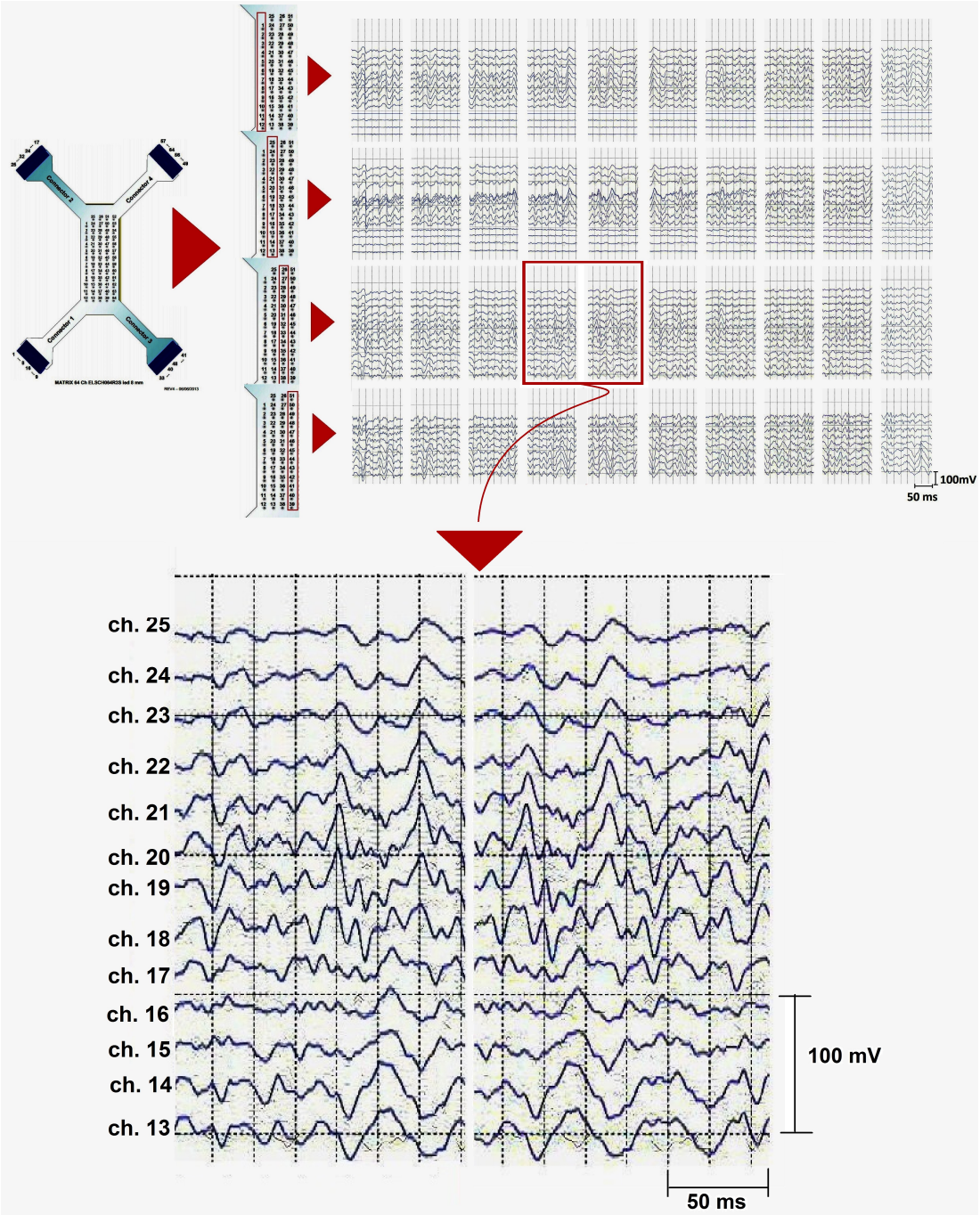

Figure 5.6: Example of sEMG Propagation from a 64-electrode Matrix Array - Surface-EMG section demonstrating the muscle contraction propagation acquired using a 64-electrode matrix array positioned on the posterior compartment of the forearm. The contraction highlighted corresponds to a random isometric voluntary contraction. Each row represents a column of electrodes from matrix array as shown at the beginning of each group. Each segment has a 50 ms overlap, and each row represents a channel from the complete electrode grid.

5.3 Amplitude Signal Analysis

To examine the EMG patterns received from signals deemed free from artefact or associated with poor recording, the RMS of each non-discarded sEMG channel was measure for each IVC. The RMS values were estimated using a 300ms window with a 50ms overlap from each grid placed on the forearm. Figure 5.7 shows 11 windows from the complete IVC for each of the thumb opposition corresponding to the anterior grid. The values displayed represent a typical participant during a typical test. A similar shape is shared across positions with a varying amplitude for each of them. Common to all, is the higher amplitude proximal to the fingers of the hand and a central activation pattern distal to the hand and towards the elbow. Greater amplitude is shown by position 4. Similarly, RMS windows for the posterior grid shown in Figure 5.8, share the same propagation shape across positions, but clear amplitude differences (position 1 is deemed to be the highest and position 4 the lowest amplitude). Localised augmented exertion areas can be seen in two regions: i) left of the grid proximal to the hand, and ii) right of the grid distal to the hand. From these activation zones we can infer that the musculature involved during thumb opposition are mainly underlying these particular areas.

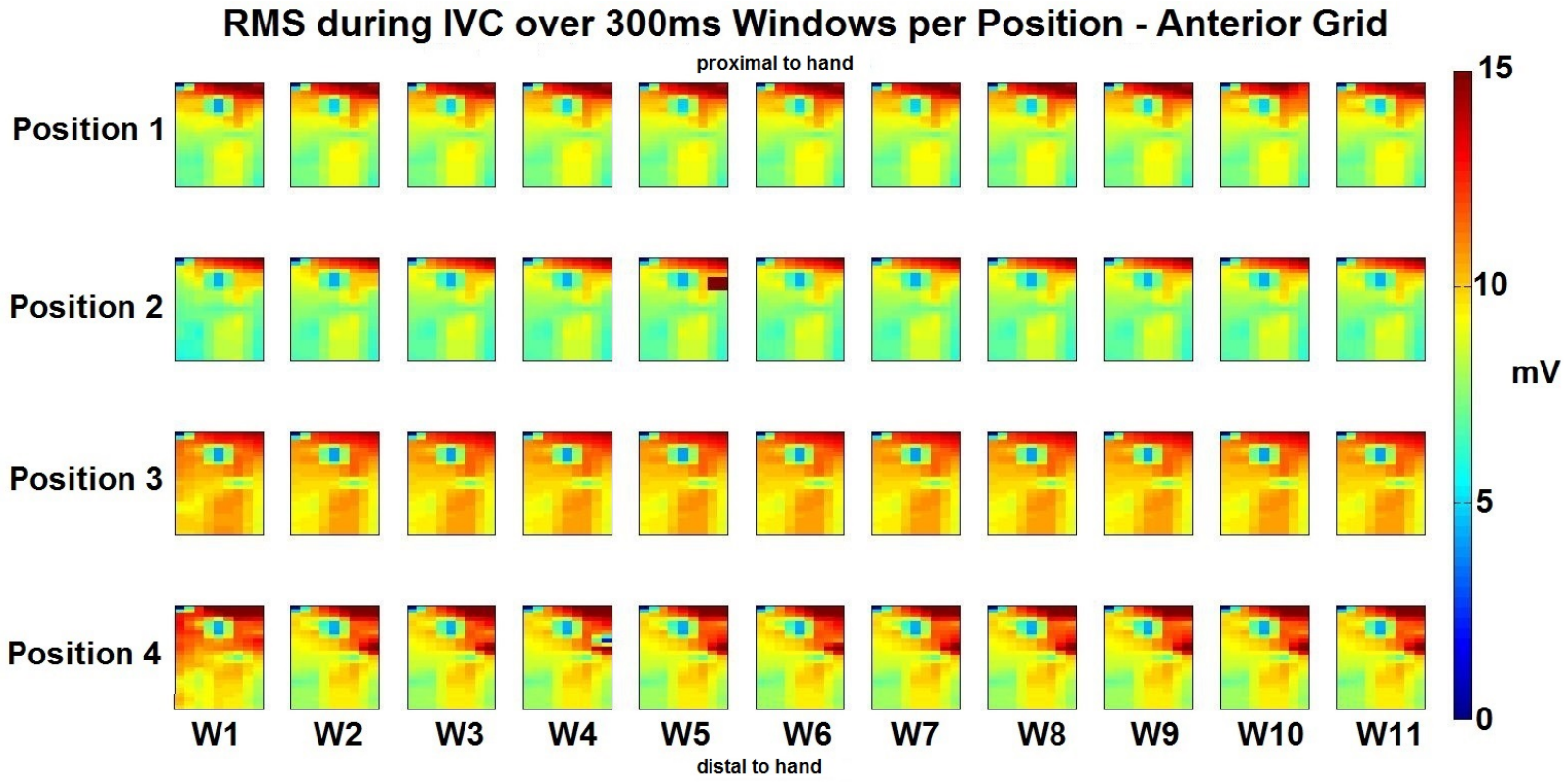

Figure 5.7: RMS Obtained During IVC Over 300ms Windows - Anterior Grid - RMS values obtained every 300ms with 50ms shift overlap between each window. The values represent a typical test for a typical subject and are separated by position of the thumb: Position 1, 2 3 and 4. Even though these four positions share a similar shape in the shading, their amplitude levels vary and therefore, are appreciated in different colours. Localised augmented exertion is localised proximal to top and centre of each grid, which is proximal to the subject's wrist. For position 4, the shading is extended over what it would suggest to be different muscles of the forearm, implying that there are more muscles involved during this action and therefore, greater effort is applied when the thumb reaches for a little finger opposition.

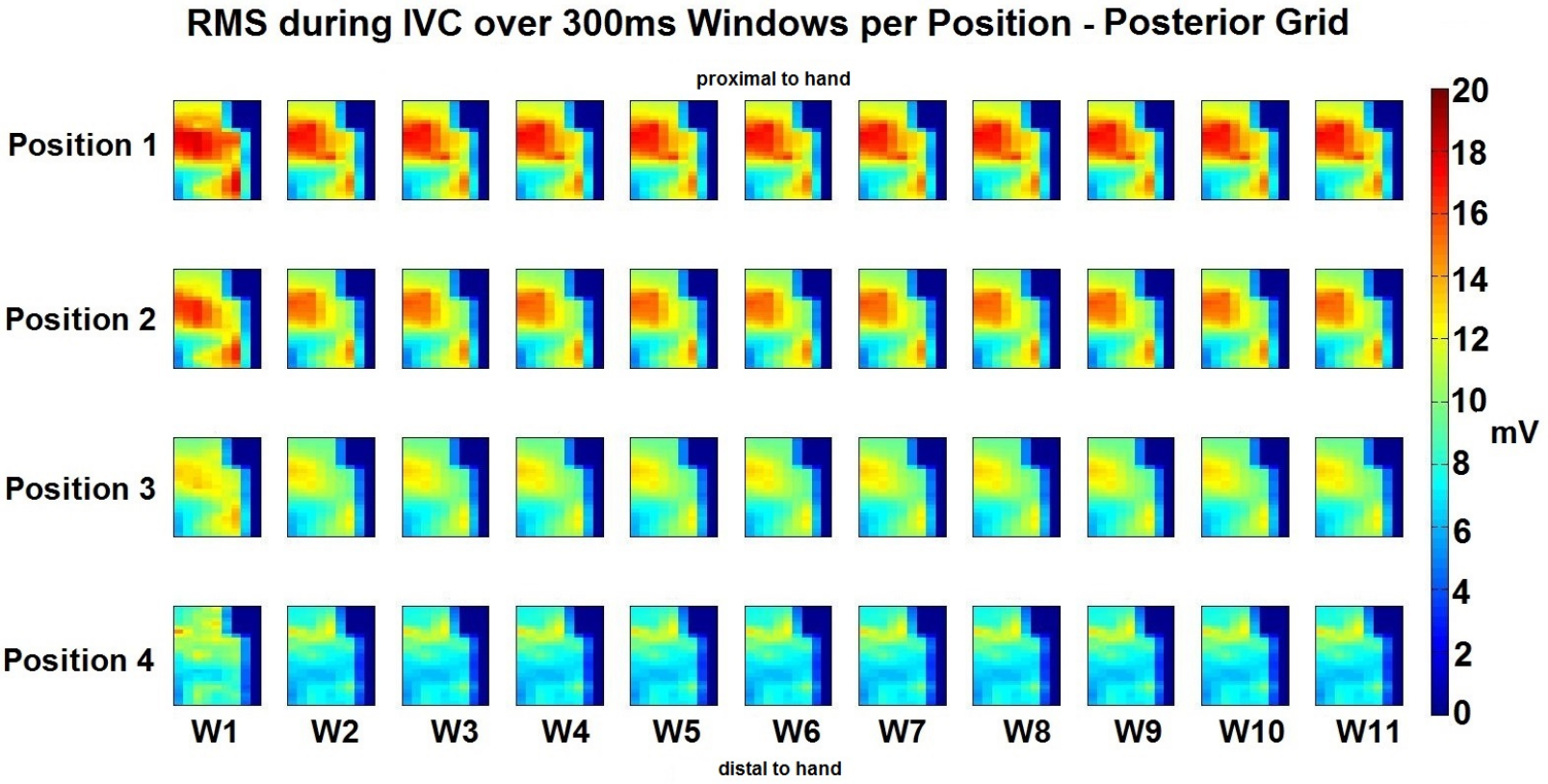

Figure 5.8: RMS Obtained During IVC Over 300ms Windows - Posterior Grid - RMS values obtained every 300ms with 50ms shift overlap between window. The values represent a typical test for a typical subject and are separated by position of the thumb. The four positions share similarity in the shape of the shading, nevertheless the amplitude levels for each one vary implying different force exerted for the different actions of the thumb. Localised augmented exertion is localised in two regions: left upper region (towards the fingers) and bottom right region (towards the elbow).

From the illustrated Figures 5.7 and 5.8, it can be seen that different spatial patterns and amplitudes of EMG are obtained when the RMS values are plotted over the 300ms windows covering the duration of the contraction. To accentuate the differences seen in these examples, the 11 windows per grid of the forearm are averaged across each repeated movement to the four different thumb postures. These grand averages are shown in Figure 5.9, by position for each grid placed on the forearm. For the Anterior grid, a different amplitude exertion is appreciated towards the hand for each position. Similar amplitude levels are appreciated for position 1 and 4, as well as in between position 2 and 3. An electrode at the centre-top of these four images seems to have a clear decremental in amplitude, this may be due to no activity on that area but most likely, and given the smooth transitions across electrodes, it is due to an electrode miss-contract. Similarly to the anterior grid, the posterior grid has a clear amplitude difference appreciated across positions, from a higher amplitude in position 1, towards the lowest amplitude for position 4. Moreover, position 4 seems to have different exertion and muscle propagation than the rest of the positions, the amplitude is clearly less than the rest, but two sources of exertion are found at similar levels in both amplitude and location.

Figure 5.9: Averaged Windows for Feature Extraction per Position - The RMS values obtained during 11 windows of the IVC are averaged for each position of the thumb per grid placed on the forearm. From the anterior grid (top 4 images) a different amplitude exertion is appreciated towards the fingers, for the different thumb movements. Furthermore, a central exertion is appreciated which also varies depending on the position. An electrode at the center-top of these four images seems to have a clear decremental in amplitude, this may be due to no activity on that area but most likely, and given the smooth transitions across electrodes, it may be due to an electrode miss-contract. Similar analysis can be done to the posterior grid (bottom 4 images). Clear amplitude difference is appreciated across positions, going from high amplitude to low amplitude from position 1 to 4. Position 4 seems to have different exertion and muscles involved than the rest of the positions, the amplitude is lessen but there are two sources of exertion at similar levels in amplitude and location.

As illustrated in Figure 5.9, raw HD-sEMG showed slight differences in amplitude for the 4 different positions, i.e. position 1-secundus digitus manus; position 2-digitus medius; position 3-digitus annularis; and position 4-digiti minimi. To further highlight these differences, RMS values were calculated over the average for all 30 repetitions per position. An additional analysis was performed over the obtained RMS values to extract the feature distribution across the positions, for each channel by grid placed on the forearm. Each position was plotted against the remaining 3 as shown in Figure 5.10. Each position of the thumb has been categorised into coloured clusters to facilitate the interpretation of this feature variation. For the anterior grid, the difference between features becomes tight for amplitudes ≥ 10. On the other side, the posterior grid has a clearer feature separation all throughout, but position 4 seems to have little feature variation, similar to the amplitude response found in Figure 5.9. The RMS analysis for feature distribution for all subjects, can be found in Appendix 8.6.

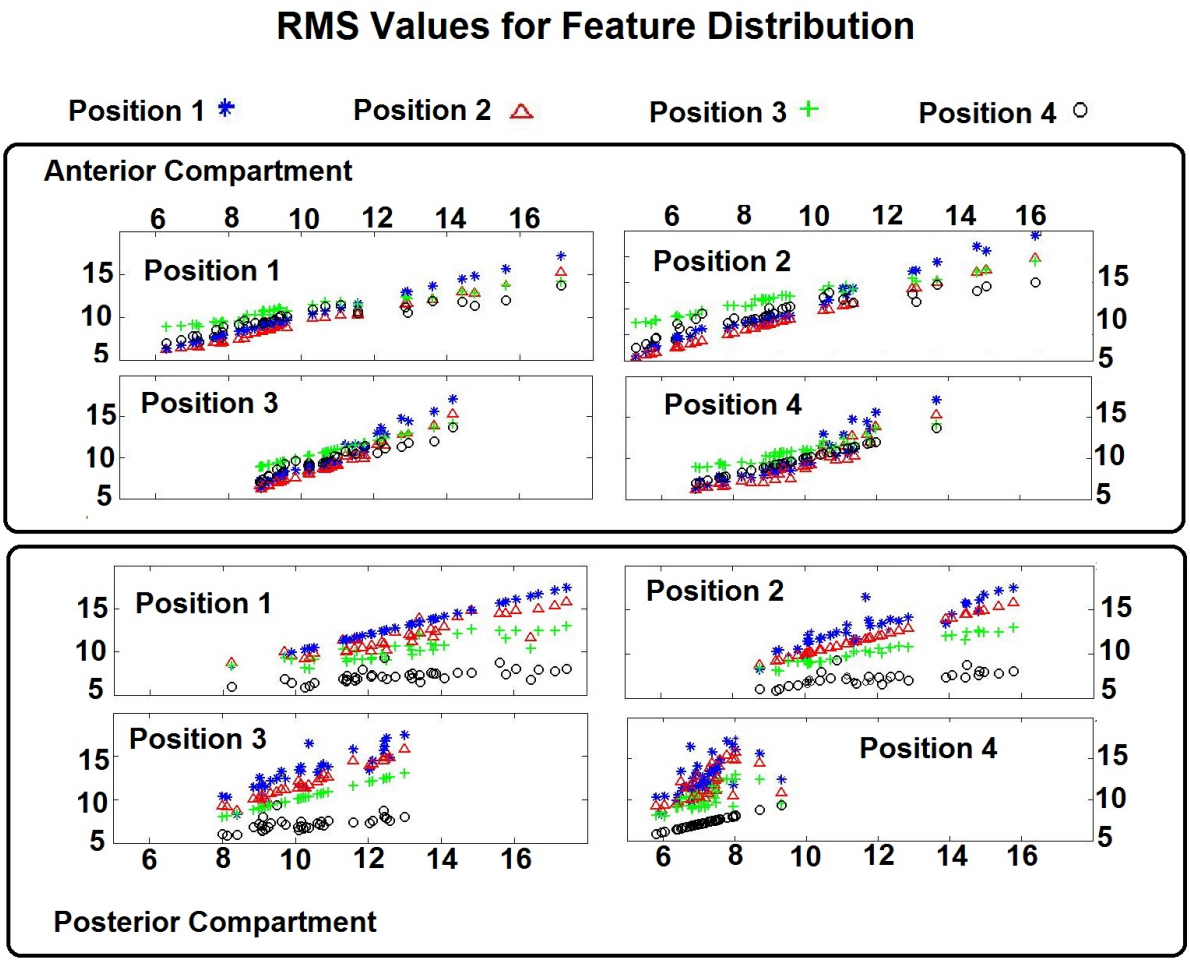

Figure 5.10: RMS Values for Feature Distribution in the Compartments of the Forearm - RMS values for the four different positions of the thumb. Position 1- thumb opposition with the index finger, position 2- thumb opposition with the middle finger, position, 3- thumb opposition with the ring finger, and position 4- thumb opposition with the pinky finger. The different positions are shown in 2D plots. These plots show the clustering when plotted against each other, making the variability amongst positions more evident. For the anterior grid, the difference between features becomes tight for amplitudes ≥ 10. On the other side, the posterior grid has a clearer feature separation all throughout, but position 4 seems to have little feature variation, similar to the amplitude response found in Figure 5.9. The RMS analysis for feature distribution for all subjects, can be found in Appendix 8.6

The RMS exertion graphs were similar all throughout the subjects. In the next section, a statistical approach was undertaken to better our understanding regarding the muscle propagation whilst different thumb oppositions.

5.3.1 Statistical Analysis Between the Different Thumb Oppositions

The one-way ANOVA tested the equality in the distribution of the four thumb positions. Firstly, the ANOVA was applied throughout the IVC split into the same windows as before (300ms with 50ms overlap). Secondly, ANOVA was applied over the averaged RMS exertions (grand averages) to further understand the differences across positions of the thumb.

Figure 5.11 summarises the analysis performed when the data were split into windows of 300ms time. This was separated by compartment and by thumb opposition. The sEMGs graphs during the IVC (per position) are shown in blue; furthermore, 4 windows were randomly chosen: 1st- whilst at rest (before contraction); 2nd- at the beginning of the exertion; 3rd- at the end of the exertion; and 4th- after the contraction. Each of these windows display the ANOVA analysis and the comparison between the obtained p-values (multiple comparison). These configuration allowed to further understand the variability between positions. The resulting p-values obtained with this analysis are shown in Appendix 8.8 separated by subject, grid and timed windows.

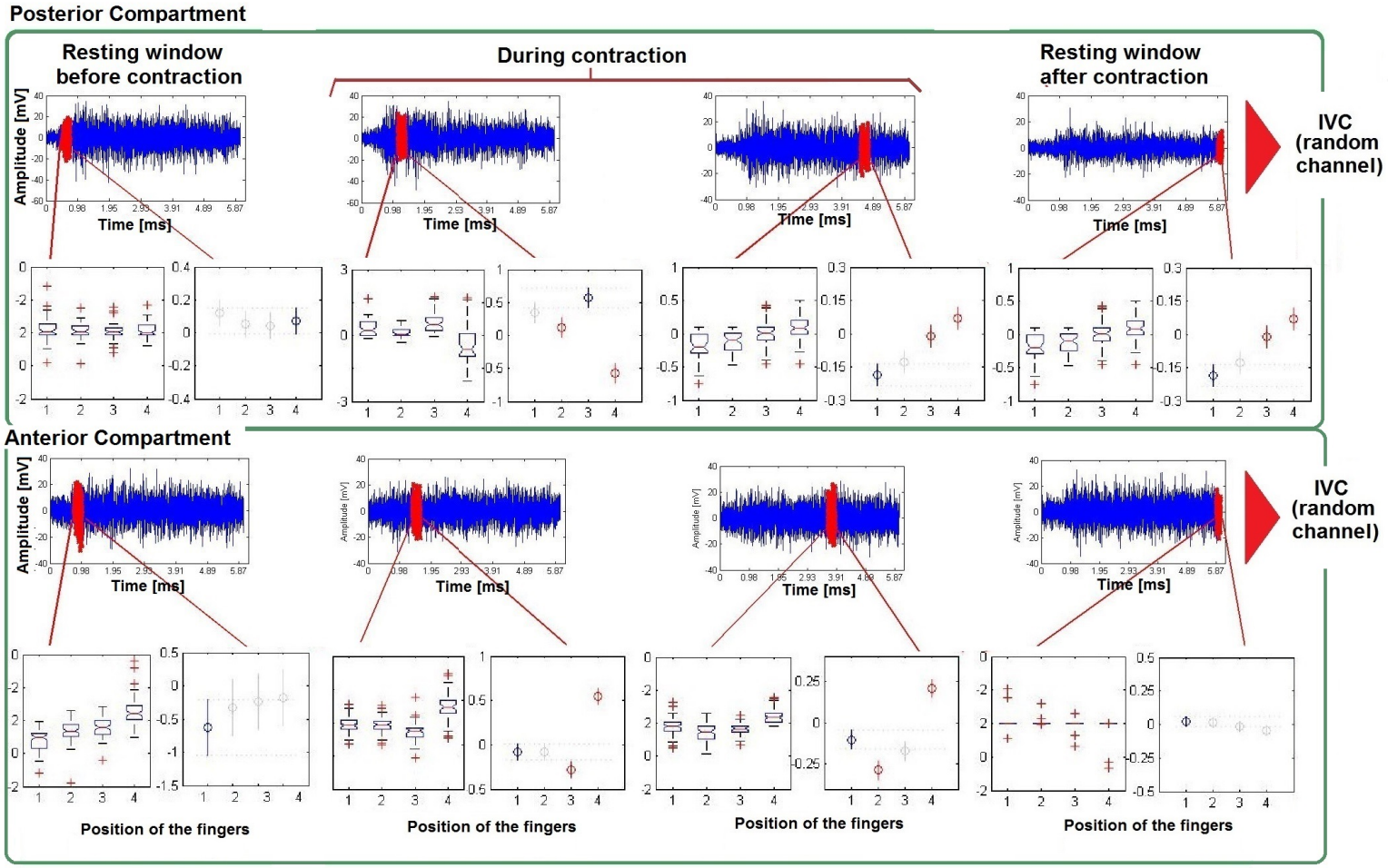

Figure 5.11: ANOVA Analysis for a Typical Subject for the IVC for a Channel chosen at Random - In this figure the resulting averaged sEMG signals during IVCs (blue graphs) are shown for each of the position of the thumb, and by compartment: Posterior (extensor muscles) - top, and Anterior (flexor muscles) - bottom. Onto these signals, red shading indicates the window used for the ANOVA analyses represented underneath each graph. As for the ANOVA Analyses, on the left side of each group, the boxplots represent the one-way ANOVA analysis for each of the positions of the thumb; on the right side a multi-comparison is performed and therefore, we are able to extract further details regarding the probability of each position to be different to each other, highlighting the statistically different position(s).

The p-values obtained from the windowed ANOVA analysis are shown in Table 5.2 as a % of the significance in the means by the two separate grids placed on the forearm. The significance between the means for the posterior grid ranges from 81% for Participant 1 to 98% for Participants 2, 3, 4, 5 and 7. Similarly, the range in the anterior grid found is 92% for Participant 1 to 98% for Participants 2 and 4. The distribution of the p-values across participants is found in Figure 5.12 and 5.13for the anterior and posterior grids, respectively. The significant p-values (≤ 0.05) are highlighted by the grey shaded area. A p-value expected to be outside the significance range, and common for both grids, is that of the 48th window (representative to resting period), and the means for all the positions are expected to be similar between each other.

Table 5.2: Significant P-Values per Subject Separated by Electrode Grids Across 48 Bins of Timed Windows (350ms each)

Participant	Yield as % of significant p-values	
	Posterior Grid	Anterior Grid
1	81	92
2	98	98
3	98	92
4	98	98
5	98	96
6	96	94
7	98	96

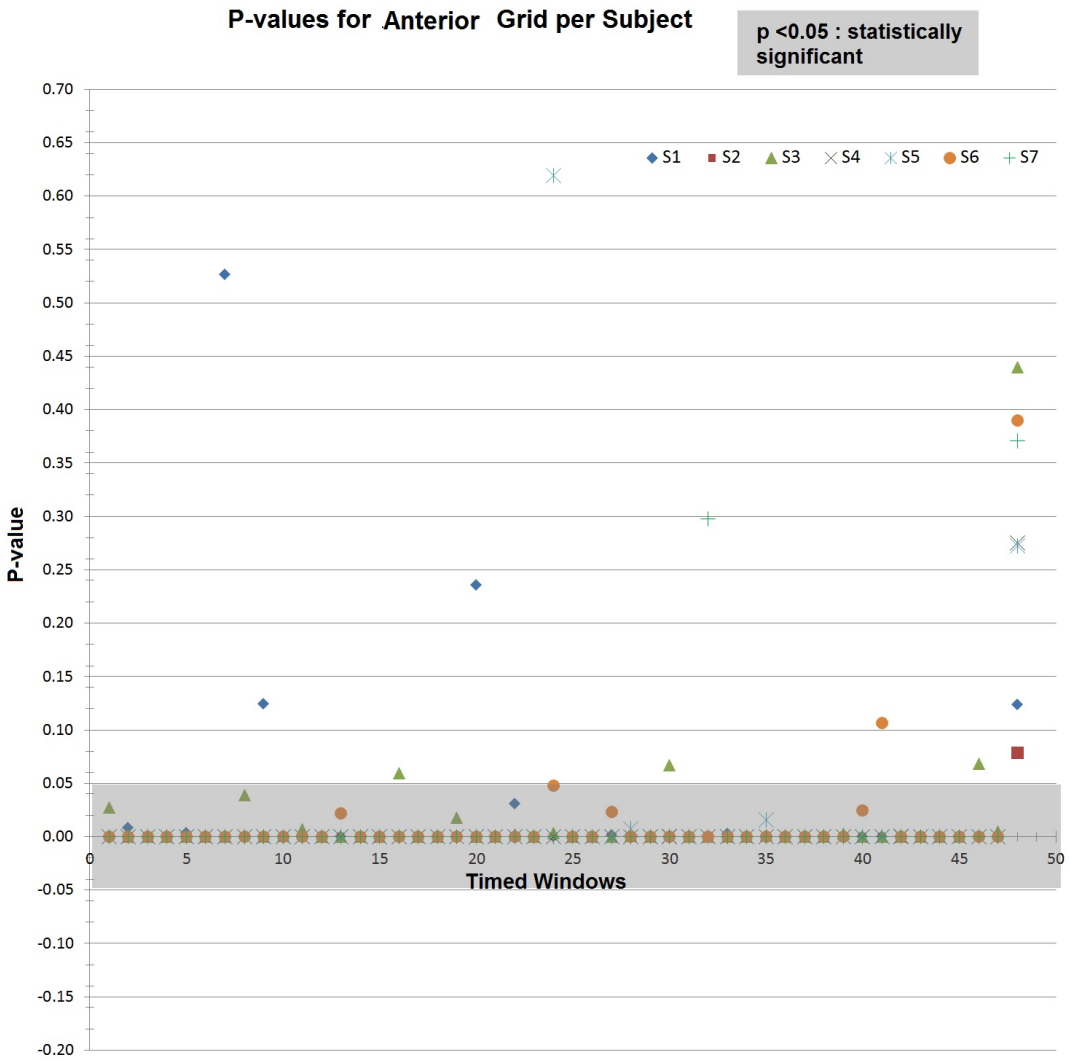

Figure 5.12: P-values for Anterior Grid per Subject - P-values obtained from the grid placed on the anterior compartment of the forearm separated by 48 windows of 300 ms each, as well as by subject. The last 3 windows, corresponding to the last 750ms of the IVC represent the transition of movement from contraction towards a relax position, therefore, the last 3 timed window values are expected not to be in within the range of significance. In shaded blue we find the statistically significant range were the p-values are ≤ 0.05. The values outside this range and between the 1st and the 45th window refers to the impossibility to differentiate between the means of the different positions of the thumb. The last 3 windows are associated to a section of the resting period.

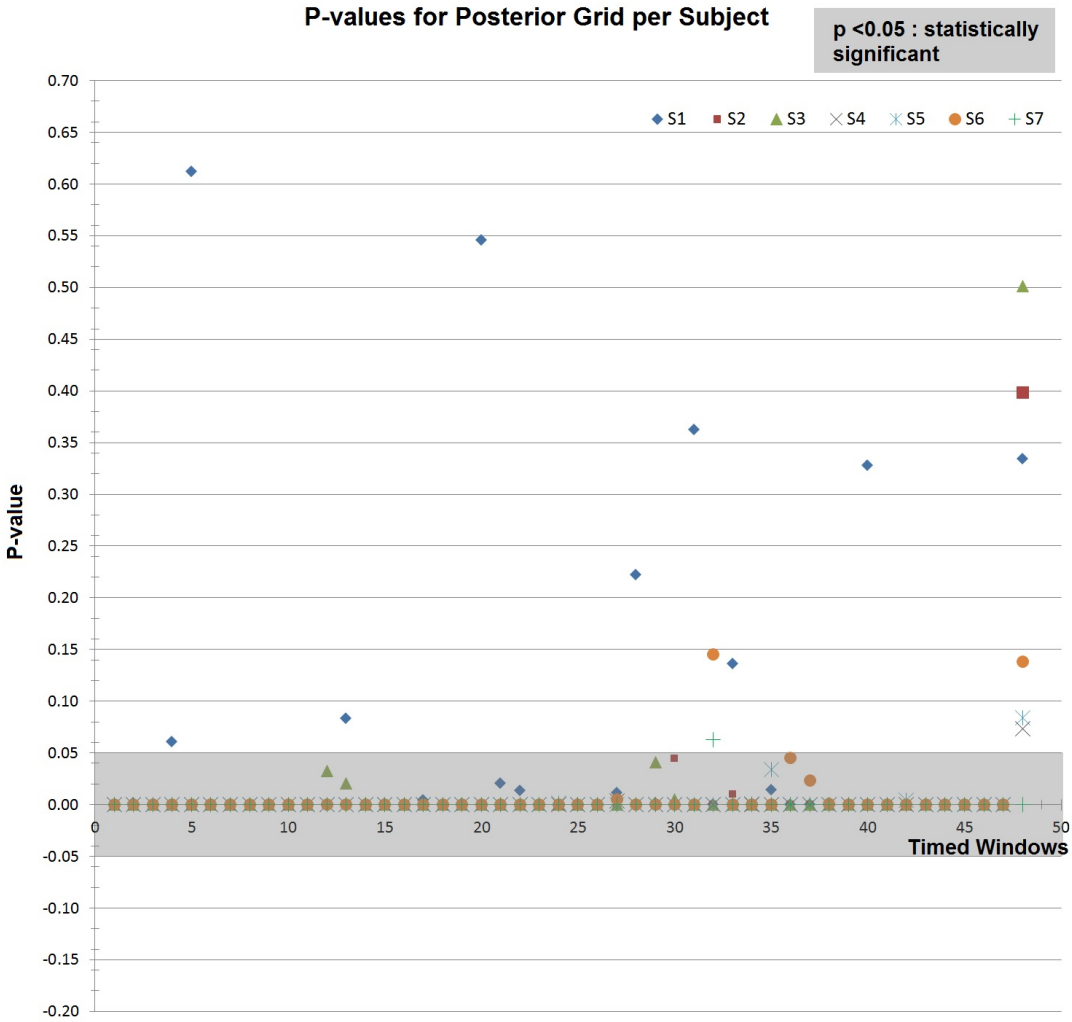

Figure 5.13: P-values for Posterior Grid per Subject - P-values obtained from the grid placed on the posterior compartment of the forearm separated by 48 windows of 300 ms each, as well as by subject. The last 3 windows, corresponding to the lst 750ms of the IVC represent the transition of movement from contraction towards a relax position, therefore, the last 3 timed window values are expected not to be in within the range of significance. In shaded blue we find the statistically significant range were the p-values are ≤ 0.05. The values outside this range and between the 1st and the 45th window refers to the impossibility to differentiate between the means of the different positions of the thumb.

The single case shown in the preceding Figure 5.9 illustrated a clear change in the sEMG spatial activation and amplitude when a subject moves from one thumb opposition position to another (P1 $\longrightarrow$ P4). To explore this further across all subjects, a second ANOVA analysis was performed over the averaged RMS exertions (grand averages) to further understand the differences across positions of the thumb. In Figure 5.14 the ANOVA analysis on the anterior grid is presented. From Figure 5.14-A, the ANOVA across the 4 positions is shown with a p-value of $7.26 \times 10^{-6} \leq 0.05$, this result is further explored in Figure 5.14-B where the multiple comparison is applied and can be seen that the positions whose means are different in between are: i) position 1 and 4; ii) position 2 and 3; and iii) position 2 and 4. and it can be seen that and in Figure 5.15 the corresponding analysis on the posterior grid.

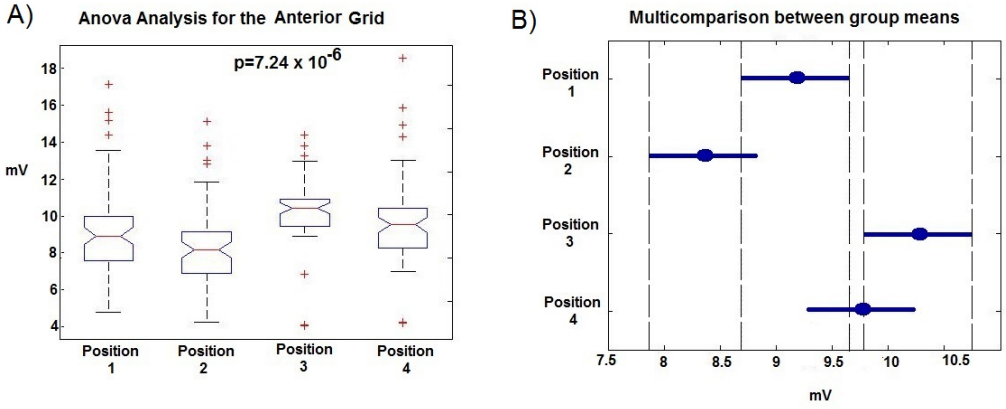

Figure 5.14: ANOVA Analysis Applied in Anterior Grid for the Averaged Positions - One-way ANOVA with 95% confidence interval (0.05 significance level) applied on the averaged RMS values obtained over 11 windows of time during each IVC for the anterior grid. On the left, the ANOVA analysis shows the different variability in within the amplitude of each position of the thumb with a p value of 7.26×10^{-6} suggesting that at least one mean is significantly different than the others. On the right side, a multiple comparison was performed to fully understand how the means are different amongst each other: the mean of position 1 is significantly different to that of position 3 and 4; position 2 is significantly different to position 4; position 3 is significantly different to position 1 and 4; and position 4 is significantly different to position 1, 2 and 3.

Similar results are found for the posterior grid shown in Figure 5.15. From Figure 5.15-A, the ANOVA across the 4 positions is shown with a p-value of $1.93 \times 10^{-14} \leq 0.05$, this result is further explored in Figure 5.15-B where the multiple comparison is applied

and the variation between means are clearly seen. The position whose means are different in between are: i) position 1 and 3; ii) position 1 and 4; iii) position 2 and 4; and iv) position 3 and 4.

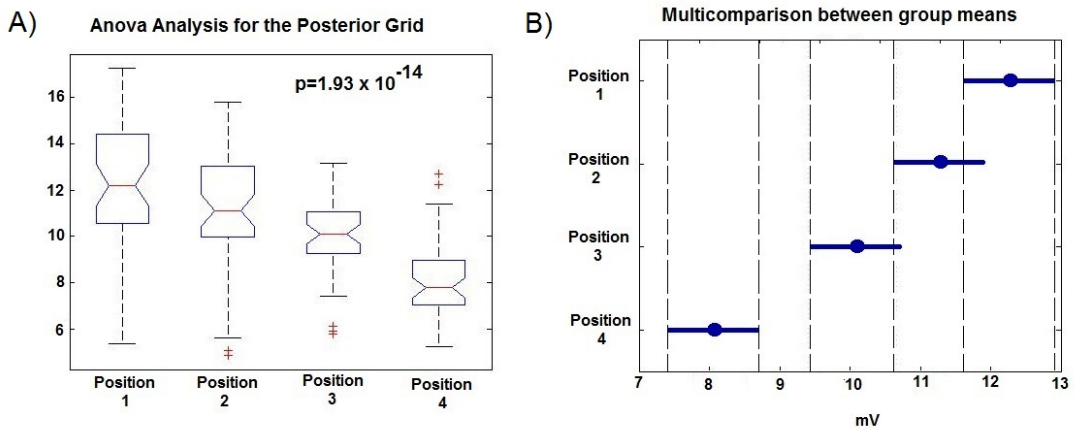

Figure 5.15: ANOVA Analysis Applied in Posterior Grid for the Averaged Positions - One-way ANOVA with 95% confidence interval (0.05 significance level) applied on the averaged RMS values obtained over 11 windows of time during each IVC for the posterior grid. On the left, the ANOVA analysis shows the different variability in within the amplitude of each position of the thumb with a p value of 1.93×10^{-14} suggesting that at least one mean is significantly different than the others. On the right side, a multiple comparison was performed to fully understand how the means are different amongst each other: the mean of position 1 is only significantly different to that of position 3; position 2 is significantly different to that of position 3 and 4; position 3 is significantly different to position 1; and position 4 is significantly different to position 1 and 2.

No correction (e.g. Bonferroni correction) was applied since the data was only being tested to one hypothesis, hence, no multiple comparison error was encountered.

The difference found for each of section of the forearm is due to the extent of activity detected by the electrode grids. This difference in the signal propagation is related to the anatomical differences between compartments.

5.4 Time-Frequency Analysis

In this section, the time-frequency analyses on the HD-sEMG data are shown. Coherence analysis (EMG-EMG) was applied which was separated into two different set of results: First one, modulated response (due to the exerted force modulation) and

the second one, a steady response (where no load was applied while thumb exertion and therefore, no feedback was provided to the participant).

5.4.1 EMG-EMG Coherence

This analysis aims to highlight the synergistic behaviour in between the intrinsic and extrinsic muscles of the hand. This information will lead to a better understanding with regards the possibility of a neurophysiological control for prosthetic hands specifically for thumb movement.

As described in section 4.3.5.1, the coherence analysis applied to the data collected using the test rig led to modulations (functional task) of the signal in the frequency content, therefore, a later acquisition from one additional (randomly chosen) subject was used to further investigate these frequencies when a steady condition (postural task) was met. This set of testing (modulated and steady conditions) has been previously described by Farmer(198).

5.4.1.1 Coherence Analysis - Functional Task

The coherence analysis was performed between the electrode grids placed on the intrinsic (thenar and FDI muscles) and the extrinsic (flexor and extensor muscle groups) hand muscles: i,ii) 64-electrode grid in the forearm overlying the flexor and extensor muscles; iii) 8-electrode grid overlying the FDI muscle; and iv) single site on the Thenar muscles. The available channels per subject from the grids have been previously shown on Table 5.1. These channels were cross-correlated in both time and frequency. Throughout this analysis, some signals showed a high level of signal cross-talk. The results that were found to have cross-talk were characterised by a narrow central peak in the cumulant frequency as well as a higher amplitude in the cross-intensity than the rest. A cross-talked coherence value was considered to be ≥ 0.4, with a steady and perfectly synchronised frequency spectra as shown in Figure 5.16.

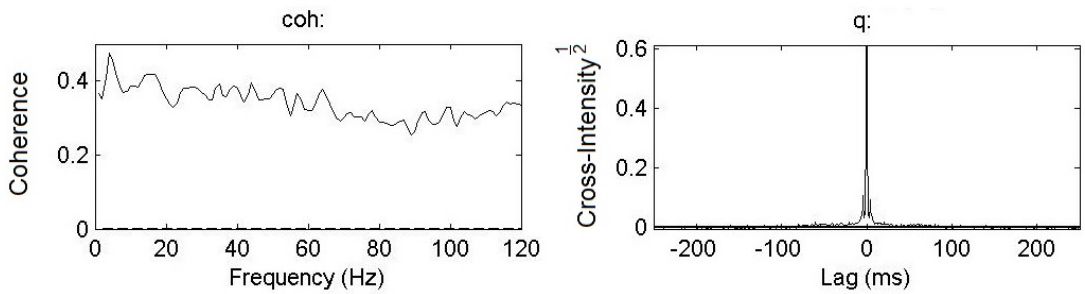

Figure 5.16: Example of a Cross-talked Signal Discarded For Coherence Analysis - Resulting coherence analysis between two electrode pairs from different the thenar muscles and the extensors of the hand. It is shown that there is clear crosstalk with steady coherence at 0.4 (left hand side) perfectly synchronised (graph on the right side). The signals analysed that shared these characteristics were discarded for this analysis.

As not all the acquired channels were viable for the coherence analysis due to cross-talk, the number of available channels per subject varied. This channel variation is summarised in Table 5.3 as well as the yield of available channels for coherence analysis.

Table 5.3: Channels without Cross-Talk Available for Coherence Analysis for each Subject, Separated by Compartments of the Forearm

Participant	Posterior Grid	Anterior Grid	Yield as % of maximum channels Posterior - Anterior
1	37	15	97 - 48
2	46	23	100 - 51
3	48	0	74 - 0
4	29	1	64 - 2
5	7	38	20 - 69
6	16	60	55 - 97
7	1	2	2 - 5

Although in the above table the yield of channels without the presence of cross-talk is highlighted, this does not necessarily mean that all the channels will have significant coherence. The rhythmic coupling between the muscles of the hand is different across subjects, and therefore, the coherence between them will be different. The channels that showed significant coherence values are summarised in Table 5.4

Table 5.4: Channels Showing Significant Coherence Between Muscle Groups per Subject - Modulated Condition

Participant	Posterior Grid		Anterior Grid	
	and FDI	and Thenar Muscles	and FDI	and Thenar Muscles
1	-	-	-	-
2	-	-	ch. 34 and FDI	ch. 34
3	-	-	-	-
4	-	-	-	-
5	-	-	-	
6	-	-	-	-
7	-	-	-	-

The results displayed in Section 5.4.1.2 show the coherence analysis in time and frequency between the 3 sites: i) Anterior grid located superior to the flexor muscles, and ii) The intrinsic muscles of the hand (FDI and thenar muscles). These results are further separated by position of the thumb. As depicted in Table 5.4 only 2 pair of sites were significant for coherence analysis during an IVC while modulating the response targeting a determined force exertion level.

5.4.1.2 Coupling Between Flexor Muscles and Intrinsic Hand Muscles

The coherence analysis results were found to be between the channel 34 and the complete electrode grid positioned on the FDI muscle , and the thenar muscles (Figure 5.17). From the anterior grid, the site underlying the coherent electrode corresponds to the flexor pollicis longus muscle, this muscle is in charge of thumb flexion and the only muscle from the extrinsic-anterior muscles of the hand, exclusively in charge of thumb movement.

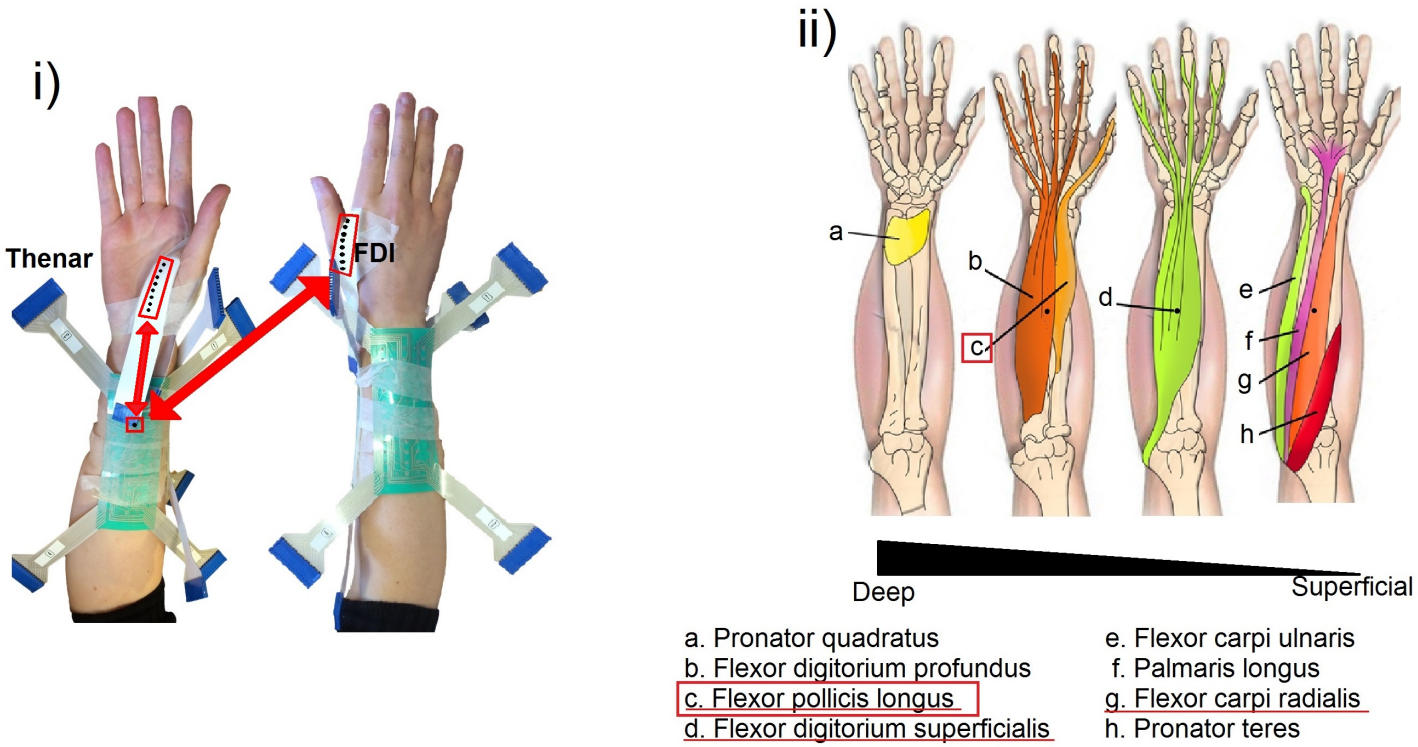

Figure 5.17: Sites of Coherence Found Between Anterior Grid and the Intrinsic (FDI & Thenar) Hand Muscles - Sites of the hand that were found to have coherence between the anterior grid, specifically channel 34 with two sites of the intrinsic hand muscles, the thenar and the FDI muscles. i) Electrode grid placed overlying the flexor, FDI and thenar muscles. The site where coherence was found is shown by the red rectangle surrounding the electrode sites. ii) The musculature underlying the electrode grid separated by muscle layers. From the site where coherence was found for the flexor muscles, it is appreciated that on the site where coherence was present 3 different muscles from different layers are underlying: flexor pollicis longus; flexor digitorium superficialis; and flexor carpi radialis. From these, the flexor pollicis longus (c.) is the only muscle amongst them that is in charge of a thumb movement, specifically that of flexion.

The complete coherence analysis between these sites separated by positions is shown next.

Position 1: Thumb opposed to secundus digitus manus - Figures 5.18 and 5.19 show the coherence estimate and cumulant analysis between rectified ch. 34 of the flexor muscles (located superior to the flexor pollicis longus) and the FDI muscle while the thumb was being opposed to the secundus digitus manus (position 1). The site represented by the FDI muscle is composed by an 8 electrode array. From Figure 5.18, it can be appreciated that the 8 electrodes follow a similar shape with a variable amplitude. The shape of the coherence estimate shows a tendency for low frequency coupling (1-17Hz) with peaks at 4, 8 and 15Hz. These rhythmic coupling components of the sEMG coherent estimate are not evident separable features, this becomes clear when we further inspect Figure 5.19 and note the absence of the appropriate delays ($\pm$250 ms, $\pm$125ms, and $\pm$66ms, respectively). The cumulant itself is dominated by a broad central peak at 0ms and tailing off out to $\pm$50ms. Even though the coherence peaks appear to scale depending on the level of the FDI muscle that is being analysed, none of these features are present in the cumulant, suggesting that the changes in coherence estimate peaks amplitude are not simply related to changes in the sEMG amplitude, but reflect differences in the rhythmic waves of the EMG patterns received from spatially distributed hand sEMG recordings.

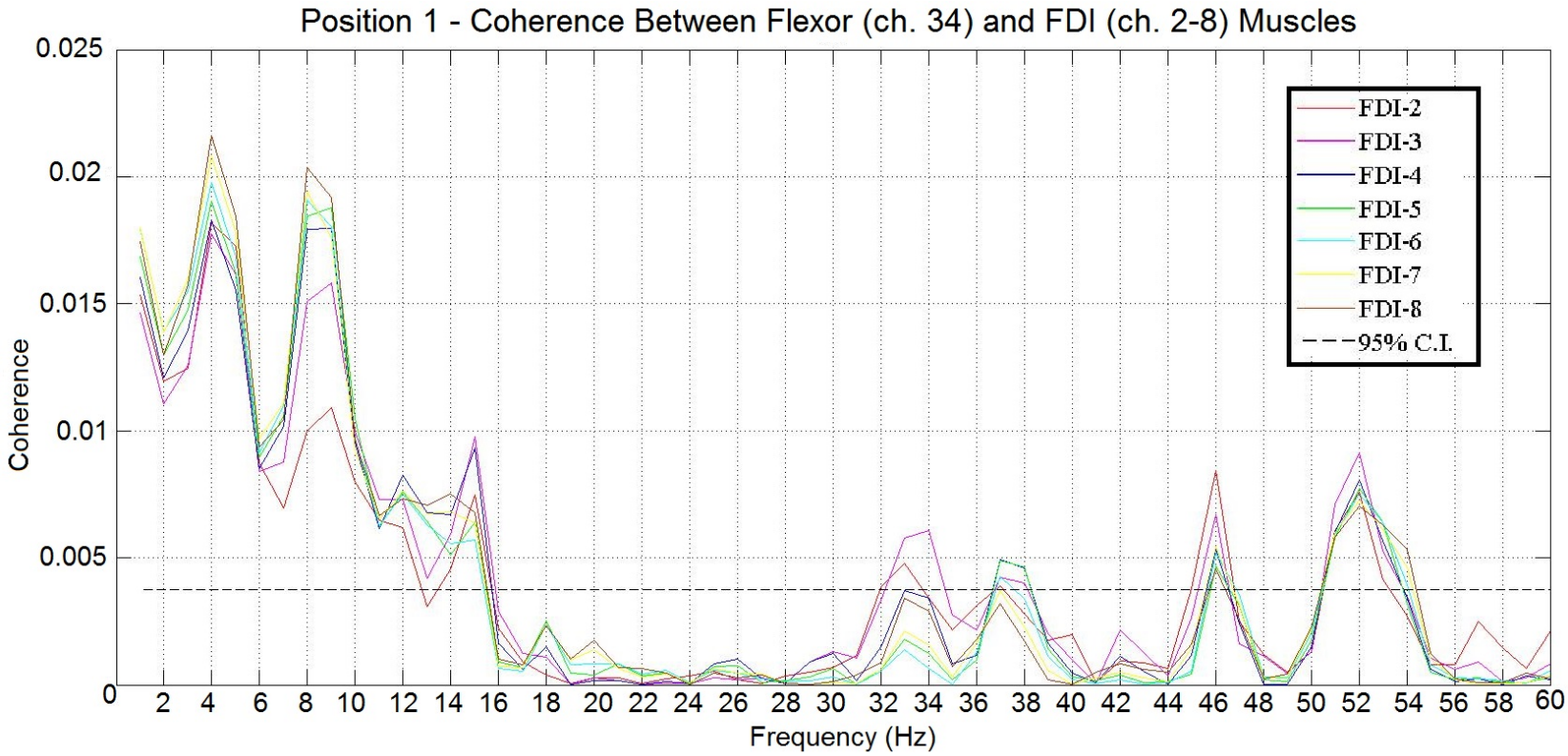

Figure 5.18: Coherence Estimate Analysis Between FDI and Flexor Ch. 34 - Position 1 - Coherence estimate analysis results for Position 1 between a site in the anterior grid (corresponding to the flexor pollicis longus muscle) and the FDI muscle. Common to the 8-electrode array grid on the FDI muscle is a low frequency range of (1-17)Hz. Similar shape but different coherence estimate in the peaks magnitude show a rhythmic coupling of the sEMG. Peaks at 4Hz with a magnitude of (0.0184 ± 0.0027), 8Hz with (0.0188 ± 0.0020) and finally a peak at 15Hz with (0.0074 ± 0.0015) magnitude. Smaller peaks can be appreciated above 30Hz which are not significant to this study. The information obtained from this Figure is complemented and better understood when it is used in conjunction with Figure 5.19.

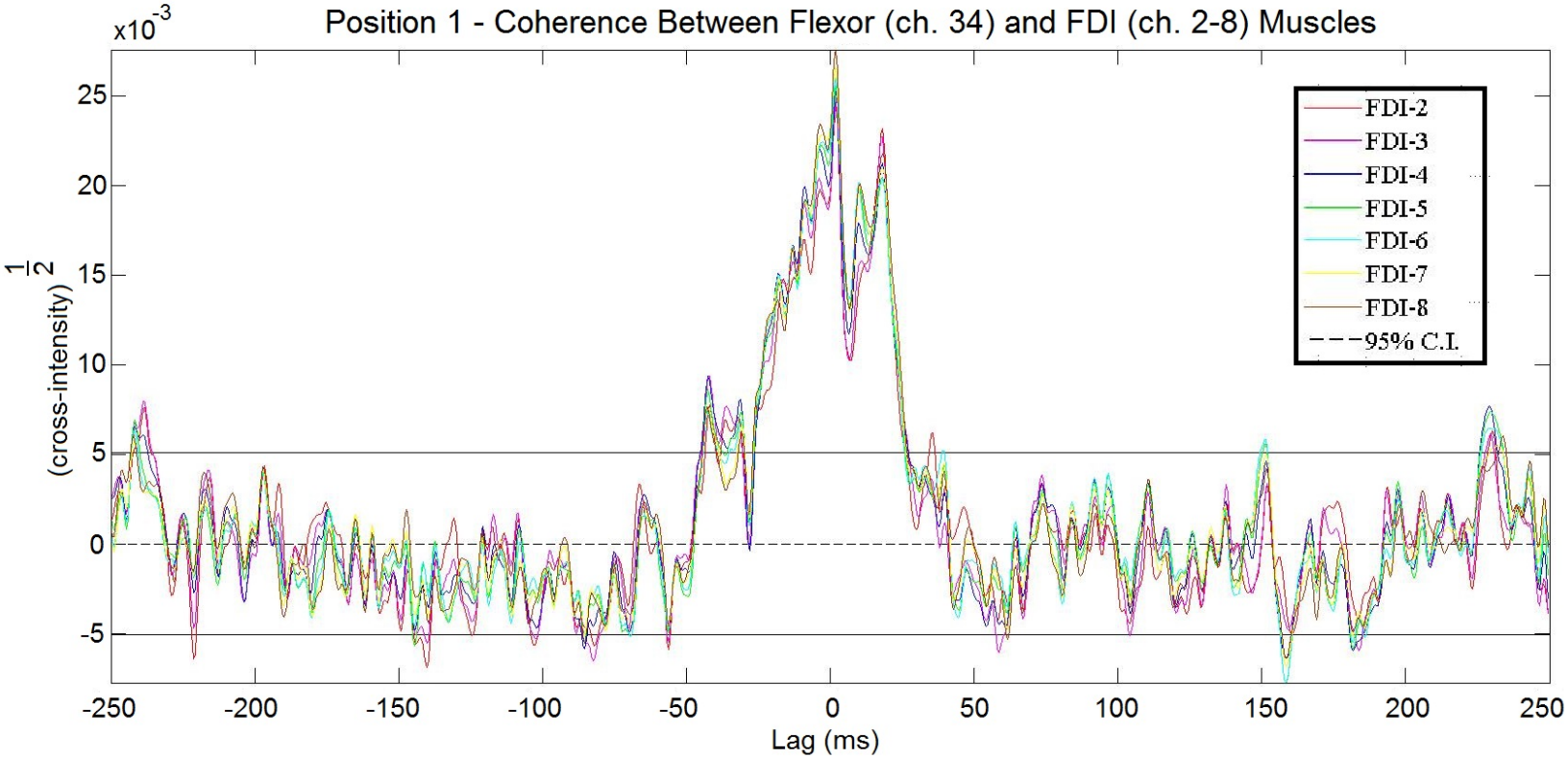

Figure 5.19: Cumulant Analysis from the Coherence Estimate Between FDI and Flexor Ch. 34 - Position 1 - The cumulant contains a central peak at 0ms of magnitude q(u)=0.0276 tailing off out to ±50ms. The peaks found at 4, 8 and 15Hz from the coherence estimate are not evident in the cumulant. This is displayed by the absence of delayed peaks at ±250ms, ±150ms and ±66ms. This absence suggests that the difference in coherence peak amplitude is not simply related to the changes in sEMG amplitudes but reflect differences in the rhythmic waves of the EMG patterns received from spatially distributed hand sEMG recordings.

Similarly, Figures 5.20 and 5.21 show the coherence estimate and cumulant analysis between rectified ch. 34 of the flexor muscles (located superior to the flexor pollicis longus) and the thenar muscles while the thumb was being opposed to the secundus digitus manus (position 1). From Figure 5.20, it can be appreciated that in general, this shape follows the same pattern as the ones compared between the FPl and the FDI muscles. The shape of the coherence estimate shows a tendency for low frequency coupling (1-11Hz) with peaks at 4 and 9Hz. These rhythmic coupling components of the sEMG coherent estimate are not evident separable features, this becomes clear when we further inspect Figure 5.21 and note the absence of the appropriate delays ($\pm$250 ms and $\pm$111ms, respectively). The cumulant itself is dominated by a broad central peak at 0ms and tailing off out to $\pm$50ms. None of features from the coherence estimate are present in the cumulant, suggesting that the changes in coherence estimate peaks amplitude are not simply related to changes in the sEMG amplitude, but reflect differences in the rhythmic waves of the sEMG patterns received from spatially distributed hand sEMG recordings.

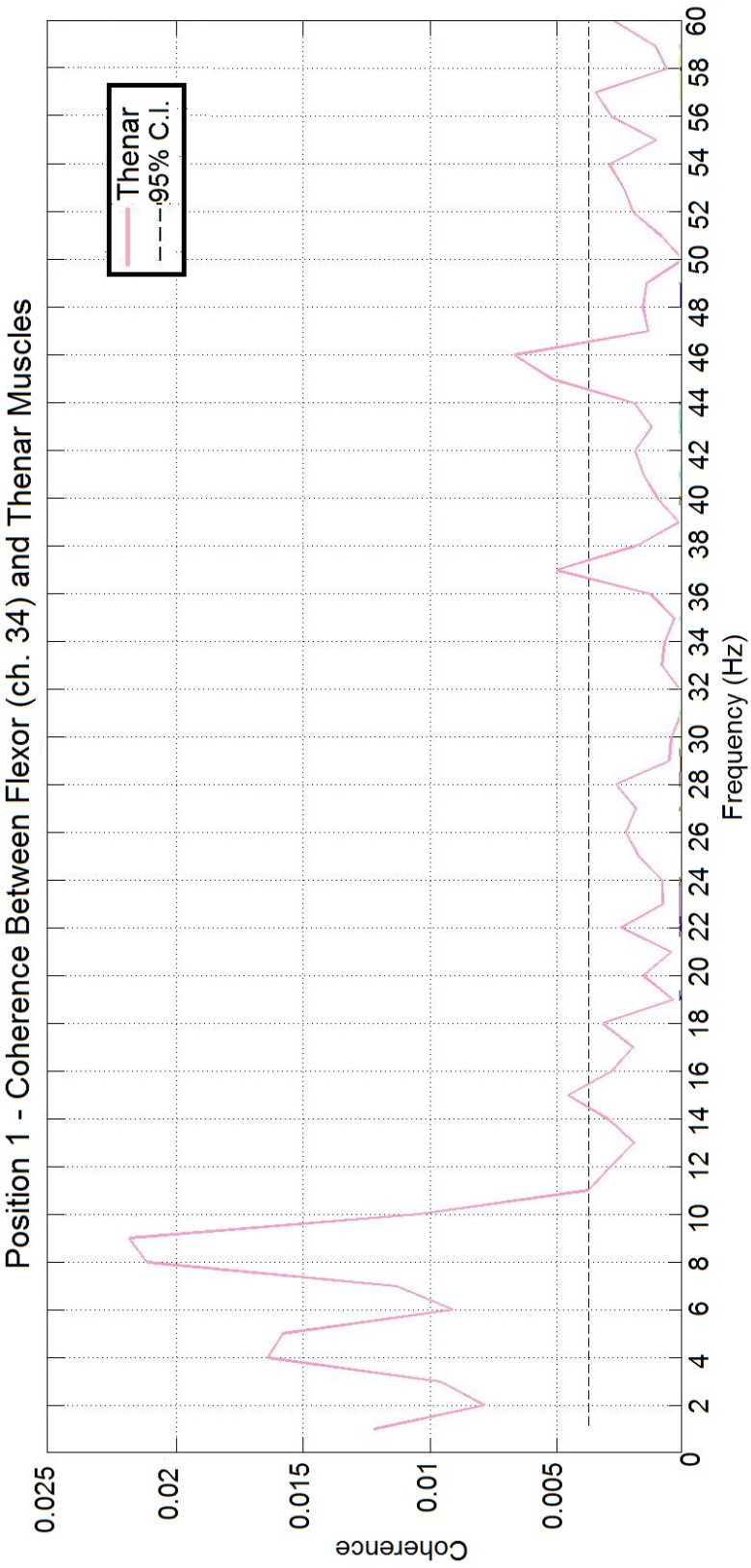

Figure 5.20: Coherence Estimate Analysis Between the Thenar and Flexor (Ch. 34) Muscles - Position 1 - Coherence estimate analysis results for Position 1 between a site in the anterior grid (corresponding to the flexor pollicis longus muscle) and a site on the thenar muscles. A significant low frequency of (1-11)Hz peaking at 4 and 9Hz. The peak at 4Hz has a magnitude of 0.018 and 0.022 for the latter frequency. Smaller peaks can be appreciated above 35Hz which are not significant for this study and therefore, will be excluded for further analysis. The information obtained from this Figure is complemented and better understood when is used in conjunction with Figure 5.21

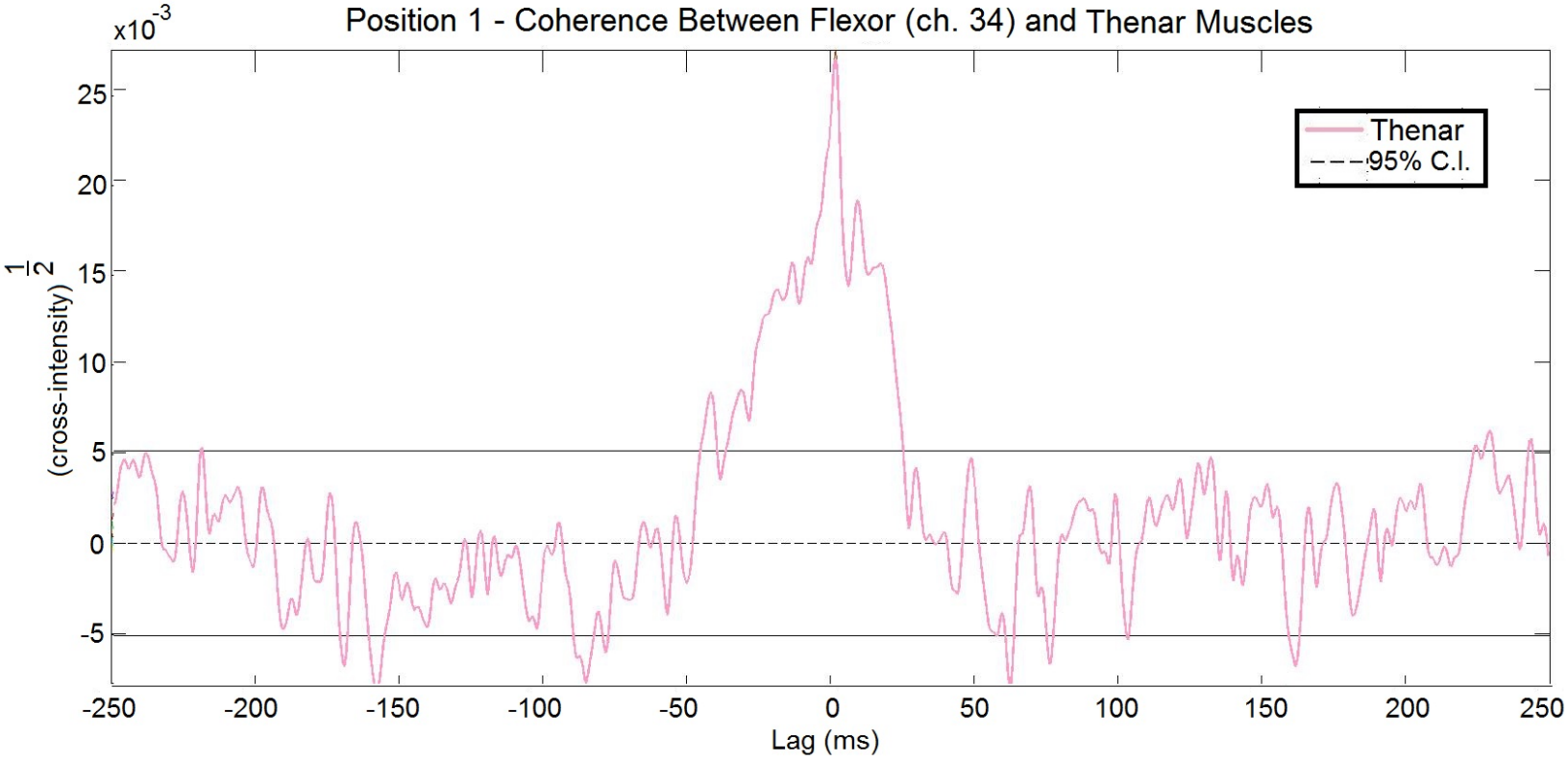

Figure 5.21: Cumulant Analysis from the Coherence Estimate Between the Thenar and Flexor (Ch. 34) Muscles - Position 1 - The cumulant analysis contains a central peak at 0ms with a magnitude of 0.027. This central peak tails off out to ±50ms. The narrow spike in this central peak suggests a short-time synchronisation between the coupling muscles. The peaks at 4 and 9Hz extracted from Figure 5.20 are absent in the cumulant, this is evident by the absence of the corresponding delay (±250 ms and ±111ms, respectively). The absence of this peaks in the cumulant suggests that the presence of coherence at those frequencies is not merely related to changes in the sEMG amplitude, but a reflection of the differences in the rhythmic waves of the sEMG patterns obtained from spatially distributed hand sEMG recordings.

Position 2: Thumb opposed to digitus medius - Figures 5.22 and 5.23 show the coherence estimate and cumulant analysis between rectified ch. 34 of the flexor muscles (located superior to the flexor pollicis longus) and the FDI muscle while the thumb was being opposed to the digitus medius (position 2). The site represented by the FDI muscle is composed by an 8 electrode array. From Figure 5.22, it can be appreciated that the 8 electrodes follow a similar shape with a variable amplitude. A significant low frequency (3-13)Hz coherence estimate peaking at 5Hz with a magnitude of (0.0386 ± 0.0028) is appreciated. These rhythmic coupling components of the sEMG coherence estimate are not evident separable features when the cumulant is analysed in Figure 5.23 presenting a clear absence of $\pm$200 ms delay. The cumulant itself is dominated by a broad central peak at 0ms and tailing off out to $\pm$50ms. Even though the coherence peak appear to scale depending on the level of the FDI muscle that is being analysed, none of these features are present in the cumulant, suggesting that the changes in coherence estimate peaks amplitude are not simply related to changes in the sEMG amplitude, but reflecting differences in the rhythmic waves of the EMG patterns received from spatially distributed hand sEMG recordings.

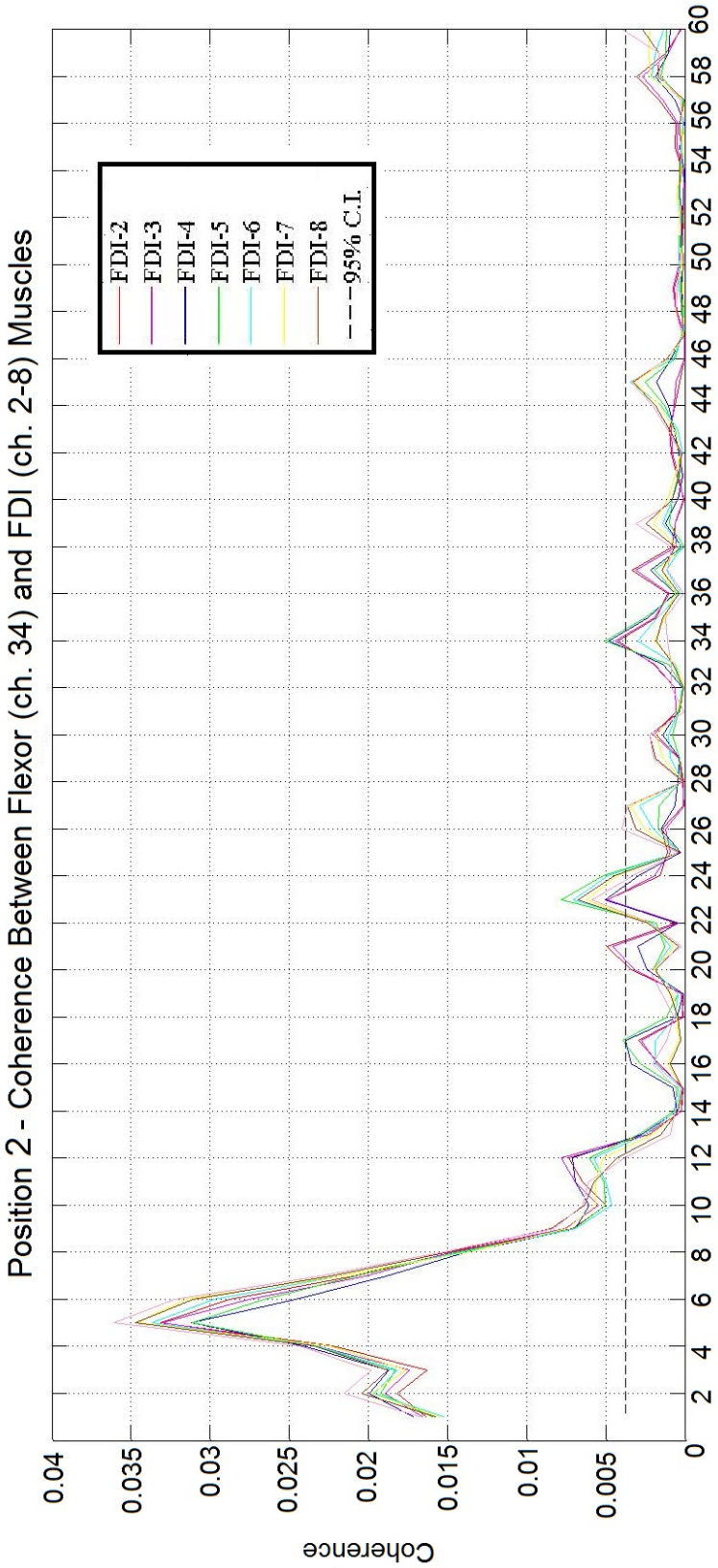

Figure 5.22: Coherence Estimate Analysis Between FDI and Flexor (Ch. 34) Muscles - Position 2 - Coherence estimate analysis results for Position 2 between a site in the anterior grid (corresponding to the FPl muscle) and the FDI muscle. Common to the 8-electrode array grid on the FDI muscle is a significant low frequency range coherence of (3-13)Hz with a peak at 5Hz and a magnitude of (0.0334 ± 0.0016). The information obtained from this Figure is complemented and better understood when it is used in conjunction with Figure 5.22

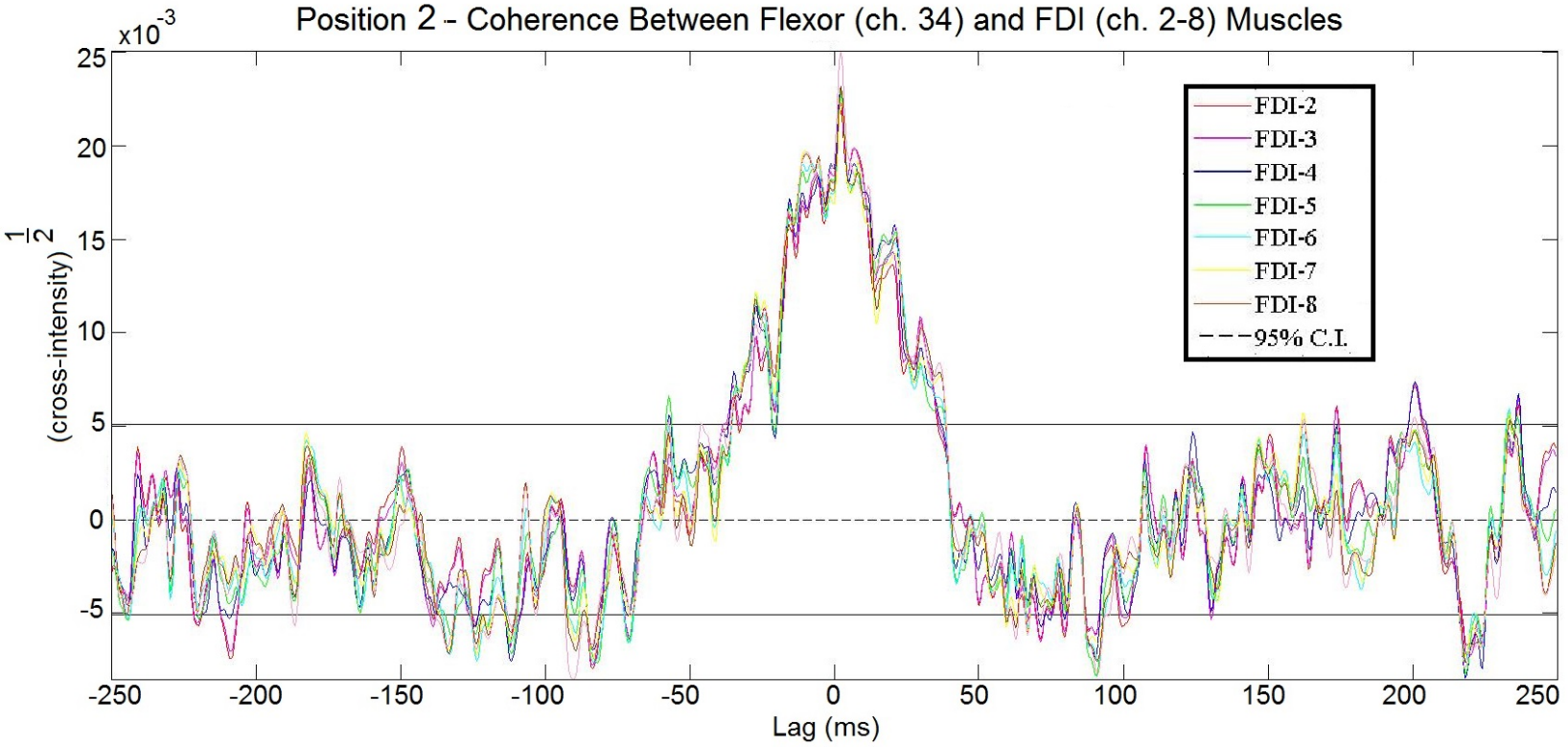

Figure 5.23: Cumulant Analysis from the Coherence Estimate Between FDI and Flexor Ch. 34 - Position 2 - The cumulant contains a central peak at 0ms with a magnitude of 0.0251 tailing off out to ±50ms. The peak found at 5Hz form the coherence estimate is not evident in the cumulant. This is evident by the absence of delayed peaks at ±200ms. This absence suggests that the differences in the coherence peak amplitudes are not simply related to the changes in sEMG amplitudes, but reflect differences in the rhythmic waves of the sEMG patterns received from the spatially distributed hand recordings.

Similarly, Figures 5.24 and 5.25 show the coherence estimate and cumulant analysis between rectified ch. 34 of the flexor muscles (located superior to the flexor pollicis longus) and the thenar muscles while the thumb was being opposed to the digitus medius (position 2). From Figure 5.24, it can be appreciated that in general, this shape follows the same pattern as the ones compared between the FPl and the FDI muscles. The shape of the coherence estimate shows a tendency for low frequency coupling (3-11)Hz with a peak at 5Hz. This rhythmic coupling component of the sEMG coherent estimate is not an evident separable feature, becoming clear when we further inspect Figure 5.25 and note the absence of the appropriate delay at $\pm$200 ms. The cumulant itself is dominated by a broad central peak at 0ms and tailing off out to $\pm$50ms. The peak from the coherence estimate is not present in the cumulant, suggesting that the changes in coherence estimate peak amplitude is not simply related to changes in the sEMG amplitude, but a reflection of the differences in the rhythmic waves of the sEMG patterns received from spatially distributed hand sEMG recordings.

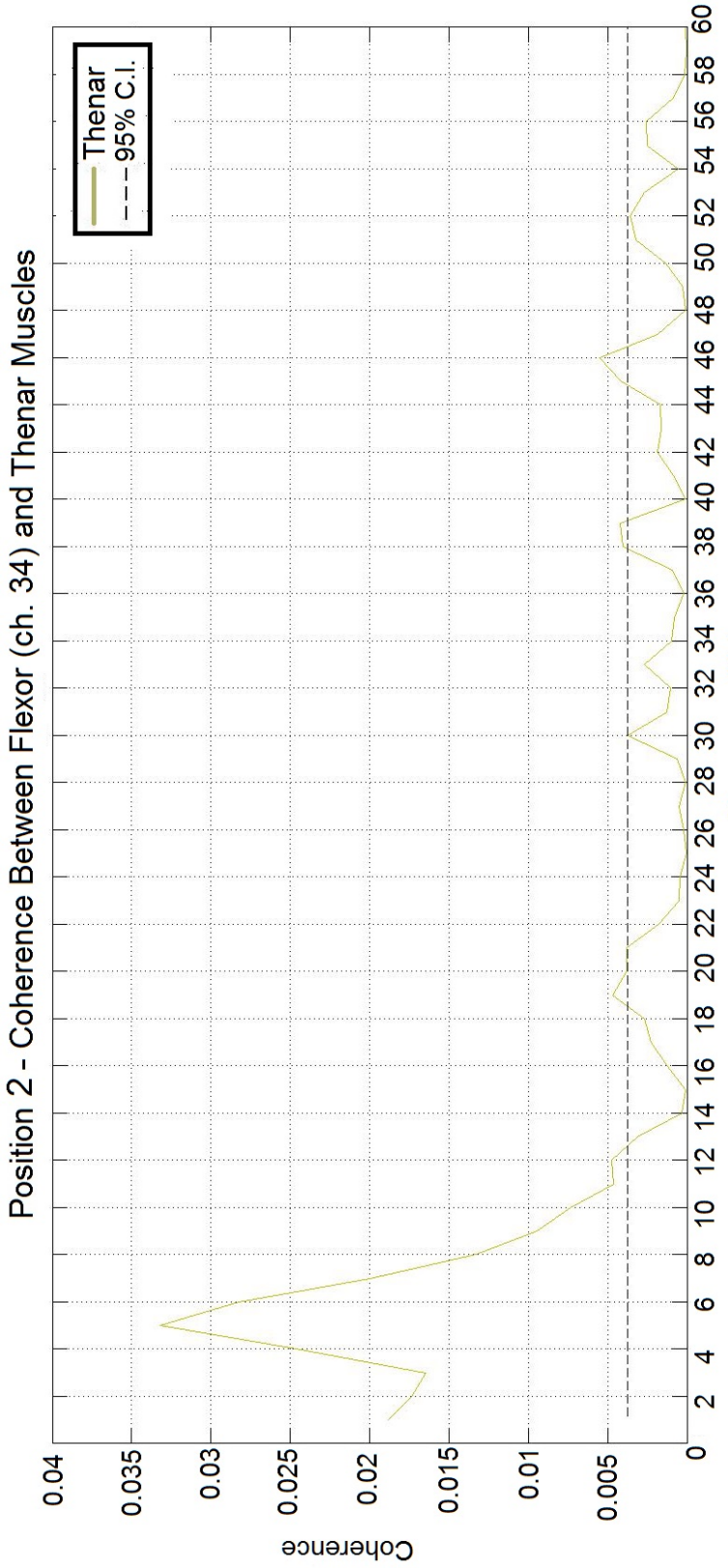

Figure 5.24: Coherence Estimate Analysis Between Thenar and Flexor (Ch. 34) Muscles - Position 2 - Coherence estimate analysis results for Position 2 between a site from the anterior grid (corresponding to the FP1 muscle) and a site on the thenar muscles. A significant low frequency range of (3-13)Hz peaking at 5Hz with a magnitude of 0.0325 is appreciated. The information obtained from this Figure is complemented and better understood when Figure 5.25 is used.

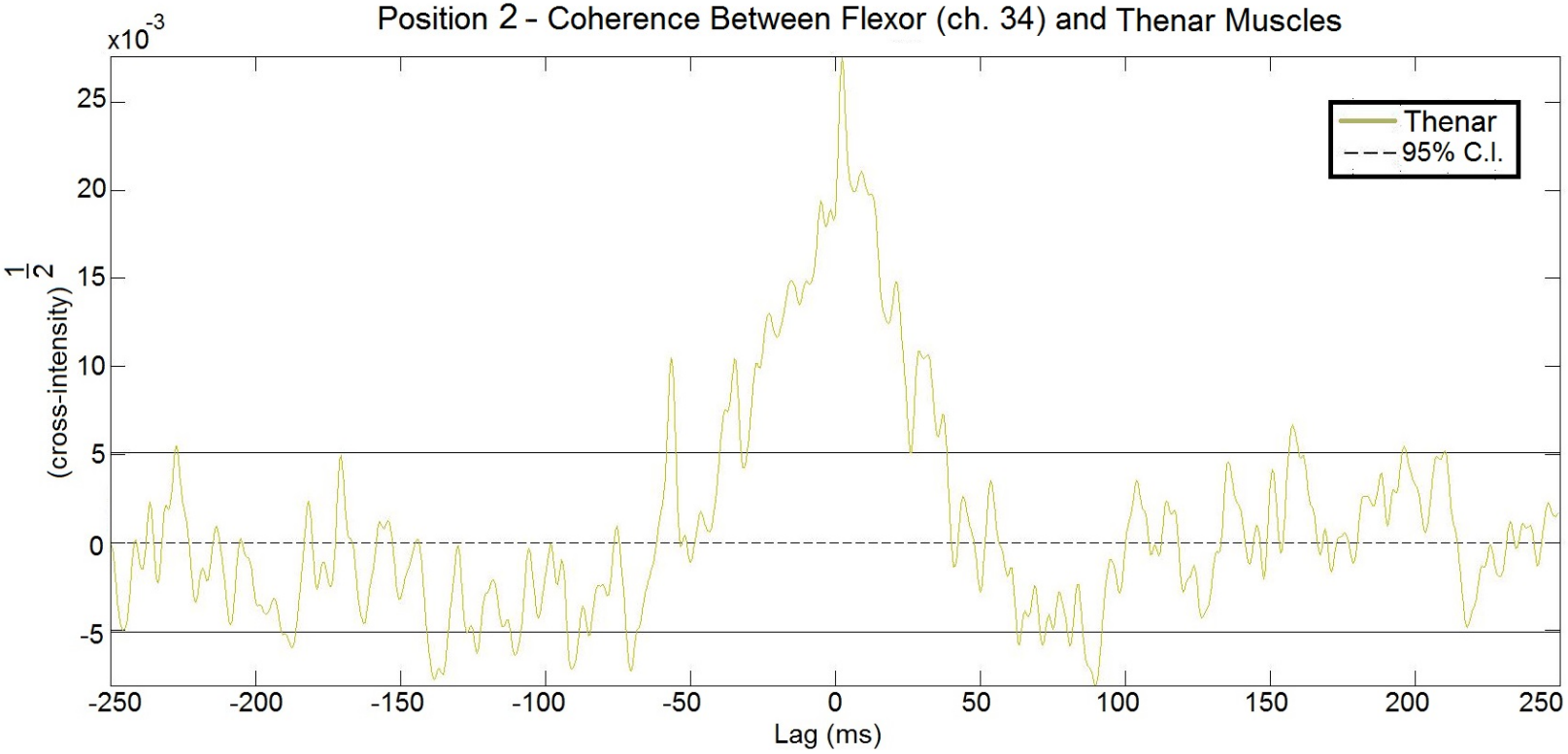

Figure 5.25: Cumulant Analysis from the Coherence Estimate Between Thenar and Flexor (Ch. 34) Muscle - Position 2 - The cumulant analysis contains a central peak at 0ms with a magnitude of 0.027. This central peak tails off out to ±50ms. The narrow spike at the top of the central peak suggests that there is short-time synchronisation between the coupling muscles. The peak at 5Hz visible in Figure 5.24 is absent in the cumulant, this becomes evident by the absence of the ±200ms delay. The absence of these delayed peaks suggests that the presence of the peaks in the coherence estimate at that specific frequency is not merely related to the changes found in the sEMG amplitude, but more of a reflection of the differences in the rhythmic waves of the sEMG patterns from the spatially distributed hand recordings.

Position 3: Thumb opposed to digitus annularis - Figures 5.26 and 5.27 show the coherence estimate and cumulant analysis between rectified ch. 34 of the flexor muscles (located superior to the flexor pollicis longus) and the FDI muscle while the thumb was being opposed to the digitus annularis (position 3). The site represented by the FDI muscle is composed by an 8 electrode array. From Figure 5.26, it can be appreciated that the 8 electrodes follow a similar shape with a variable amplitude. A significant low frequency (2-17)Hz coherence estimate peaking at 4 and 15Hz with a magnitude of (0.0386 ± 0.0028) and (0.0096 ± 0.0032), respectively, is appreciated. These rhythmic coupling components of the sEMG coherence estimate are not evident separable features when the cumulant is analysed in Figure 5.27 presenting a clear absence of $\pm$250ms and $\pm$66ms delays. The cumulant itself is dominated by a broad central peak at 0ms and tailing off out to $\pm$50ms. Even though the coherence peaks appear to scale depending on the level of the FDI muscle that is being analysed, none of these features are present in the cumulant, suggesting that the changes in coherence estimate peaks amplitude are not simply related to changes in the sEMG amplitude, but reflecting differences in the rhythmic waves of the EMG patterns received from spatially distributed hand sEMG recordings.

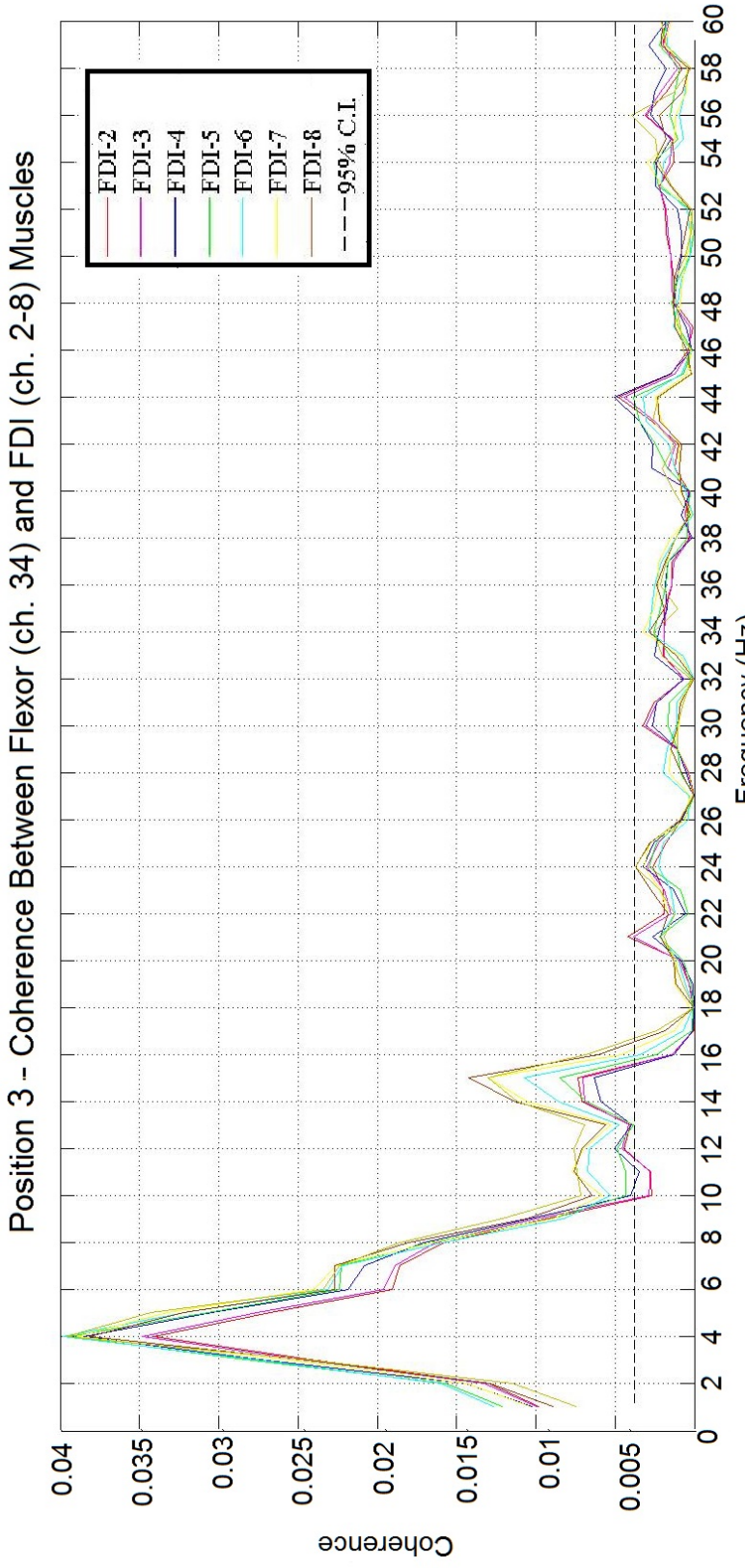

Figure 5.26: Coherence Estimate Analysis Between FDI and Flexor (Ch. 34) Muscles - Position 3 - Coherence estimate analysis results for Position 3 between a site located in the anterior grid (corresponding to the FPl muscle). Common to the 8-electrode array grid on the FDI muscle is a significant low frequency range coherence of [2-17]Hz with a peak at 4 Hz and a magnitude of $(0.0386 \pm 0.0028)$and a peak at 15Hz with magnitude of (0.0096 ± 0.0032). The information obtained from this figure should be used in conjunction with Figure 5.27 for the rhythmic coupling to be fully understood.

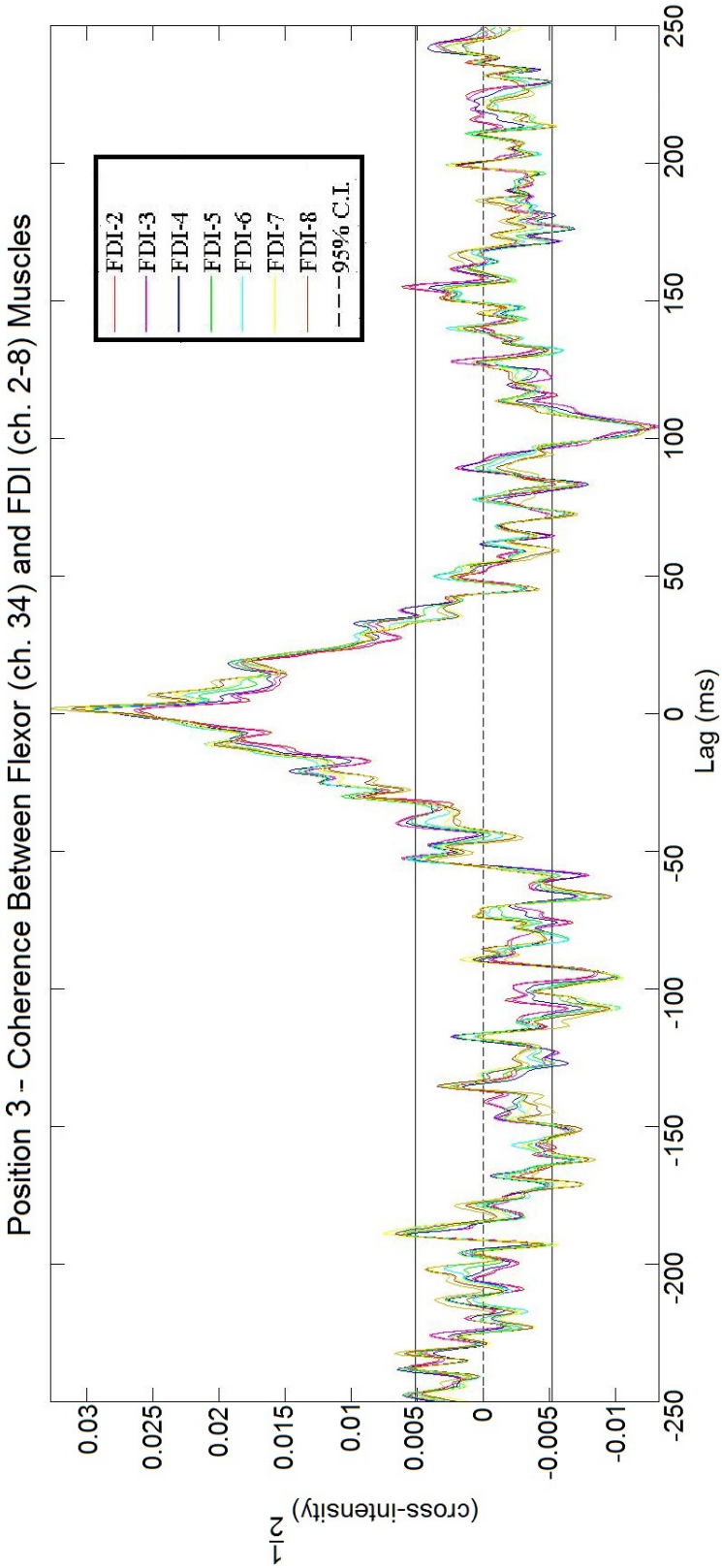

Figure 5.27: Cumulant Analysis from the Coherence Estimate Between FDI and Flexor Ch. 34 - Position 3 - The cumulant contains a central peak at 0ms and a magnitude of 0.0328 tailing off out to ±50ms. The peaks found at 4 and 15Hz are not evident in this analysis. This become clear by the absence of delayed peaks at ±250ms and ±66ms. This absence suggests that the differences in the coherence peaks amplitudes are not simply related to the changes in sEMG amplitudes, but also a reflection of the differences in the rhythmic waves of the sEMG patterns from the spatially distributed hand recordings.

Similarly, Figures 5.28 and 5.29 show the coherence estimate and cumulant analysis between rectified ch. 34 of the flexor muscles (located superior to the flexor pollicis longus) and the thenar muscles while the thumb was being opposed to the digitus annularis (position 3). From Figure 5.28, it can be appreciated that in general, this shape follows the same pattern as the ones compared between the FPl and the FDI muscles. The shape of the coherence estimate shows a tendency for low frequency coupling (2-17)Hz with a peak at 4Hz. This rhythmic coupling component of the sEMG coherent estimate is not an evident separable feature, becoming clear when we further inspect Figure 5.29 and note the absence of the appropriate delay at $\pm$250 ms. The cumulant itself is dominated by a broad central peak at 0ms and tailing off out to $\pm$50ms. The peak from the coherence estimate is not present in the cumulant (at $\pm$250ms), suggesting that the changes in coherence estimate peak amplitude is not simply related to changes in the sEMG amplitude, but a reflection of the differences in the rhythmic waves of the sEMG patterns received from spatially distributed hand sEMG recordings.

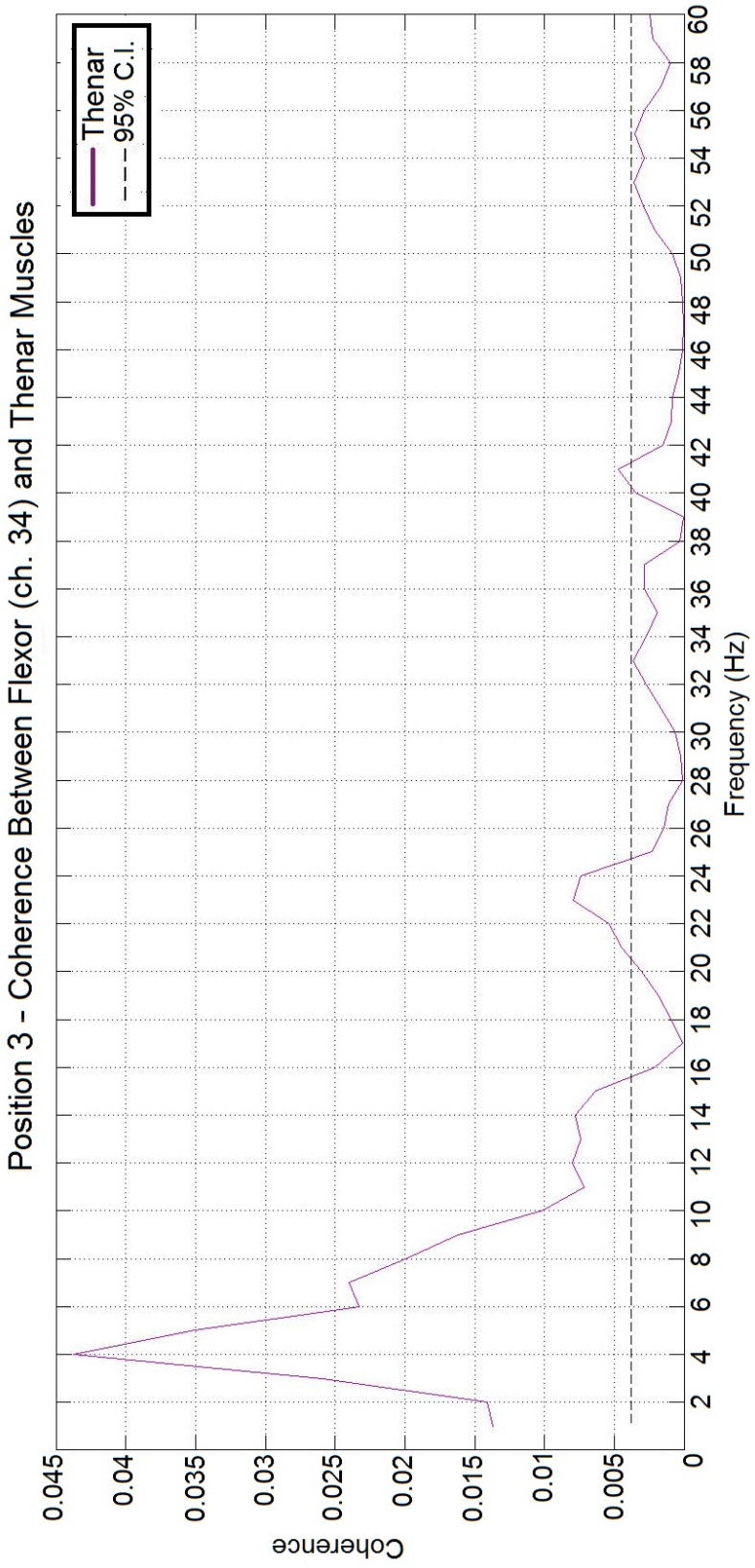

Figure 5.28: Coherence Estimate Analysis Between Thenar and Flexor (Ch. 34) Muscles - Position 3 - Coherence estimate analysis results for Position 3 between a site from the anterior grid (corresponding to the FP1 muscle) and a site on the thenar muscles. A significant low frequency of (2-17)Hz peaking at 4Hz with a magnitude of 0.049 can be appreciated. The information obtained from this Figure is further complemented in conjunction to Figure 5.29.

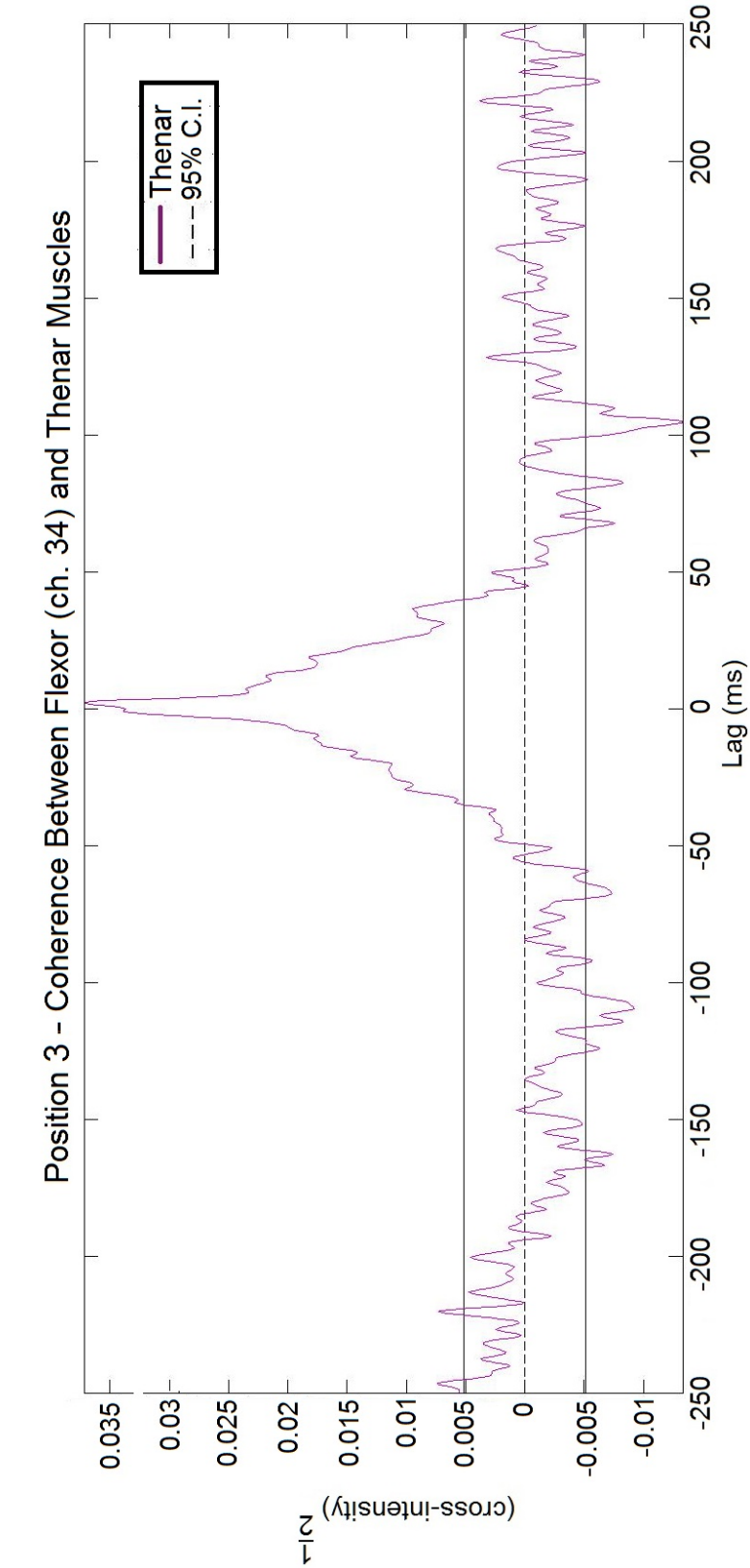

Figure 5.29: Cumulant Analysis from the Coherence Estimate Between Thenar and Flexor (Ch. 34) Muscles - Position 3 - The cumulant analysis contains a central peak at 0ms with a magnitude of 0.037. This central peak tails off out to ±50ms. The narrow spike at the top of this central peak suggests a short-time synchronisation between the coupling muscles. The peak at 4Hz extracted from Figure 5.28 are absent in the cumulant. This is evident when its corresponding ±250ms delay peak is absent. This suggests that the presence of the peaks in coherence at 4Hz is not merely related to the changes in the sEMG amplitude, but to a reflection of the differences in the rhythmic waves of the sEMG patterns obtained from the spatially distributed hand recordings.

Position 4: Thumb opposed to digitus minimus manus - Finally, Figures 5.30 and 5.31 show the coherence estimate and cumulant analysis between rectified ch. 34 of the flexor muscles (located superior to the flexor pollicis longus) and the FDI muscle while the thumb was being opposed to the digitus minimus manus (position 4). The site represented by the FDI muscle is composed by an 8 electrode array. From Figure 5.30, it can be appreciated that the 8 electrodes follow a similar shape with a variable amplitude. A significant low frequency (2-20)Hz coherence estimate peaking at 3, 8, 12 and 18Hz with a magnitude of (0.0193±0.0019), (0.0136±0.0015), (0.0082±0.0013) and (0.0070 ± 0.0009), respectively, are appreciated. These rhythmic coupling components in the sEMG coherence estimate are not evident separable features when the cumulant is analysed in Figure 5.31 presenting a clear absence of ±333ms, ±125ms, ±83ms and ±55ms delays. The cumulant itself is dominated by a broad central peak at 0ms and tailing off out to ±50ms with a peak at the top inferring a short-time synchronisation. Even though the coherence peaks appear to scale depending on the level on the FDI muscle that is being analysed, none of these features are present in the cumulant, suggesting that the changes in coherence estimate peaks amplitude are not simply related to changes in the sEMG amplitude, but reflecting differences in the rhythmic waves of the EMG patterns received from spatially distributed hand sEMG recordings.

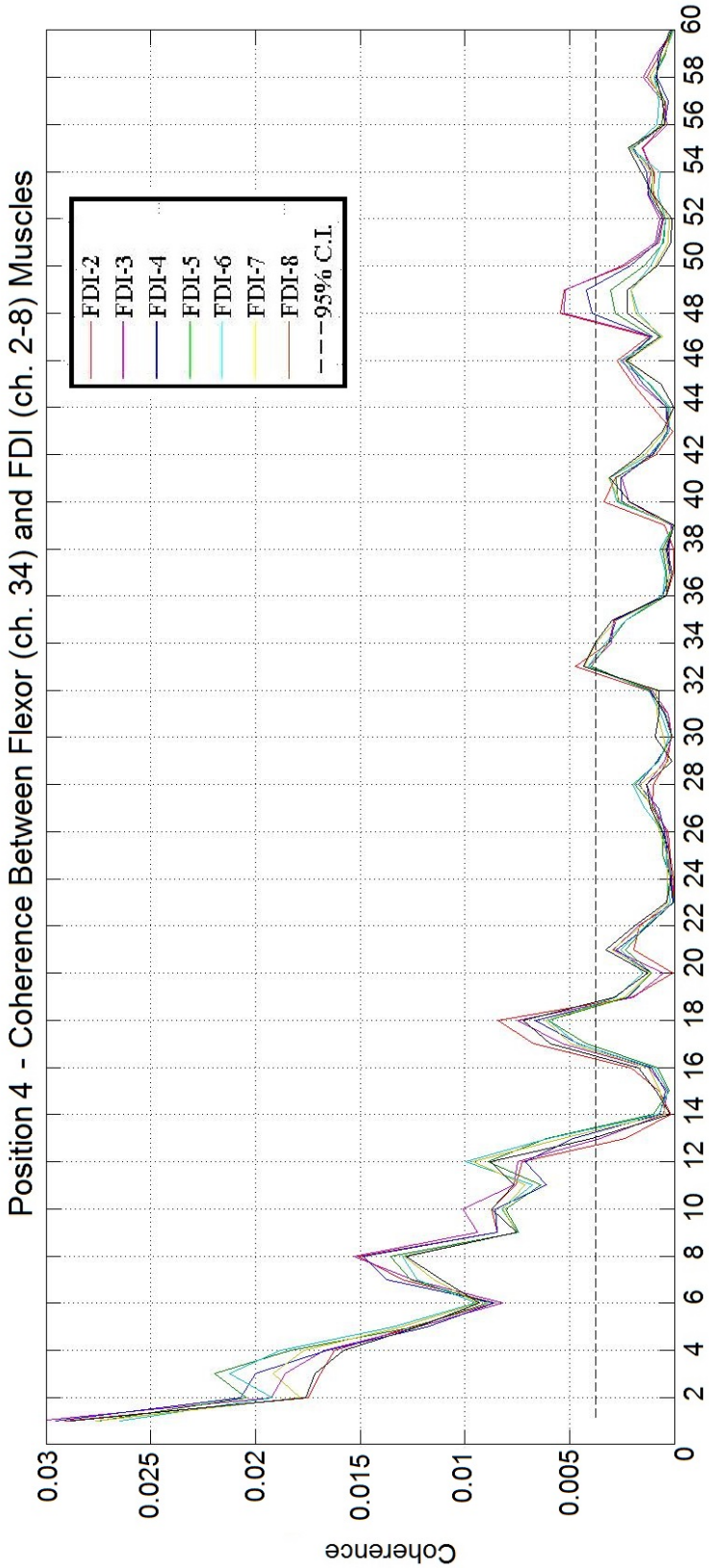

Figure 5.30: Coherence Estimate Analysis Between FDI and Flexor (Ch. 34) Muscles - Position 4 - Coherence estimate results for position 4 between a site in the anterior grid (corresponding to the FPl muscle) and the FDI muscle. Common to the 8-electrode array grid placed on the FDI muscle, is a significant low frequency coherence range of (2-20)Hz peaking at 3, 8, 12 and 18Hz with a magnitude of (0.0193 ± 0.0019), (0.0136 ± 0.0015), (0.0082 ± 0.0013) and (0.0070 ± 0.0009), respectively. The information extracted from this Figure is complemented and better understood when Figure 5.31 is used.

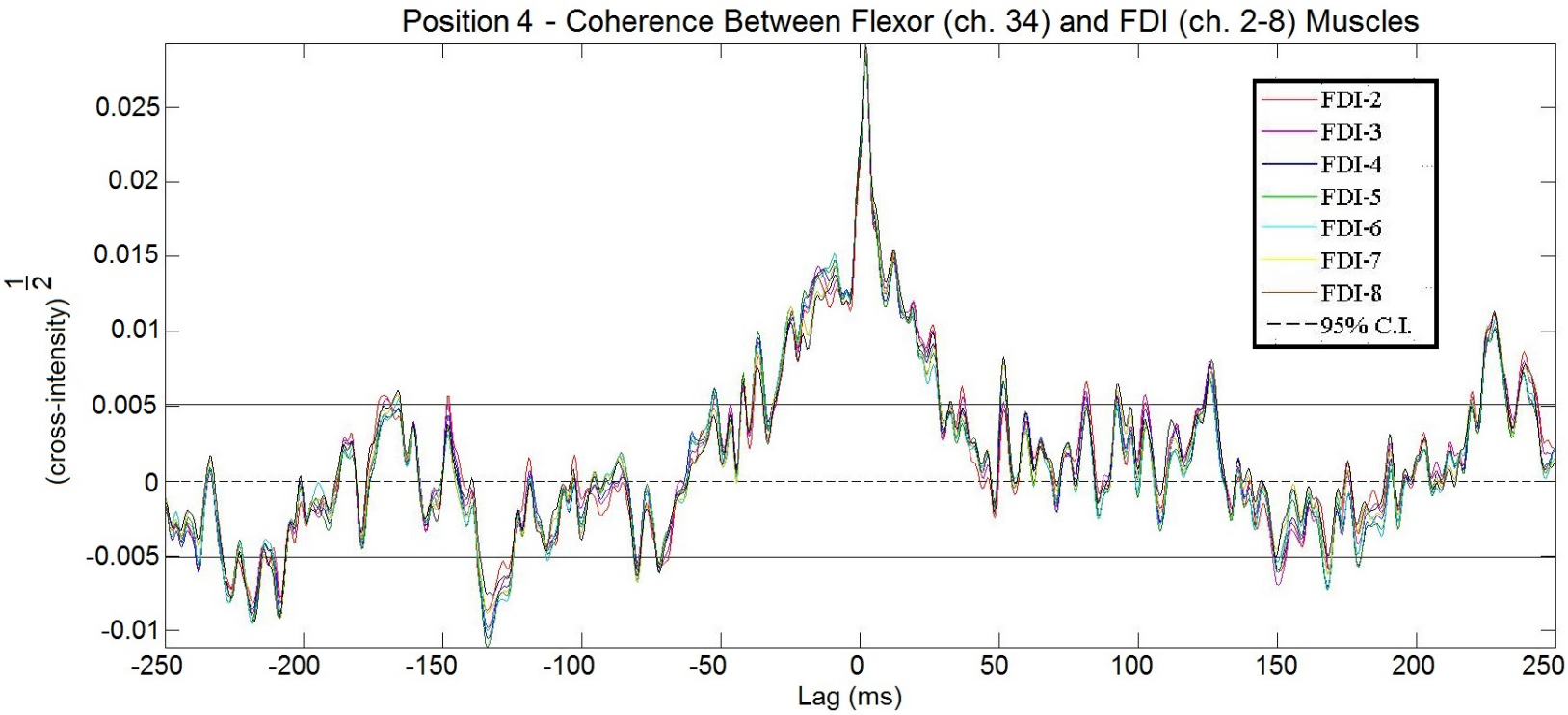

Figure 5.31: Cumulant Analysis from the Coherence Estimate Between FDI and Flexor Ch. 34 - Position 4 - The cumulant analysis contains a central peak at 0ms with a magnitude of tailing off out to ±50ms. A short-time synchronisation is further appreciated as a narrower spike at the top of this central peak. The peaks found in the coherence estimate are absent in the cumulant. This is evident by the absence of delayed peaks at ±333ms, ±125ms, ±83ms and ±55ms. These absences suggest that the differences in the coherence peaks amplitude are not simply related to the changes in the sEMG amplitudes, but as a reflection of the differences in the rhythmic waves of the sEMG patterns received from the spatially distributed recordings in the hand.

Similarly, Figures 5.32 and 5.33 show the coherence estimate and cumulant analysis between rectified ch. 34 of the flexor muscles (located superior to the flexor pollicis longus) and the thenar muscles while the thumb was being opposed to the digitus annularis (position 3). From Figure 5.32, it can be appreciated that in general, this shape follows the same pattern as the ones compared between the FPl and the FDI muscles. The shape of the coherence estimate shows a tendency for low frequency coupling (2-14)Hz with peaks at 7 and 11Hz. These rhythmic coupling component of the sEMG coherent estimate is not an evident separable feature, becoming clear when we further inspect Figure 5.33 and note the absence of the appropriate delay at ±142ms and ±90ms. The cumulant itself is dominated by a broad central peak at 0ms and tailing off out to ±50ms. The peaks from the coherence estimate are not present in the cumulant (at ±142ms and ±90ms), suggesting that the changes in coherence estimate peak amplitude is not simply related to changes in the sEMG amplitude, but a reflection of the differences in the rhythmic waves of the sEMG patterns received from spatially distributed hand sEMG recordings.

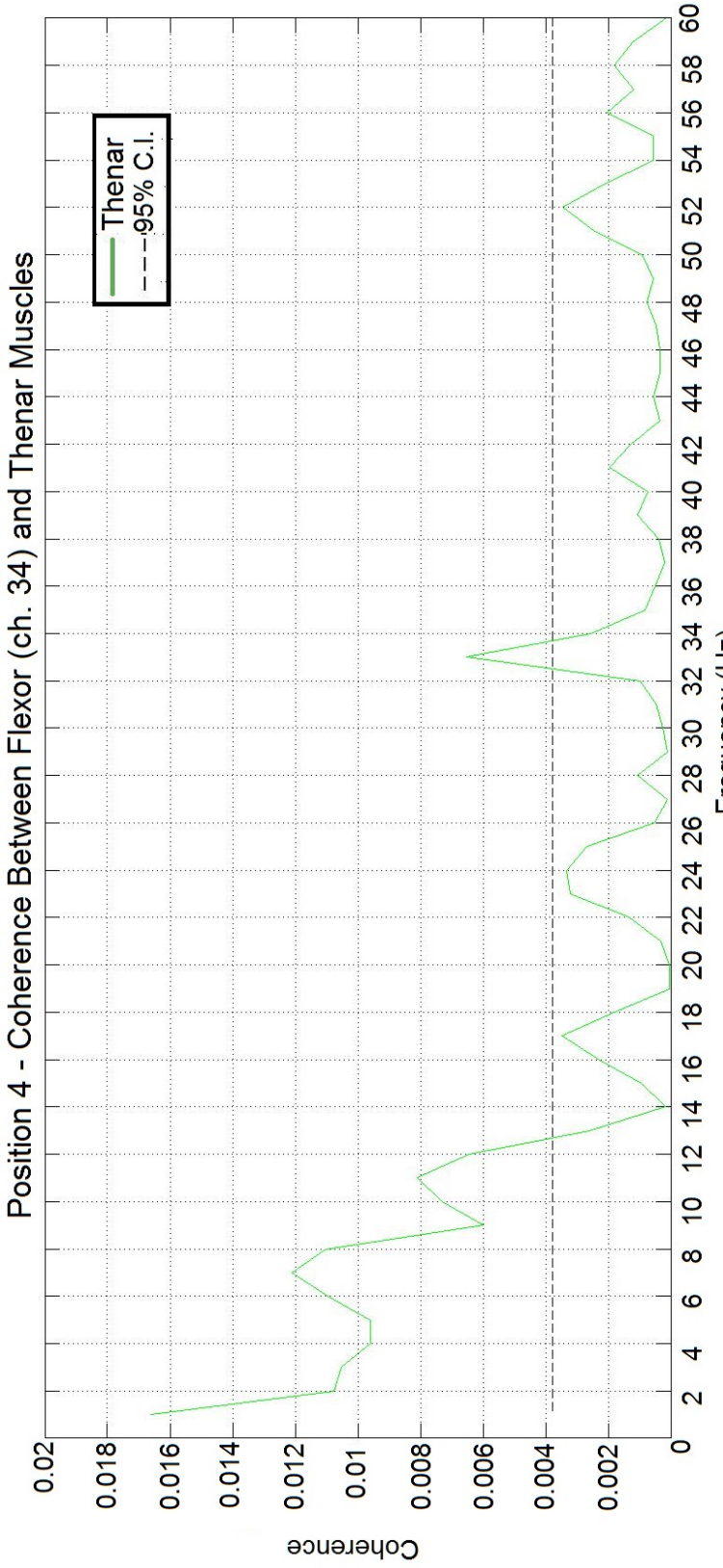

Figure 5.32: Coherence Estimate Analysis Between Thenar and Flexor (Ch. 34) Muscles - Position 4 - Coherence estimate analysis results for Position 4 between a site in the anterior grid (corresponding to the FPl muscle) and a site on the thenar muscles. A significant low frequency coherence range of (2-14)Hz with peaks at 7 and 11Hz with a magnitude of 0.012 and 0.008, respectively, are appreciated. The information obtained from this Figure is complemented and better understood when Figure 5.33 is used in conjunction.

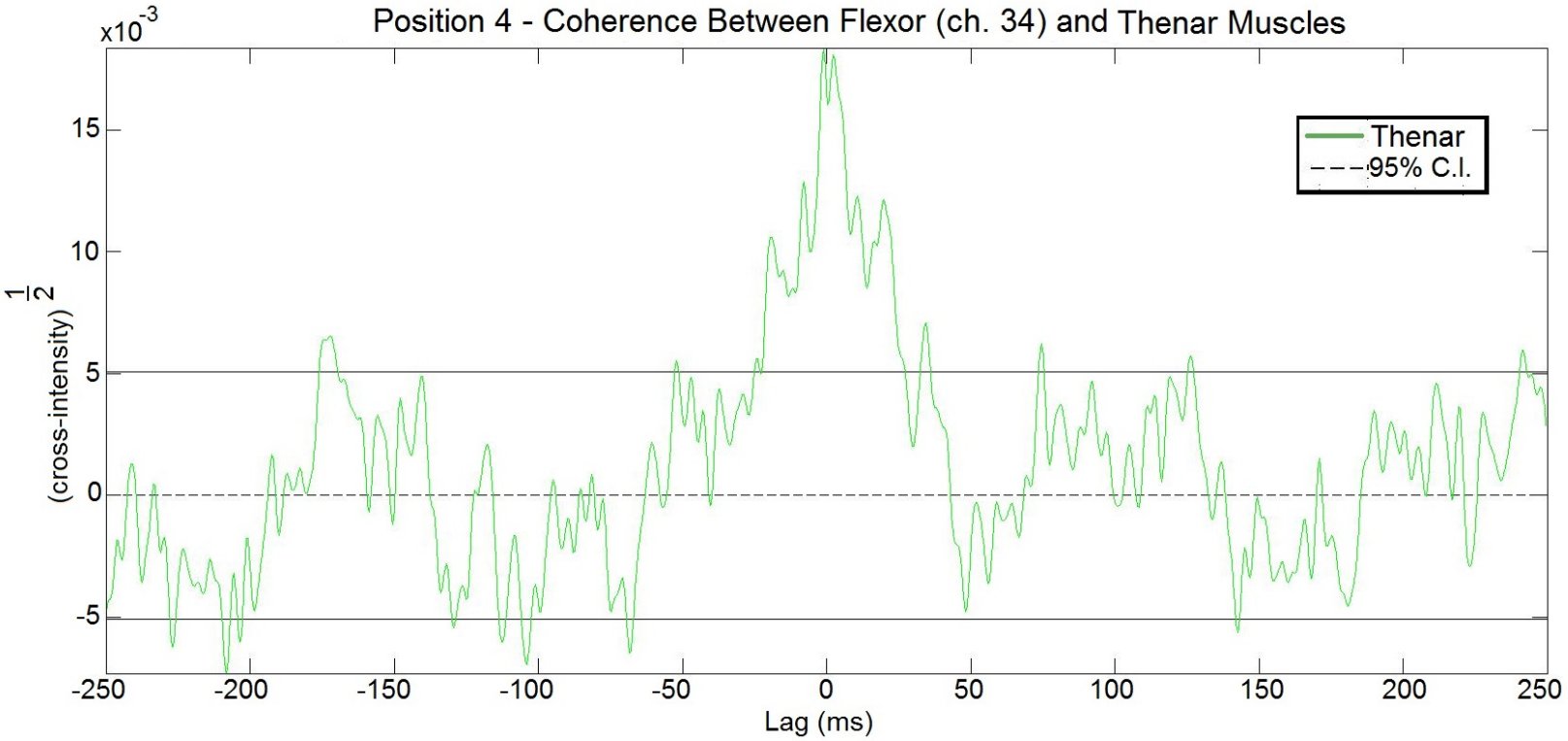

Figure 5.33: Cumulant Analysis from the Coherence Estimate Between Thenar and Flexor (Ch. 34) Muscles - Position 4 - The cumulant analysis contains a central peak at 0ms with a magnitude of . This central peak tails off out to ±50ms. The narrow spike in the top of this central peak suggests a short-time synchronisation between the coupling muscles. The peaks at 7 and 11Hz extracted from the cumulant estimate are absent in the cumulant, this becomes evident by the absence of the corresponding delays at ±142ms and ±90ms, respectively. The absence of this peaks in the cumulant suggests that the presence of coherence at those frequencies is not merely related to changes in the sEMG amplitude, but a reflection of the differences in the rhythmic waves of the sEMG patterns obtained from spatially distributed hand recordings.

5.4.1.3 Summary of all Positions

Finally, in Figure 5.34 and 5.35 the different positions of the thumb are shown for the coherence analysis between the FDI muscle belly (located in the middle of the 8-electrode grid) and channel 34 of the flexor muscles (positioned over the FPl). The first Figure shows the coherence estimate across the positions that the thumb was opposed to. These graphs show a similar significant low frequency range (2-20)Hz. With regards to the shape, position 2 and 3 follow the same type of trace with different amplitude, where position 1 and 4 share similar traces and similar amplitude peaks. From the cumulant analysis in the latter figure, a central peak, common to all positions, is appreciated at 0ms tailing off to ±50ms with a short-time synchronisation burst at the top of the central peak. In Table 5.5 a summary of these differences are shown.

Table 5.5: Summary of Coherence Between FDI Muscle Belly and Flexor Pollicis Longus (Ch. 34 of Anterior Grid)

Position	Range (Hz)	Peaks (Hz - magnitude)
1	(1-17)	(4 -0.0184) (8 - 0.0188) (15 - 0.0074)
2	(3-13)	(5 - 0.0386)
3	(2-17)	(4 - 0.0386) (15 - 0.0096) (3 - 0.0193)
4	(2-20)	(8 - 0.0136) (12 - 0.0082) (18 - 0.0070)

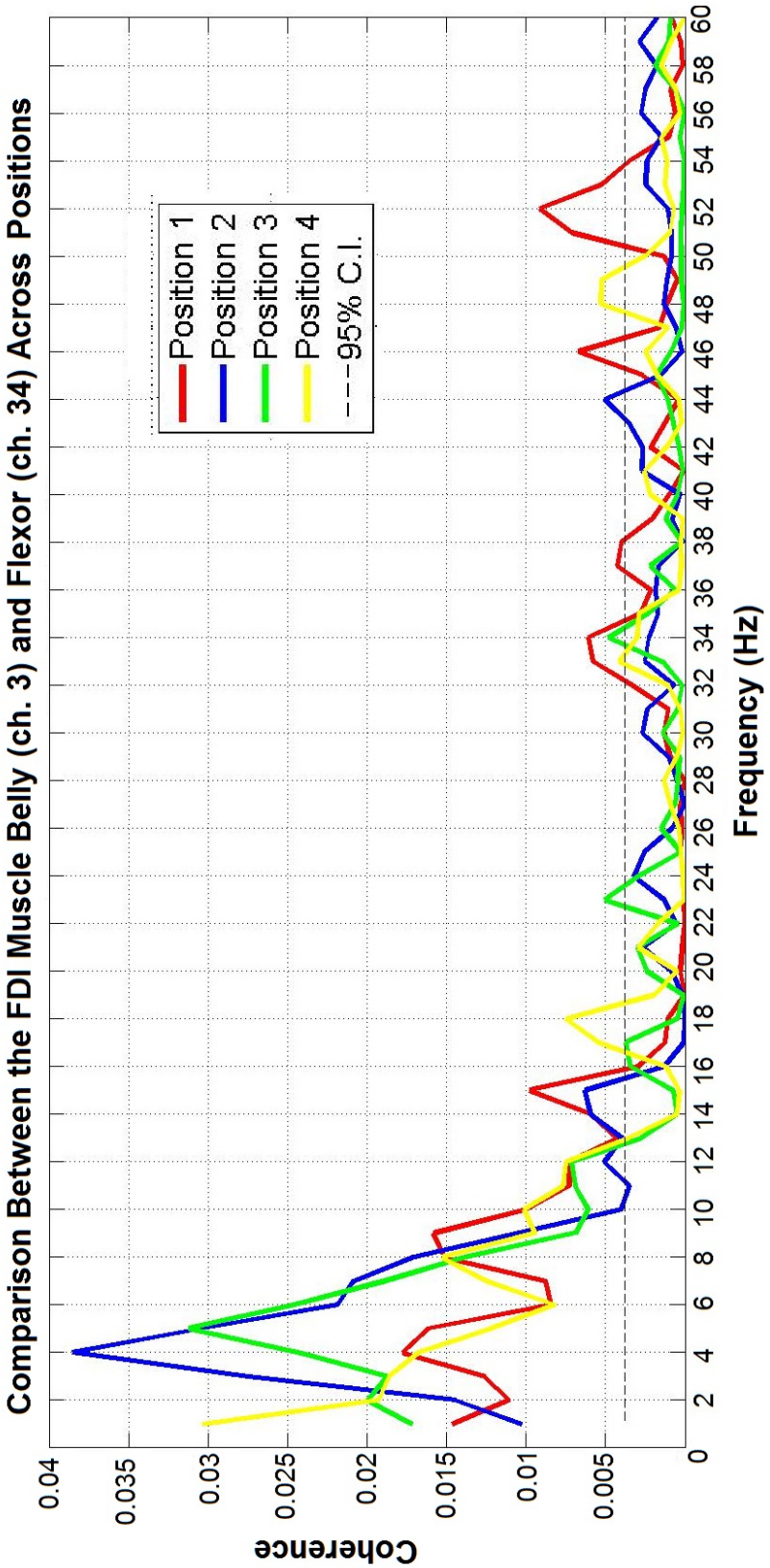

Figure 5.34: Coherence Estimate Comparison Across All the Positions Between FDI (ch. 3) and Flexor Muscles (ch.34) - Coherence estimate across the positions that the thumb was opposed to. These graphs show a similar significant low frequency range (2-20)Hz. With regards to the shape, position 2 and 3 follow the same type of trace with different amplitude, where position 1 and 4 share similar traces and similar amplitude peaks. The overall information obtained from this Figure is complemented and better understood when Figure 5.35 is used in conjunction.

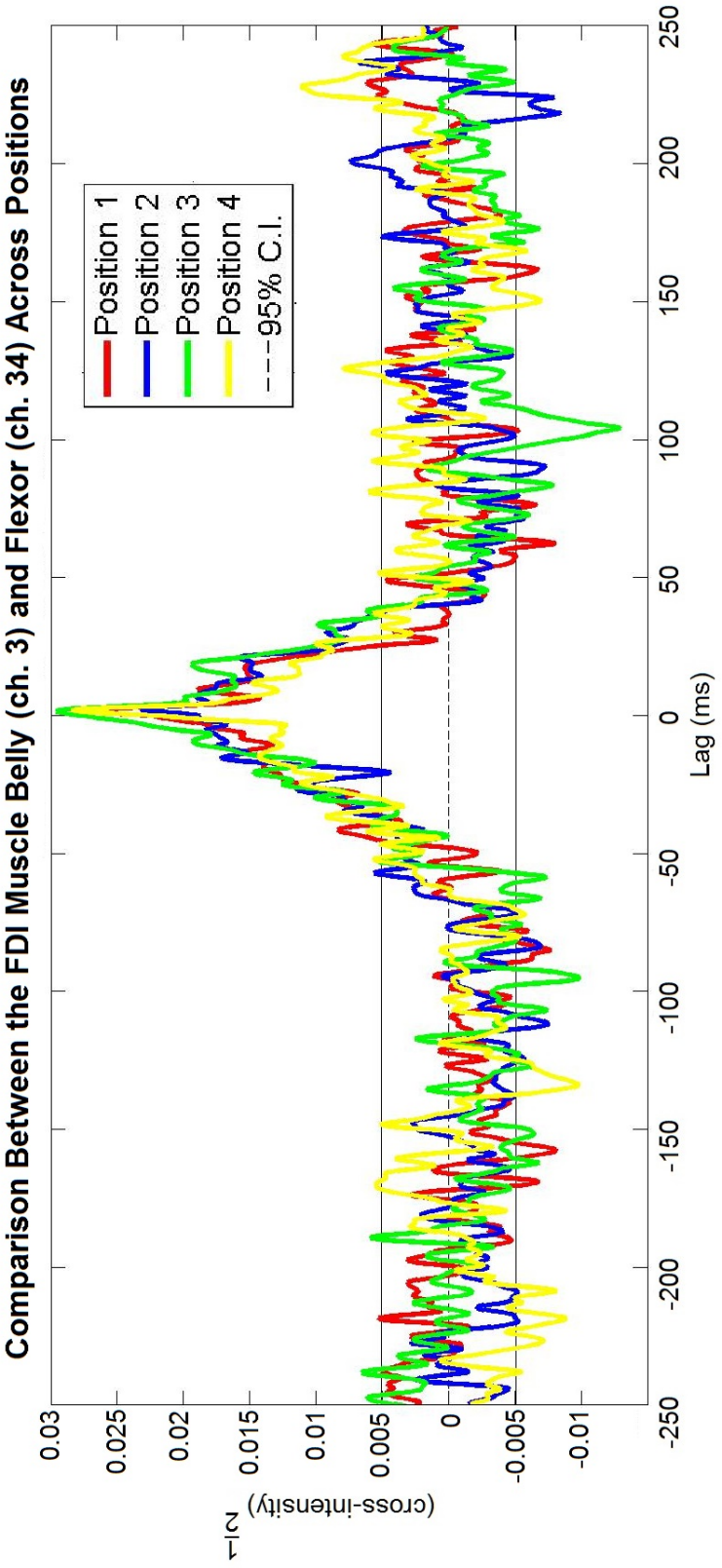

Figure 5.35: Coherence Cumulant Comparison Across All the Positions Between FDI (ch. 3) and Flexor Muscles (ch.34) - The cumulant analysis shows a central peak, common to all positions, at 0ms tailing off to ±50ms with a short-time synchronisation burst at the top of the central peak. No clear delayed peaks related to the peaks found in the coherence estimate are found, therefore, these absences suggest that the differences in the coherence peaks amplitude are not simply related to the changes in the sEMG amplitudes, but they reflect differences in the rhythmic waves of the sEMG patters from the spatially distributed recordings from the hand.

In Figure 5.36 and 5.37 the different positions of the thumb are shown for the coherence analysis between the thenar muscles and channel 34 of the flexor muscles (positioned over the FPl). The first Figure shows the coherence estimate across the positions that the thumb was opposed to. This graph shows similar traces across the positions, alike significant low frequency range (2-17)Hz. With regards to the shape, position 2 and 3 follow the same type of trace shape with different amplitude, and position 1 and 4 share little similarities amongst them. From the cumulant analysis in the latter Figure, a central peak, common to all positions, is appreciated at 0ms tailing off to ±50ms with a short-time synchronisation burst at the top of the central peak, this is particularly evident for position 3. In Table 5.6 a summary of these differences are shown.

Table 5.6: Summary of Coherence Between Thenar Muscle and Flexor Pollicis Longus (Ch. 34 of Anterior Grid)

Position	Range (Hz)	Peaks (Hz - magnitude)
1	(1-11)	(4 -0.0180) (9 - 0.0220)
2	(3-11)	(5 - 0.0325)
3	(2-17)	(4 - 0.0490)
4	(2-14)	(7 -0.0120) (11 - 0.0080)

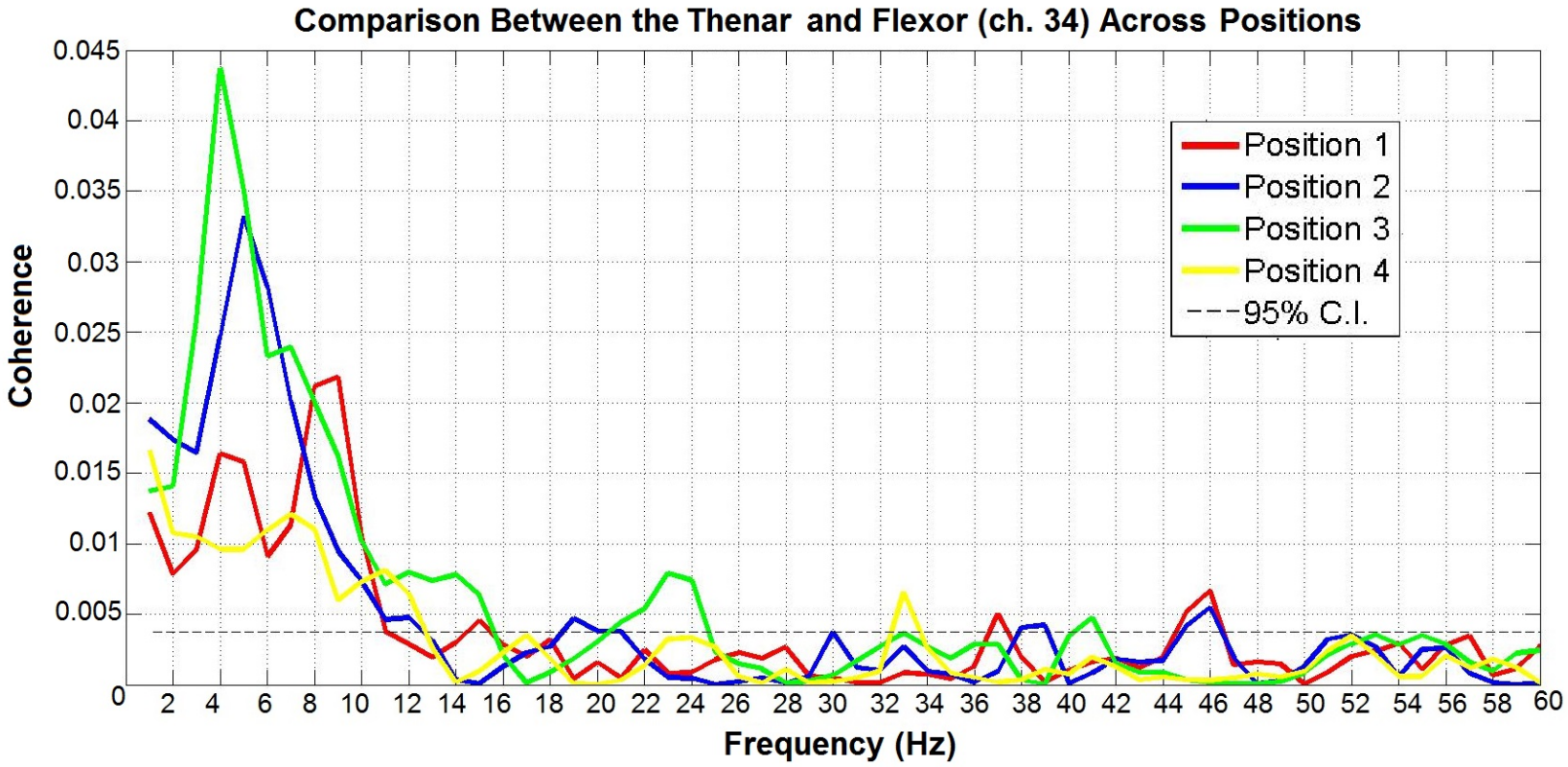

Figure 5.36: Coherence Estimate Comparison Across All the Positions Between Thenar and Flexor Muscles (ch.34) - Coherence estimate across the positions that the thumb was opposed to. These graphs show a similar significant low frequency range (2-17)Hz. With regards to the shape, position 2 and 3 follow the same type of trace with different amplitudes, and position 1 and 4 share little similarities amongst them. The overall information obtained from this Figure is complemented and better understood when Figure 5.37 is used in conjunction.

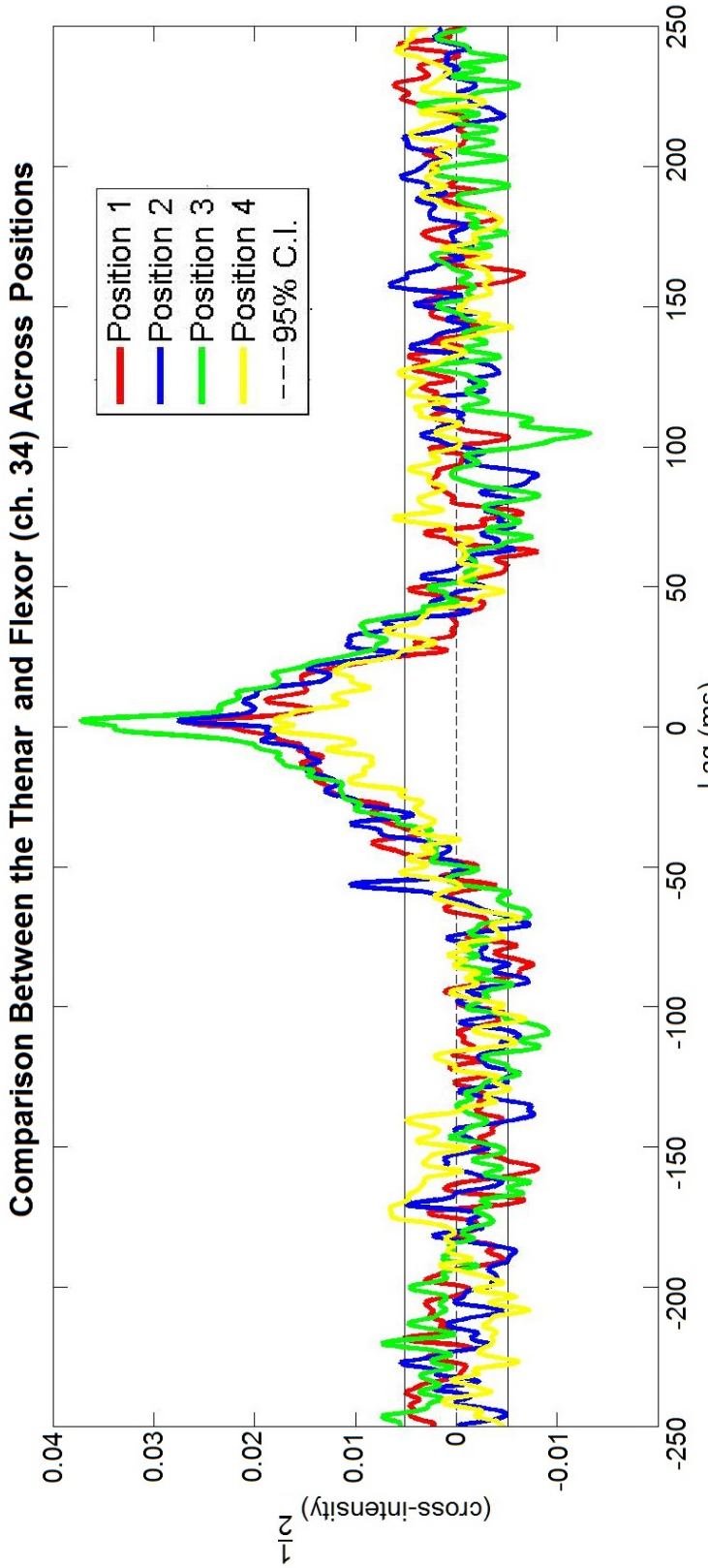

Figure 5.37: Coherence Cumulant Comparison Across All the Positions Between Thenar and Flexor Muscles (ch.34) - The cumulant analysis show a central peak, common to all positions, at 0ms tailing off to ±50ms with a short-time synchronisation burst at the top of the central peak, particularly evident for position 3. No clear delayed peaks related to the peaks found in the coherence estimate are found, therefore, these absences suggest that the differences in the coherence peaks amplitude are not simply related to the changes in the sEMG amplitudes, but they reflect differences in the rhythmic waves of the sEMG patters from the spatially distributed recordings from the hand.

5.4.2 Relation Between the RMS Values of the sEMG and the Area Under the Curve Obtained from the Coherence Analysis

The RMS values obtained in Section 5.2 were related to the area under the curve from the lower range of frequencies (approximately between 1-18Hz) of each position of the thumb. This results help in the understanding with regards to the amplitude of the sEMG as a feature distribution (positions) against the coherence estimate values as the area under the curve found for each pair of muscles. On one side, the RMS values show that the pattern of activity level is different, on the other side, the coherence analysis shows that the patterns of coupling between muscles seem to change also in relation to the different positions. If these two results are merge together, a further distribution can be obtained as it is shown in Figure 5.38.

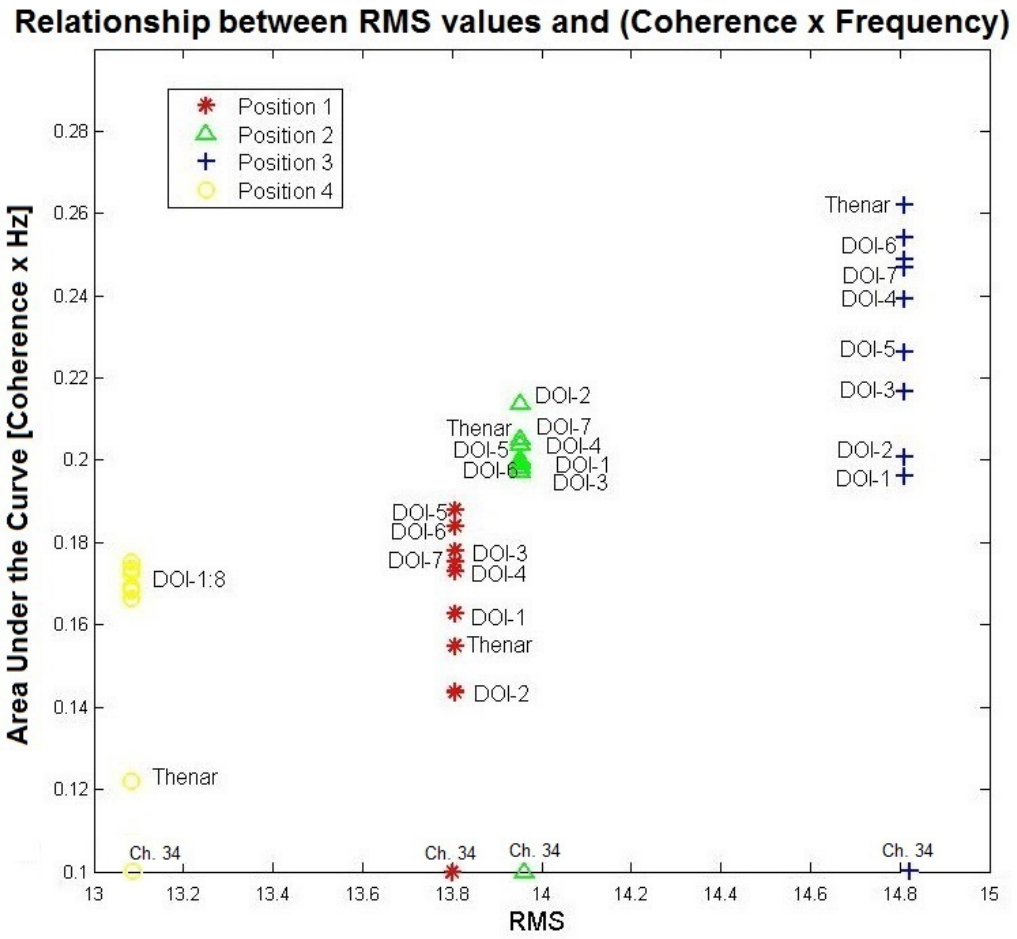

Figure 5.38: Comparison Between RMS Values and Coherence Amplitude, calculated as Area Under the Curve - In this figure, the RMS values obtained from Section 5.2 and the area under the curve for each of the electrodes on the Thenar and FDI muscles from ch. 34 from the Flexor muscles are shown.

5.4.3 Coherence Analysis - Postural Task

As for the steady condition, the same analysis (as the modulated counterpart) was performed, and is shown from Figures 5.40 to 5.47. This analysis was performed from a later data acquisition (with the same setup that has been described throughout this thesis) to further investigate the frequencies when a steady condition was met. It was found that common for all the coherence analysis, position 1 (thumb opposed to index finger) had a clear constant positive coherence from 1-80Hz. This steady coherence is generally associated with cross-talk, therefore, position 1 was eliminated for the steady contraction analysis for most of the cases. An example of this phenomena is shown in Figure 5.39. Moreover, as it will be shown in some of the signals in time, when position 1 is exerted, the amplitude is the same as the baseline, inferring that during that task, there is from very little to none muscular activity. This last part might be due to this movement being the same as the natural position of the hand. On Table 5.7, the summary of the frequency range found for the coherence analysis during the steady contraction and the peaks found with their corresponding magnitude is shown.

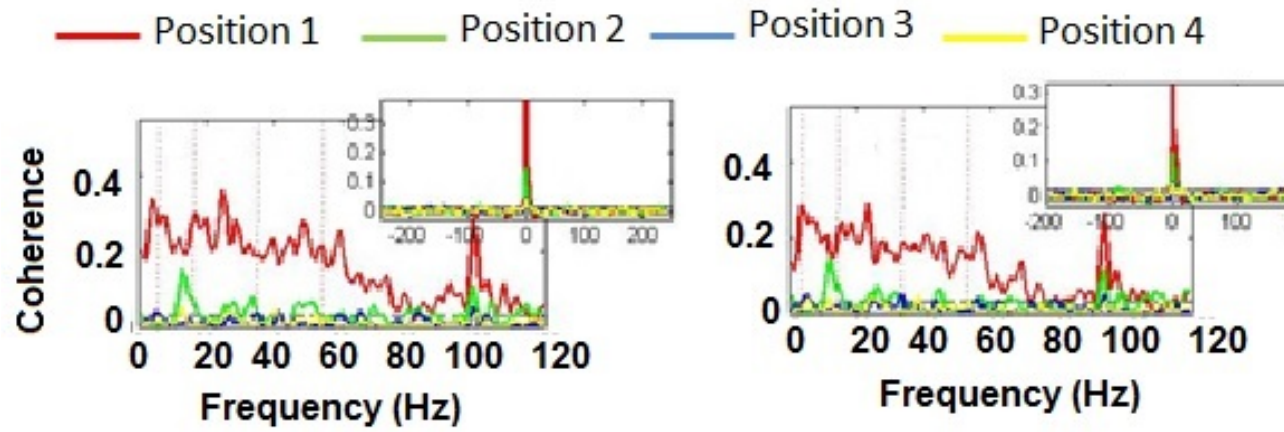

Figure 5.39: Cross-talk shown for Position 1 from Coherence and Cross-Intensity Analysis performed during a Steady Contraction for All Positions - The red line (corresponding to Position 1) represents constant coherence from 1-80Hz. This is more evident when compared to the other positions where the peaks vary in amplitude and duration. This constant coherence for such a wide frequency range is defined as cross-talk and, therefore, this position has been discarded for most of the steady condition analysis.

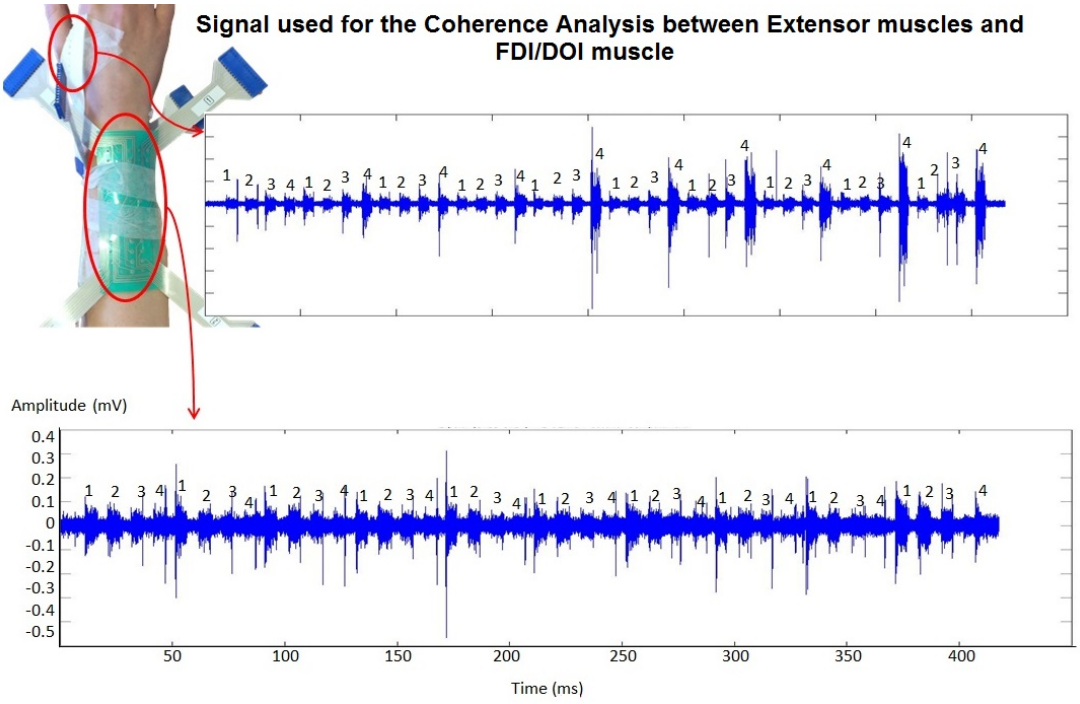

Figure 5.40: Signals used for Coherence Analysis between the FDI Muscle and the Extensor Muscles During Steady Contractions - Top - Signal acquired during the opposition tasks, from an electrode from an 8-electrode array placed on top of the FDI muscle. Bottom - Signal acquired from an electrode of the 64-electrode array placed onto the Extensor muscles. The numbers in both of the graphs indicate the position that was opposed for each resulting contraction.

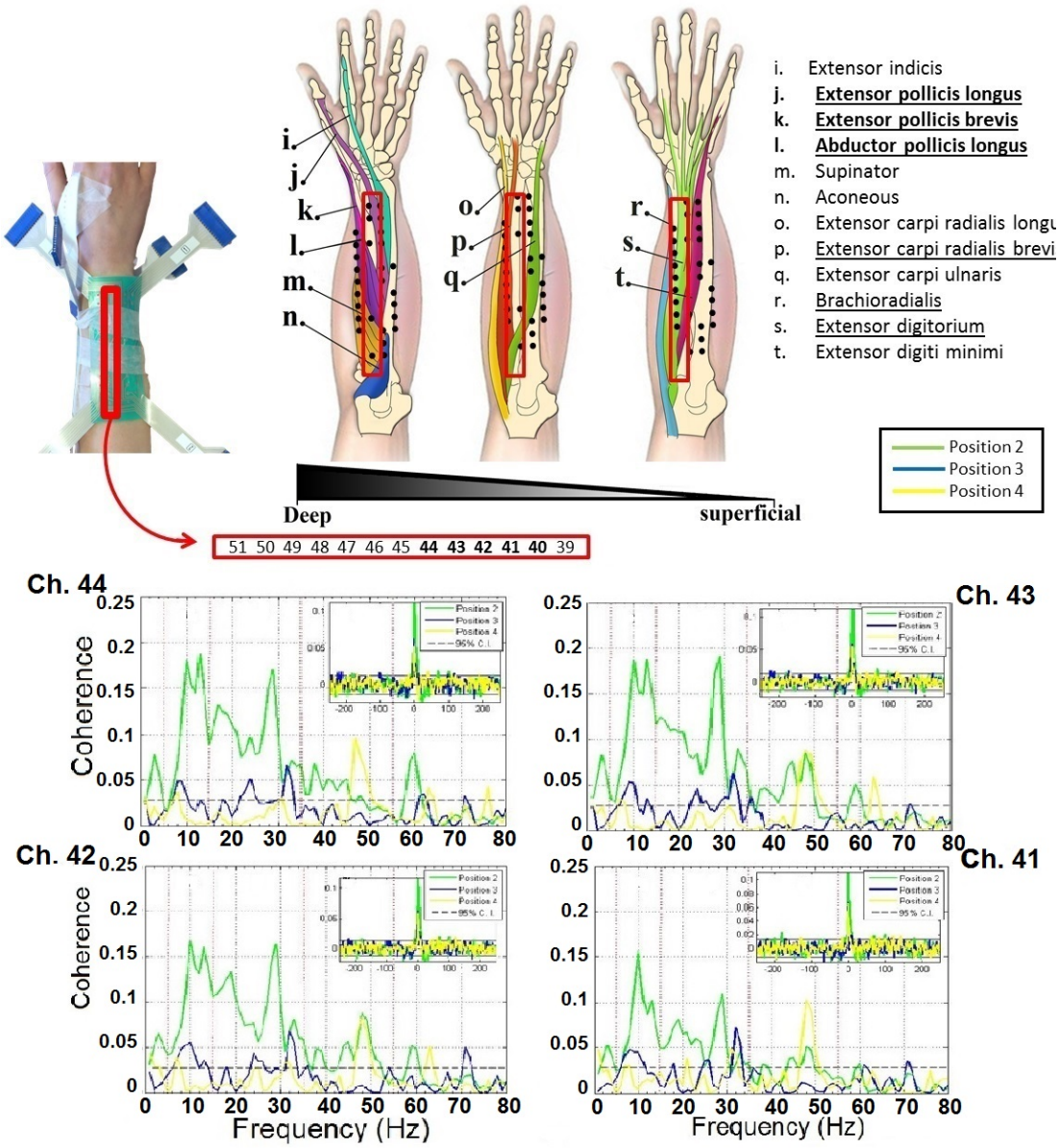

Figure 5.41: Coherence Analysis Results between the FDI Muscle and the Extensor Muscles During Steady Contractions for Different Positions of the Thumb - Resulting coherence found in 4 electrodes placed over of the Extensor muscles: 41, 42, 43 and 44. At the top of this image, the four electrode placement is shown by the red rectangle. Coherence was found for all the electrodes in the 64-electrode array but the ones proximal to the wrist. The extended results of this analysis can be found in Appendix 8.9.1. A lower frequency range of 2-18Hz and a higher of 20-40Hz are shown. At the top right, the muscles represented in the image of the forearm are underlined; muscle names that are in bold, are the ones that have a direct involvement on the movement of the thumb. In most cases, these muscles are found in the deep layer of the forearm.

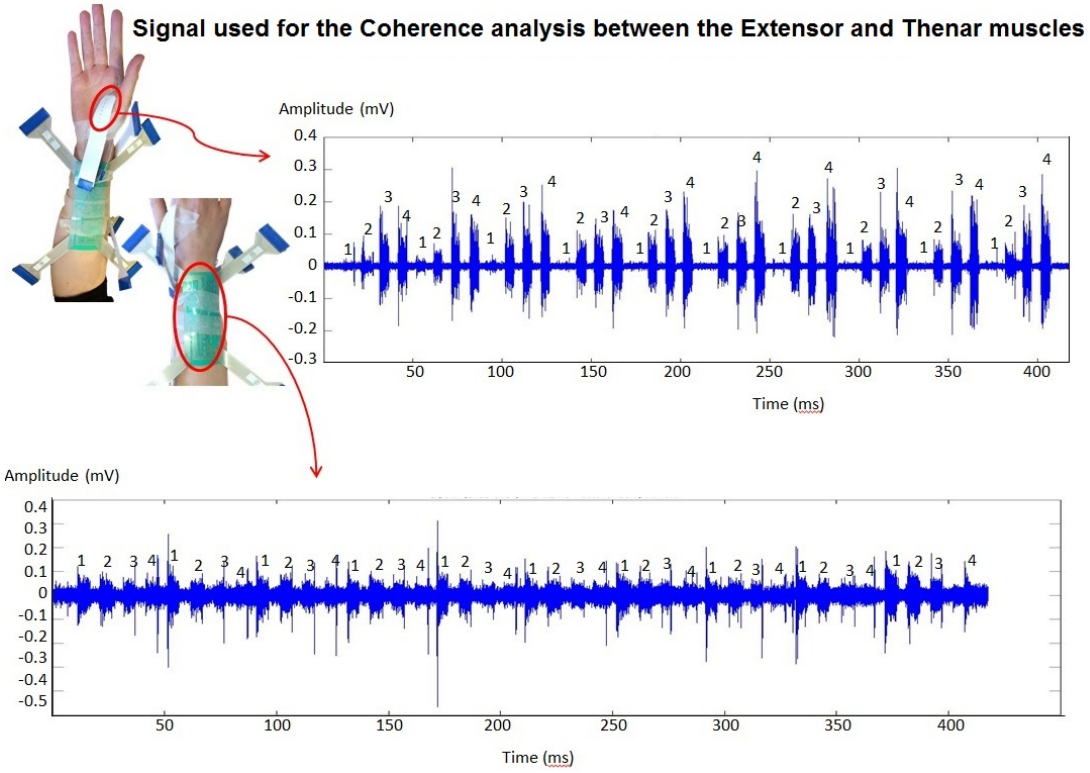

Figure 5.42: Signals used for Coherence Analysis between Thenar and Extensor Muscles During Steady Contractions - Top - Signal acquired during the opposition tasks,from an electrode in an 8-electrode array placed over the thenar muscles. There is a clear lack of significant muscular activity when position 1 is maintained. Bottom - Signal acquired from an electrode of the 64-electrode array placed over the extensor muscles. The numbers in both graphs indicate the position that was opposed for each resulting contraction.

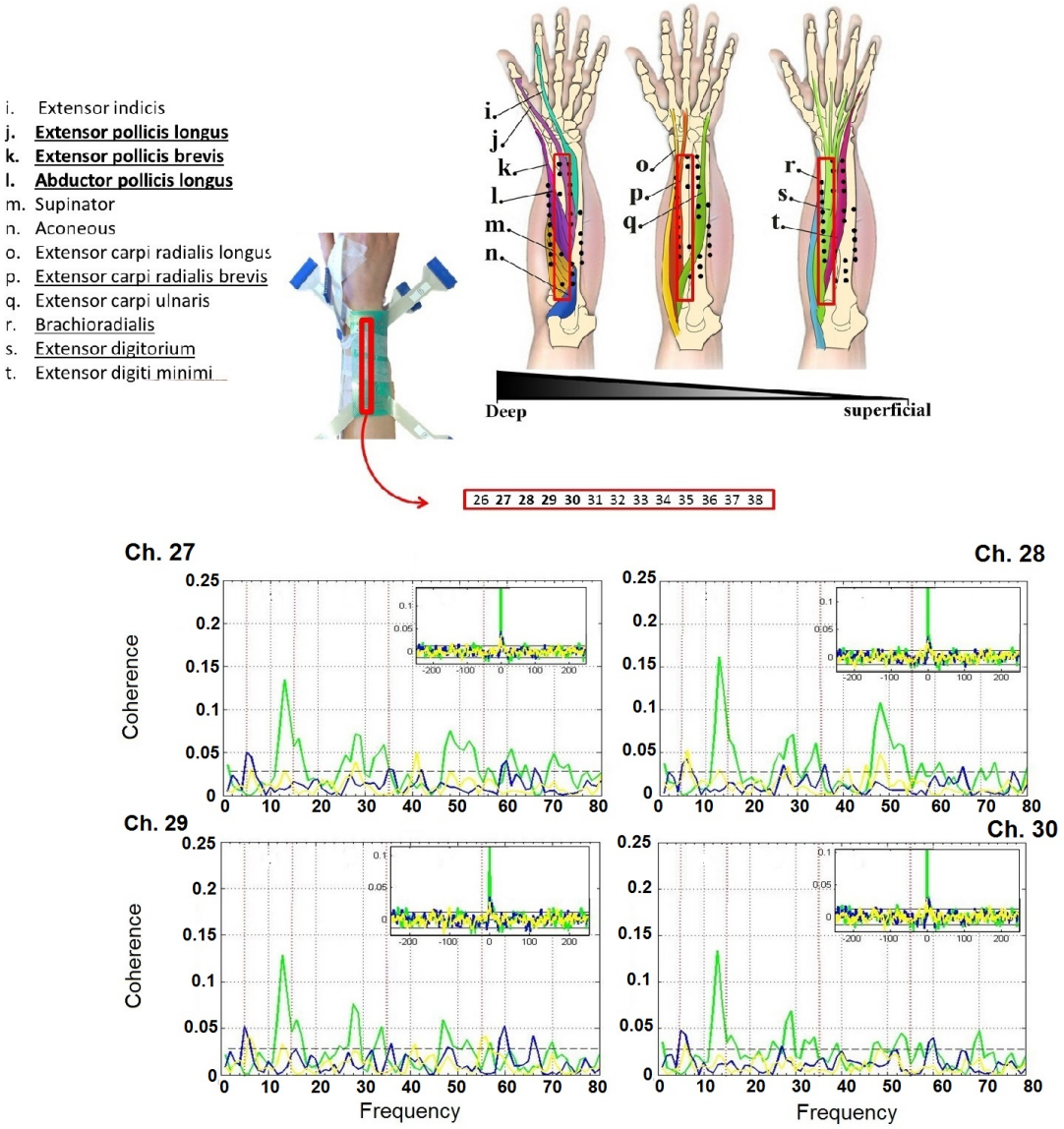

Figure 5.43: Coherence Analysis Results between Thenar and Extensor Muscles During Steady Contractions for the Different Positions of the Thumb - Resulting coherence found in 4 electrodes placed on top of the Extensor muscles: 27, 28, 29 and 30. At the top of this image, the location of these electrodes is shown by the red rectangle, furthermore, the coherence found for all the electrodes in the 64-electrode array are shown in Appendix 8.9.2. For this coherence analysis, three frequency ranges can be seen, particularly for position 3, the lower frequency range is found between 10-20Hz, the middle range from 25-35Hz and the higher frequency range between 45-55Hz. The greatest amplitude is found during the lower frequency range. At the top right, the muscles represented in the image of the forearm are underlined; muscle names that are in bold, are the ones that have a direct involvement on the movement of the thumb. In most cases, these muscles are found in the deep layer of the forearm.

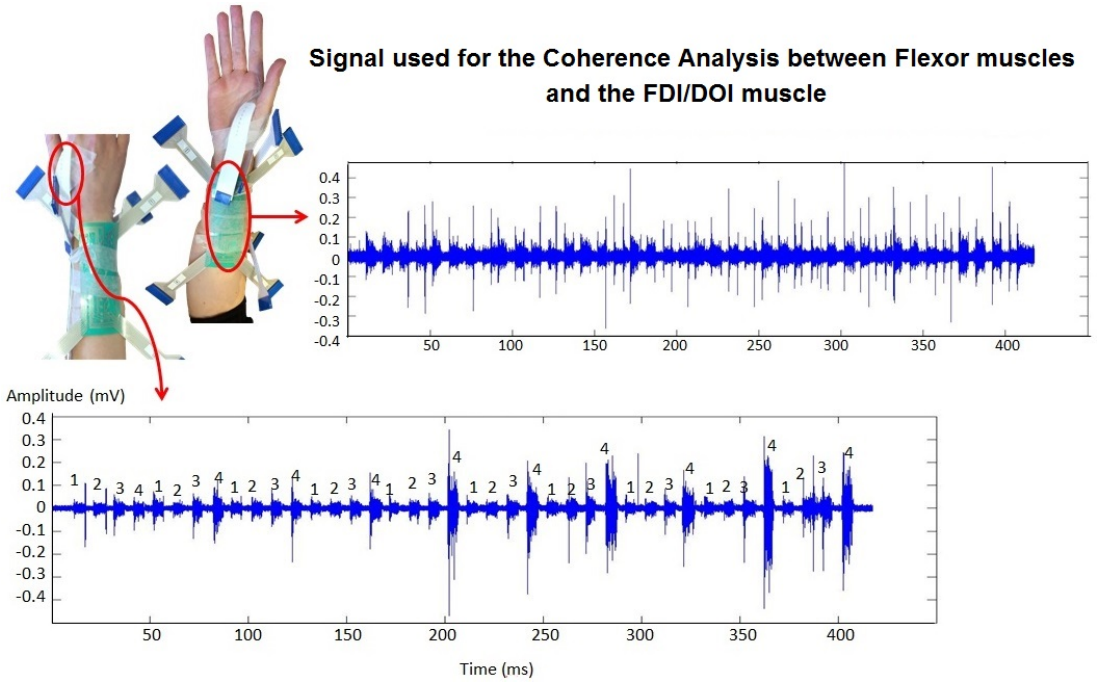

Figure 5.44: Signals used for Coherence Analysis between the FDI Muscle and the Flexor Muscles During Steady Contractions - Top - Signal acquired during the opposition tasks, from an electrode from an 8-electrode array placed over the FDI muscle. Bottom - Signal acquired from an electrode of the 64-electrode array placed over the flexor muscles. The numbers in both graphs indicate the position that was opposed for each resulting contraction.

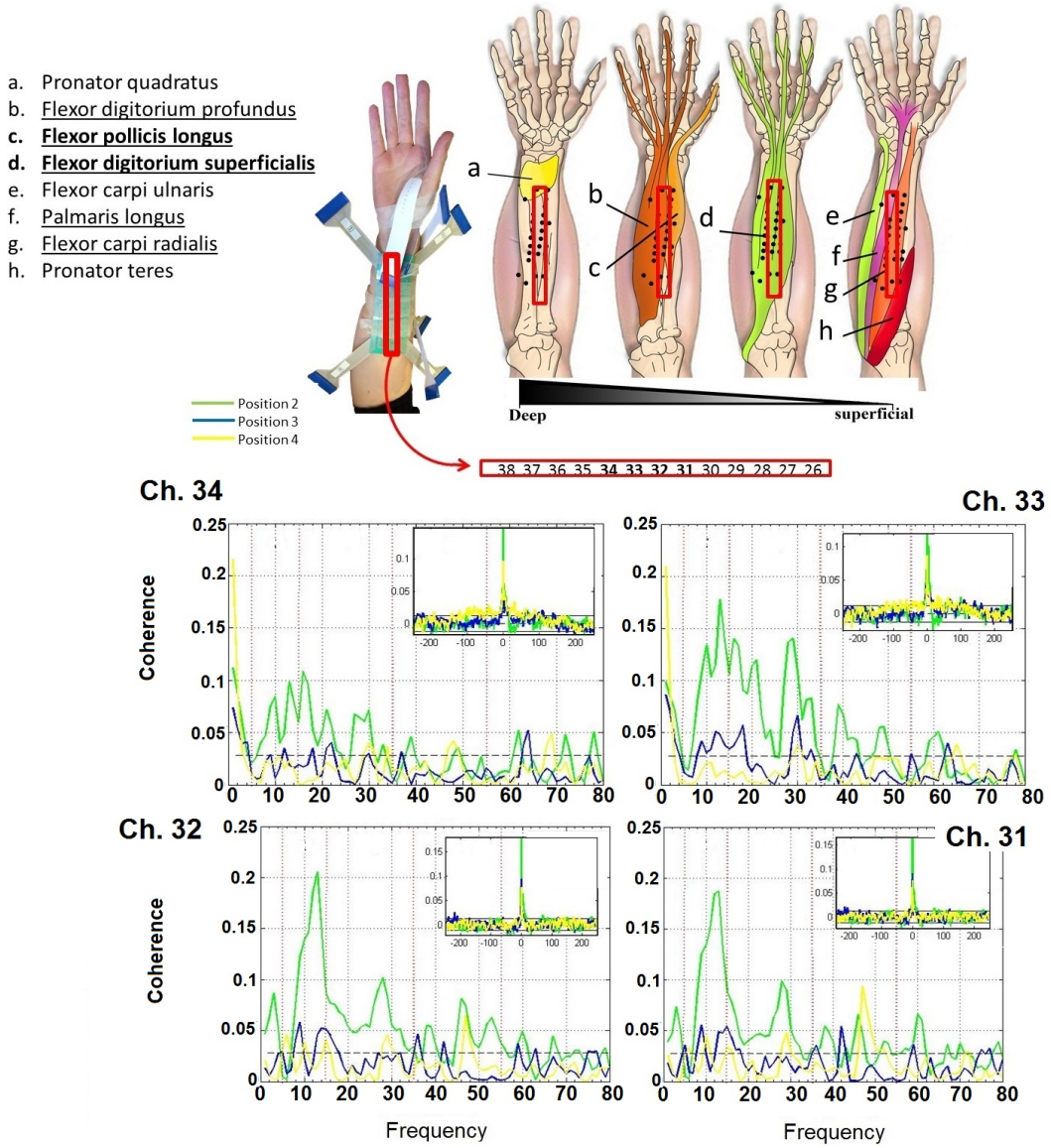

Figure 5.45: Coherence Analysis Results between the FDI Muscle and the Flexor Muscles During Steady Contractions for the Different Positions of the Thumb - Resulting coherence found in 4 electrodes placed over the Flexor muscles: 31, 32, 33 and 34. At the top, the location of these electrodes is shown by the red rectangle; the coherence results for all the electrodes in the 64-electrode array are shown in Appendix 8.9.3. For this coherence analysis, two frequency ranges can be seen, the lower frequency range is found between 5-25Hz, the higher range from 25-45Hz. The difference between position is clearly seen by different amplitude in within the same frequency range. At the top left, the muscles represented in the image of the forearm are underlined; muscle names that are in bold, are the ones that have a direct involvement on the movement of the thumb. In most cases, these muscles are found in the deep layer of the forearm. There is also a large central cumulant peak (bottom) indicating significant EMG-EMG coherence.

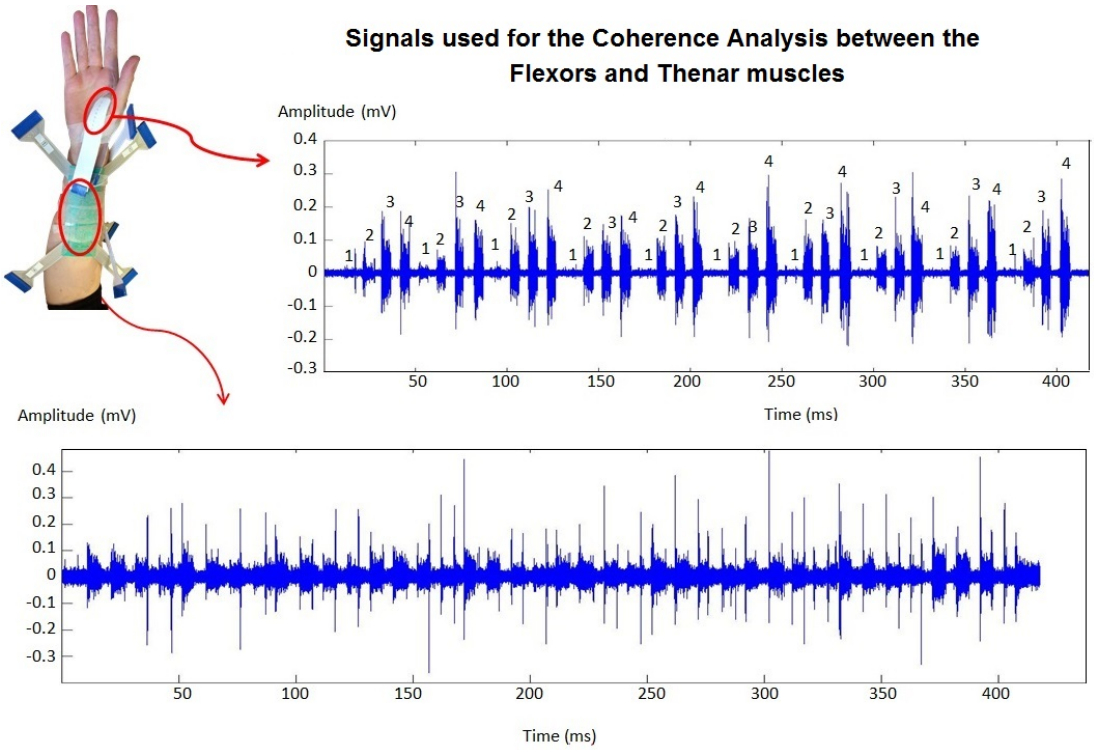

Figure 5.46: Signals used for Coherence Analysis between Thenar and Flexor Muscles During Steady Contractions - Top - Signal acquired during the opposition tasks,from an electrode from an 8-electrode array placed over the thenar muscles. Bottom - Signal acquired from an electrode of the 64-electrode array placed onto the Flexor muscles. The numbers in both graphs indicate the position that was opposed for each resulting contraction.

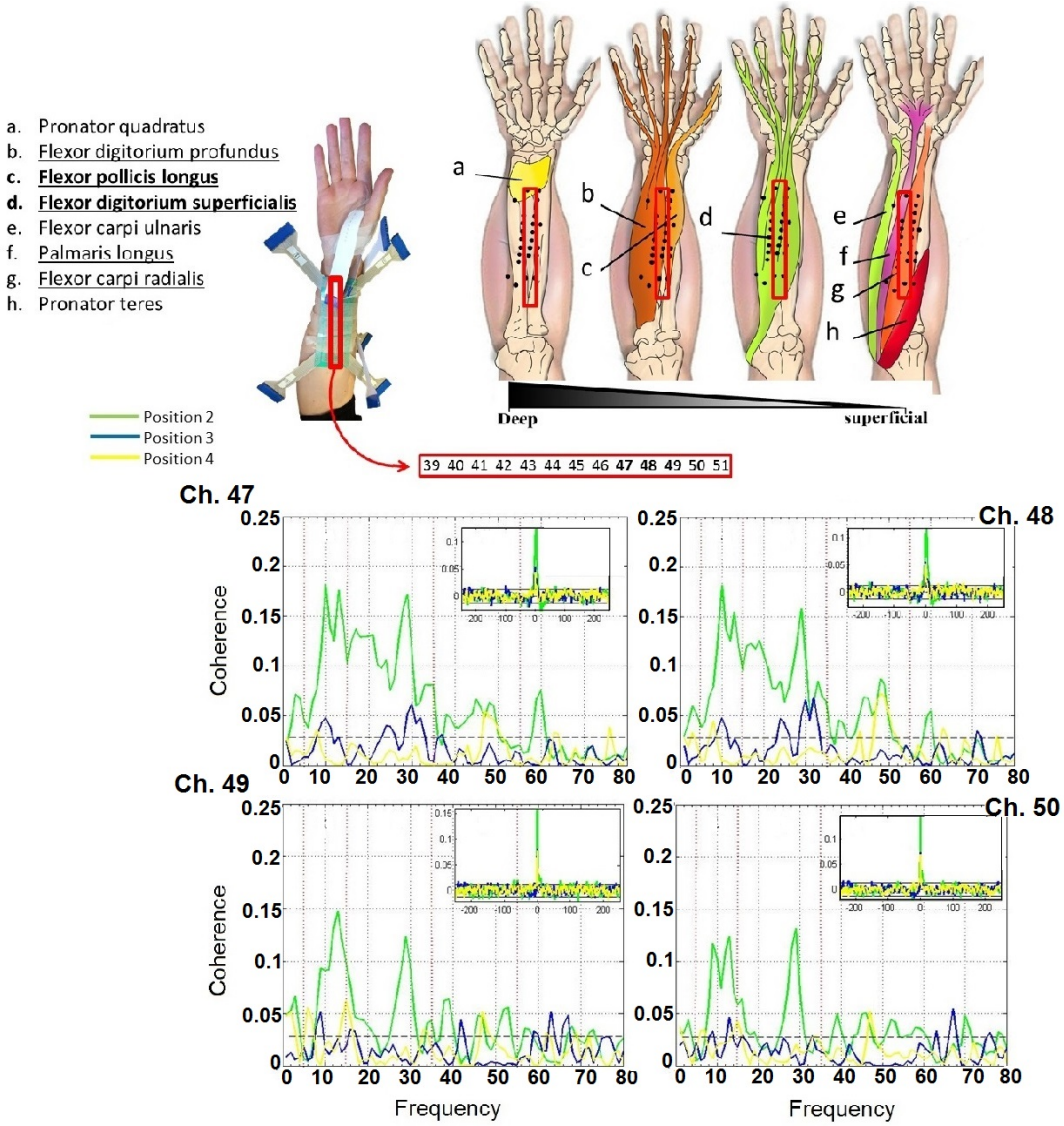

Figure 5.47: Coherence Analysis Results between Thenar and Flexor Muscles During Steady Contractions for the Different Positions of the Thumb - Resulting coherence found in 4 electrodes placed over the Flexor muscles: 47, 48, 49 and 50. At the top, the location of these electrodes is shown by the red rectangle; the coherence results found for all the electrodes in the 64-electrode array are shown in Appendix 8.9.4. For this coherence analysis, the top electrodes depicted in the graphs have a constant frequency range peak for position 2, from 5-35Hz, the 15-25Hz range has a decremental in amplitude in the bottom 2 electrodes shown here. For position 3 and 4, two frequency ranges can be seen, the lower frequency range is found between 5-15Hz, the higher range from 25-35Hz. The difference between position is clearly seen by different amplitude in within the same frequency range. At the top left, the muscles represented in the image of the forearm are underlined; muscle names that are in bold, are the ones that have a direct involvement on the movement of the thumb. In most cases, these muscles are found in the deep layer of the forearm. In most cases, the muscles are found in the deep layer of the forearm. There is also a large central cumulant peak (bottom) indicating significant EMG-EMG coherence.

Table 5.7: Coherence Range Results For All The Participants Across the Different Thumb Oppositions - Steady condition

Position	Muscle Groups	Range [Hz]	Peaks [Hz-magnitude]
1	Thenar-Extensors	cross-talk	cross-talk
	Thenar-Flexors	cross-talk	cross-talk
	FDI - Extensors	cross-talk	cross-talk
	FDI-Flexors	cross-talk	cross-talk
2	Thenar-Extensors	10-18 & 25-35	[12-0.13] & [28-0.07]
	Thenar-Flexors	3-35	[15-0.15]
	FDI - Extensors	5-32	[7,12 & 30 - 0.17]
	FDI-Flexors	5-25	[15-(0.17 ± 0.036)]
3	Thenar-Extensors	4-7	[5-0.05]
	Thenar-Flexors	5-10 & 20-35	[10-0.05] & [30-0.07]
	FDI - Extensors	7-12 & 25.32	[10-0.05] & [32-0.07]
	FDI-Flexors	18-25	[22-0.03] & [30-0.07]
4	Thenar-Extensors	4-7	[5-0.04]
	Thenar-Flexors	5-25	[5,15-0.05]
	FDI - Extensors	5-7	[6-0.02]
	FDI-Flexors	3-15	[5-0.04] & [30-0.04]

5.5 Chapter Conclusion

In this chapter the performance of the volunteers participating in experiments designed to investigate sEMG patterns related to differentiation of thumb opposition to each of the fingers was analysed. The results presented were based on time-domain analysis and joint time and frequency-domain analysis.

Initially, electrophysiological correlation resulting from the experiments and method for investigating the isometric exertion for thumb opposition were presented, according to statistical and coherence analysis results.

6

Machine Learning Results

6.1 Summary

This chapter describes the performance of the volunteers participating in experiments designed to investigate sEMG patterns related to differentiation of thumb opposition to different fingers. The results presented are based on machine learning unsupervised methods later validated through supervised methods.

6.1.1 Self-Organising Feature Maps (SOFM)

As discussed in Section 1.1.5.2, a SOFM consists of a group of neurones (prototypes) organised on a low-dimensional grid. All the neurones are connected to each other by a neighbourhood relation that must be predefined to dictates the topology of the map. The same SOFMs setup was applied across the subjects: hexagonal lattice, rectangular sheet, and randomly initialisation.

The size of the map was obtained using the equations described in Section 1.1.5.2 through the SOM-toolbox. All the subjects had a resulting map size of 15 by 15 neurones. A batch training process was applied through a Gaussian neighbourhood function. Finally, all the subjects were trained using 60% (randomly selected) of the total feature vectors, the remaining 40% was used to validate the clusters made by the first group of data (testing).

A subjective method was used to evaluate the resulting clustering, and therefore, the performance of these algorithms was using visualisations. The initial visualisations are provided in Figure 6.1, from a randomly selected subject. The resulting map

topography and unified distance matrices (U-matrix) are shown for the grids placed on the flexor (Figure 6.1-A.1,2), and extensor (Figure 6.1-B.1,2) muscles. The map topography including the labels from the feature maps organisation is provided in Figure 6.1-A.1 and B.1. In addition, to the right to each map topography (Figure 6.1-A.2 and B.2), the U-matrices are depicted highlighting the boundaries between the clusters (higher values are related to longer distances between clusters) in a 3-D space.

Hit histograms are another valuable visualisation tool which can be used to analyse the clustering relationship between FV. These histograms are based on the gray-scaled U-matrix in 2-D. Hit histograms are markers showing the distribution of the best matching unit for a given FV. In Figure 6.2, these hit histograms are provided and have been separated by thumb opposition (with the same colour coding as the previous cases), and by electrode grid placed on the forearm. This type of visualisation makes it possible to compare different data sets by the distribution of their hits in the topographical map.

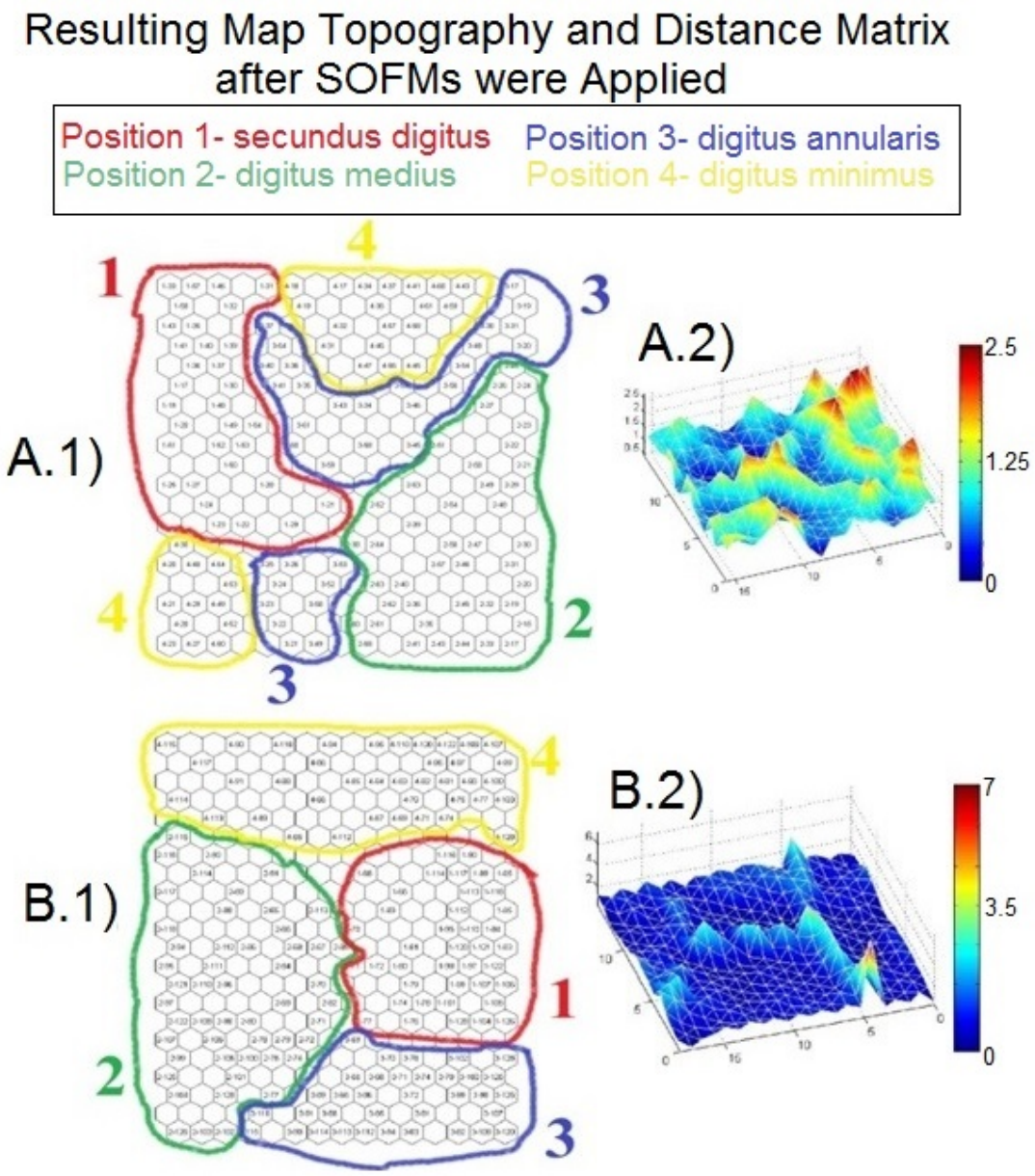

Figure 6.1: Resulting Map Topography and Distance Matrices after Applying SOFMs for Flexor and Extensor Muscles - Resulting visualisations after applying SOFMs. A) Results from the grid positioned on the anterior compartment of the forearm overlying the flexor muscles. A.1) Labelled and colour-circled resulting clusters shown in the map topography. Each colour represents a position of the thumb opposition exertions. It is clear that the 4th position (opposition to the digiti minimi) has a wider spread of amplitudes throughout the map, therefore, two regions can be appreciated. A.2) The U-matrix highlights in a 3-D space the boundaries between clusters where a higher amplitude relates to a longer distance between neurones. B) Results from the grid positioned on the posterior compartment of the forearm overlying the extensor muscles. B.1) Labelled and colour-circled resulting clusters shown in the map topography. Each colour represents a position of the thumb opposition exertions. For this case, all the clusters seem equally distributed throughout the map. B.2) The U-matrix highlights in a 3-D space the boundaries between clusters where a higher amplitude relates to a longer distance between neurones. This U-matrix has softer relations in intra-cluster and very defined boundaries inter-clusters.

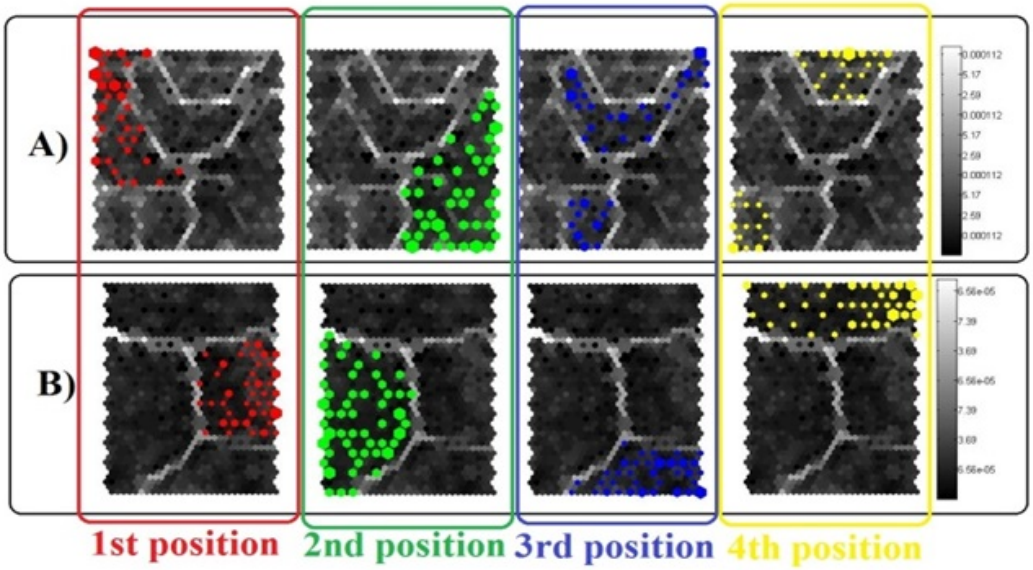

Figure 6.2: Resulting Hit Histograms Visualised in the U-Matrix - SOFM - Resulting hit histograms for each grid positioned on the different muscle groups of the forearm: A) extensors, B) flexors. Each hit was produced by the best matching unit found for each feature vector trained. Each unified matrix (gray scale colour map) corresponds to each position of the thumb colour coded for each muscle group. 1st position refers to the opposition of the thumb to the secundus digitus, 2nd position to the opposition to the digitus medius, 3rd position to the digitus annularis, 4th position to the digitus minimi.

One method used to verify the SOFMs accuracy, was by assessing different quality measures or error measures. The two most commonly used error measures for this algorithm are the quantisation error and the topographical error. The quantisation error, is the mean of the distance from each data vector to its best-matching unit (BMU), while the topographical error gives the percentage of FVs for which the BMU and the second BMU are not neighbouring map units. In other words, the topographical error measures the segment of FVs for which the two nearest map units are not neighbours in the array topology. As expected, if the number of neurones in the map increases (map units), the quantisation error decreases and the topographical error increases. A third measurement can be extracted from the previous errors. This measurement was proposed by Kaski and Lagus (1996) (224), and is known as the combined error. This error is computed by the sum of the aforementioned errors along with the shortest path following the neighbourhood relations. In Table 6.1 these errors are provided across subjects for the grids positioned in the forearm. The errors are measured in a scale from 0-100%, where 100 means maximum possible error.

Table 6.1: Quantisation, Topographical and Combined Errors After Training of SOFMs

Subject (Muscle Group)	Quantisation Error (%)	Topographical Error (%)	Combined Error (%)
S1 (Flexors)	1.04	<0.01	1.35
(Extensors)	1.08	0.04	1.68
S2 (Flexors)	0.67	0.09	1.12
(Extensors)	0.65	0.02	1.12
S3 (Flexors)	0.93	0.05	1.30
(Extensors)	0.79	0.02	1.37
S4 (Flexors)	0.70	0.10	1.06
(Extensors)	0.73	0.01	1.20
S5 (Flexors)	1.02	0.05	1.24
(Extensors)	0.78	0.05	1.05
S6 (Flexors)	0.88	0.03	1.15
(Extensors)	0.87	0.07	1.17
S7 (Flexors)	0.57	0.04	0.88
(Extensors)	0.62	0.02	1.02

Once the maps were trained, the 40% of remaining data were tested as a mean of validation. The validation was performed using hit histograms comparing the results of the un-presented datasets to the already trained U-matrix. The resulting performance measures can be found in Tables 8.11 and 8.12 for the forearm flexor and extensor muscles for each thumb position, respectively.

Table 6.2: Performance Measures for SOFM Test data - Forearm Flexor Muscles

BMU \ FV	1st Position	2nd Position	3rd Position	4th Position
1st Position	87%	4%	5%	4%
2nd Position	7%	83%	3%	7%
3rd Position	0%	8%	86%	6%
4th Position	6%	5%	6%	83%

Table 6.3: Performance Measures for SOFM Test data - Forearm Extensor Muscles

BMU \ FV	1st Position	2nd Position	3rd Position	4th Position
1st Position	91%	6%	0%	3%
2nd Position	5%	82%	6%	7%
3rd Position	3%	5%	88%	4%
4th Position	1%	7%	6%	86%

The remaining of the results for the rest of the subjects are found in Appendix 8.10.

6.1.2 Principal Component Analysis (PCA)

Another useful method to inspect the distribution of the FVs in space was performed using Principal Component Analysis (PCA). PCA was performed over the already trained maps created by SOFMs in order to visualise the clustering arrays in a new space (a.k.a. PC space). Illustrated in Figure 6.3 and 6.4 the resulting PC conversion is provided for the same random subject as in the previous results for the forearm flexor and extensor muscles per thumb position. For the forearm flexor muscles, four very well defined 'clouds' can be identified. These highlight how tight the clusters are, and how big the cluster boundary is. For the latter, although the datasets are noticeable to be in a wider spread, the clusters are consistent and clear boundaries are found amongst different thumb positions. The vector projection algorithms like PCA, find low-dimensional coordinates for a set of high-dimensional FVs preserve the clustering as well as possible. The results for the remaining participants are given in Appendix 8.10.

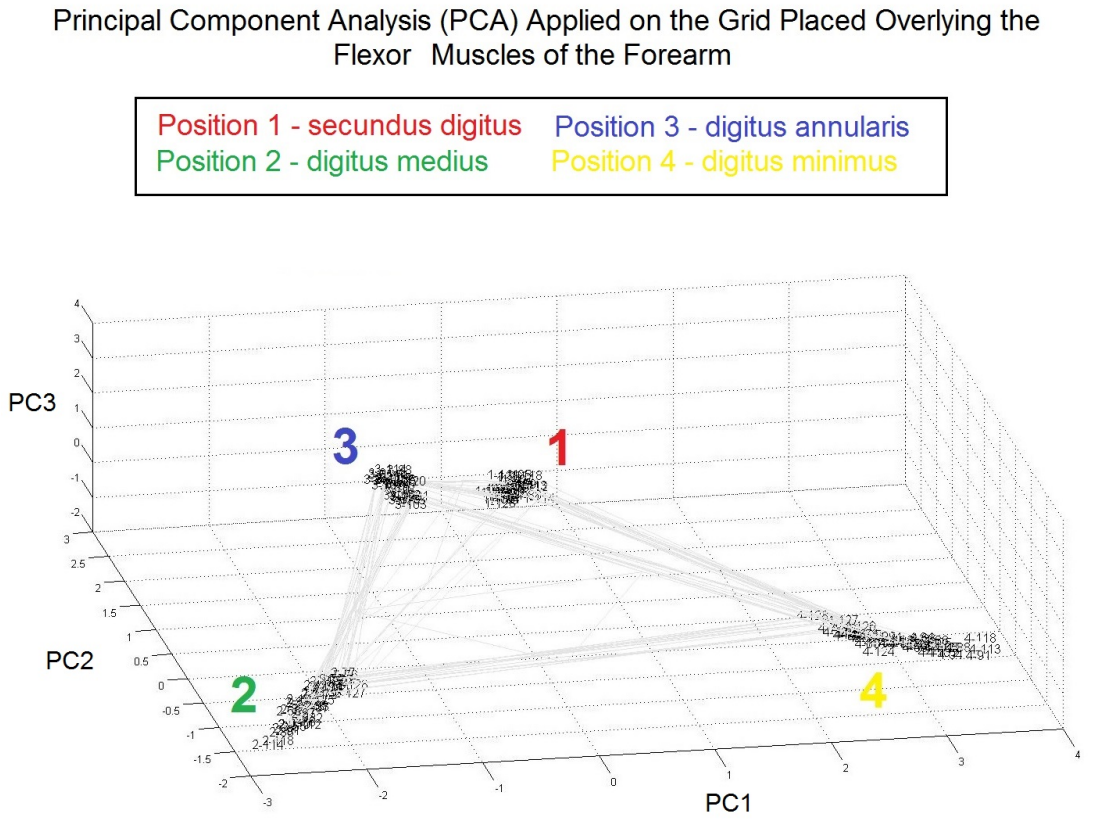

Figure 6.3: Principal Component Analysis of the Feature Vectors after Data were Trained applying SOFM - Forearm Flexor Muscles - PCA of the feature vectors after SOFMs were applied to the trained data for a randomly chosen subject. As depicted, each colour represents each position that the thumb was opposed to. The resulting PC conversion shows tight clusters. This clustering also reflects the wide distance between neighbourhoods.

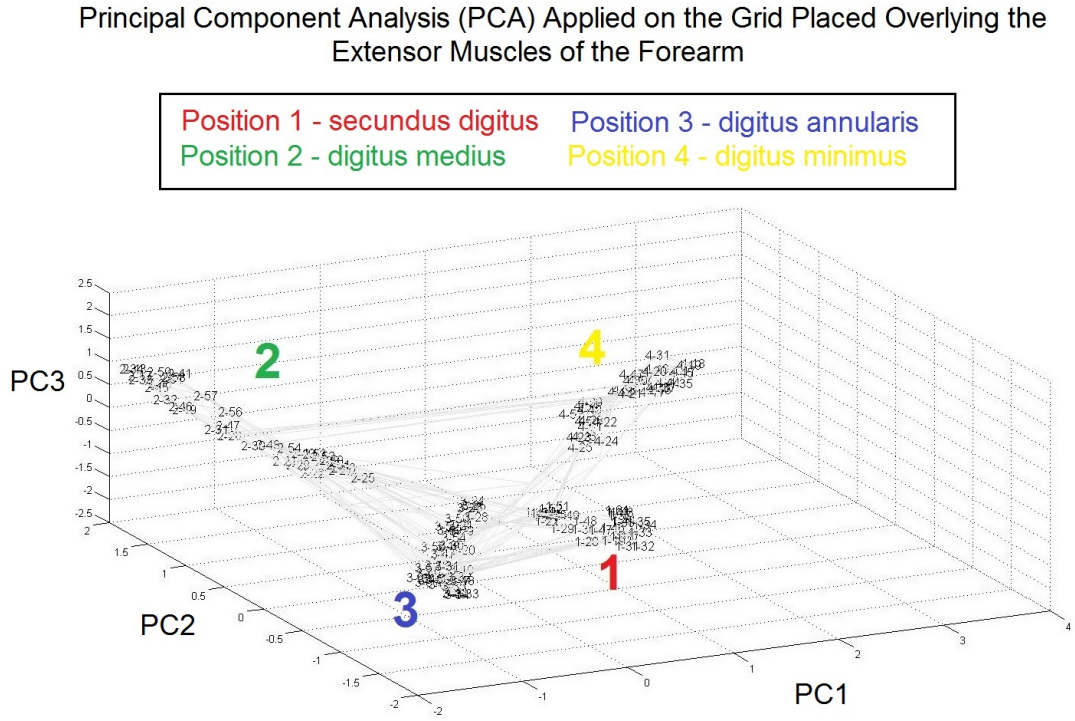

Figure 6.4: Principal Component Analysis of the Feature Vectors after Data were Trained applying SOFM - Forearm Extensor Muscles - PCA of the feature vectors after SOFMs were applied to the trained data for a randomly chosen subject. As depicted, each colour represents each position that the thumb was opposed to. The resulting PC conversion shows a wide spread within each cluster, nevertheless, the boundaries between clusters are still well preserved.

6.1.3 Supervised Machine Learning as SOFMs Validation

For further data validation, supervised training was applied using Matlab's Pattern Recognition toolbox. The sEMG data inputs were provided with labels so the the program could recognise which cluster each of the presented FVs belonged to. The parameter distribution for all subjects was i) training: 30%; ii) validation: 35%; and iii) testing: 35%. The neural network performance was assessed through the values from cross-entropy, the percentage error and the confusion matrices.

Cross-entropy is defined as the loss function in machine learning, therefore, lower values mean a good result in classification. In Figure 6.5, the cross-entropy and the resulting performances are shown for each grid placed on the forearm flexor (anterior) and extensor (posterior) muscles. For the forearm flexor muscles, the best validation performance was achieved at 111 epochs with a cross-entropy value of 0.002. For the forearm extensor muscles, the best performance was achieved faster, at epoch 84 with a cross-entropy value of 0.101. For both muscle groups, the cross-entropy values are close to zero, therefore, these results yield a good classification.

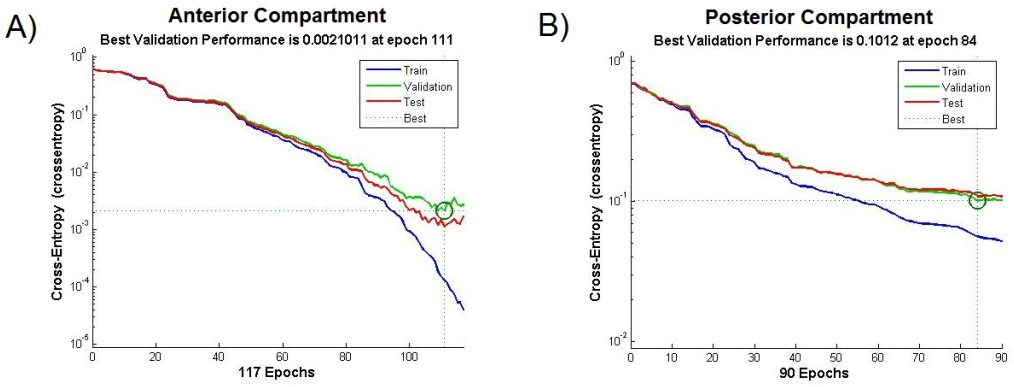

Figure 6.5: Best Validation Performance found for Flexor and Extensor Muscles - Best validation performance found after the unsupervised Levenberg-Marquardt validation applied with Matlab's feature pattern recognition toolbox. A) Resulting performance from the flexor muscles of the forearm for randomly chosen subject (consistent with the previous results), and during a typical test. The best validation performance is found at epoch 111 with a cross-entropy of 0.0020. B) Resulting performance from the extensor muscles of the forearm for typical subject (consistent with the previous results), and during a typical test. The best validation performance is found at epoch 84 with a cross-entropy of 0.1012.

The percentage error indicates the fraction of samples which are misclassified between 0 and a maximum of 100.

As a summary of the performance measures obtained previously, in Table 6.4 and 6.5, the resulting cross-entropy and percentage error across the parameter distribution (training, validation, and testing) and the FVs in each distribution, are shown for the forearm flexor and extensor muscles, respectively.

Table 6.4: Parameter Distribution and Resulting Cross-Entropy and Percentage Error from Supervised Levenberg-Marquardt Validation (Matlab Routine) - Flexor Muscles

Subject	Stage	Feature Vector	Cross-Entropy	Percent Error
1	Training	1476	6.23	<0.01
	Validation	1722	5.82	0.05
	Testing	1722	58197	0.11
2	Training	1656	9.27	<0.01
	Validation	1932	86217	<0.01
	Testing	1932	8.62	0.05
3	Training	1908	1.90	17.24
	Validation	2226	1.8104	19
	Testing	2226	1.80	16.03
4	Training	1908	5.67	<0.01
	Validation	2226	5.29	0.22
	Testing	2226	5.26	0.17
5	Training	2052	5.40	0.34
	Validation	2394	5.06	1.29
	Testing	2394	5.10	1.37
6	Training	1656	5.72	<0.01
	Validation	1932	5.32	0.05
	Testing	1932	5.33	0.31
7	Training	1260	4.46	17.85
	Validation	1470	4.20	18.02
	Testing	1470	4.19	17.89

Table 6.5: Parameter Distribution and Resulting Cross-Entropy and Percentage Error from Supervised Levenberg-Marquardt Validation (Matlab Routine) - Extensor Muscles

Subject	Stage	Samples	Cross-Entropy	Percent Error
1	Training	1368	2.85	0.21
	Validation	1596	2.70	3.94
	Testing	1596	2.71	6.20
2	Training	1368	2.85	0.21
	Validation	1596	2.70	3.94
	Testing	1596	2.71	6.20
3	Training	1728	3.29	2.08
	Validation	2016	3.10	4.31
	Testing	2016	3.12	5.20
4	Training	1620	4.68	0.06
	Validation	1890	4.36	0.74
	Testing	1890	4.36	1.26
5	Training	1260	4.23	<0.01
	Validation	1470	3.94	0.06
	Testing	1470	3.93	<0.01
6	Training	1728	5.05	<0.01
	Validation	2016	4.70	0.44
	Testing	2016	4.70	0.24
7	Training	1584	4.21	6.88
	Validation	1848	3.93	9.36
	Testing	1848	3.94	7.94

The performance measures results for the remaining participants are given in Appendix 8.11.

The performance of these type of systems is commonly evaluated using confusion matrices. A confusion matrix contains the information about the real and predicted classifications performed by the neural network algorithm, in Figure 6.6 an example of a 2x2 confusion matrix for two samples is depicted.

Confusion Matrix		Target			
		Positive	Negative		
Model	Positive	a	b	*Positive Predictive Value*	a/(a+b)
	Negative	c	d	*Negative Predictive Value*	d/(c+d)
		Sensitivity	*Specificity*	**Accuracy** = (a+d)/(a+b+c+d)	
		a/(a+c)	d/(b+d)		

Figure 6.6: Example of a Two Classes Confusion Matrix - This table shows a 2 by 2 confusion matrix for two classes (positive and negatives). The accuracy represents the proportion of the total number of correct predictions, the positive predictive value represents the proportion of positive cases that were correctly identified, on the other side, the negative predictive values reflect the negative cases that were correctly identified. As for the sensitivity and specificity, the first value reflects the actual positives which are correctly identified and the latter, the negative cases correctly identified. Adapted from: $http://www.saedsayad.com/model_evaluation_c.htm$

Depicted in Figures 6.7 and 6.8, are the confusion matrices that correspond to the same random subject during a typical test, for each muscle group separately (flexor and extensor muscles, respectively). The entries in the confusion matrices are governed by the different positions that the thumb was opposed to (4 classes); as with the previous performance measures, the data was split into training, validation, testing and an additional matrix summarising all of the previous. More, the correct predictions are shown in green and, they are allocated diagonally. The accuracy is depicted by the blue squares which yields the total of correct predictions as a percentage of the whole data used in each of the different stages of the method (i.e. training).

The confusion matrix for all of the subjects can be found in Appendix 8.11.2.

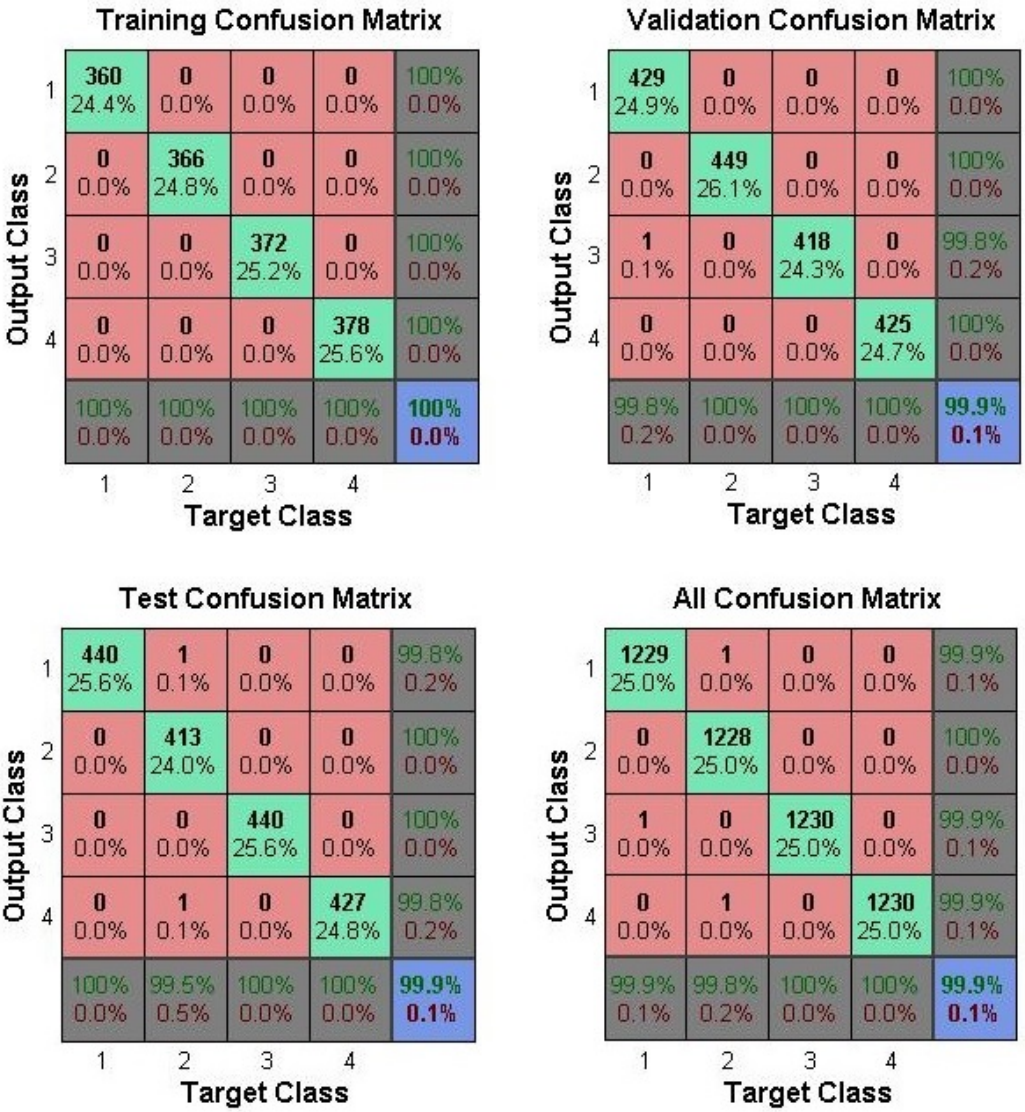

Figure 6.7: Confusion Matrix Results in the Flexor Muscles - S1 - Confusion matrix from the different stages of the supervised machine learning, i.e. training; validation; testing; and the summation of all the previous. The accuracy of the classification is shown for each case. For all but training, the accuracy was 99.9% with a 0.1% of classification error. For the flexor muscles, it is not clear which position is mostly a false classification.

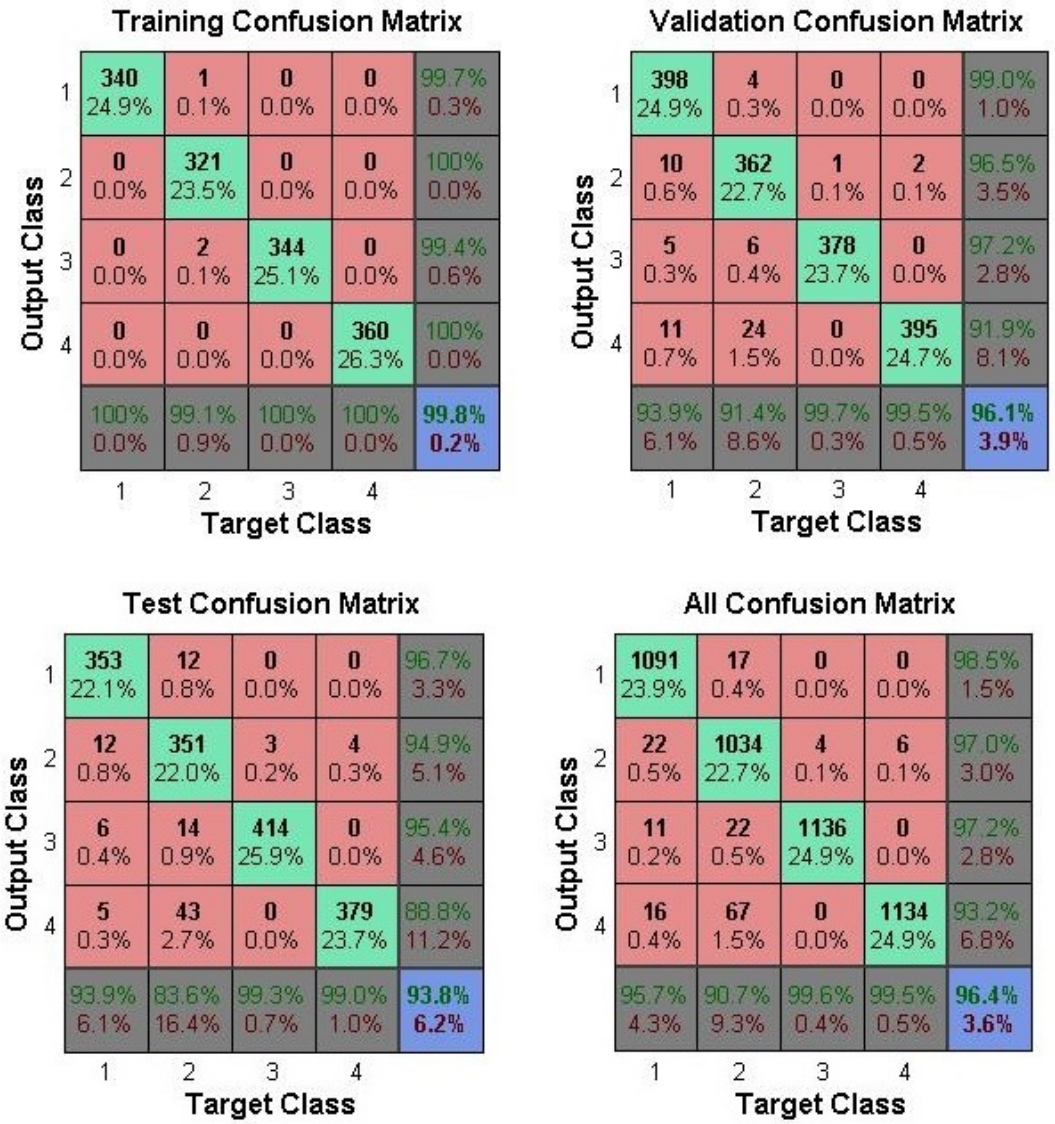

Figure 6.8: Confusion Matrix Results in the Extensor Muscles - S1 - Confusion matrix from the different stages of the supervised machine learning, i.e. training; validation; testing; and the summation of all the previous. The accuracy of the classification is shown for each case. For the training classification, the accuracy was 99.8% with a 0.2% of misclassification; the validation accuracy is 96.1% with the misclassification (3.9%); the test accuracy was the least of all four stages, with a 93.8% accuracy and most misclassification for position 2 (6.2% overall); and finally, the overall results for the extensor muscles of the forearm was 96.4% accuracy with 3.6% of misclassification (with position 2 being the least accurately classified).

6.2 Chapter Conclusion

In this chapter the performance of the volunteers participating in experiments designed to investigate sEMG patterns related to differentiation of thumb opposition to each of the fingers was analysed. The results presented were based on machine learning unsupervised algorithms. The movements were classified using non-supervised machine learning methodologies in the form of self-organising feature maps and principal component analysis. To validate these, supervised machine learning algorithms were applied using Matlab's pattern recognition toolbox. In the next chapter, the results are further discussed, interpreted and compared.

7

Discussion and Conclusions

In this chapter the relevance of results to previous muscle recording studies, interpretation of results, potential impacts and limitations are summarised, reviewed and discussed. The key findings, impact and contributions are described in Section 7.1, the overall findings in the results are underlined in Section 7.2 and then compared to other studies relevant to this research in Section 7.3. In Section 7.4 the considerations and limitations are discussed. Furthermore,the interpretation of results and final discussions are covered in Section 7.5. Finally, in Section 7.6 the future work is highlighted.

7.1 Key Findings, Contributions, and Impact

This section summarises the main contributions of this research to knowledge. To the best of the author's understanding, the following contributions have not been explored nor recorded in the literature. This research has proved:

- A successful differentiation of different thumb opposition tasks, for muscle activation patterns during isometric voluntary contractions performed in time domain using amplitude signal, RMS analyses.
- A statistically significant interpretation of sEMG amplitude changes from forearm muscles whilst different thumb positions.
- A novel insight into motor drive controlling the extrinsic muscles of the hand providing meaningful contrasts through statistical analysis (ANOVA).

- Variations in the spectral composition reflect changes in the muscle synergy with different sEMG coupling with the performance of the different thumb grips.
- The frequency ranges found for the different thumb grip postures studied (3-42Hz) had differences in shape of the local maxima across the different positions exerted.
- A successful classification through unsupervised machine learning algorithms, i.e. self-organising feature maps of the different thumb grips.
- An implementation of the classification methods through a controllable prosthetic thumb for transradial amputees.

7.2 Overview of Results

In this study, the high-density sEMG correlates of isometric contractions during exertion of different thumb oppositions were explored. To my knowledge, this has not been attempted before or results of such experiments published. Common and local time frequency features of HD-sEMG signals across 7 subjects were assessed. Time and frequency domain analysis (see Section 7.2.2) as well as machine learning algorithms (see Section 7.2.3) applied to the HD-sEMG signals demonstrated the feasibility to classify different thumb position based on indirect monitoring of forearm sEMG signals. This has application for control of robotic hand that incorporate an active thumb.

7.2.1 HD-sEMG Data Acquisition

The data acquisition using a multi-channel sEMG provided with enough dimensionality to inspect the spatial muscle activations in the forearm, during grips made with different thumb positions. A challenging problem encountered during the recordings, was that of signal contamination associated with cross-talk, interference, and artefact noise. More, the high-dimensionality made visual assessment during data acquisition and review difficult using standard sEMG graphs (time vs. amplitude), therefore, colour maps had to be created to assist in visualisation of data gathered during experiments.

7.2.2 Time-Frequency Analysis

Preliminary visualisation and RMS analyses suggest significant differences between the muscle activation patterns during isometric voluntary contractions associated with the four thumb postures explored, and thereby provide classifiable information regarding the posture of the opposed thumb position. These mainly reflect differences in the amplitude, and therefore, the synergy and force of the effort exerted (muscles recruited) in holding the different positions despite the actual grip force being equivalent at all thumb positions tested. The interpretation of these sEMG amplitude changes from muscles, with no direct action on the thumb, is that in generating a specific thumb opposition the pattern activation of the forearm musculature also co-varies in a specific way. This variation in activity is statistically significant.

7.2.2.1 Statistical Analysis

One-way ANOVA was performed with repeated measures on task (thumb opposition to secundus digitus; digitus medius; digitus annularis; and digitus minimi). ANOVAs were performed to test whether the muscular contraction varied across positions when visual feedback was provided to regulate the force grip.

ANOVA analysis was also used to identify temporal features characterising the differences between waveforms across conditions. A time window of 300ms was chosen to be able to find statistical differences in within a time-span that is considered to be shorter than the estimated reaction time ($\leq$ 350ms). From the 48 total bins, 5 out of 7 subjects had a maximum of 8 bins statistically insignificant, with at least 2000ms in between insignificant bins. Thus ANOVA can reveal meaningful contrasts across different thumb positions that may not be apparent in visual inspection due to feature size, and potentially providing novel insight into underlying neural mechanisms that control the extrinsic muscles of the hand.

7.2.2.2 EMG-EMG Coherence Analysis

The purpose of this analysis was to use high-density surface EMG to study the changes in the common oscillatory drive whilst the thumb was held in different grip postures. Due to the sensitivity of spectral measures to artefacts, this analysis yielded sensitivity issues related to the presence of ambient noise, artifact noise, interference,

etc. thereby reducing the number of channels and reliable data sets that could be used. In addition, the decrease in EMG-EMG coherence when the electrodes are located over the innervation zone in the FDI muscle were apparent as a decrease amplitude of the sEMG signal at those sites (see Keenan et al. (2012) (225)).

Nevertheless, this analysis demonstrates that pairs of muscles (FDI proximal to the carpals and flexor pollicis longus, and thenar and flexor pollicis longus) during isometric contractions share certain frequency components that are different in magnitude, when different thumb grip positions are performed. The frequency range between the thenar and flexor muscle compartment exertion was (3-12Hz) with different coherence magnitudes occurring for each thumb posture. Coherence was greatest for position 3 (opposition to digitus annularis) with a peak @$4Hz$.

For the coupling between the FDI and flexor muscles, the coherence showed a wider range (3-26Hz) than for the previous case, and greater magnitudes for coherence and cross-intensity analysis. The larger peak was found at 9Hz, and as for higher frequencies, peaks were found at a wider range (20-45Hz) but their amplitude was found to be lower.

As for the steady condition testing (where the subject had no force modulation), peaks were found at 12Hz with no coherence found after 35Hz. This was true for all positions but the first one due to the similarity of the thumb opposition against secundus digitus to the natural hand position at rest.

The experimental evidence suggests that, in addition to differences in EMG amplitude in forearm muscle activity during the thumb grips studied here, there are also changes in the spectral composition of the sEMG signals. These reflecting changes in the muscle synergy with different sEMG coupling being apparent with performance of the different grips. The different synergies appear to be driven by changes in common drive that affect the peak coherence and the features of synchronisation between muscles.

7.2.3 Machine Learning Analysis

Based on the visualisations including map topography, distance matrix, hit histograms in the U-matrix , and PCA projections (all of them produced for every case separately) it became clear that the cluster mechanisms all throughout the subjects

correctly separated the different positions of the thumb. Therefore, it was expected for supervised methodologies to successfully classify the four oppositions of the thumb.

SOFMs have intrinsic properties that make it capable of preserving topological relationships allowing visualisation of complex data (such as the high-dimensionality of the HD-sEMG). The overall performance that SOFMs when the flexor muscles were assessed was 84.75% for all the positions. The best position classified was when the thumb was opposed to the secundus digitus manus (87%) with less classification accuracy for position 2 and 4 (opposition against digitus medius and digitus minimus manus), with an 83% accuracy each. As for the forearm extensor muscles, the overall performance was 86.75% with the position 1 being the most accurate with a 91% of successful classification and the position 4 as the least accurate with 86% accuracy. When compared across subjects, the best classification accuracy rate for the flexor muscles was found to be Subject 7 with a 88.25% accuracy, and Subject 3 for the extensor muscles with an 87.25% accuracy.

The supervised methodologies performed using the Matlab - Pattern Recognition toolbox based on Levenberg Marquardt algorithms yield higher classification rates for both muscle groups. This better performance is due to the a priori knowledge that is provided to the method, i.e. the target classes are provided before training, and therefore, the network has higher rate for success. When compared across subjects, the poorest classification accuracy rate was found to be Subject 7 with a 82.1% success rate for the flexor muscles and a 91.9% for the extensor muscles. This SOFM methodology opens a new paradigm, where it is possible to extract information regarding the movement of the hand, specifically thumb rotation, but a higher level of processing is required in the commercially available below-elbow prosthesis for this process to be immediate.

7.3 Comparison to others

7.3.1 Comparison in EMG-EMG Analysis

With regards to EMG-EMG coherence analysis, its primary use has been in the study of motor drive in healthy subjects and patient groups(i.e. stroke, affected pathways, congenital motor movements, and tremor). These analyses commonly report a

clear coherence ranges occurring at (1-12)Hz and (16-32)Hz with a local maxima of approximately 20Hz [(226) and (198)]. The results here are consistent with the frequency ranges discovered by others. What is new is the change in peak coherence associated with change grip postures.

A study by Farmer et al. (202) examined the EMG-EMG coherence between long and short abductor muscles of the thumb across different subjects varying the age [based on a similar to a study by Gibbs et al. (227)]. These studies showed clear coherence in the frequency range of (16-32)Hz with a local maxima at 20Hz for young populations (4-11 years old) and a range of (5-35)Hz with a local maxima at 10 and 20Hz for adult and late-young populations (22-59 and 12-14 years old, respectively).

In this study, and to the best of the author's knowledge, no study prior to this one, has assessed whether different positions of the thumb yield differences in EMG-EMG coherence or cross-intensity. The frequency ranges found for all the variables was (3-42Hz) with a difference in shape of the local maxima across the different positions exerted. Furthermore, there was a clear difference with regards to the magnitude of the coherence between the flexor and extensor muscles. To understand the processes involved a more extensive investigation will be needed. Nevertheless, the results highlight that with changes in thumb position, there are marked changes in the EMG of the forearm muscles despite these muscles having no action on the thumb itself.

7.3.2 Comparison in Machine Learning

Although simultaneous proportional control has been used as a preferred technique for controlling the motors in prostheses devices, these controllers only produce very defined prosthetic range of motions, none of them articulating the thumb. The machine learning algorithms applied are in a vast majority through supervised algorithms in contrast to the one proposed in this research.

Sebelius et al. (2006) (228), tested on 2 patients, a single degree of freedom of the thumb (as well as other movements of the hand) using an in-house algorithm having a 90% accuracy. They used the support of virtual feature classification through a computer-animated phantom hand.

Nielsen et al. (2009) (229), used time-domain (TD) algorithms to extract four features to control a multi-degree of freedom prosthesis, then training a multilayer perception neural network for myoelectric control task. The movements analysed were: wrist

flexion/extension, ulnar/radial deviation and supination/pronation. The performance across movements was 81.1 ± 5.3%

Nielsen et al. (2010) (230) trained an ANN for force estimation for bilateral mirrored contractions for myoelectric prosthesis. Nielsen accuracy was 90 ± 2% for able-bodied subjects and 72% for patients with congenital malformations.

Ziai and Menon (2011) (231) applied support vector machines (SVM), ANN and locally weighted projection regression (LWPR) to study the muscle synergies while torque was applied without finger movement. Although an initial accuracy of 97% for SVM, 96% for ANN, and 87% for LWPR, all models were considered to be sensitive to passage of time and electrode displacement (final accuracy was 63% - SVM; 61% ANN; and 67% LWPR).

Silva and Farina (2012) (232), applied simultaneous and proportional estimation through eight MLPs during mirrored movements with an accuracy in estimation of 79-88% for four DOF (flexion/extension of wrist, radial/ulnar deviation, pronation/supination and opening/closing the hand) in fully able-bodied subjects.

Pulliam et al. (2011) (233) applied time-delayed artificial neural networks (TDANNs) decoding movement trajectories of seven distal degrees of freedom (pronation-supination, wrist ulnar-radial deviation, wrist flexion-extension, thumb rotation, thumb abduction-adduction, finger MCP flexion-extension, and finger PIP flexion-extension). Different accuracy was found for the different movements, the best performance was that of wrist flexion and deviation with approximately 75% and the worst performance was that of pronation/supination with an accuracy of 65% approximately.

In contrast with all the previous and to the best of the author's knowledge, no other study prior to this one has analysed the different positions of the thumb while exerting rotation reaching different positions. Furthermore, unsupervised algorithms were used which reduce the training times and become adaptable to each case of study. The performance accuracy for all the position across all the subjects was (88.25-91.25)±(0.5-2.5)%. This is acceptable for use in device control but would still likely see user errors in grip formation. Ways to improve accuracy still need to be defined and a control system that is robust and reliable require to be implemented. This would be the focus of future work. Moreover, the accuracy for successfully classify each position across all the subjects was: position 1: 90.83 ± 1.6%; position 2: 89.50 ± 1.8%; position 3:

90.17 ± 2.1%; and position 4: 88.83 ± 2.6%. On table 7.1 a comparison between the previous methodologies, recording methods, features and accuracy rate are depicted.

Study	Features	Algorithm	Accuracy Rate
Sebelius et al. (2006)(228)	hand movements and one DOF of the thumb	In-house developed	90%
Nielsen et al. (2009)(229)	wrist flexion/extension, ulnar/radial deviation and supination/pronation	Time-domain and MLPNN	81.1 ± 5.3%
Nielsen et al. (2010)(230)	bilateral mirrored contractions	ANN analysis	90 ± 2%
Ziai and Menon (2011) (231)	torque without finger movement	SVM, ANN and LWPR	initial: 97% (SVM), 96% (ANN), and 87% (LWPR) final: 63% (SVM), 61%(ANN), and 67% (LWPR)
Silva and Farina (2012) (232)	flexion/extension of wrist, radial/ulnar deviation, pronation/supination, and opening/closing the hand	MLPs	79-88%
Pulliam et al. (2011) (233)	pronation-supination, wrist ulnar-radial deviation, wrist flexion-extension, thumb rotation, thumb abduction-adduction, finger flexion-extension	TDANNs	75% and 65%
This study	**Thumb opposition SOFMs against the 4 digits**		**position 1: 90.83±1.6%, position 2: 89.50±1.8%; position 3: 90.17±2.1%; and position 4: 88.83±2.6%.**

Table 7.1: Comparison of Classification Accuracy for Upper Limb Prostheses between the Literature and the Present Study

7.4 Considerations and Limitations of Study

7.4.1 Source and Nature of Observed Electromyographic Activity

While HD-sEMG provides greater spatial resolution than low density sEMG, it is still a technology that needs to be further developed for ease of use. The electromyographic data acquired with this high-end technology was found at times to be unusable and difficult to acquire due to sensitivity of the electrodes, to displacement and noise. Furthermore, several algorithms had to be developed to be able to assess the signals correctly. The appropriate signal acquisition was found to be very time consuming and it is recommended to use these type of equipments in a dedicated environment where all the electrical/electronic sources are controlled and shielded from mains sources.

7.5 Interpretation of Results

7.5.1 Relevance to Research Hypotheses

Until now, neural control mechanisms are lacking in the upper limb prosthetic development. This lag is due to the complex anatomy of the human hand. When an amputation happens, a great amount of muscles are lost and therefore, information regarding how the fingers move starts to be missing depending on the level of amputation.

As it was explained throughout this research, the thumb is the most important finger in the hand. Without thumb-rotating mechanisms, functional tasks are challenging for any amputee to control their device. Moreover, common to all commercially available prosthetic developers, is the lack of mechanisms to drive the thumb from the muscle patterns from the forearm, making it challenging for any amputee to control their device in a dexterous way.

Further to aim improving the control mechanisms for transradial amputees, the difference reflecting different muscle patterns while different thumb positions found can also be applied for partial hand amputations. In many ways, this seems to be a straight forward implementation since most of the muscles of the hand are preserved, therefore, a more accurate classification could be extracted from a combination between intrinsic and extrinsic hand muscles providing a dexterous control in the device.

Although this research was performed using specific electrode grids, these would not be applied to amputees. Instead, by assessing full able bodied subjects, muscular pattern maps can be extracted highlighting the areas of localised activity in relation to specific thumb movements and therefore, accurate location corresponding to specific thumb positions can be extracted. The extraction of this information may also have impact in the surgical procedure, where specific muscle groups would be likely to be preserved while an amputation takes place.

Even though amputees would be most benefited from this research, it is not limited to. Affections from syndromes such as Apert Syndrome, where the patients suffer from malformations in the thumbs, amongst others, could also be benefited by applying the different mechanisms explained throughout aiming for an alternative control of their fingers.

7.6 Future Work

It is clear that new methodologies and new strategies most be taken into consideration in order to improve and better the amputees' involvement using such devices.

The future work suggest to improve the accuracy in the methods and to create a reliable robust controller to implement a thumb opposition natural gesture in the current myoelectric transradial prostheses. Furthermore, this research can be extended towards the classification of movement for each separate finger, and for their own degrees of freedom. To apply them in amputees with the new hypothesis inferring that upper limb prosthetics can be controlled based solely in the remaining muscles' movement contractions.

Furthermore, this research suggests the exploration of the motor drive oscillations as means to modulate the force exertion levels of transradial myoelectric prostheses.

Finally, although this research successfully classifies different thumb opposition movements from muscle propagation patterns extracted from the forearm, the question with regards thumb classification while having movement from the fingers and/or the wrist is still to be explored.

8

Appendices

8.1 Summary

In this chapter all the additional information referred on the previous chapters are shown aiming to provide the reader with a complete insight of the research carried out throughout this study.

8.2 Ethics Consent Form

Consent Form

Title of the study: Electromyography studies of upper limb
Name of department: Biomedical Engineering

- I confirm that I have received information on the purpose of the study, what it involves and had the opportunity to answer any queries to my satisfaction.
- I understand that my participation is voluntary and that I am free to withdraw from the project at any time, without having to give a reason and without any consequences.
- I understand that I can withdraw my data from the study at any time.
- I understand that any information recorded in the investigation will remain confidential and no information that identifies me will be made publicly available.
- I consent to being a participant in the project

In agreeing to participate in this investigation I am aware that I may be entitled to compensation for accidental bodily injury, including death or disease, arising out of the investigation without the need to prove fault. However, such compensation is subject to acceptance of the Conditions of Compensation, a copy of which is available on request.

Yes/ No]

(PRINT NAME)	Hereby agree to take part in the above project
Signature of Participant:	Date

8.3 Force Sensor Resistors

The designed test-apparatus had some variations from its conception to its final design. Initially, four-force sensors resistors (FSRs) were used and attached onto the rig (Fig. 8.1). This type of resistor was used with a simple circuit to guarantee the correct output range for the HD-sEMG's auxiliary input, i.e. ±5V. More, the output signal of the FSRs was used to time-stamp the sEMG signals being acquired.

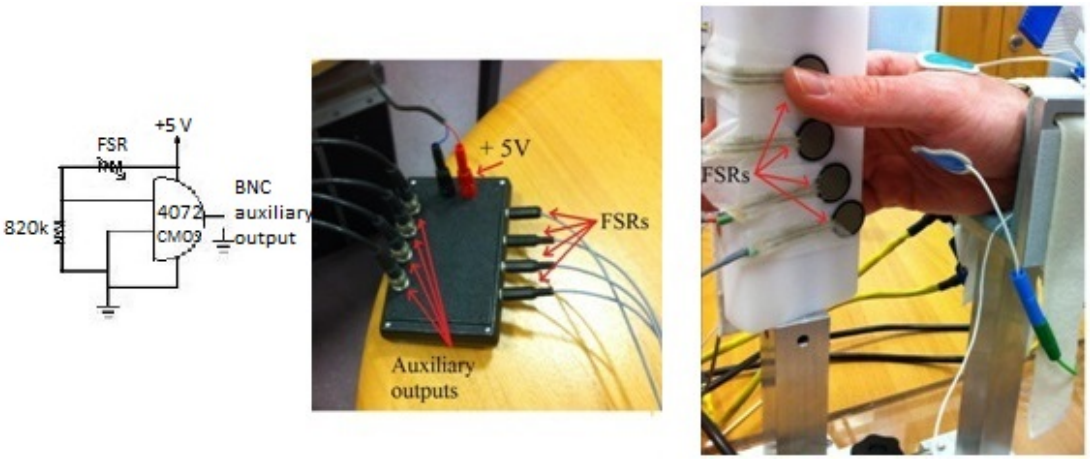

Figure 8.1: First Design For Test Rig Finger Sensors - Left - Simple circuit that guaranteed the salient voltage range was in between 0 and +5 V, within the ranges of the HD-sEMG auxiliary inputs. Middle - box that contained the circuitry described previously, and left - FSRs that were used for a first test-rig design.

8.4 Technical Specs of the EMG-USB2 and Electrode Arrays

The HD-sEMG system used was the EMG-USB2 amplifier manufactured by OT-Bioelettronica, Italy. This amplifier has the capability of acquiring surface or intramuscular EMG signals, electroencephalography (EEG) and electrocardiography (EKG). The EMG-USB2 can acquire monopolar, bipolar or differential data from up to 256 electrodes (channels). With configurable independent or global settings, if desired. The settings that could be applied independently for each group of 16 channels are gain, bandwidth and acquisition type e.g. monopolar, bipolar or differential.

The technical specifications of the EMG-USB2 (fig. **??**) are as follow:

- Power Supply: 90 V_{AC} - 260 V_{AC} and 27 Hz - 440 Hz
- Number of Channels: from 16 up to 256 EMG/EEG/EKG plus 16 auxiliary inputs
- Gain: OFF, 100, 200, 500, 1000, 2000, 5000, and 10000 V/V
- Selectable bandwidth:

  High-pass cut frequency: 3, 10, 100, 200 Hz

  Low-pass cut frequency: 130, 500, 900, 4400 Hz
- Sampling frequency: 512, 2048, 4096, 10240 Hz
- Noise referred to the input(RTI): $< 1\mu V_{RMS}$
- Input resistance: $> 10^{12}\Omega$
- Common mode rejection ratio (CMRR):>95dB
- Output range: 0-5 V_{PP}

The different sEMG electrode arrays that were available by the manufacturer when this experiment was carried out can be found in figure 8.2.

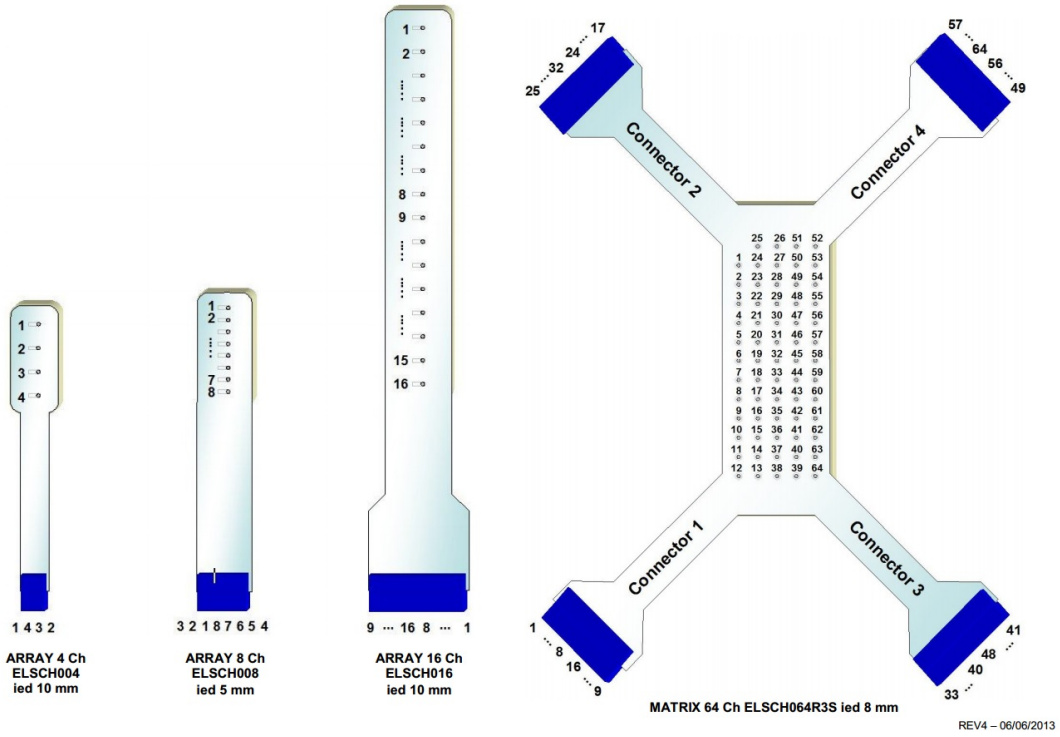

Figure 8.2: Adhesive Arrays Available for sEMG Acquisition with the EMG-USB2 - From left to right: 4 electrode array with an inter-electrode distance (IED) of 10mm; 8 electrode array with an IED of 5mm; 16 electrode array with an IED of 10mm; 64 electrode array with an IED of 8mm. Source: OT Bioelettronica. (2011). Arrays & Matrices Pin-out-Rev4. Available: OT Bioelettronica - Last accessed 1st April 2014.

8.5 Calibration Curves for All the Load-Sensor Resistors

Calibration curves for the LSRs used for the thumb opposition tasks

Load Sensor Resistors Calibration Curves

Weight increments: 83/84 g

Transducer #1								
	Trial #1		Trial #2		Trial #3		Trial #4	
Weight [g]	Rise [mV]	Fall [mV]	Rise [mV]	Fall [mV]	Rise [mV]	Fall [mV]	Rise [mV]	Fall [mV]
0	0	-0.7	0	3	0	-1	0	0
83	49	49	50	53	49	48	49	49
166	99	99	99	104	98	98	99	100
249	150	150	150	154	148	149	149	150
332	200	201	200	205	199	200	200	201
415	250	251	251	256	250	251	250	251
498	301	302	303	306	300	301	301	302
581	352	352	354	354	351	351	352	352

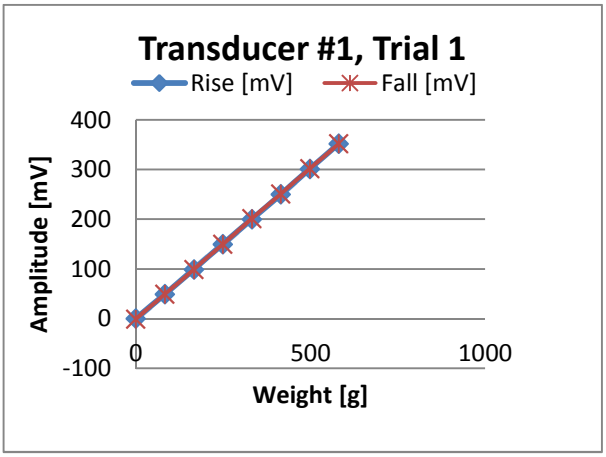

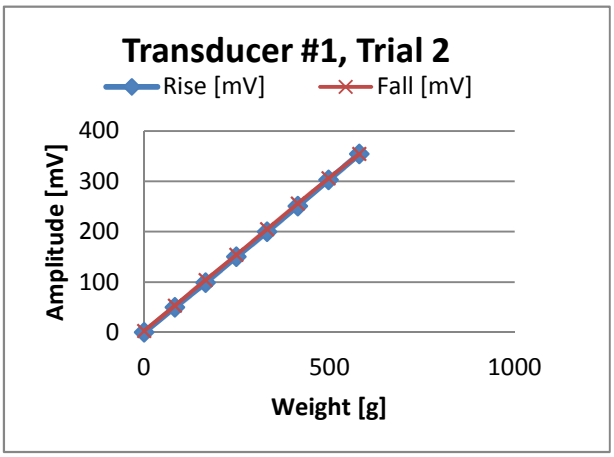

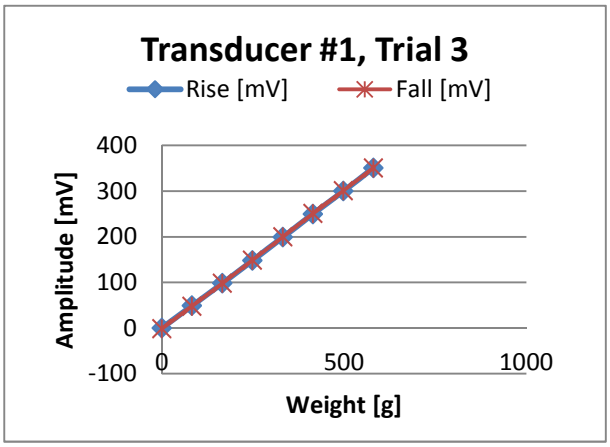

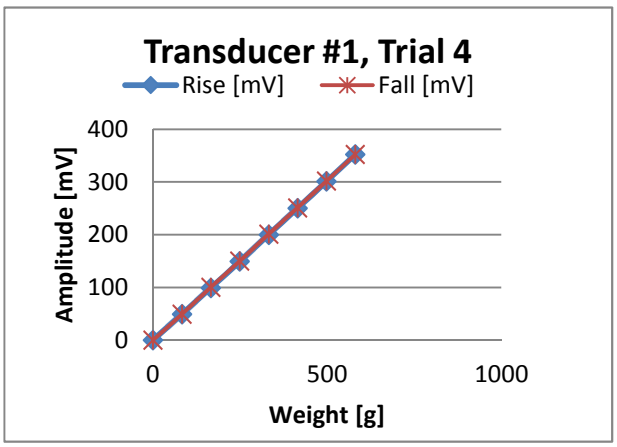

Load Sensor Resistors Calibration Curves

Weight increments: 83/84 g

Transducer #2								
	Trial #1		Trial #2		Trial #3		Trial #4	
Weight [g]	Rise [mV]	Fall [mV]	Rise [mV]	Fall [mV]	Rise [mV]	Fall [mV]	Rise [mV]	Fall [mV]
0	0	0.8	0	1.3	0	1.4	0	1
83	44.5	46.2	44.5	47	44.7	47.2	45	47
166	89.4	91.8	89.6	92.8	90	93.1	91	92
249	134.9	137.2	135	138.3	135.6	138.7	136	138
332	181	183.8	181.4	184.4	182	184.7	182	183
415	226.9	229	227.4	229.5	227.6	230.2	228	229
498	273	274.3	273.2	274.7	273.4	275.6	273	274
581	319	319	319.3	319.3	320	320	319	319

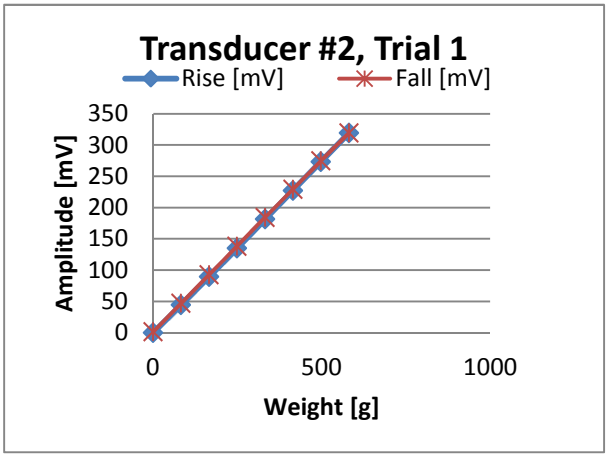

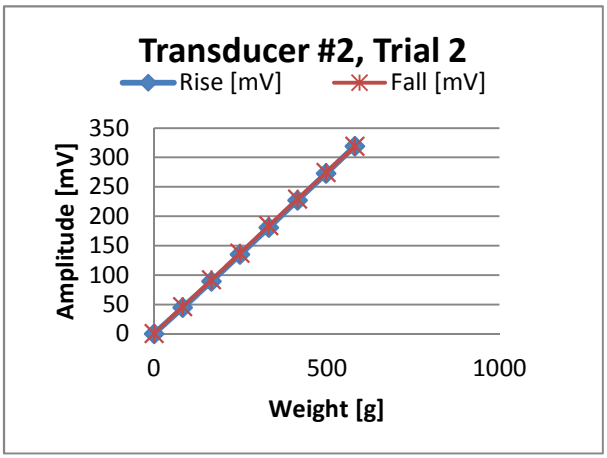

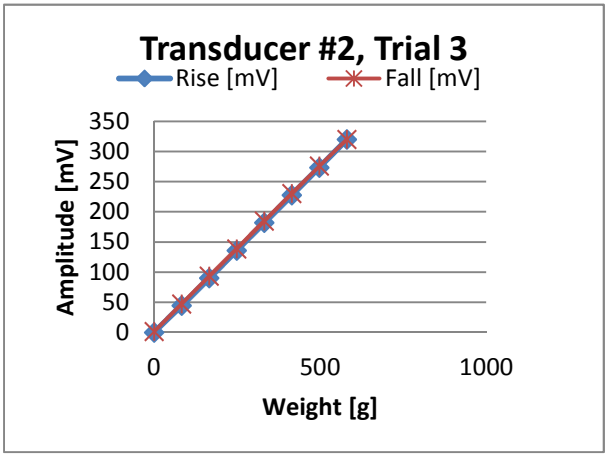

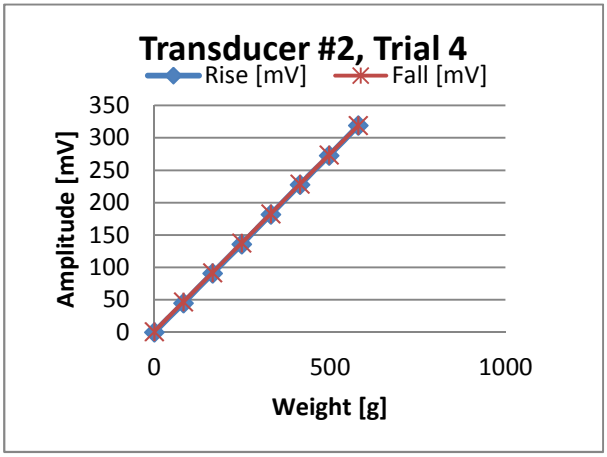

Load Sensor Resistors Calibration Curves

Weight increments: 83/84 g

Transducer #3								
	Trial #1		Trial #2		Trial #3		Trial #4	
Weight [g]	Rise [mV]	Fall [mV]	Rise [mV]	Fall [mV]	Rise [mV]	Fall [mV]	Rise [mV]	Fall [mV]
0	0	1.3	0	1.1	0	1	0	1.5
83	43.8	45.6	43.8	45.3	43.7	45.3	43.3	45.5
166	88	89.8	87.8	89.8	87.8	89.8	87	89.7
249	132	134.4	132.1	134.1	132	134.3	131	133.6
332	177.5	179.4	177.4	179.1	177.3	179.4	176	178.3
415	222	223.7	222.1	223.5	222	223.6	220.4	222.2
498	266.8	268	266.8	268	267.3	268	265.3	266.2
581	311.9	311.9	311.9	311.9	312.1	312.1	309.4	309.4

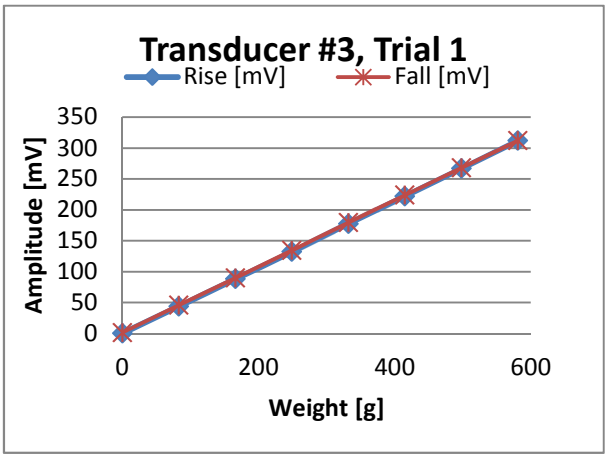

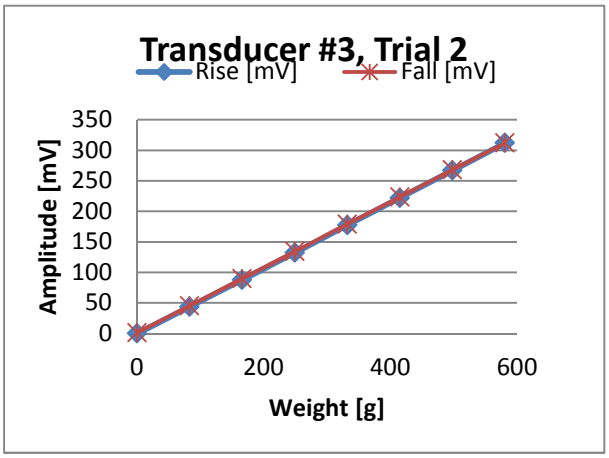

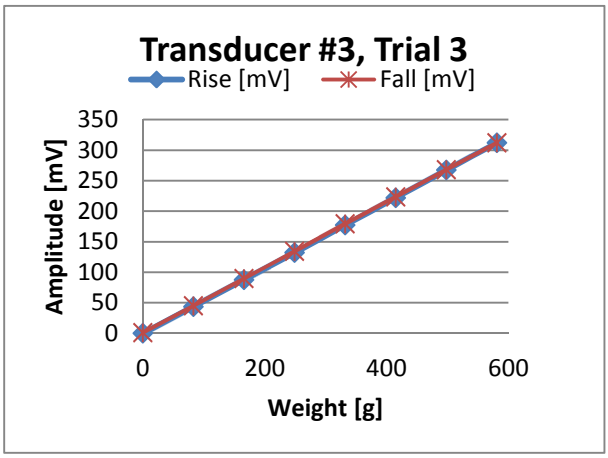

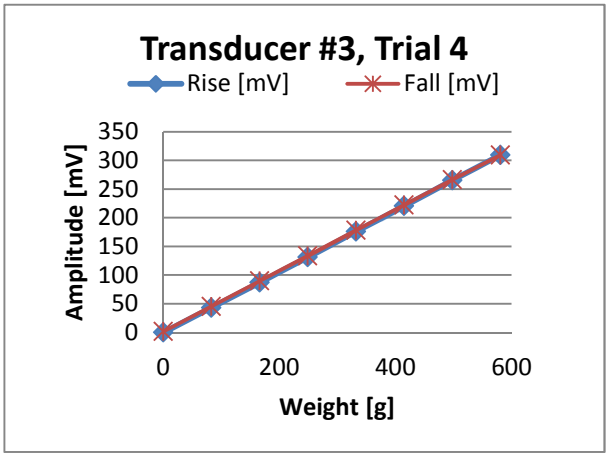

Load Sensor Resistors Calibration Curves

Weight increments: 83/84 g

Transducer #4								
	Trial #1		Trial #2		Trial #3		Trial #4	
Weight [g]	Rise [mV]	Fall [mV]	Rise [mV]	Fall [mV]	Rise [mV]	Fall [mV]	Rise [mV]	Fall [mV]
0	0	1.3	0	1.5	0	1.3	0	1.3
83	47	48.4	47	48.9	47	48.5	47.2	48.9
166	94.1	95.8	94.3	96.3	94.2	95.8	94.6	96.8
249	141.4	143.1	141.4	143.5	141.3	143.2	142.2	144.2
332	189.3	191.2	189.4	191.6	189.4	191.1	190.7	192.5
415	237	238.4	237	238.9	237	238.4	238.5	239.9
498	285	285.9	285.1	286.4	285	285.8	286.5	287.5
581	333.1	333.1	333.4	333.4	333.1	333.1	334.7	334.7

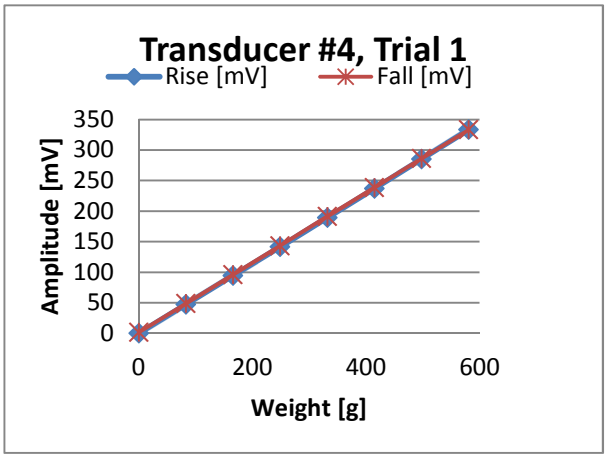

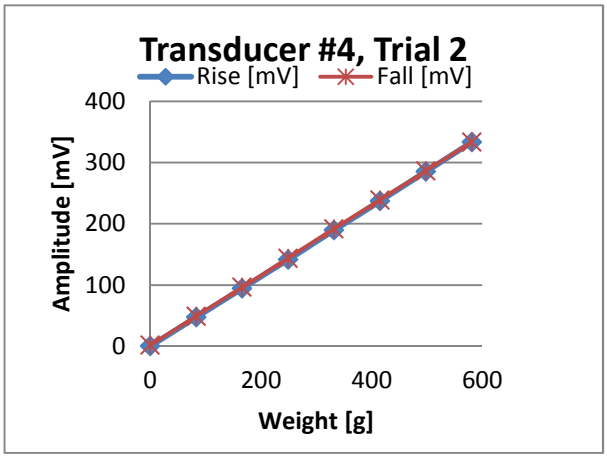

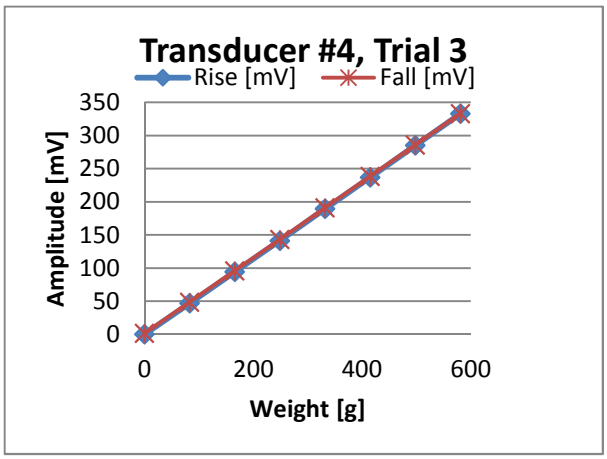

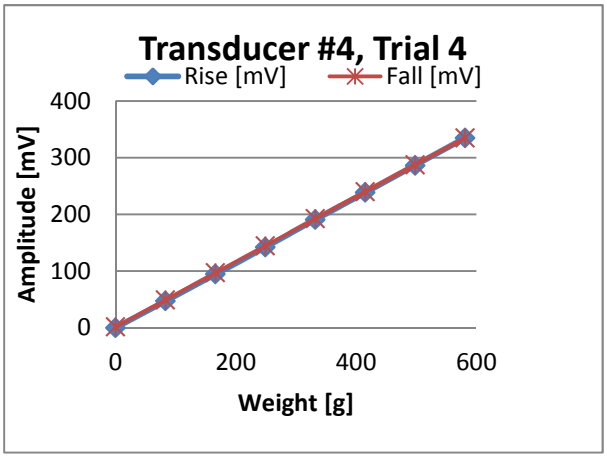

8.6 Root-Mean Square Values for Feature Distribution in the Forearm per Subject.

RMS Values for Feature Distribution

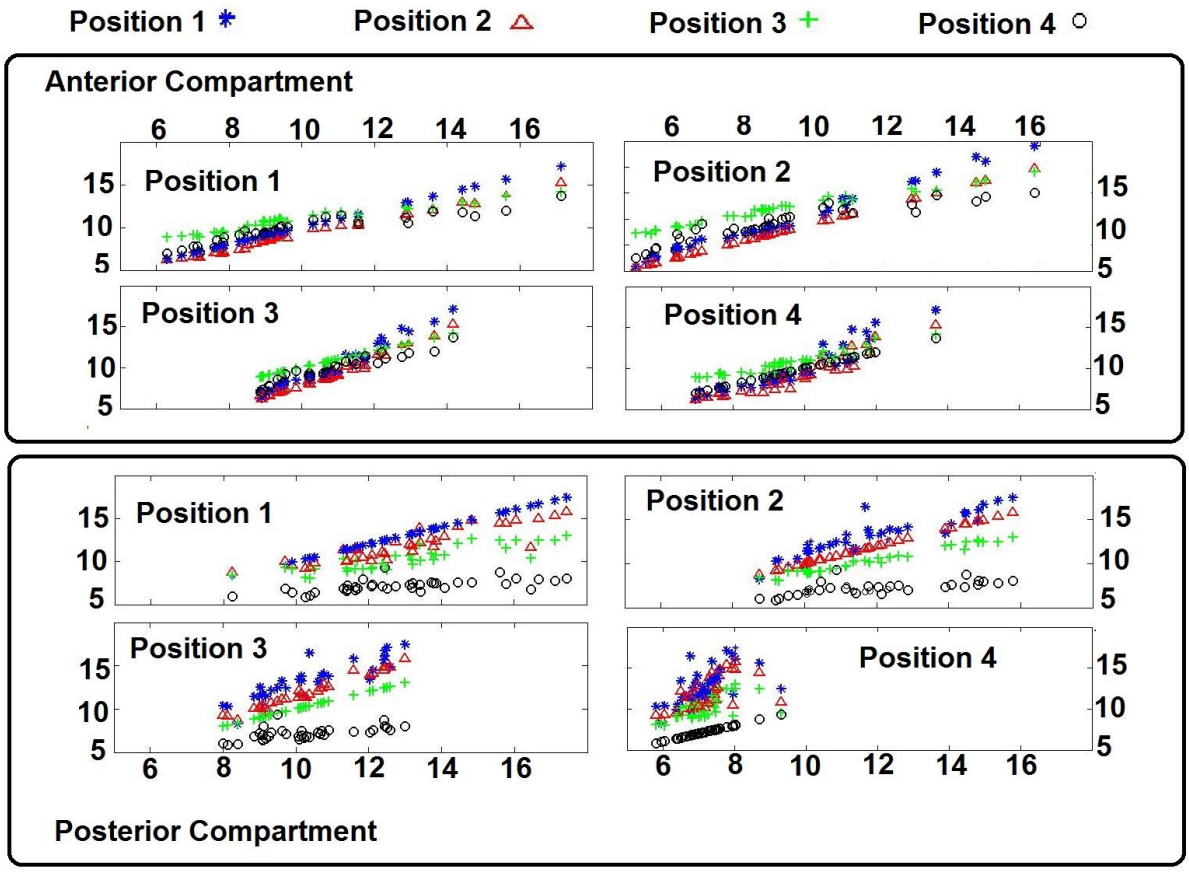

RMS Values for Feature Distribution

S2

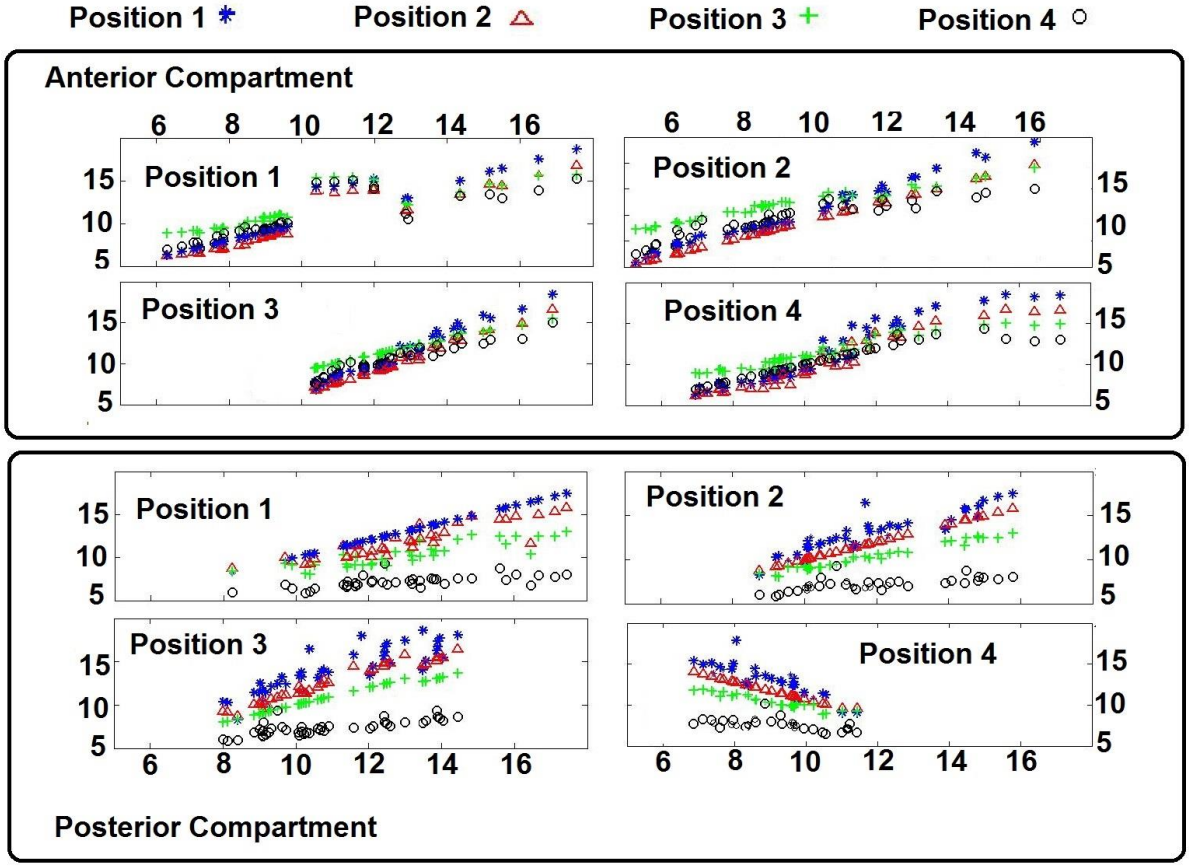

RMS Values for Feature Distribution

S3

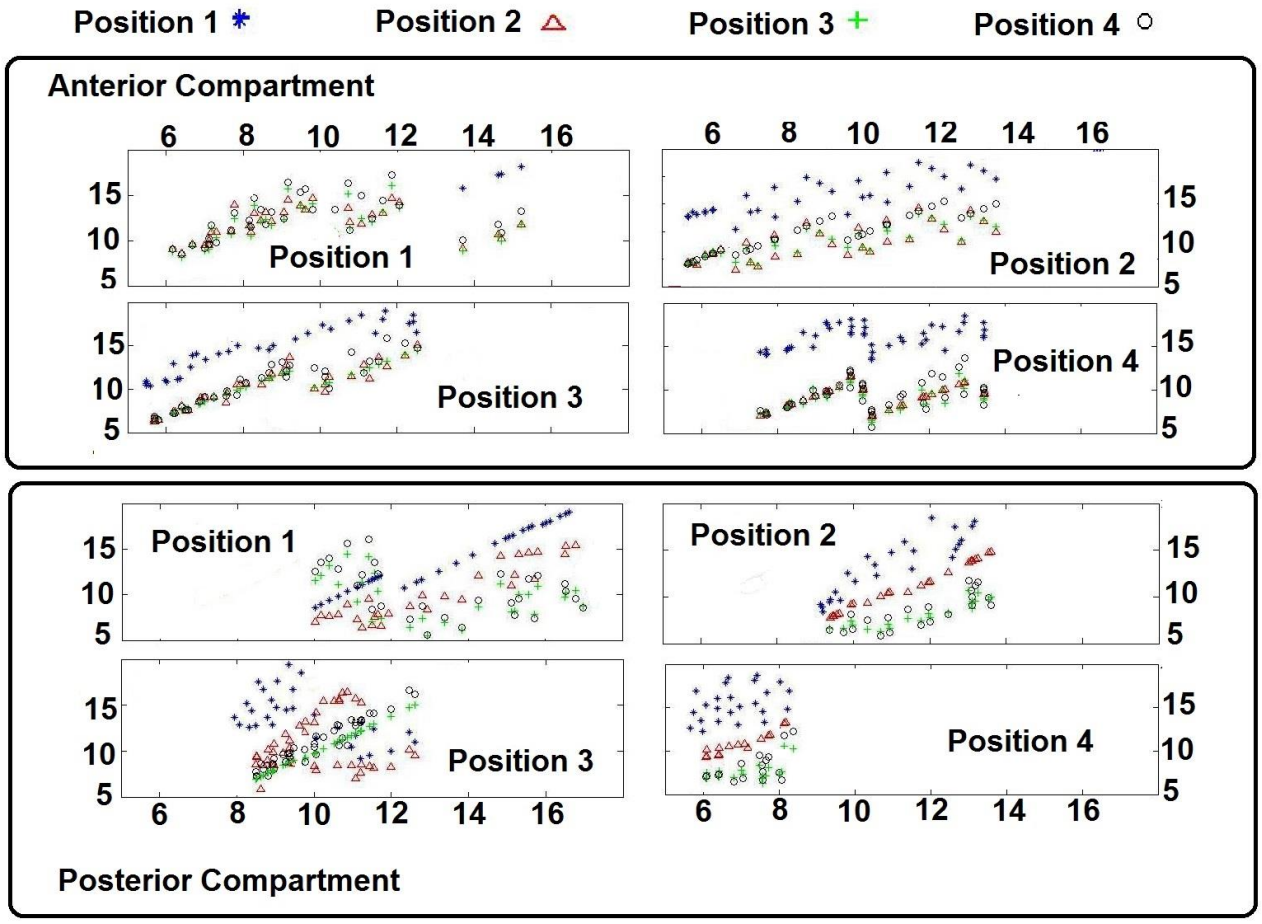

RMS Values for Feature Distribution

S4

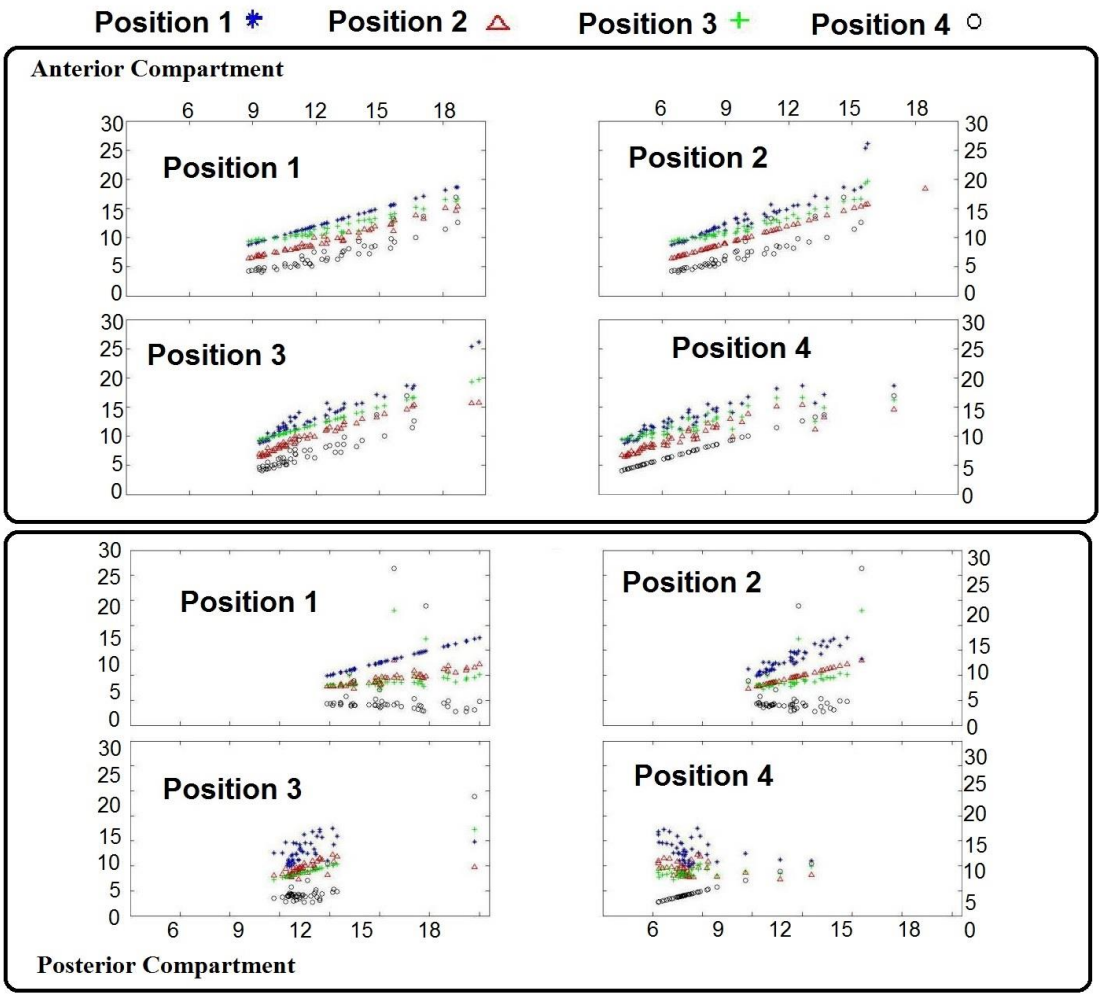

RMS Values for Feature Distribution

S5

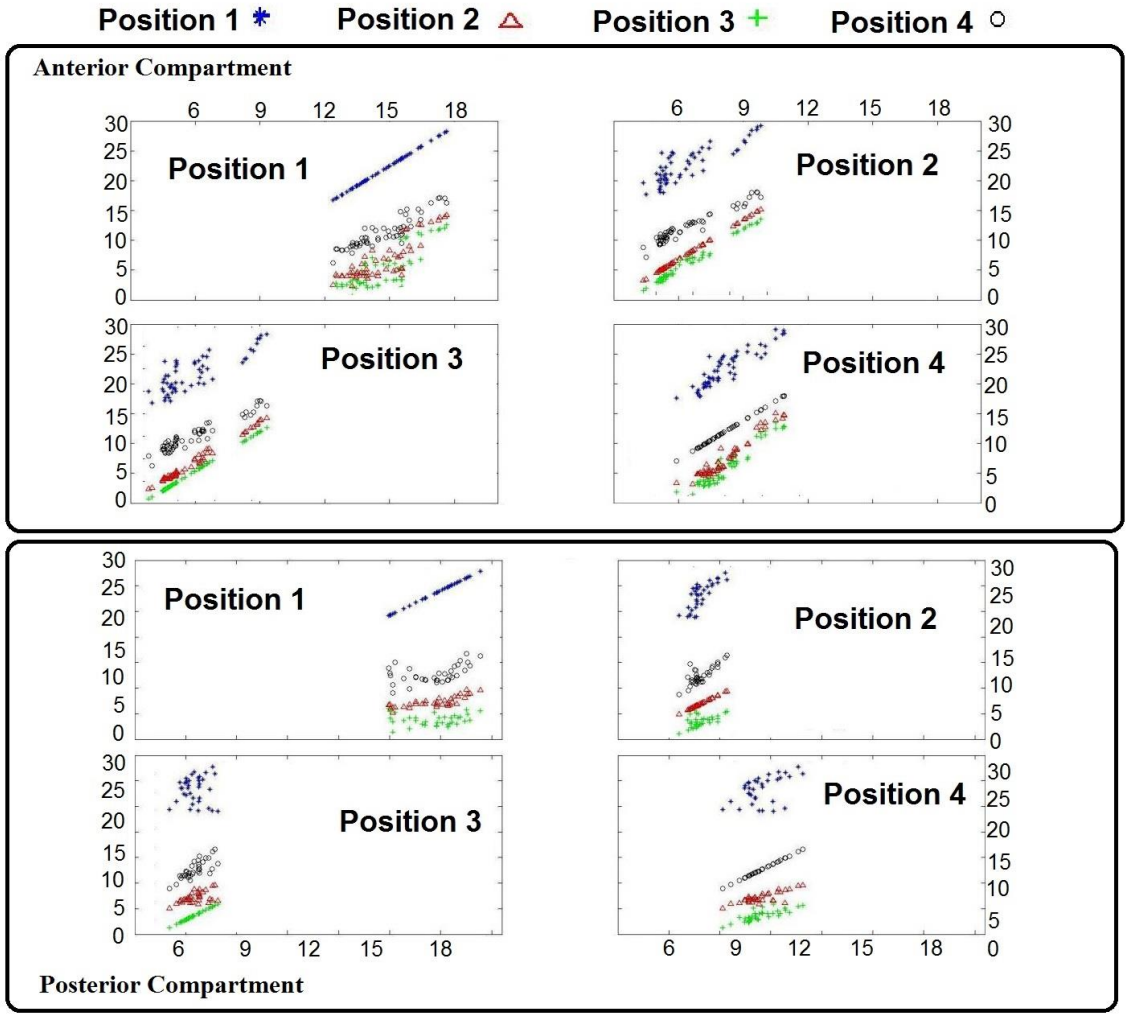

RMS Values for Feature Distribution

S6

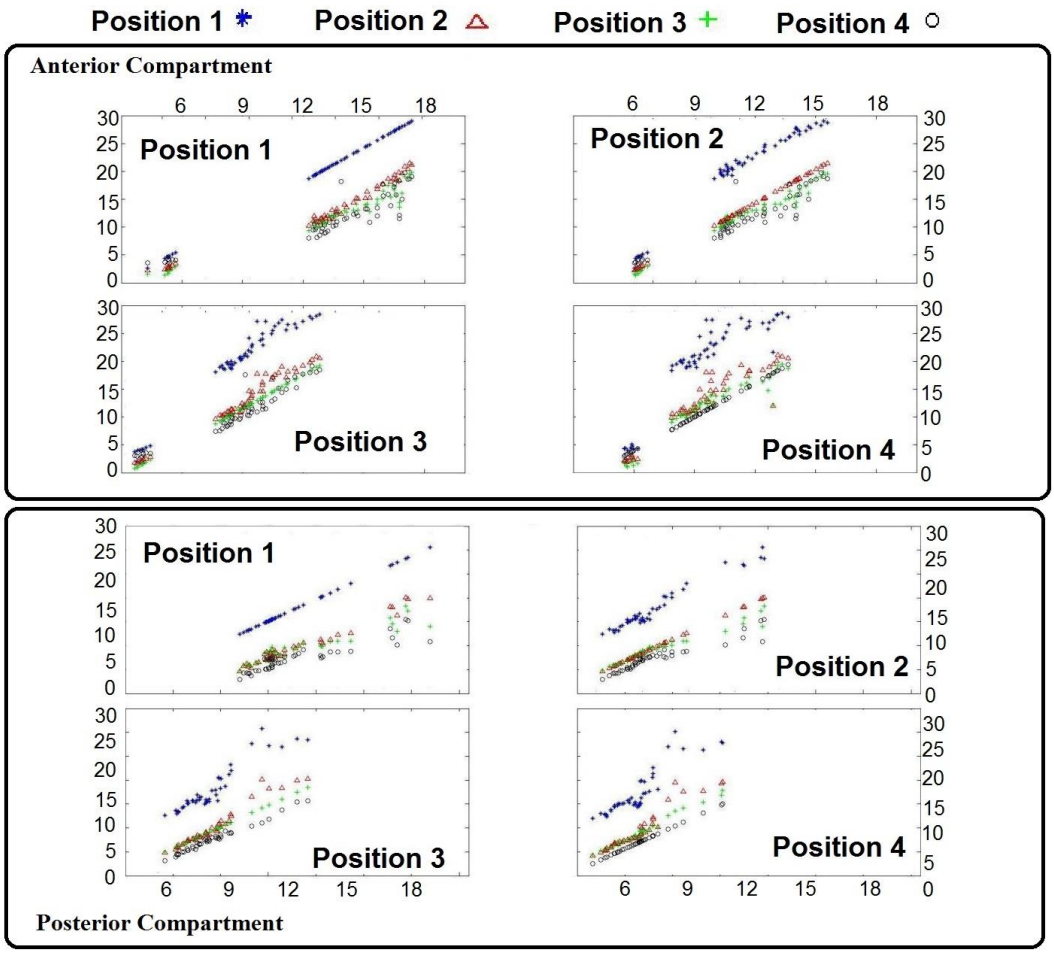

RMS Values for Feature Distribution

S7

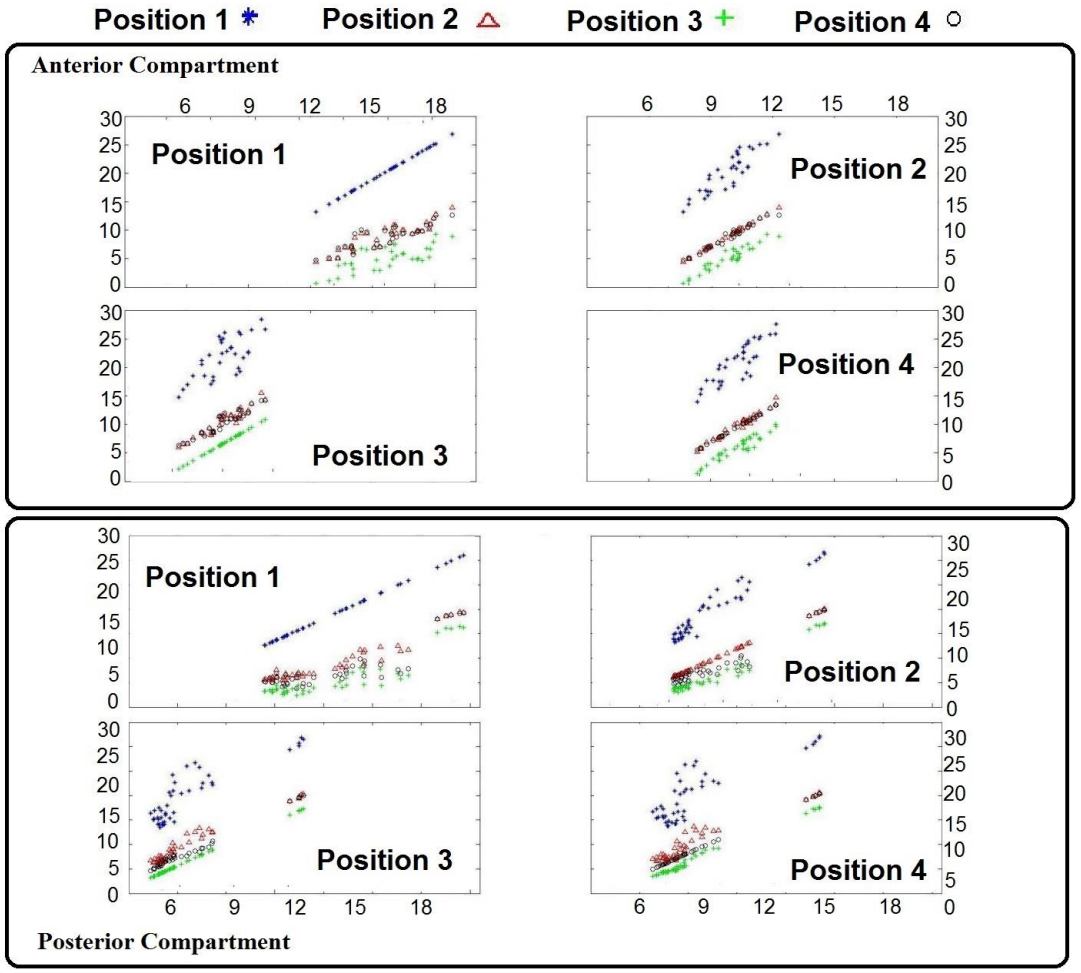

8.7 One-way Analysis of the Variance

In this section the ANOVA equations used are shown and explained:

In one-way ANOVA, the variation due to the interaction between the data points is denoted *SS(B)* for Sum of Squares Between groups (Equation (8.6). If the sample means are close to each other, the variation will be small. There are k samples assumed to be involved with one data value per sample mean, so there are *k-1* degrees of freedom. The employed measure of central tendency, a.k.a arithmetic average or mean ($\bar{Y}$), is defined by Rutherford, 2012(234) in Equation (8.1):

$$\bar{Y} = \frac{\sum_{i-1}^{N} Y_i}{N} \tag{8.1}$$

where $\bar{Y}_i$ is the ith subject's data point, and N is the total number of data points. The subscript i indexes the individual data points and in the instance it takes the values from 1 to N. The variance (σ^2) is defined as

$$\sigma^2 = \frac{\sum_{i-1}^{N} (Y_i - \bar{Y})^2}{N} \tag{8.2}$$

The variance reflects the average of the squared deviations from the mean. Equation (8.2) defines the population variance. Nevertheless, this equation provides a biased estimate due to the loss of a degree of freedom from the denominator given that the mean (which the scores are based on), is used in this calculation. The unbiased estimate of the sample variance (s^2) is given by

$$s^2 = \frac{\sum_{i-1}^{N} (Y_i - \bar{Y})^2}{N - 1} \tag{8.3}$$

Substituting (8.1) into (8.3):

$$s^2 = \frac{\sum_{i-1}^{N} Y_i^2 - \left[(\sum_{i-1}^{N} Y_i)^2 / N \right]}{N - 1} \tag{8.4}$$

As a result, the standard deviation (σ) is given by the square root of the variance, the sample standard deviation (s) is given by

$$s = \sqrt{\frac{\sum_{i-1}^{N} Y_i^2 - \left[(\sum_{i-1}^{N} Y_i)^2 / N \right]}{N - 1}} \tag{8.5}$$

The total sum of squares according to Rutherford, 2012(234), is understood as the deviation of all the observed scores from the general mean (equation (8.1)). The only modification to the equation (8.4) is to exclude the denominator

$$SS_{total} = \sum_{i-1}^{N} Y_i^2 - (\sum_{i-1}^{N} Y_i)^2/N \tag{8.6}$$

8.8 ANOVA Analysis Results For All Subjects

8.8.1 ANOVA table for all subjects per Grid

Windows (Time (ms))	S1		S2		S3		S4		S5		S6		S7		
	Posterior Compartment	Anterior Compartment	Posterior Compartment	Anterior Compartment	Posterior Compartment	Anterior Compartment	Posterior Compartment	Anterior Compartment	Posterior Compartment	Anterior Compartment	Posterior Compartment	Anterior Compartment	Posterior Compartment	Anterior Compartment	
[0 - 256]	6.1202E-09	8.3370E-06	2.1195E-07	4.7788E-13	5.8827E-05	2.7002E-02	2.6261E-30	3.7154E-22	6.5756E-37	5.4782E-38	7.2036E-07	1.9539E-23	7.7156E-15	1.0971E-12	IVC
[128 - 384]	1.3686E-03	8.0462E-03	9.2382E-20	6.4294E-41	3.2879E-08	7.3337E-05	3.0483E-28	1.6286E-36	1.4198E-14	1.1410E-13	8.7572E-11	4.0217E-08	3.6391E-23	3.8693E-18	
[256 - 512]	3.9055E-07	2.8776E-11	1.0540E-48	1.4367E-59	1.4073E-28	1.5878E-07	7.2808E-35	1.9398E-38	6.7276E-44	6.9058E-92	1.7579E-26	2.7162E-32	1.1496E-23	4.0076E-41	
[384 - 640]	6.0894E-02	1.1517E-06	1.4155E-14	2.7005E-15	1.0101E-07	1.4076E-15	1.5557E-50	4.3855E-85	5.9356E-44	2.9932E-101	9.6696E-09	5.6999E-25	2.0660E-57	6.1045E-68	
[512 - 768]	6.1221E-01	3.5739E-03	1.6665E-96	3.1866E-139	9.4682E-45	8.6689E-13	1.3230E-63	2.7072E-85	6.6750E-55	1.0842E-121	1.8410E-12	1.2454E-21	4.1787E-62	1.2065E-88	
[640 - 896]	1.4010E-06	1.9324E-05	3.7713E-59	1.9419E-96	1.1604E-32	1.5572E-11	8.8598E-94	1.4541E-126	3.1489E-18	1.5342E-72	5.8396E-11	2.2818E-25	4.8924E-50	3.0789E-52	
[768 - 1024]	3.1975E-05	5.2674E-01	9.5783E-88	1.3022E-134	2.5926E-29	3.4236E-11	1.4145E-81	6.2408E-113	1.3006E-27	4.6001E-87	1.8432E-07	3.2479E-15	3.9711E-62	4.9464E-82	
[896 - 1152]	8.4083E-07	5.3159E-08	5.3020E-65	3.7297E-96	1.1190E-38	3.9125E-02	2.4923E-110	8.4499E-134	1.0954E-24	3.2554E-83	1.0226E-17	3.4889E-37	2.6597E-32	2.9586E-31	
[1024 - 1280]	4.3757E-13	1.2408E-01	2.0089E-73	1.1337E-104	1.0434E-05	1.5690E-05	9.0223E-98	5.1825E-128	2.8295E-10	1.3750E-26	7.2376E-22	1.9734E-15	8.5483E-62	4.6577E-71	
[1152 - 1408]	2.4828E-18	6.6799E-10	1.2940E-91	5.4987E-137	6.6554E-11	3.7344E-04	1.5535E-90	8.8517E-105	4.3818E-23	2.2958E-75	1.4670E-13	2.1248E-16	1.2365E-40	3.0364E-45	
[1280 - 1536]	4.0832E-14	5.7715E-04	5.7692E-85	1.2687E-120	5.6108E-14	6.7781E-03	2.8055E-78	6.3970E-101	2.8954E-20	3.3862E-32	7.4174E-23	3.9077E-25	5.7535E-54	1.4889E-57	
[1408 - 1664]	4.7338E-19	1.4233E-26	4.9517E-85	7.4840E-119	3.2680E-02	6.9402E-05	2.8088E-102	7.5000E-115	8.9253E-06	8.3019E-19	1.3311E-25	1.5377E-29	2.2287E-49	1.8375E-26	
[1536 - 1792]	8.3411E-02	4.8037E-07	1.8321E-62	5.8775E-71	2.0557E-02	3.1315E-05	1.7634E-81	2.2538E-75	5.8379E-27	3.3066E-24	8.1614E-10	2.1766E-02	2.7393E-20	3.9339E-53	
[1664 - 1920]	5.3608E-04	2.2602E-24	1.1173E-12	6.3465E-11	2.4025E-18	1.0406E-05	2.1273E-21	2.3581E-47	3.4642E-41	4.7786E-51	1.0294E-05	1.4719E-22	7.4616E-29	8.2157E-46	
[1792 - 2048]	4.6123E-04	2.0436E-14	1.0911E-36	3.4227E-31	6.7361E-07	1.1435E-04	5.1546E-40	5.1852E-63	4.0098E-29	2.8251E-28	1.7844E-14	6.9515E-10	1.3323E-26	2.2622E-28	
[1920 - 2176]	2.8753E-05	5.0231E-30	1.0132E-16	7.5912E-20	1.4987E-09	5.9333E-02	2.4355E-56	8.7085E-77	3.9113E-47	5.2178E-53	1.2571E-04	1.6451E-11	2.0000E-40	2.1925E-38	
[2048 - 2304]	4.5222E-03	4.8115E-08	7.4666E-35	3.2548E-48	1.1801E-13	4.4492E-08	8.7980E-05	6.1672E-19	2.9523E-10	4.9774E-23	4.6524E-06	7.7187E-07	1.8005E-33	1.3752E-20	
[2176 - 2432]	1.1655E-04	1.3004E-18	1.7710E-18	1.6249E-31	1.9263E-17	1.1177E-04	1.4594E-47	3.6738E-67	2.3956E-15	2.4065E-25	9.3027E-08	1.8762E-07	2.5005E-29	1.1366E-33	
[2304 - 2560]	9.4307E-04	6.8421E-08	2.1725E-08	2.5014E-20	7.6916E-07	1.7504E-02	2.2700E-07	1.2695E-53	3.9974E-08	6.5930E-20	8.6637E-06	2.9888E-10	8.6008E-66	1.5942E-44	
[2432 - 2688]	5.4547E-01	2.3555E-01	2.0714E-56	5.9887E-31	2.7958E-26	8.5784E-16	2.6965E-10	9.3735E-29	1.2513E-42	1.7838E-45	2.3327E-08	3.1261E-17	1.4561E-16	5.6904E-42	
[2560 - 2816]	2.0257E-02	1.0735E-18	1.0134E-04	6.5973E-16	2.8218E-06	1.0903E-19	2.7743E-21	4.7681E-34	3.1253E-09	7.2727E-08	3.8771E-17	2.8462E-31	2.4929E-20	9.5723E-39	
[2688 - 2944]	1.3612E-02	3.0732E-02	1.4201E-35	1.1357E-29	7.0464E-31	1.7491E-03	2.4261E-07	3.1661E-09	1.9686E-44	6.9026E-44	1.5003E-08	2.4686E-06	3.9224E-13	1.7412E-39	
[2816 - 3072]	3.0374E-04	7.4298E-32	1.5563E-05	2.3418E-16	6.8364E-15	8.7831E-14	1.0263E-25	2.1888E-52	9.5733E-08	2.8190E-09	9.1500E-12	1.0623E-09	3.2784E-19	3.3911E-26	
[2944 - 3200]	1.1121E-07	2.4384E-14	1.3822E-12	8.6376E-38	1.7455E-05	3.7150E-03	3.0070E-20	5.2428E-52	1.4772E-03	6.1920E-01	1.4225E-05	4.7868E-02	3.2546E-11	2.5862E-22	
[3072 - 3328]	5.1898E-04	6.8045E-05	1.6625E-05	1.0686E-19	1.2511E-12	5.9615E-05	9.0082E-11	1.8395E-42	2.7769E-38	3.6574E-57	1.9952E-04	1.0063E-04	5.3921E-34	2.8038E-29	
[3200 - 3456]	9.0228E-10	6.2483E-16	2.3973E-09	1.5619E-38	1.3836E-16	8.7586E-08	4.9057E-22	1.0111E-36	6.0305E-06	1.9085E-05	8.7794E-11	3.0218E-08	1.0620E-19	4.0912E-35	
[3328 - 3584]	1.1682E-02	1.4293E-03	4.9052E-10	2.0791E-11	4.1658E-08	9.2708E-09	3.3038E-03	1.8228E-15	8.0569E-48	9.7427E-54	5.2118E-03	2.3292E-02	5.4908E-05	3.5367E-15	
[3456 - 3712]	2.2186E-01	4.7511E-05	1.3874E-12	9.9665E-26	8.2964E-01	3.7999E-04	3.8176E-06	1.8657E-25	3.8668E-08	7.2690E-03	1.8004E-12	7.2869E-15	1.3757E-18	1.6600E-19	
[3584 - 3840]	1.5839E-03	5.6810E-21	1.4654E-18	6.1596E-21	4.1293E-02	9.4443E-13	4.3312E-24	5.2878E-51	4.2947E-11	4.3794E-19	4.0530E-21	1.2613E-16	1.1319E-20	1.2312E-70	
[3712 - 3968]	5.2746E-06	1.0082E-23	4.4544E-02	5.1019E-05	4.7670E-03	6.6881E-02	3.9280E-17	4.5104E-53	2.8236E-18	4.7371E-04	6.2737E-21	7.1281E-21	1.8439E-06	1.1654E-21	
[3840 - 4096]	3.6212E-01	7.9337E-31	4.3298E-14	4.7152E-18	2.4121E-18	2.3642E-12	1.0454E-10	3.4040E-24	1.3751E-18	2.3517E-18	6.9216E-19	1.0570E-17	7.2686E-04	3.3584E-19	
[3968 - 4224]	4.2337E-04	3.2797E-10	1.0741E-09	1.8856E-18	1.5635E-08	1.3189E-07	2.3989E-30	6.7205E-56	2.3252E-11	1.2071E-07	1.4500E-01	5.0847E-06	6.2503E-02	2.9737E-01	
[4096 - 4352]	1.3604E-01	2.5548E-03	9.7743E-03	4.7526E-25	3.9065E-39	1.3715E-09	4.1496E-16	9.3776E-23	2.5805E-20	2.4163E-29	6.7718E-09	2.3788E-14	2.9564E-21	3.3350E-06	
[4224 - 4480]	3.0678E-04	9.7402E-05	7.3434E-09	9.5266E-17	3.6153E-05	9.8162E-07	6.5135E-13	1.6315E-31	6.9508E-04	2.1323E-04	5.0039E-20	5.2084E-15	3.8363E-09	6.3140E-16	
[4352 - 4608]	1.3876E-02	6.7234E-07	2.8559E-12	4.5827E-07	1.7166E-21	1.1090E-03	5.5275E-15	2.8557E-33	3.4195E-02	1.5986E-02	7.1300E-16	1.6898E-14	1.4070E-06	4.7352E-05	
[4480 - 4736]	2.1126E-09	2.8190E-15	4.7831E-18	9.9314E-34	2.7653E-18	5.0905E-14	2.9903E-32	5.0921E-59	8.3961E-09	6.9800E-05	4.5505E-02	3.6738E-07	1.1575E-06	8.8644E-24	
[4608 - 4864]	2.2796E-10	1.5445E-27	1.6416E-10	1.4637E-14	4.9451E-31	2.6646E-05	5.4278E-19	1.9481E-26	2.8575E-32	1.5090E-37	2.3353E-02	1.2294E-11	1.4136E-24	2.9043E-23	
[4736 - 4992]	5.1195E-05	2.7523E-09	3.7390E-32	3.8133E-24	2.6121E-13	8.1652E-11	1.5436E-57	8.8923E-64	1.0301E-11	5.0473E-08	7.6637E-04	2.3690E-06	1.7369E-10	2.8545E-34	
[4864 - 5120]	1.1473E-09	2.2720E-19	2.5478E-54	1.7651E-55	4.2859E-11	2.3823E-03	6.5641E-17	2.9132E-42	9.8641E-12	2.0094E-20	1.0172E-14	3.5485E-05	3.4047E-16	6.5060E-31	
[4992 - 5248]	3.2781E-01	1.9885E-04	7.8508E-75	1.5236E-76	1.0073E-21	4.7803E-17	1.4068E-51	2.4766E-62	3.9600E-05	1.4476E-08	3.0626E-08	2.4584E-02	3.3496E-09	6.3206E-32	
[5120 - 5376]	3.0058E-05	5.1635E-16	3.4740E-68	7.3898E-58	2.1592E-15	2.8395E-08	4.1019E-34	2.4773E-59	1.0755E-13	7.7436E-30	2.1328E-05	1.0625E-01	3.2945E-03	7.8218E-27	
[5248 - 5504]	1.6091E-06	5.5448E-11	1.4942E-46	3.5830E-66	4.8235E-47	5.9149E-11	1.4283E-13	1.9215E-29	4.0867E-03	5.2824E-04	1.6061E-17	3.8921E-20	3.3890E-12	1.3179E-10	
[5376 - 5632]	6.3094E-06	2.4727E-06	2.8393E-80	2.3589E-84	1.9151E-47	2.5165E-20	8.1615E-53	1.9051E-79	3.2180E-42	3.2861E-54	4.0749E-13	1.4803E-09	2.6175E-22	1.6486E-37	
[5504 - 5760]	5.3558E-15	5.0074E-08	1.0922E-61	4.6406E-98	5.6824E-63	1.3367E-06	2.7114E-49	2.3935E-85	6.8954E-27	4.1619E-31	3.8178E-35	2.8668E-37	5.6221E-12	7.5850E-22	
[5632 - 5888]	4.1620E-13	9.0617E-14	2.6144E-85	2.1416E-117	2.9765E-29	1.7470E-17	1.9862E-47	1.5503E-62	2.2929E-69	2.4436E-81	1.0640E-12	3.5518E-12	2.8901E-57	1.9014E-46	
[5760 - 6016]	2.9676E-05	3.0446E-08	7.2483E-49	6.8571E-73	5.7847E-18	6.8445E-02	1.7324E-98	3.2018E-116	3.1802E-50	3.0981E-101	7.3773E-09	7.7770E-11	3.2423E-55	4.8477E-53	Rest
[5888 - 6144]	2.1810E-09	2.8302E-09	3.2128E-41	8.5717E-82	5.6636E-30	4.9829E-03	3.8297E-82	1.2386E-83	1.4420E-08	2.8081E-05	1.2354E-49	1.4846E-58	5.0902E-46	3.5868E-58	
[6016 - 6272]	3.3449E-01	1.2329E-01	3.9841E-01	7.8516E-02	5.0131E-01	4.3961E-01	7.3625E-02	2.7547E-01	8.3988E-02	2.7258E-01	1.3849E-01	3.8969E-01	1.7735E-01	3.7104E-01	

Figure 8.3: P-values for Windowed ANOVA Analysis - Resulting p-values obtained through one-way ANOVA analysis are shown separated by 350ms windows and by muscle groups. Shaded in red, the values where p is greater than 0.05, implying the impossibility of differentiating amongst positions. The first 45 windows represent the IVC, whereas the last 3 windows are that of the resting stage.

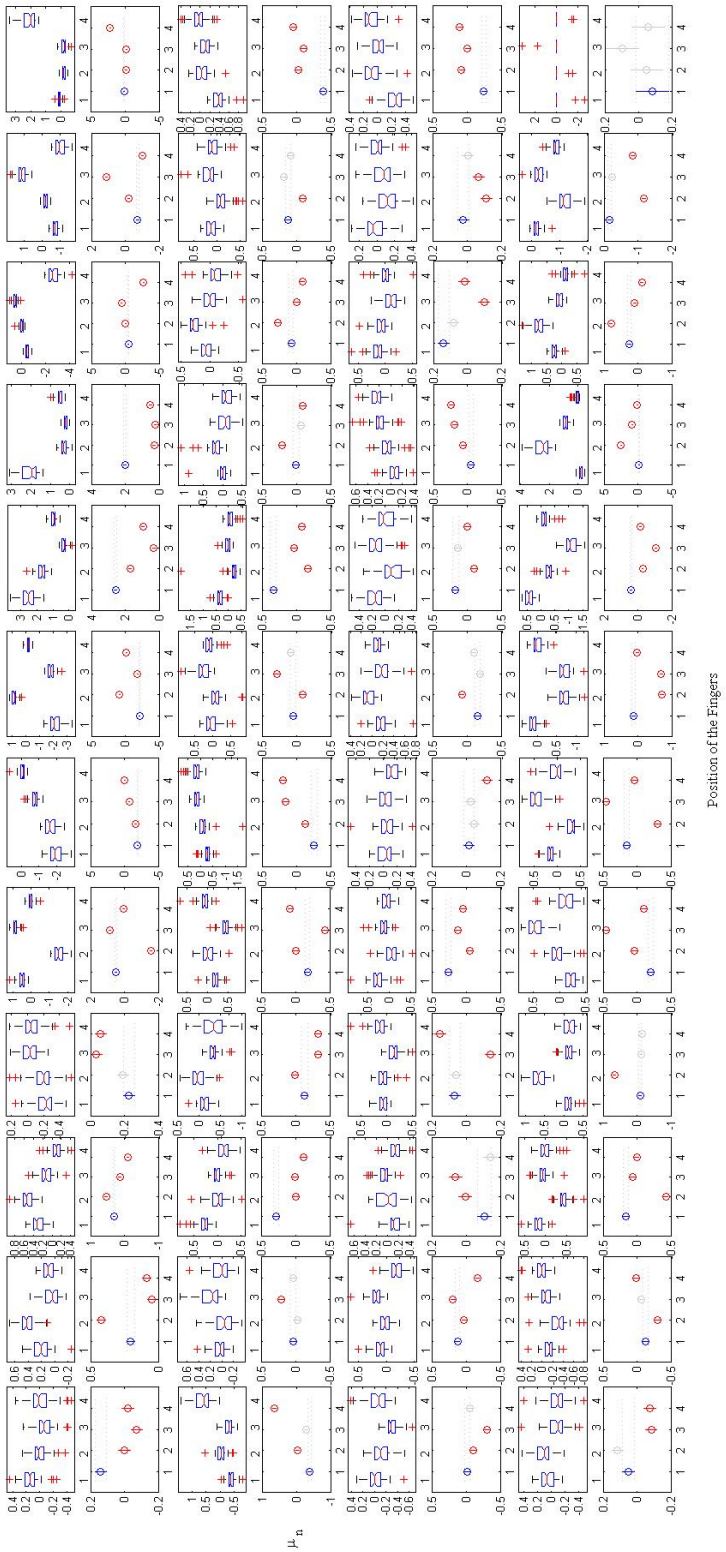

Figure 8.4: Windowed ANOVA Analyses For The Anterior Grid During Thumb Opposition Positions -

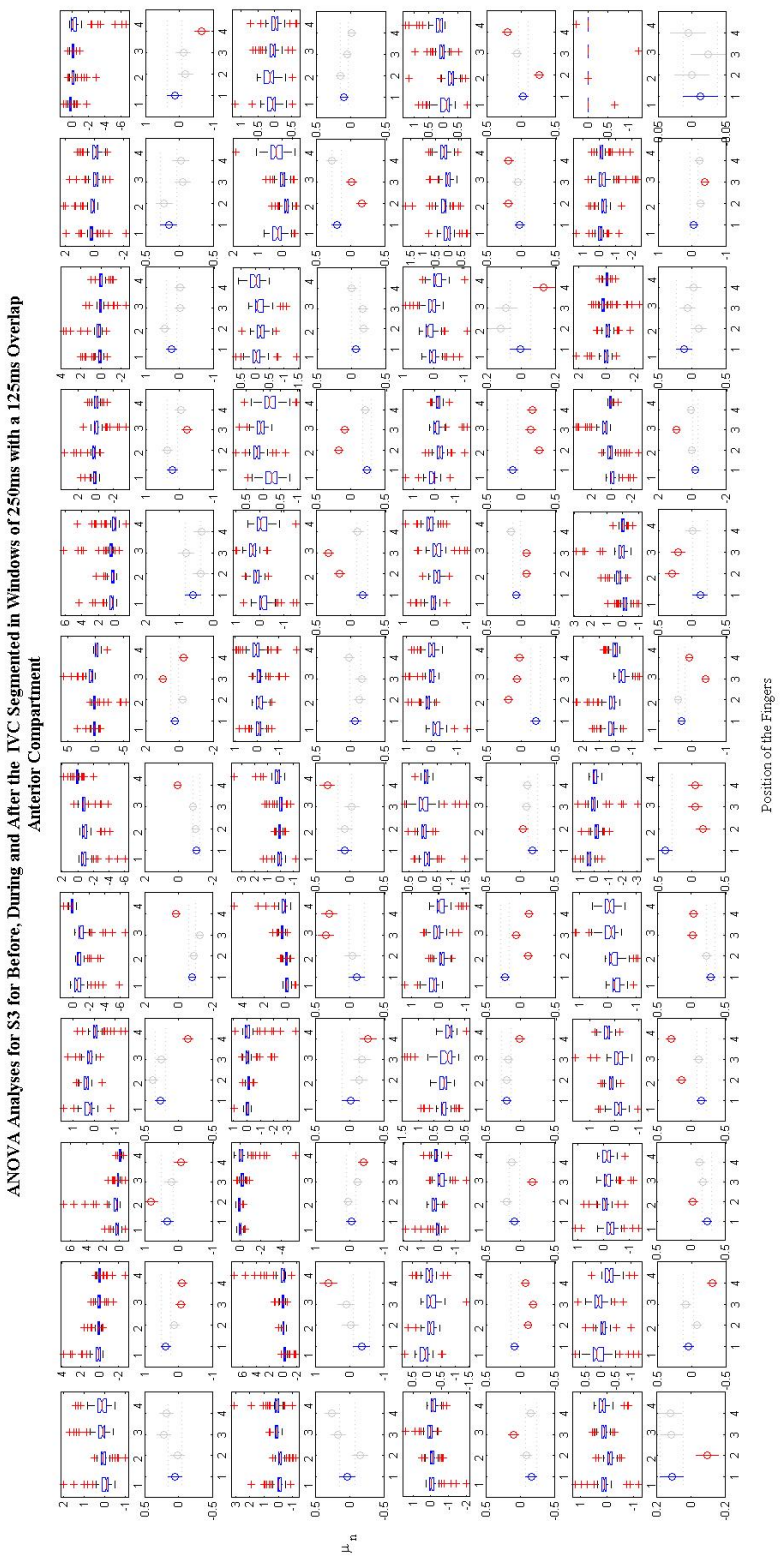

Figure 8.5: Windowed ANOVA Analyses For The Anterior Grid During Thumb Opposition Positions -

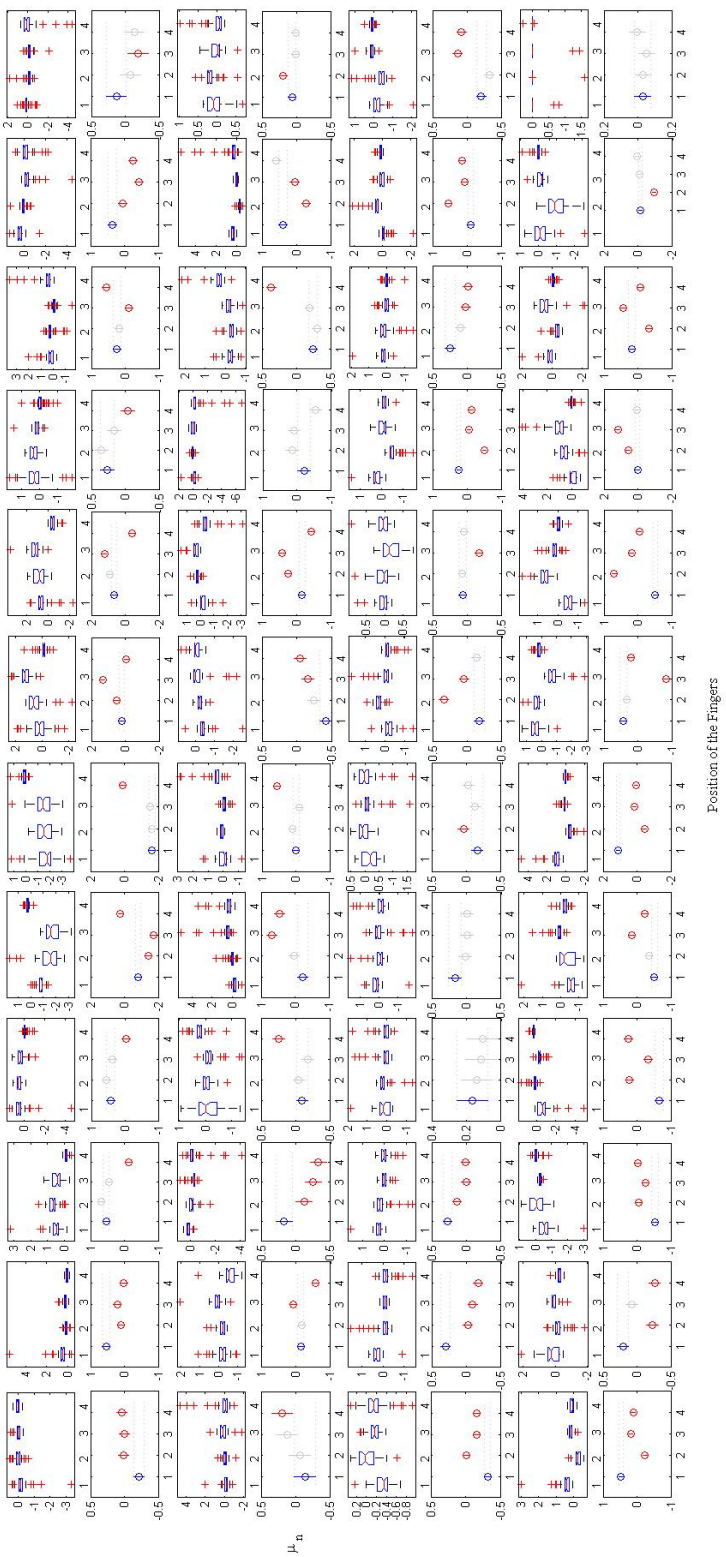

Figure 8.6: Windowed ANOVA Analyses For The Posterior Grid During Thumb Opposition Positions -

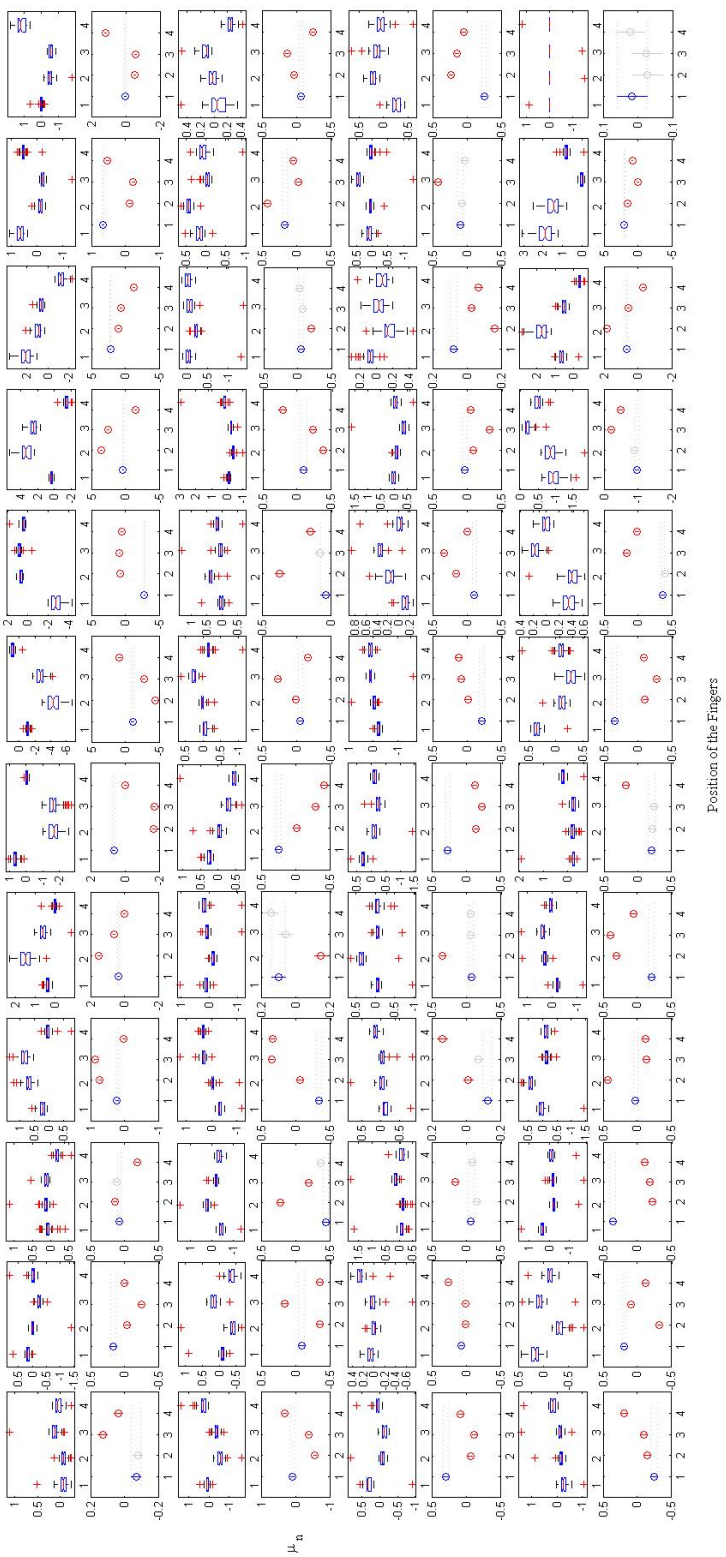

Figure 8.7: Windowed ANOVA Analyses For The Anterior Grid During Thumb Opposition Positions -

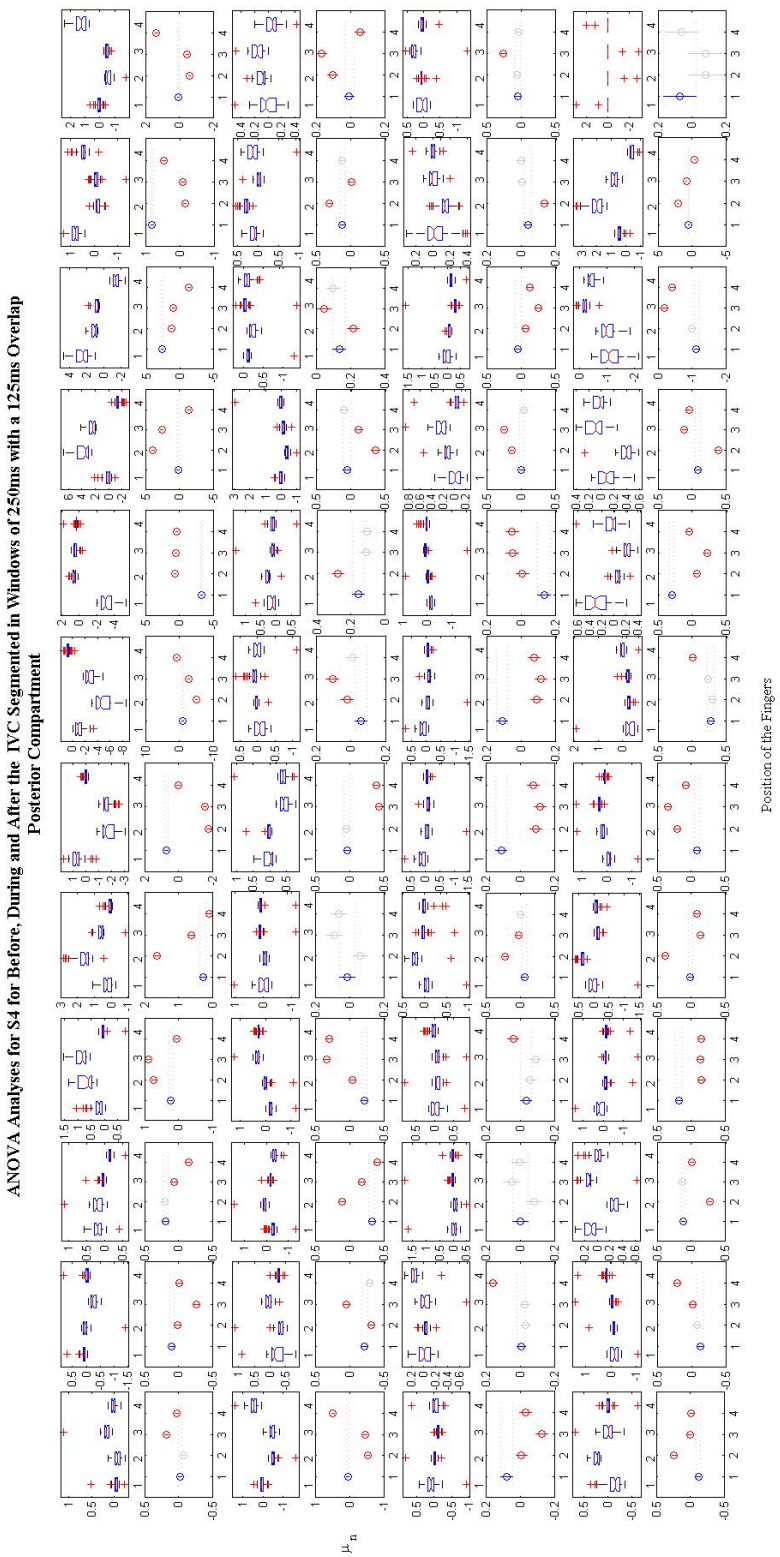

Figure 8.8: Windowed ANOVA Analyses For The Posterior Grid During Thumb Opposition Positions -

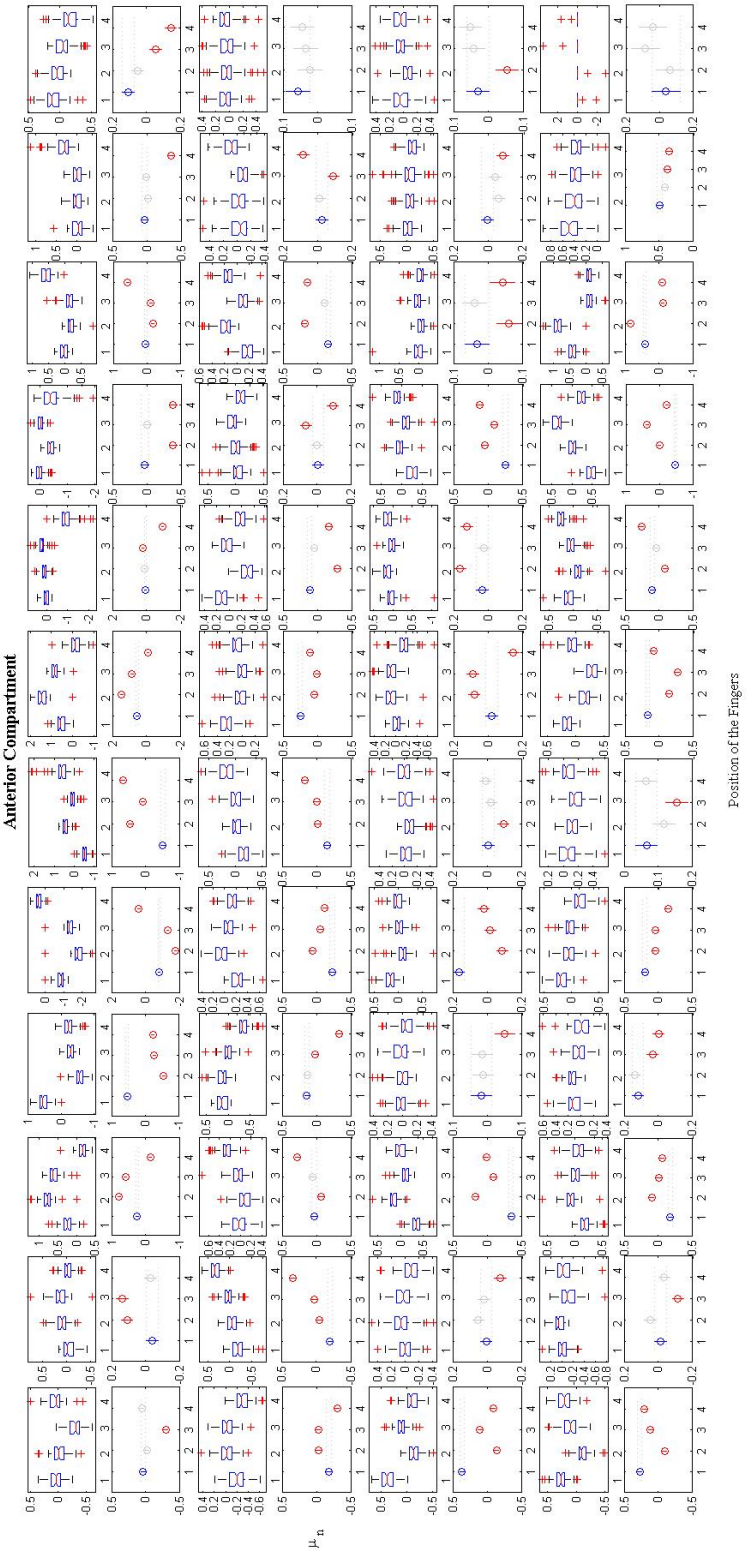

Figure 8.9: Windowed ANOVA Analyses For The Anterior Grid During Thumb Opposition Positions -

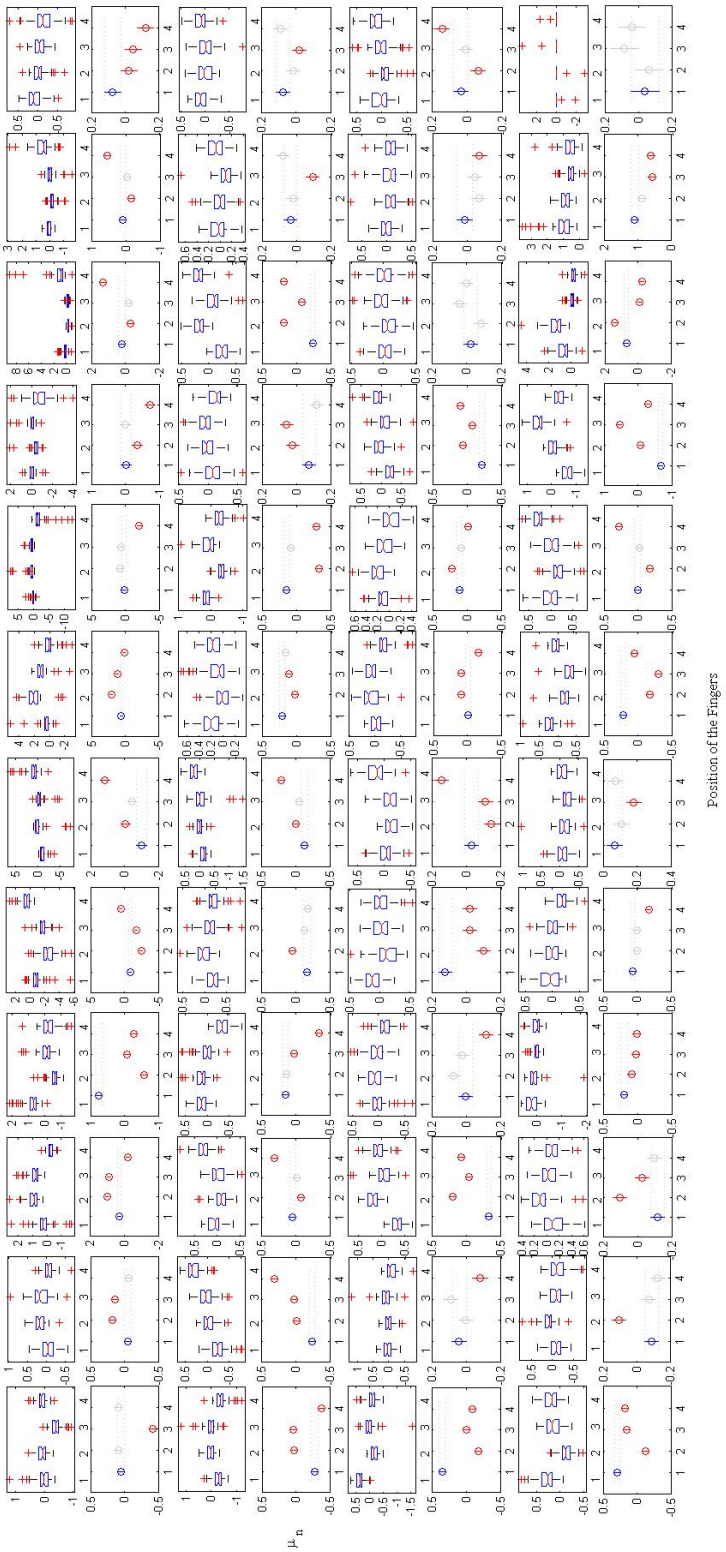

Figure 8.10: Windowed ANOVA Analyses For The Posterior Grid During Thumb Opposition Positions -

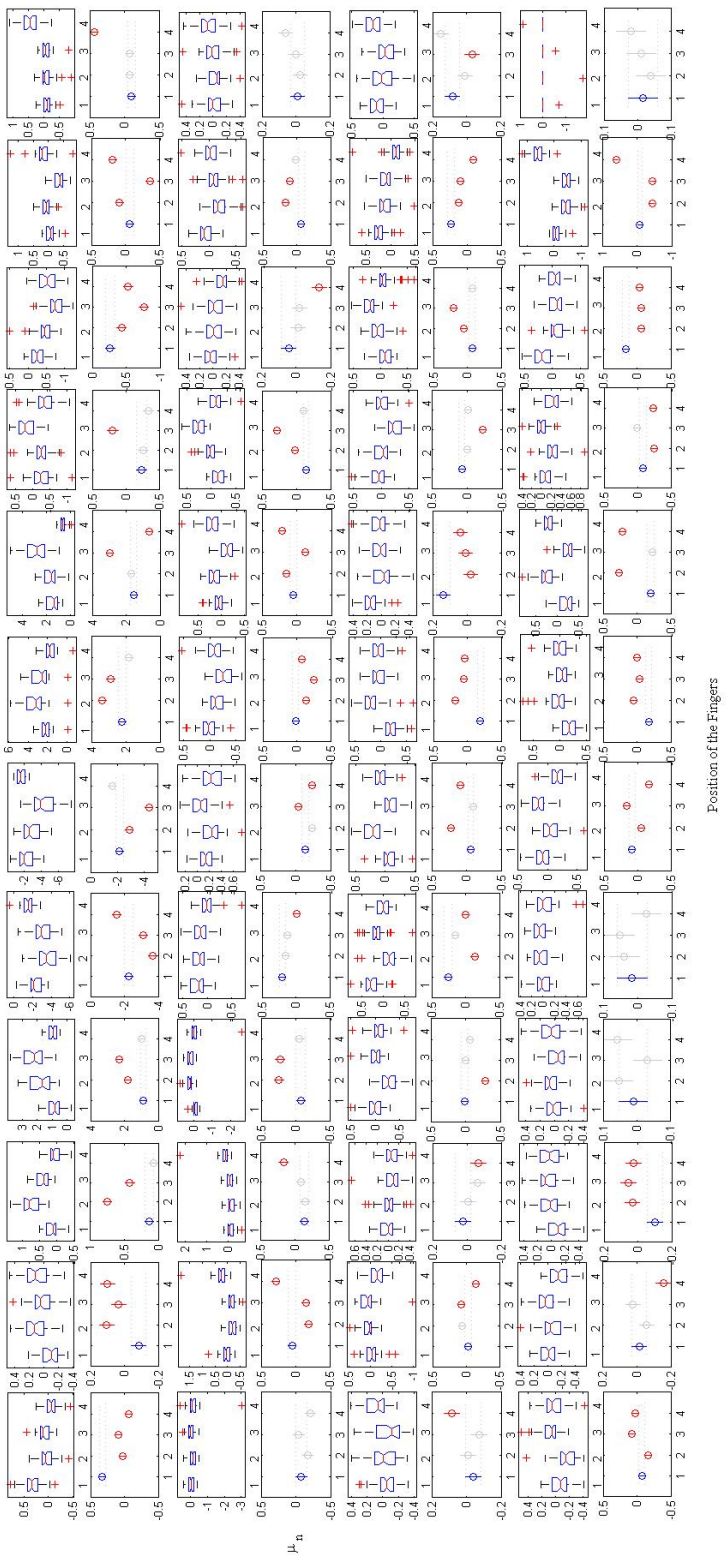

Figure 8.11: Windowed ANOVA Analyses For The Anterior Grid During Thumb Opposition Positions -

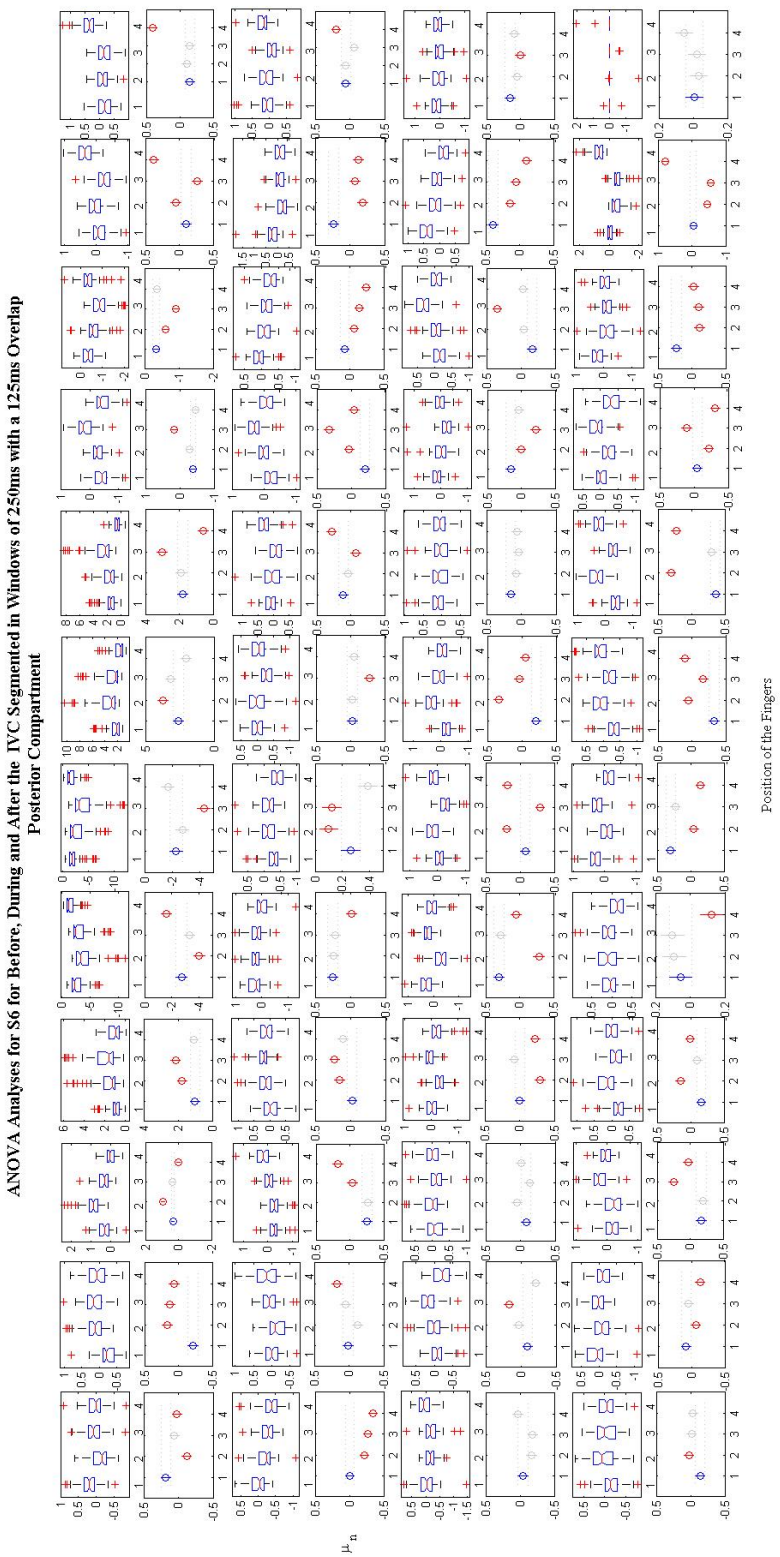

Figure 8.12: Windowed ANOVA Analyses For The Posterior Grid During Thumb Opposition Positions -

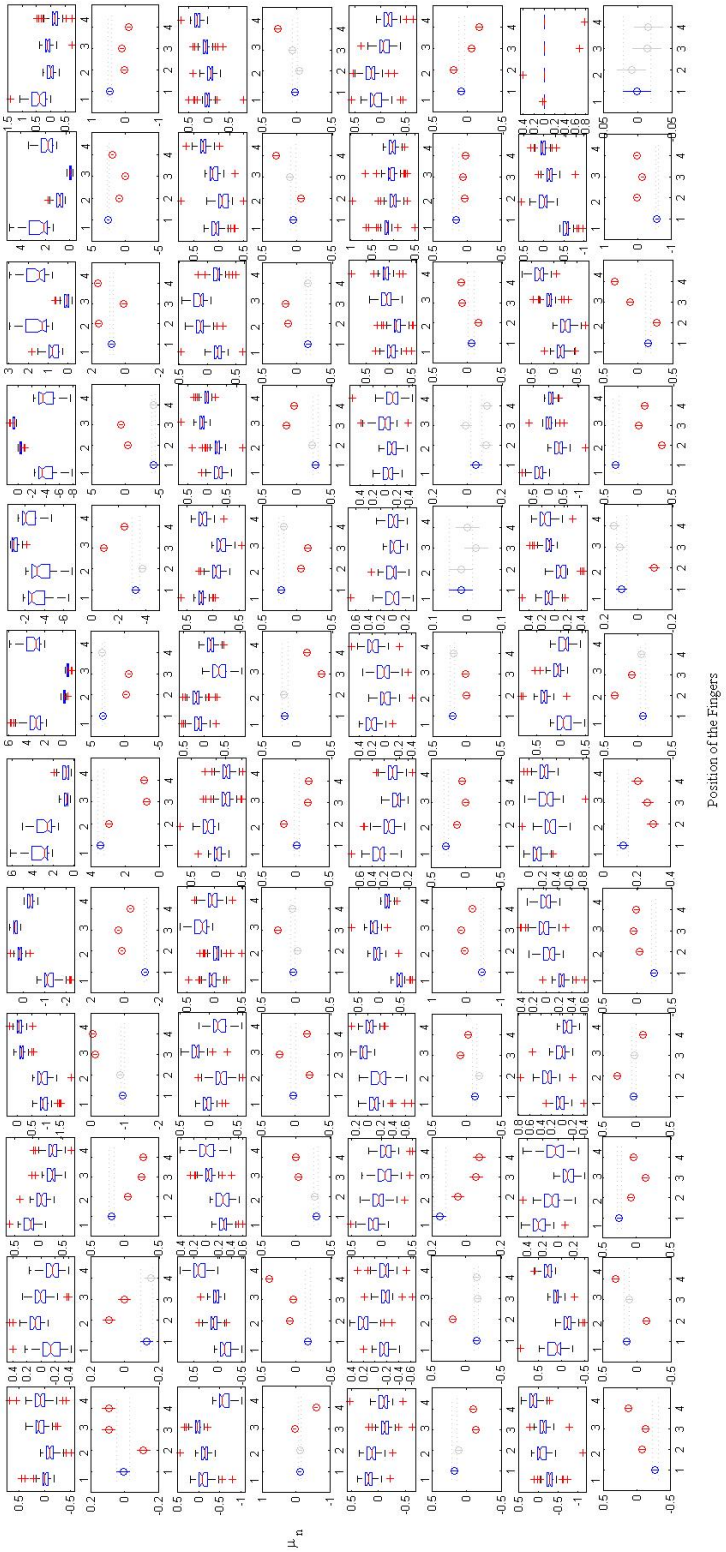

Figure 8.13: Windowed ANOVA Analyses For The Anterior Grid During Thumb Opposition Positions -

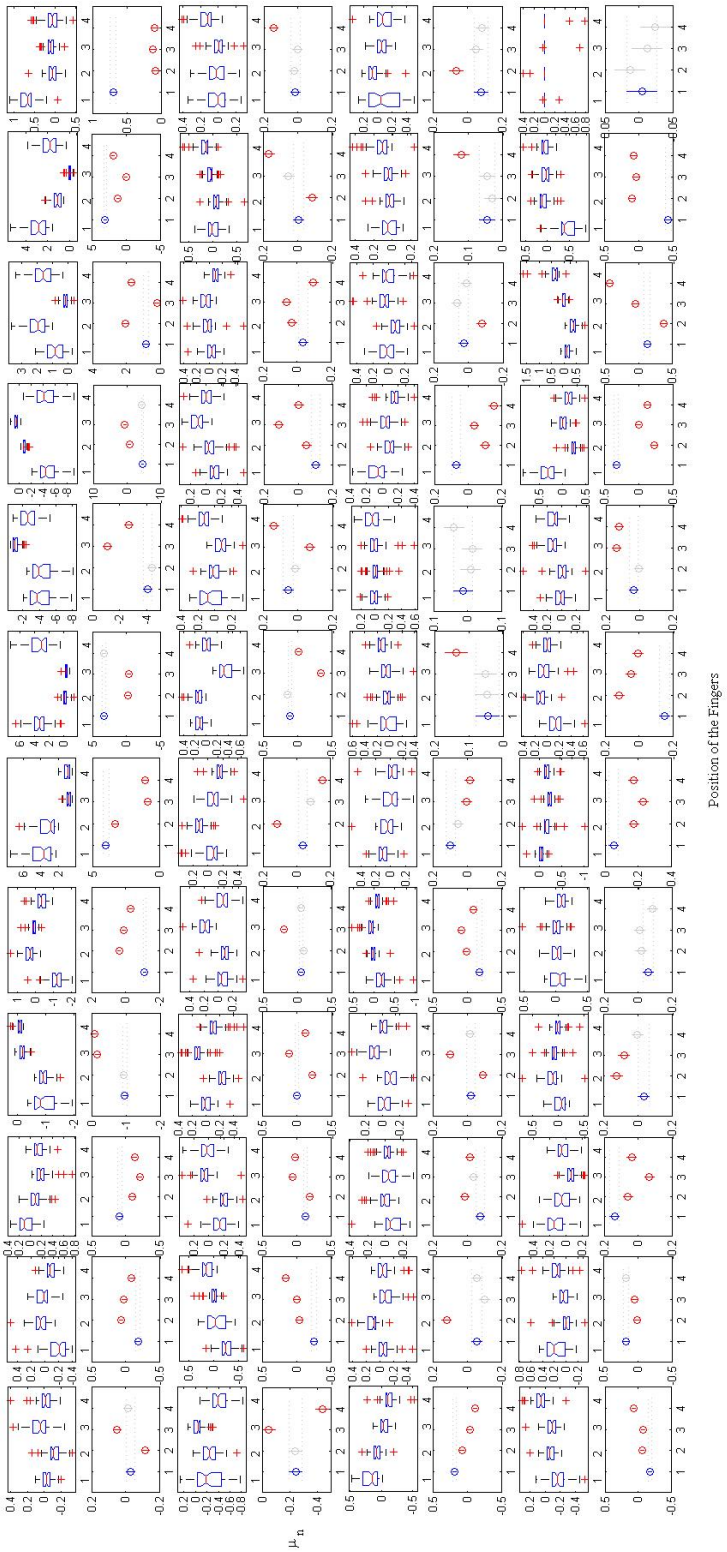

Figure 8.14: Windowed ANOVA Analyses For The Posterior Grid During Thumb Opposition Positions -

8.9 Coherence Analysis

8.9.1 Coherence Found Between Extensors and FDI Muscle During Steady Contraction

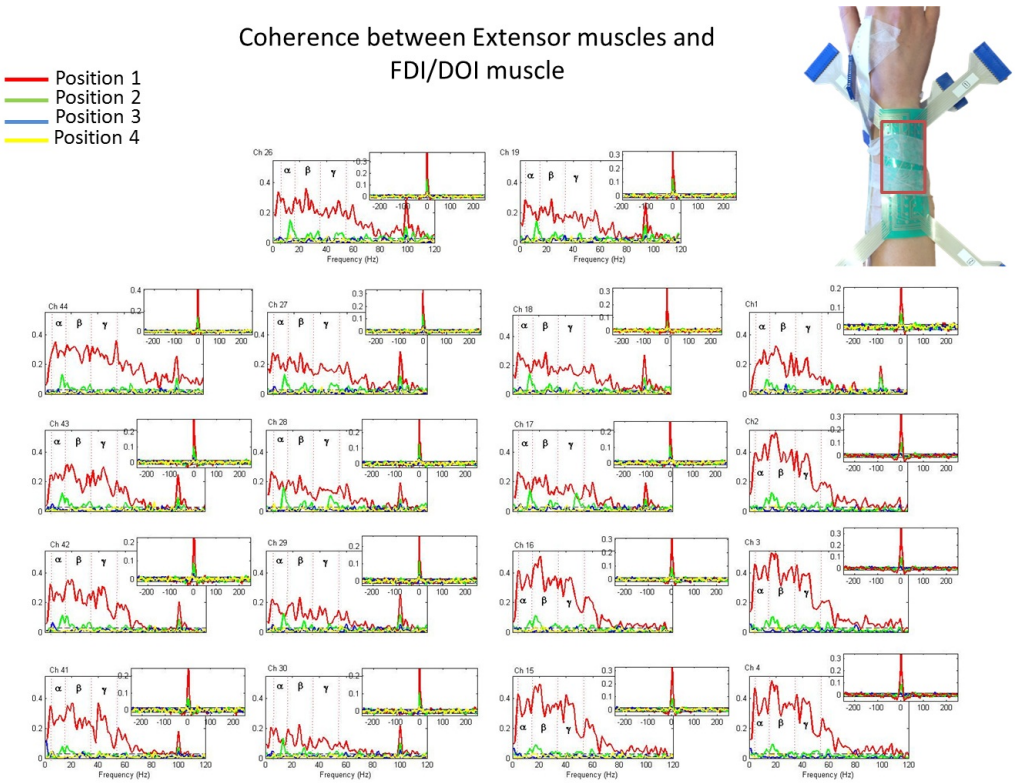

Figure 8.15: Coherence Found Between Extensors and FDI Muscle During Steady Contraction-Upper Section of the 64-electrode array - The coherence and cross-intensity analysis are shown above. On the top right it is highlighted what section of the forearm we are seeing in the graphs on the left. It can be seen that Position 1 has constant cross-talk between 1-80Hz.

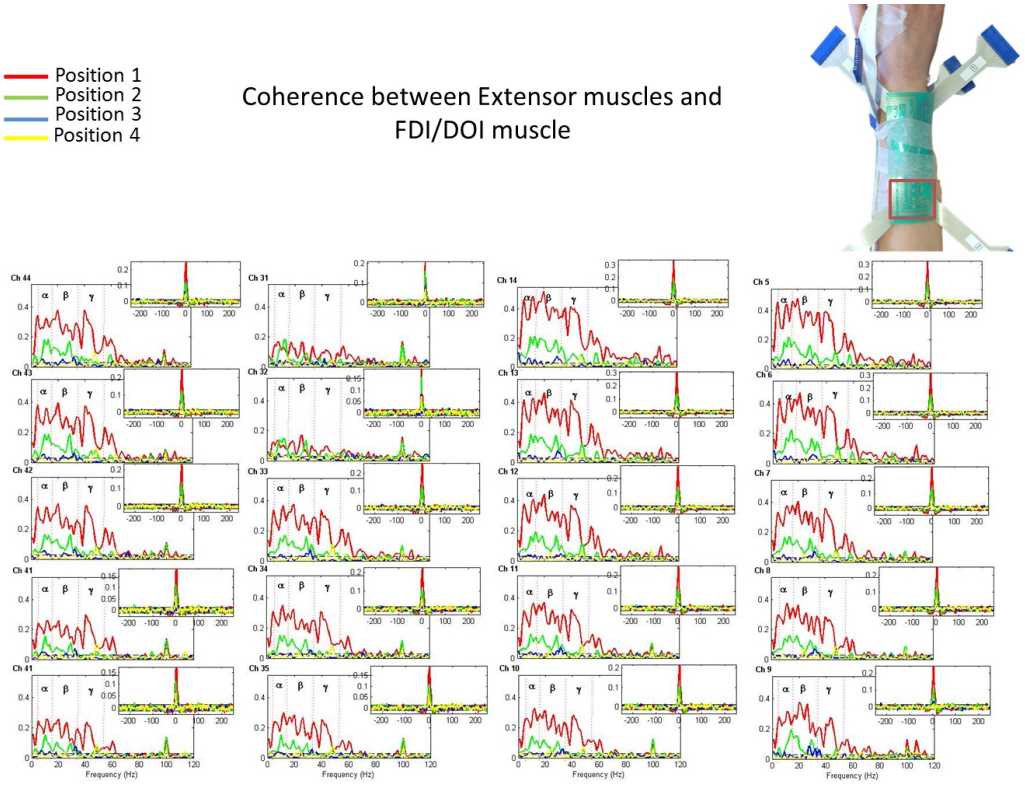

Figure 8.16: Coherence Found Between Extensors and FDI Muscle During Steady Contraction-Lower Section of the 64-electrode array - The coherence and cross-intensity analysis are shown above. On the top right it is highlighted what section of the forearm we are seeing in the graphs on the left. It can be seen that Position 1 has constant cross-talk between 1-80Hz.

8.9.2 Coherence Found Between Extensors and Thenar Muscles During Steady Contraction

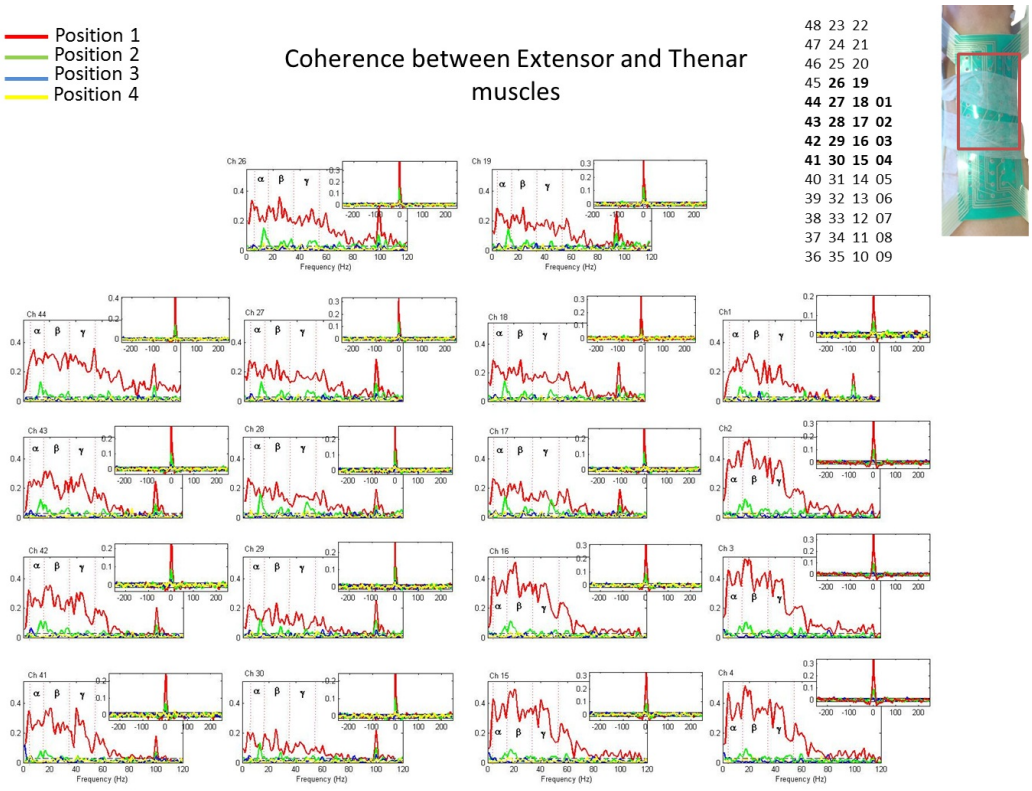

Figure 8.17: Coherence Found Between Extensors and Thenar Muscles During Steady Contraction-Upper Section of the 64-electrode array - The coherence and cross-intensity analysis are shown above. On the top right it is highlighted what section of the forearm we are seeing in the graphs on the left. It can be seen that Position 1 has constant cross-talk between 1-80Hz.

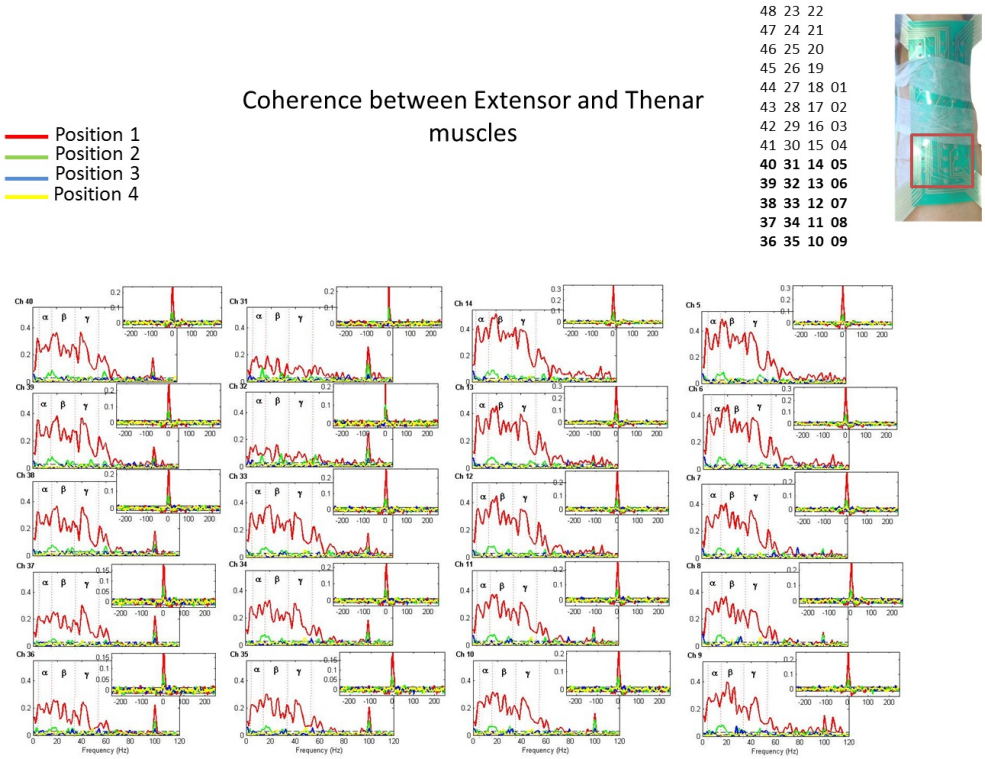

Figure 8.18: Coherence Found Between Extensors and Thenar Muscles During Steady Contraction-Lower Section of the 64-electrode array - The coherence and cross-intensity analysis are shown above. On the top right it is highlighted what section of the forearm we are seeing in the graphs on the left. It can be seen that Position 1 has constant cross-talk between 1-80Hz.

8.9.3 Coherence Found Between Flexors and FDI Muscle During Steady Contraction

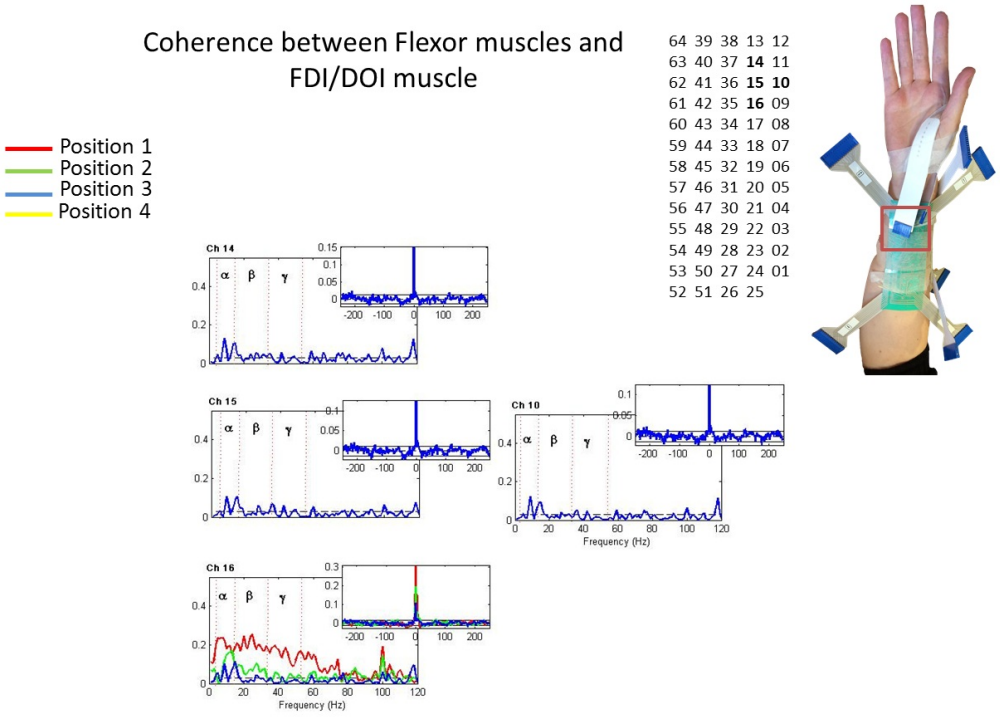

Figure 8.19: Coherence Found Between Flexor Muscles and FDI During Steady Contraction-Upper Section of the 64-electrode array - The coherence and cross-intensity analysis are shown above. On the top right it is highlighted what section of the forearm we are seeing in the graphs on the left. For three electrodes it can be seen that only position 3 was found to have coherence. This coherence is seen for a frequency range between 2-15Hz. For one electrode (shown at the bottom) the four positions are shown and position 2 is found to have a greater amplitude and a wider frequency range 5-38Hz. Furthermore, it can be seen that Position 1 has constant cross-talk between 1-80Hz.

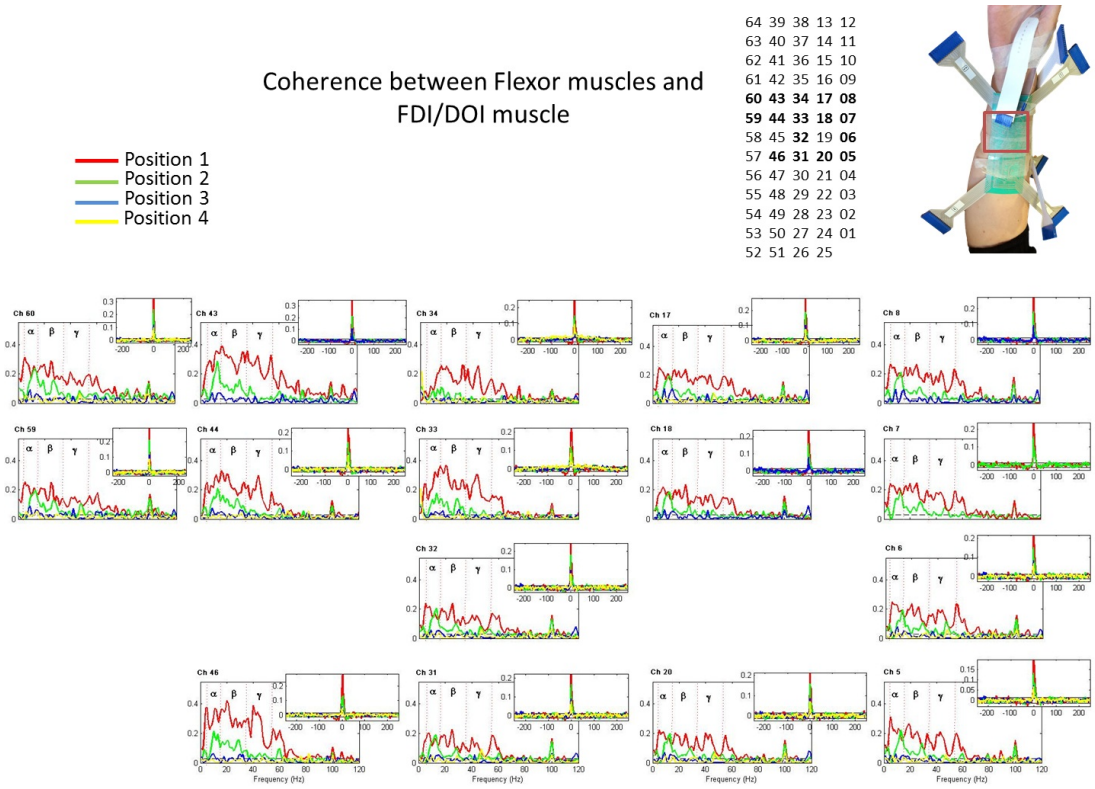

Figure 8.20: Coherence Found Between Flexor Muscles and FDI During Steady Contraction-Middle Section of the 64-electrode array - The coherence and cross-intensity analysis are shown above. On the top right it is highlighted what section of the forearm we are seeing in the graphs on the left. It can be seen that Position 1 has constant cross-talk between 1-80Hz. As for the rest of the positions, the second one has a clear single coherent frequency range from 2-35Hz. As for the third and the fourth, a frequency range of 2-15Hz is shown and a later 30-40Hz is found. It is clearly seen that these two positions have a smaller amplitude when compared to the second position.

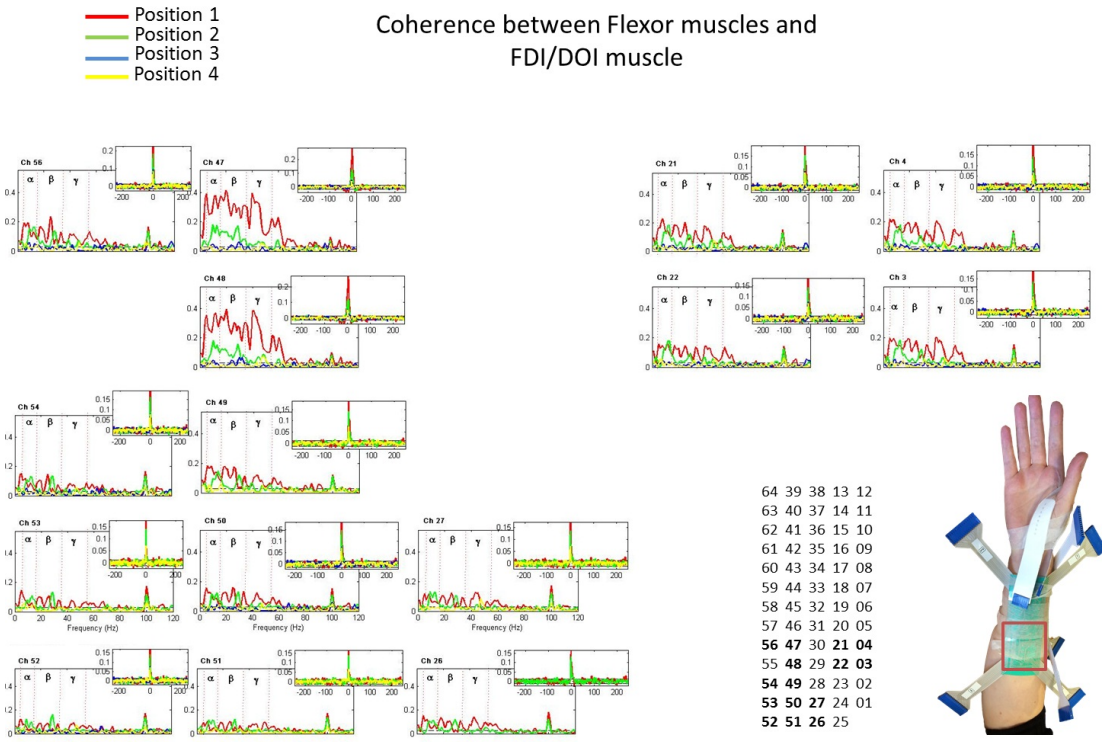

Figure 8.21: Coherence Found Between Flexor Muscles and FDI During Steady Contraction-Lower Section of the 64-electrode array - The coherence and cross-intensity analysis are shown above. On the top right it is highlighted what section of the forearm we are seeing in the graphs on the left. It can be seen that Position 1 has constant cross-talk between 1-80Hz, a decrement of the amplitude is shown from electrodes 49-54, nonetheless, it is still a constant coherence across the same frequency range as the rest. As for the other positions, the second position has a clear single coherent frequency range from 2-35Hz in most of the electrodes. As for the third, a frequency range of 2-15Hz is shown and a later 30-40Hz is found. Lastly, position four has a smaller amplitude in the peak shown in 40-45Hz.

8.9.4 Coherence Found Between Flexors and FDI Muscle During Steady Contraction

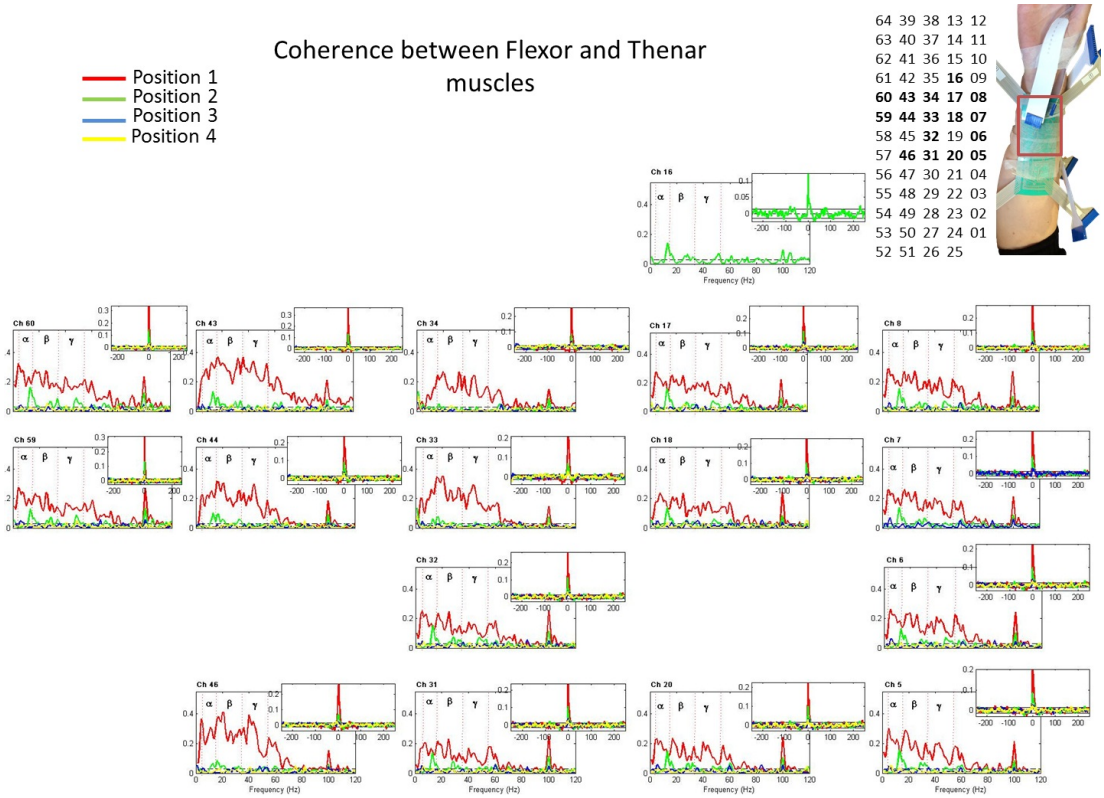

Figure 8.22: Coherence Found Between Flexor and Thenar Muscles During Steady Contraction-Upper Section of the 64-electrode array - The coherence and cross-intensity analysis are shown above. On the top right it is highlighted what section of the forearm we are seeing in the graphs on the left. Two things are visible for the coherence analysis. Firstly, position 1 has a constant cross-talk between 1-80Hz. Secondly, position 3 and 4 have none coherence for these muscle pairs and these electrodes. As for position 2, a clear lower peak is found in the frequency range of 15-20Hz overall, in some electrodes (e.g. 43,44), a second peak is found in a frequency range of 35-42Hz.

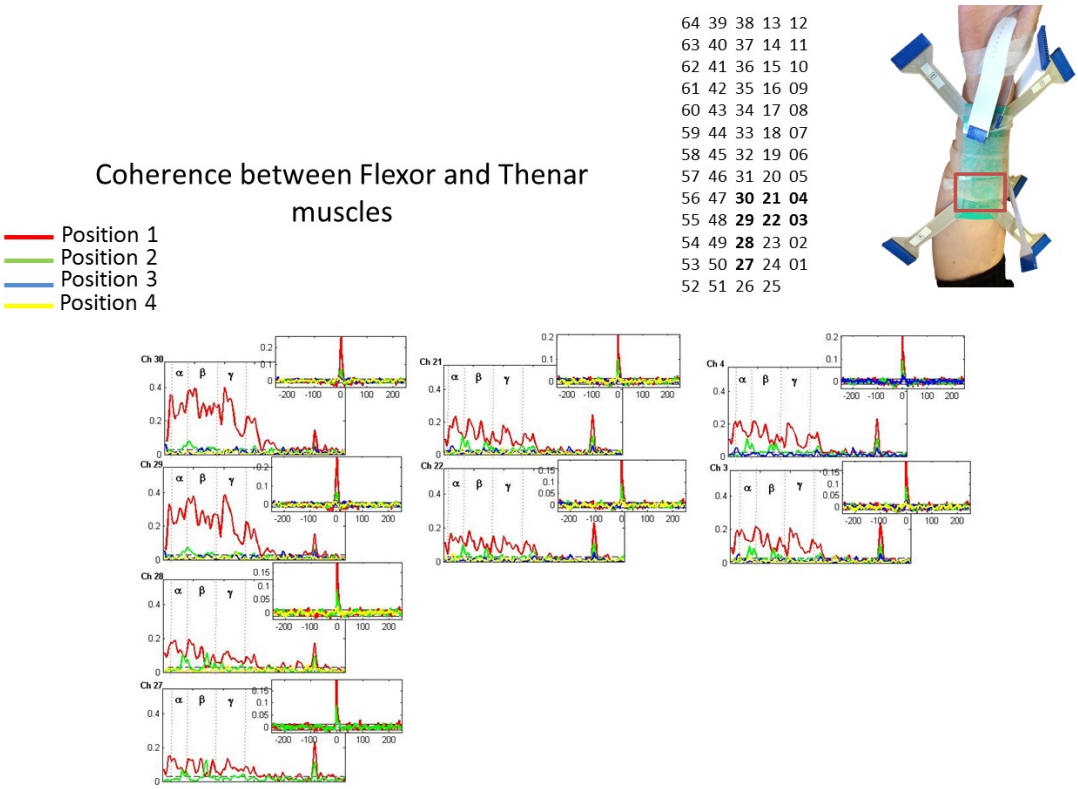

Figure 8.23: Coherence Found Between Flexor and Thenar Muscles During Steady Contraction-Middle Section of the 64-electrode array - The coherence and cross-intensity analysis are shown above. On the top right it is highlighted what section of the forearm we are seeing in the graphs on the left. Two things are visible for the coherence analysis. Firstly, position 1 has a constant cross-talk between 1-80Hz. Secondly, position 3, with exception of electrode 4 that has a peak at 5Hz, and position 4 have none coherence for these muscle pairs and these electrodes. As for position 2, a clear lower peak is found in the frequency range of 15-20Hz and a second peak is found in a frequency range of 35-42Hz.

8.10 Results After Applying SOFMs For All Subjects

As discussed in Section 1.1.5.2, a SOFM consists of a group of neurones (prototypes) organised on a low-dimensional grid. All the neurones are connected to each other by a neighbourhood relation that must be predefined which dictates the topology of the map. The same SOFMs setup was applied across the subjects: hexagonal lattice (giving no preference in the orientation the map is trained), rectangular sheet, and randomly initialised.

The size of the map was obtained through the equations described in Section 1.1.5.2 through the SOM-toolbox. All the subjects had a resulting map size of 15 by 15 neurones; furthermore, a batch training was applied through a Gaussian neighbourhood function. Finally, all the subjects were trained using 60% (randomly selected) of the total feature vectors, the remaining 40% were used to validate the clusters made by the first group of of data (testing). The results for subjects 2:7 are shown as follow:

Figure 8.24: Resulting Unified Distance Matrix in the Output Space (S2) - SOFM - Results from the grids positioned on the anterior and posterior compartment of the forearm overlying the flexor, and extensor muscles respectively. The resulting U-matrices highlight in a 3-D space the boundaries between clusters where a higher amplitude relates to a longer distance between neurones.

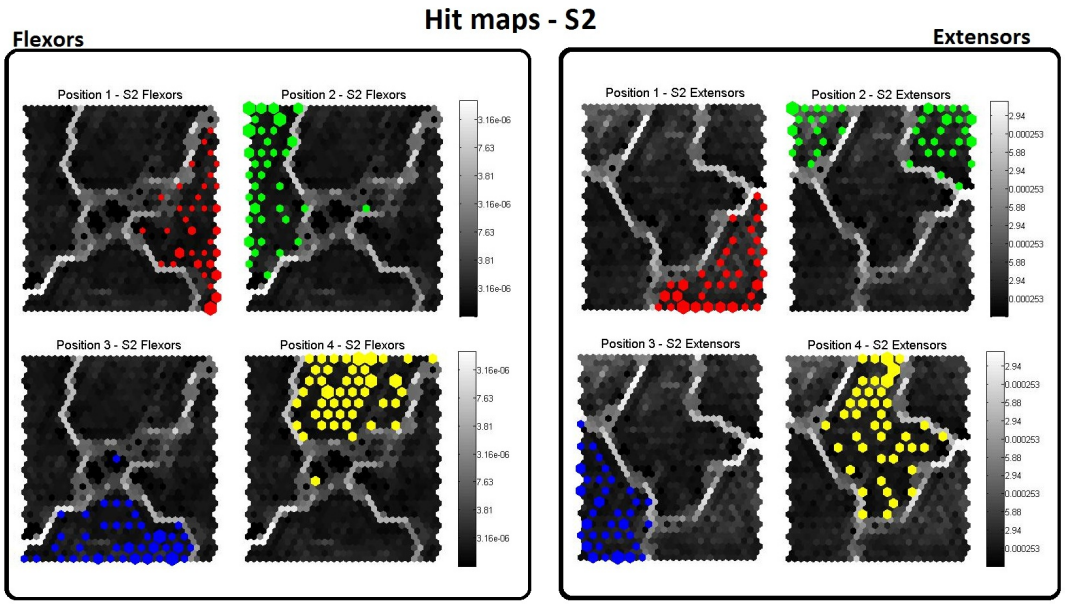

Figure 8.25: Resulting Hit Histograms Visualised in the U-Matrix - SOFM - Resulting hit histograms for each muscle group of the forearm A) extensors, B) flexors. Each hit was produced by the best matching unit found for each feature vector trained. Each unified matrix (gray scale colour map) corresponds to each position of the thumb colour coded for each muscle group.

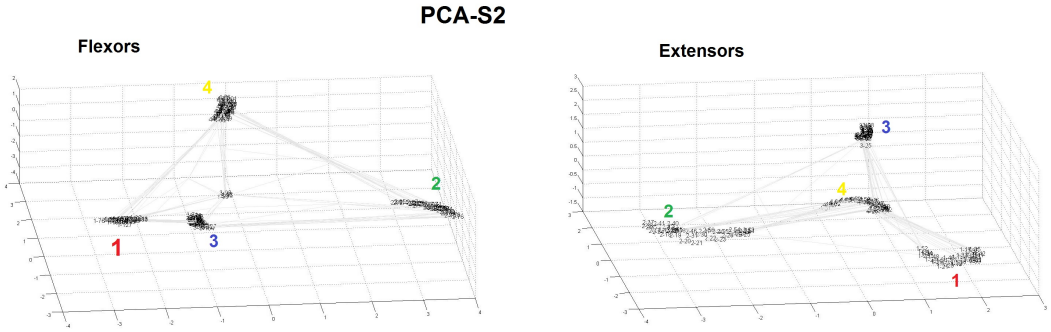

Figure 8.26: Principal Component Analysis of the Feature Vectors after Data were Trained applying SOFM - PCA of the feature vectors after SOFMs were applied to the trained data for a randomly chosen subject. Each position is represented by its corresponding number.

Table 8.1: Performance Measures for SOFM Test data (S2) - Flexor Muscles

BMU \ FV	1st Position	2nd Position	3rd Position	4th Position
1st Position	93%	1%	3%	3%
2nd Position	2%	91%	3%	4%
3rd Position	2%	5%	89%	4%
4th Position	3%	3%	5%	89%

Table 8.2: Performance Measures for SOFM Test data (S2) - Extensor Muscles

BMU \ FV	1st Position	2nd Position	3rd Position	4th Position
1st Position	89%	4%	3%	4%
2nd Position	3%	87%	5%	5%
3rd Position	2%	6%	84%	8%
4th Position	6%	3%	8%	83%

Figure 8.27: Resulting Unified Distance Matrix in the Output Space (S3) - SOFM - Results from the grids positioned on the anterior and posterior compartment of the forearm overlying the flexor, and extensor muscles respectively. The resulting U-matrices highlight in a 3-D space the boundaries between clusters where a higher amplitude relates to a longer distance between neurones.

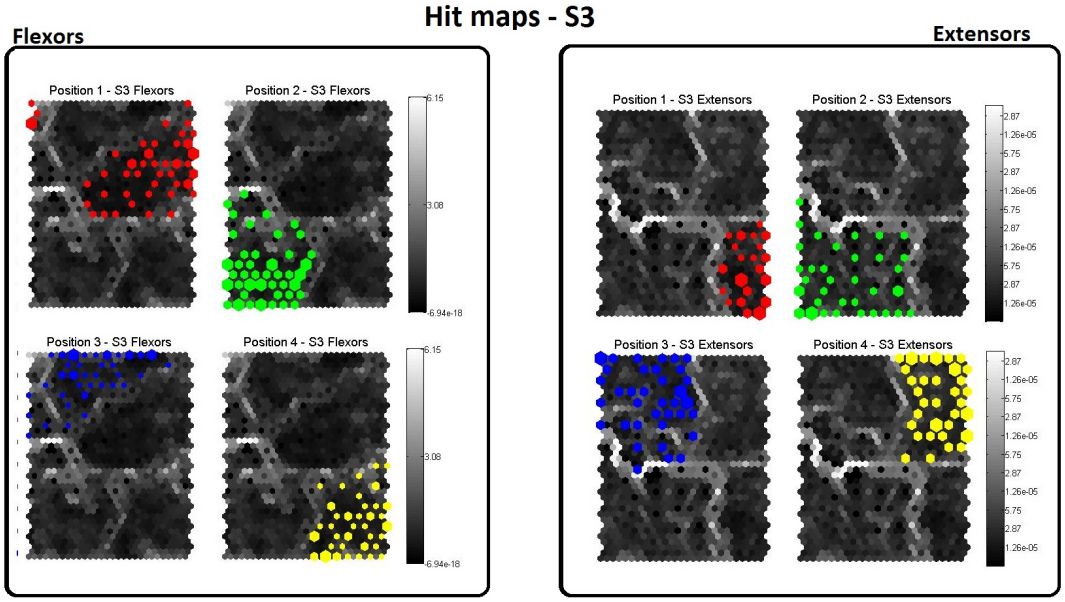

Figure 8.28: Resulting Hit Histograms Visualised in the U-Matrix - SOFM - Resulting hit histograms for each muscle group of the forearm A) extensors, B) flexors. Each hit was produced by the best matching unit found for each feature vector trained. Each unified matrix (gray scale colour map) corresponds to each position of the thumb colour coded for each muscle group.

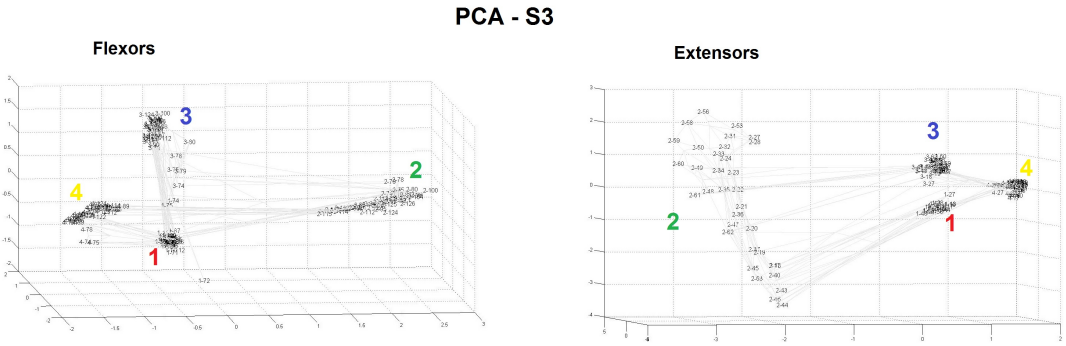

Figure 8.29: Principal Component Analysis of the Feature Vectors after Data were Trained applying SOFM - PCA of the feature vectors after SOFMs were applied to the trained data for a randomly chosen subject. Each position is represented by its corresponding number.

Table 8.3: Performance Measures for SOFM Test data (S3) - Flexor Muscles

BMU \ FV	1st Position	2nd Position	3rd Position	4th Position
1st Position	91%	3%	3%	3%
2nd Position	4%	91%	2%	3%
3rd Position	2%	3%	92%	3%
4th Position	3%	3%	3%	91%

Table 8.4: Performance Measures for SOFM Test data (S3) - Extensor Muscles

BMU \ FV	1st Position	2nd Position	3rd Position	4th Position
1st Position	86%	6%	3%	5%
2nd Position	3%	88%	4%	5%
3rd Position	4%	5%	84%	7%
4th Position	7%	1%	9%	83%

Figure 8.30: Resulting Unified Distance Matrix in the Output Space (S4) - SOFM - Results from the grids positioned on the anterior and posterior compartment of the forearm overlying the flexor, and extensor muscles respectively. The resulting U-matrices highlight in a 3-D space the boundaries between clusters where a higher amplitude relates to a longer distance between neurones.

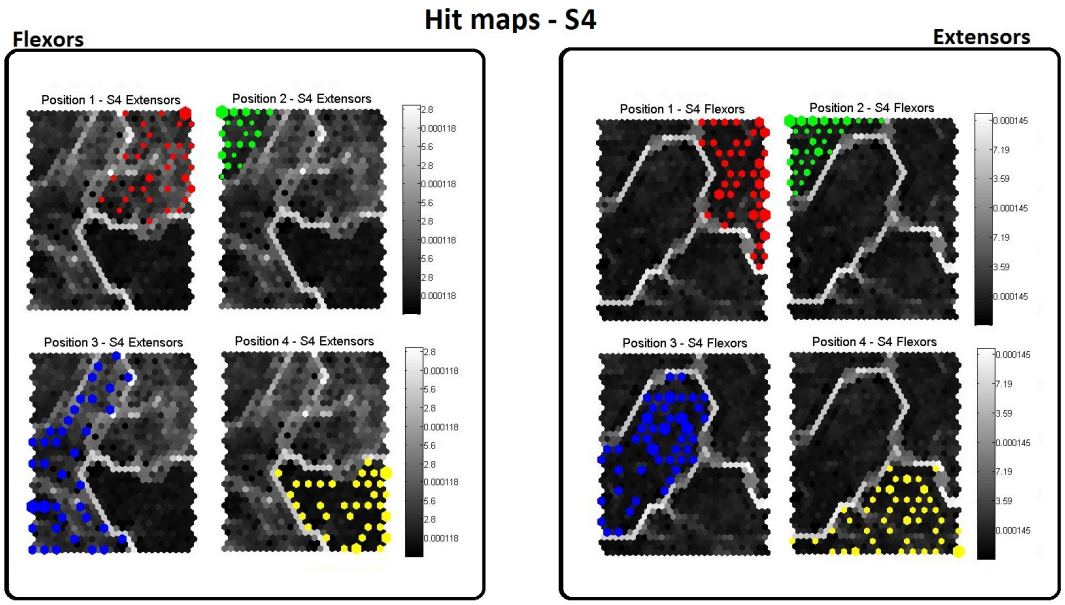

Figure 8.31: Resulting Hit Histograms Visualised in the U-Matrix - SOFM - Resulting hit histograms for each muscle group of the forearm A) extensors, B) flexors. Each hit was produced by the best matching unit found for each feature vector trained. Each unified matrix (gray scale colour map) corresponds to each position of the thumb colour coded for each muscle group.

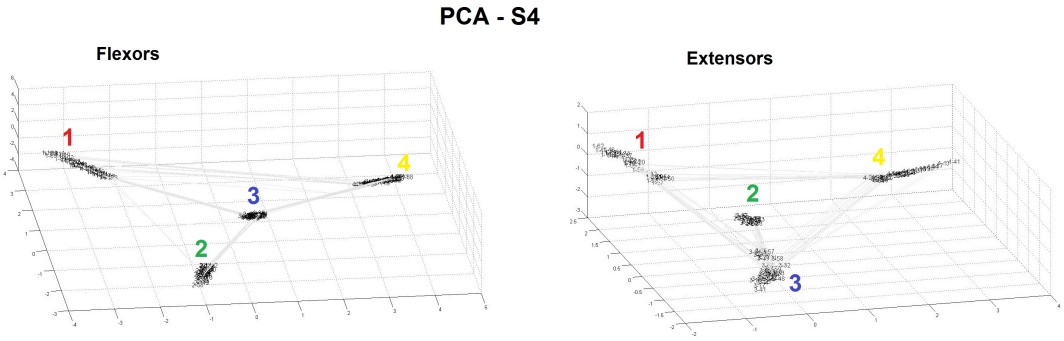

Figure 8.32: Principal Component Analysis of the Feature Vectors after Data were Trained applying SOFM - PCA of the feature vectors after SOFMs were applied to the trained data for a randomly chosen subject. Each position is represented by its corresponding number.

Table 8.5: Performance Measures for SOFM Test data (S4) - Flexor Muscles

BMU \ FV	1st Position	2nd Position	3rd Position	4th Position
1st Position	89%	4%	4%	3%
2nd Position	5%	91%	1%	3%
3rd Position	2%	3%	93%	2%
4th Position	4%	2%	2%	92%

Table 8.6: Performance Measures for SOFM Test data (S4) - Extensor Muscles

BMU \ FV	1st Position	2nd Position	3rd Position	4th Position
1st Position	85%	6%	4%	5%
2nd Position	4%	88%	4%	4%
3rd Position	3%	4%	89%	4%
4th Position	8%	2%	3%	87%

Figure 8.33: Resulting Unified Distance Matrix in the Output Space (S5) - SOFM - Results from the grids positioned on the anterior and posterior compartment of the forearm overlying the flexor, and extensor muscles respectively. The resulting U-matrices highlight in a 3-D space the boundaries between clusters where a higher amplitude relates to a longer distance between neurones.

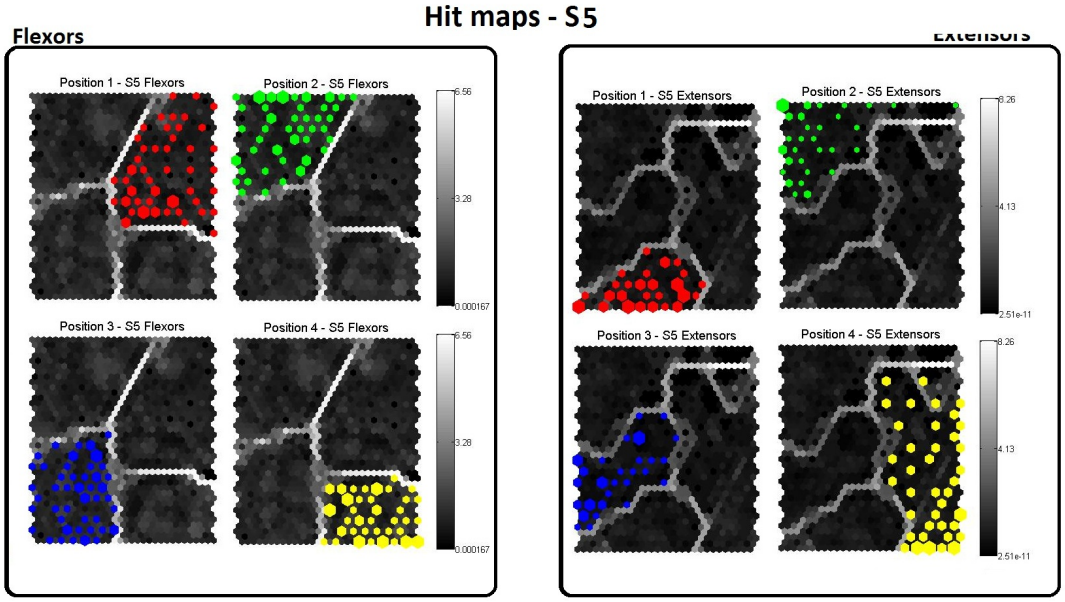

Figure 8.34: Resulting Hit Histograms Visualised in the U-Matrix - SOFM - Resulting hit histograms for each muscle group of the forearm A) extensors, B) flexors. Each hit was produced by the best matching unit found for each feature vector trained. Each unified matrix (gray scale colour map) corresponds to each position of the thumb colour coded for each muscle group.

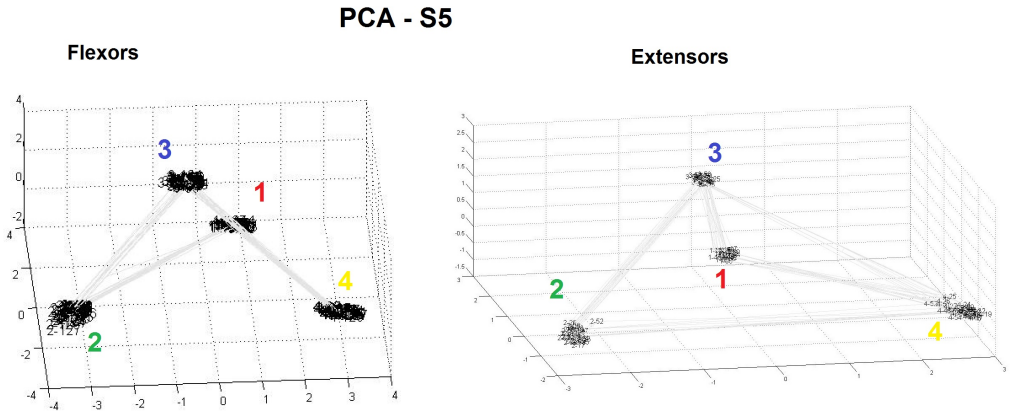

Figure 8.35: Principal Component Analysis of the Feature Vectors after Data were Trained applying SOFM - PCA of the feature vectors after SOFMs were applied to the trained data for a randomly chosen subject. Each position is represented by its corresponding number.

Table 8.7: Performance Measures for SOFM Test data (S5) - Flexor Muscles

BMU \ FV	1st Position	2nd Position	3rd Position	4th Position
1st Position	92%	2%	1%	5%
2nd Position	4%	88%	3%	5%
3rd Position	2%	4%	91%	3%
4th Position	2%	6%	5%	87%

Table 8.8: Performance Measures for SOFM Test data (S5) - Extensor Muscles

BMU \ FV	1st Position	2nd Position	3rd Position	4th Position
1st Position	86%	6%	4%	5%
2nd Position	4%	91%	4%	4%
3rd Position	3%	4%	87%	4%
4th Position	8%	2%	3%	89%

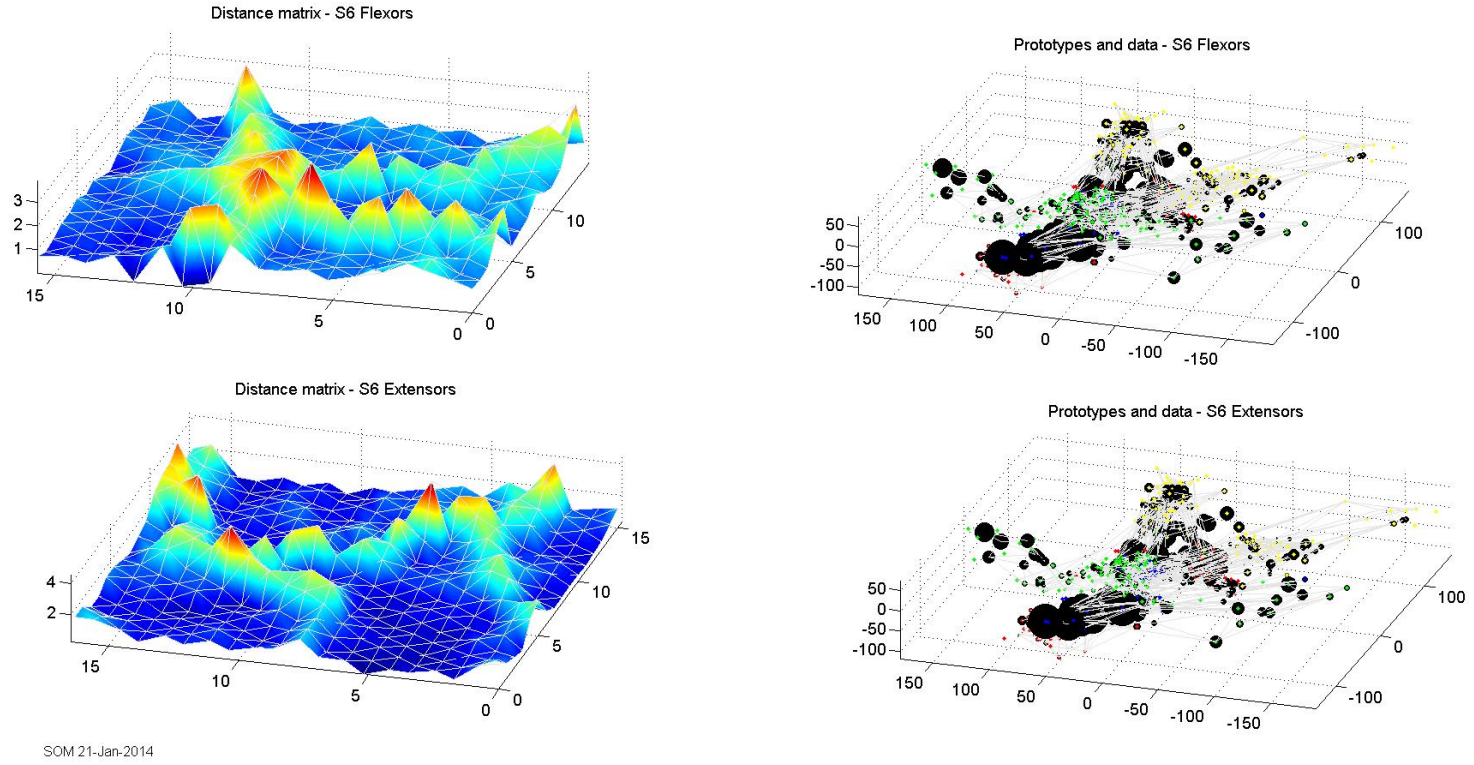

Figure 8.36: Resulting Unified Distance Matrix in the Output Space (S6) - SOFM - Results from the grids positioned on the anterior and posterior compartment of the forearm overlying the flexor, and extensor muscles respectively. The resulting U-matrices highlight in a 3-D space the boundaries between clusters where a higher amplitude relates to a longer distance between neurones.

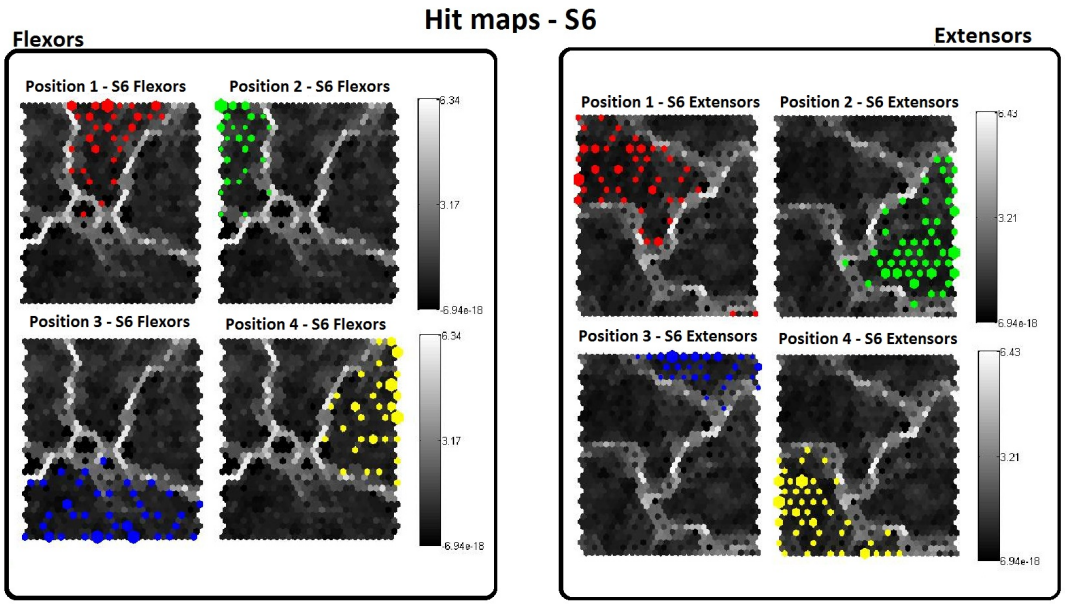

Figure 8.37: Resulting Hit Histograms Visualised in the U-Matrix - SOFM - Resulting hit histograms for each muscle group of the forearm A) extensors, B) flexors. Each hit was produced by the best matching unit found for each feature vector trained. Each unified matrix (gray scale colour map) corresponds to each position of the thumb colour coded for each muscle group.

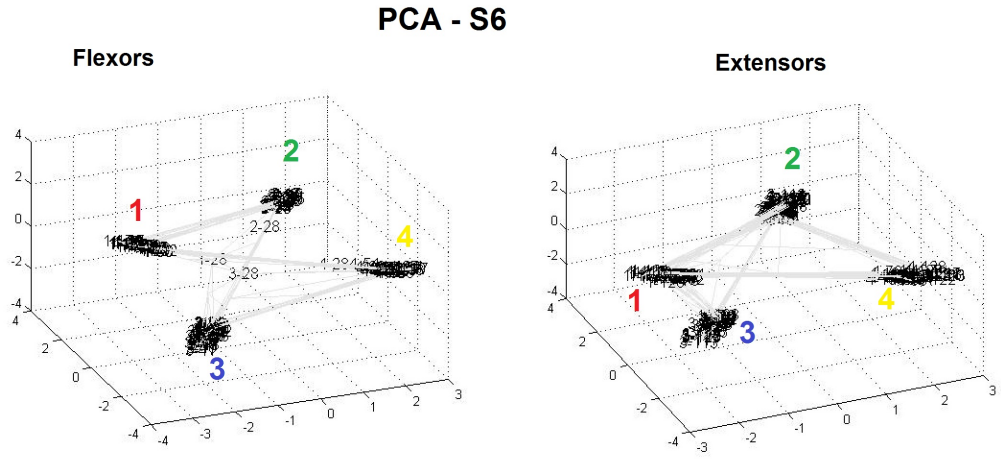

Figure 8.38: Principal Component Analysis of the Feature Vectors after Data were Trained applying SOFM - PCA of the feature vectors after SOFMs were applied to the trained data for a randomly chosen subject. Each position is represented by its corresponding number.

Table 8.9: Performance Measures for SOFM Test data (S6) - Flexor Muscles

BMU \ FV	1st Position	2nd Position	3rd Position	4th Position
1st Position	91%	2%	2%	5%
2nd Position	4%	89%	3%	4%
3rd Position	3%	3%	88%	6%
4th Position	2%	6%	7%	85%

Table 8.10: Performance Measures for SOFM Test data (S6) - Extensor Muscles

BMU \ FV	1st Position	2nd Position	3rd Position	4th Position
1st Position	87%	6%	4%	3%
2nd Position	4%	93%	1%	2%
3rd Position	3%	1%	89%	7%
4th Position	6%	0%	6%	88%

Figure 8.39: Resulting Unified Distance Matrix in the Output Space (S7) - SOFM - Results from the grids positioned on the anterior and posterior compartment of the forearm overlying the flexor, and extensor muscles respectively. The resulting U-matrices highlight in a 3-D space the boundaries between clusters where a higher amplitude relates to a longer distance between neurones.

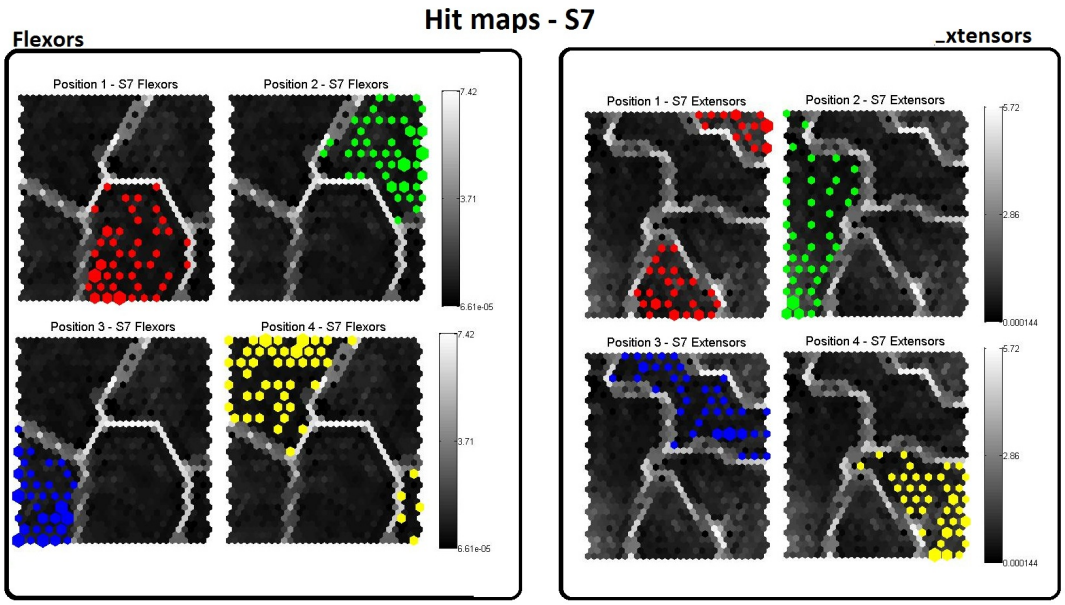

Figure 8.40: Resulting Hit Histograms Visualised in the U-Matrix - SOFM - Resulting hit histograms for each muscle group of the forearm A) extensors, B) flexors. Each hit was produced by the best matching unit found for each feature vector trained. Each unified matrix (gray scale colour map) corresponds to each position of the thumb colour coded for each muscle group.

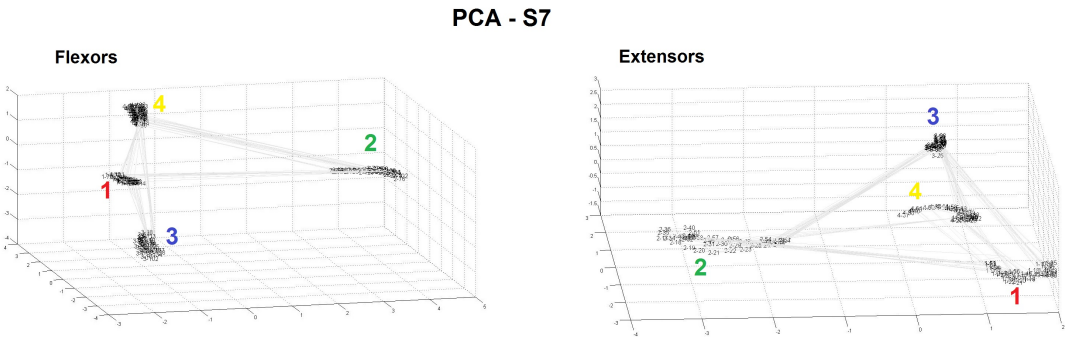

Figure 8.41: Principal Component Analysis of the Feature Vectors after Data were Trained applying SOFM - PCA of the feature vectors after SOFMs were applied to the trained data for a randomly chosen subject. Each position is represented by its corresponding number.

Table 8.11: Performance Measures for SOFM Test data (S7) - Flexor Muscles

BMU \ FV	1st Position	2nd Position	3rd Position	4th Position
1st Position	89%	2%	4%	5%
2nd Position	4%	87%	5%	4%
3rd Position	5%	5%	88%	2%
4th Position	2%	6%	3%	89%

Table 8.12: Performance Measures for SOFM Test data (S7) - Extensor Muscles

BMU \ FV	1st Position	2nd Position	3rd Position	4th Position
1st Position	87%	6%	4%	3%
2nd Position	4%	89%	4%	3%
3rd Position	3%	3%	87%	7%
4th Position	6%	2%	5%	87%

8.11 Validation Results after Applying Matlab's Pattern Recognition Toolbox

8.11.1 Best Validation Performance Separated by Subject and Muscle Group

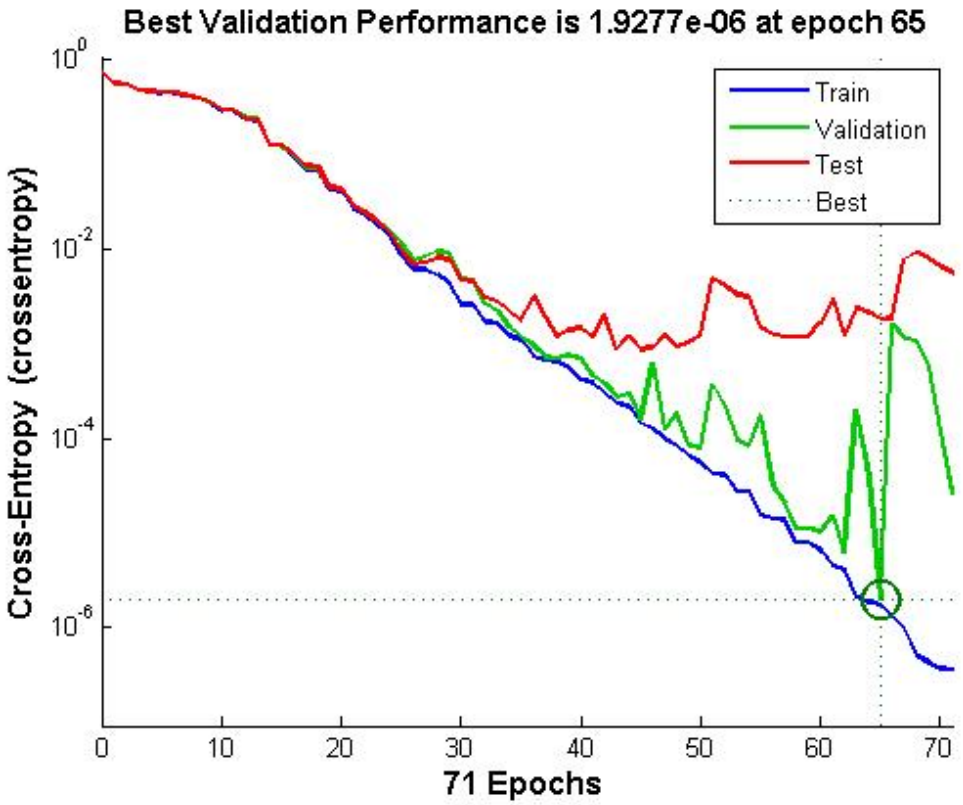

Figure 8.42: Best Validation Performance on the Anterior Compartment for S2 - Best validation performance found after the unsupervised Levenberg-Marquardt validation applied with Matlab's feature pattern recognition toolbox. The resulting performance from the flexor muscles of the forearm for randomly chosen subject (consistent with the previous results), and during a typical test. The best validation performance is found at epoch 65 with a cross-entropy of 1.927e-06.

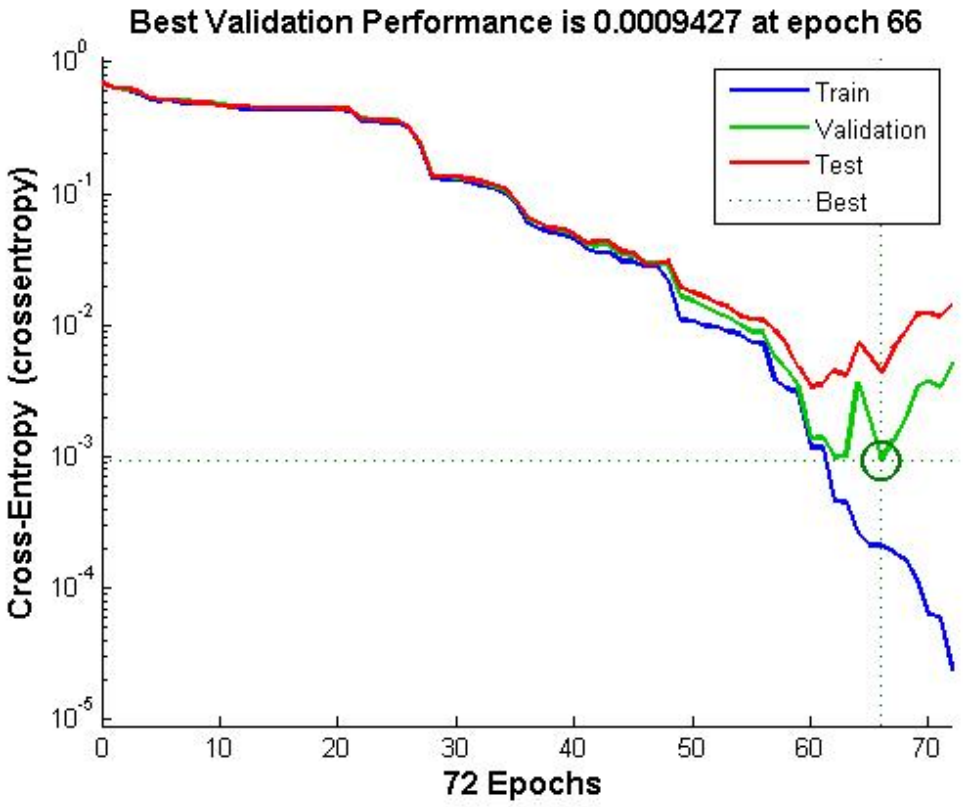

Figure 8.43: Best Validation Performance on the Posterior Compartment for S2 - Best validation performance found after the unsupervised Levenberg-Marquardt validation applied with Matlab's feature pattern recognition toolbox. The resulting performance from the extensor muscles of the forearm for typical subject (consistent with the previous results), and during a typical test. The best validation performance is found at epoch 66 with a cross-entropy of 0.00094 .

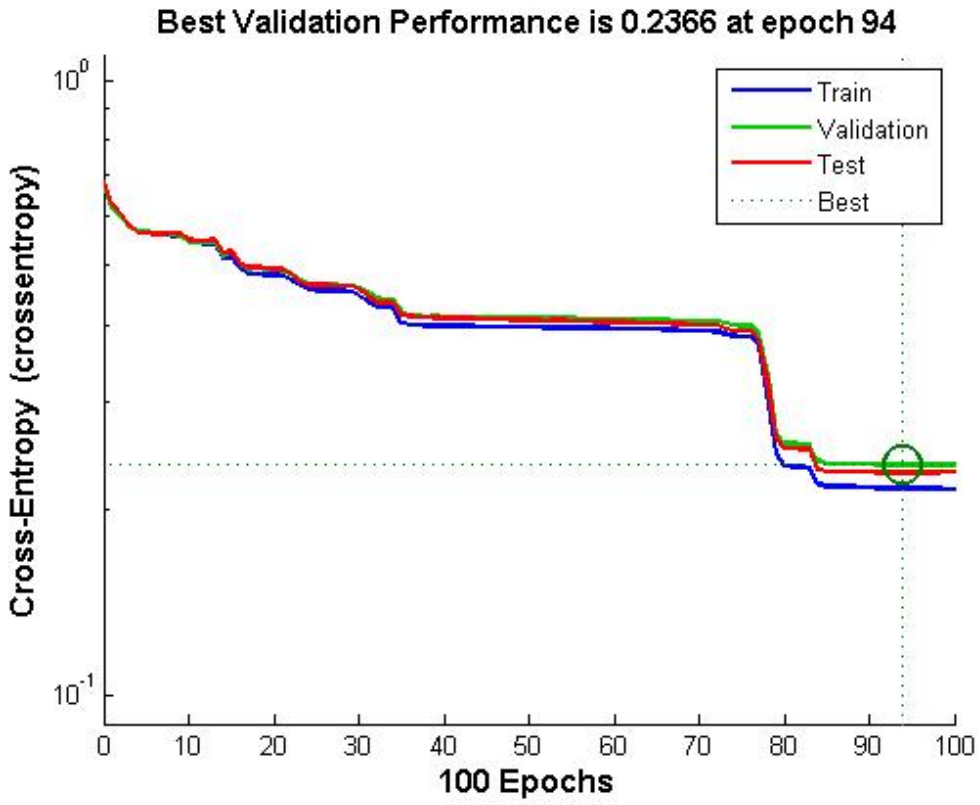

Figure 8.44: Best Validation Performance on the Anterior Compartment for S3 - Best validation performance found after the unsupervised Levenberg-Marquardt validation applied with Matlab's feature pattern recognition toolbox. The resulting performance from the flexor muscles of the forearm for randomly chosen subject (consistent with the previous results), and during a typical test. The best validation performance is found at epoch 94 with a cross-entropy of 0.2366 .

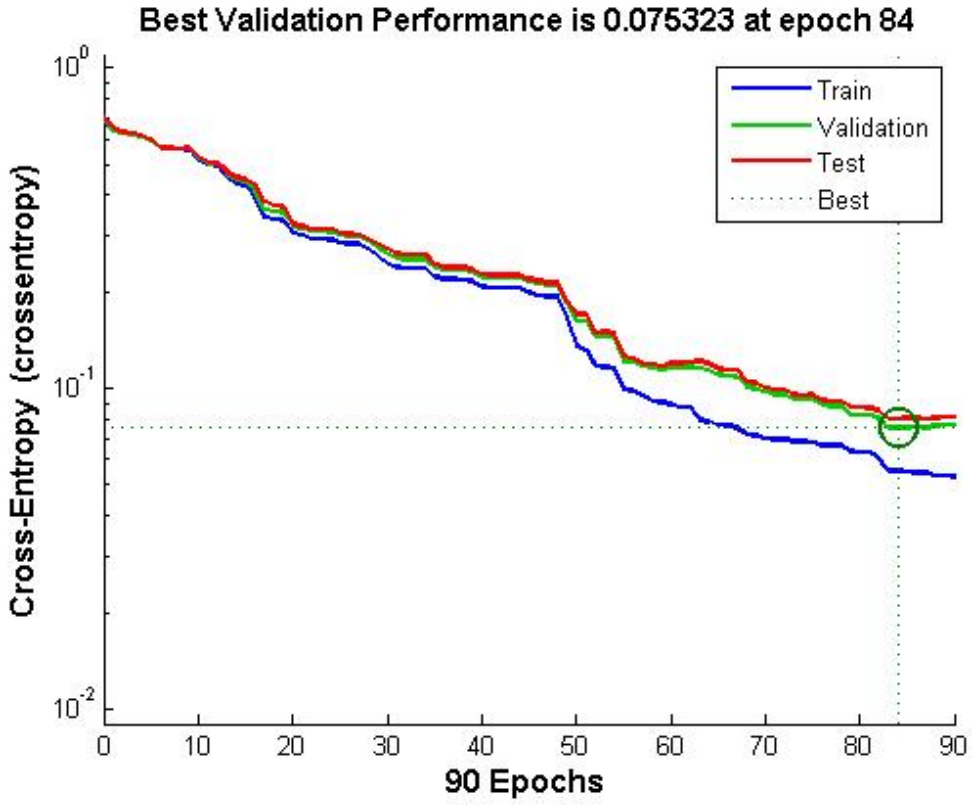

Figure 8.45: Best Validation Performance on the Posterior Compartment for S3 - Best validation performance found after the unsupervised Levenberg-Marquardt validation applied with Matlab's feature pattern recognition toolbox. The resulting performance from the extensor muscles of the forearm for typical subject (consistent with the previous results), and during a typical test. The best validation performance is found at epoch 84 with a cross-entropy of 0.0753 .

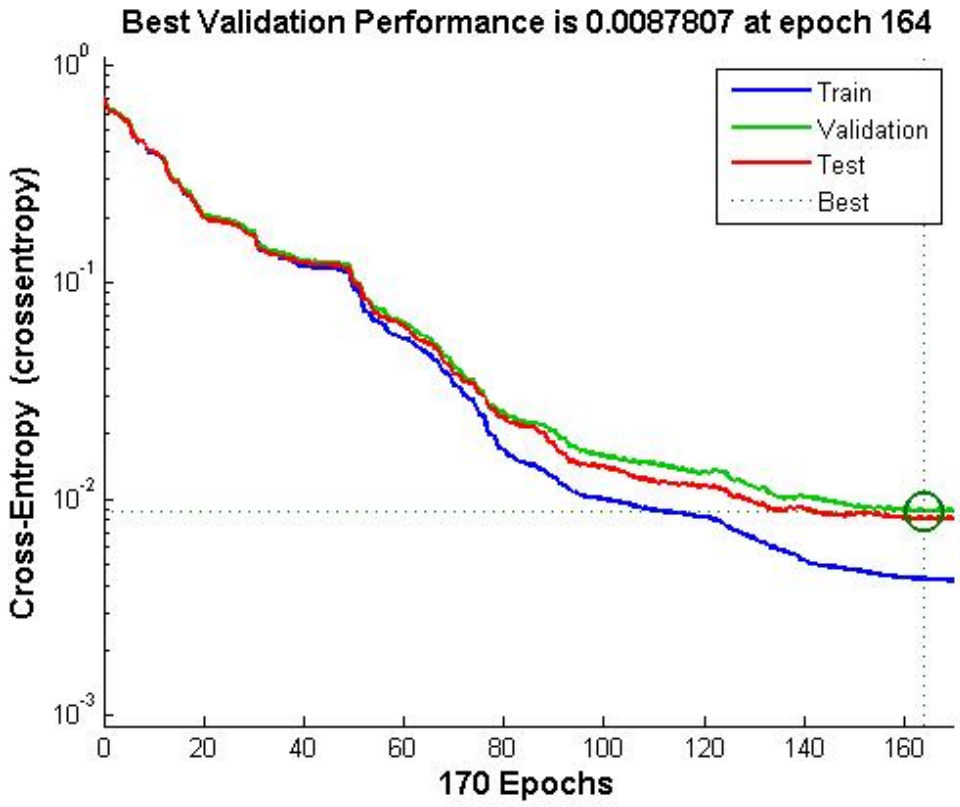

Figure 8.46: Best Validation Performance on the Anterior Compartment for S4 - Best validation performance found after the unsupervised Levenberg-Marquardt validation applied with Matlab's feature pattern recognition toolbox. The resulting performance from the flexor muscles of the forearm for randomly chosen subject (consistent with the previous results), and during a typical test. The best validation performance is found at epoch 164 with a cross-entropy of 0.0087 .

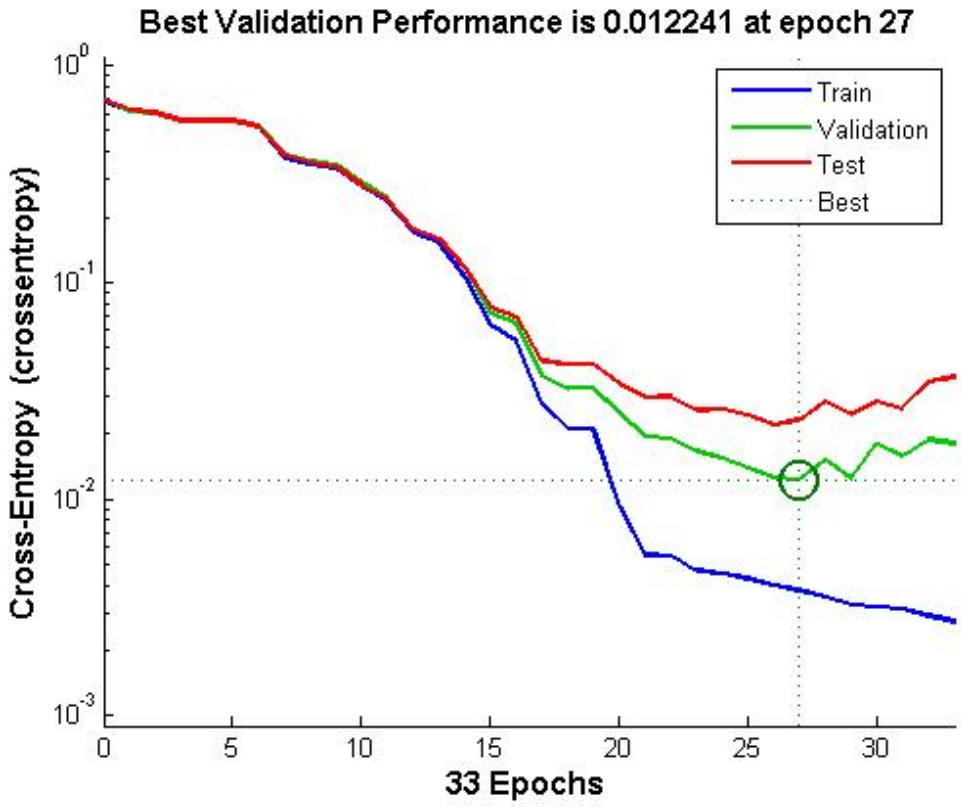

Figure 8.47: Best Validation Performance on the Posterior Compartment for S4 - Best validation performance found after the unsupervised Levenberg-Marquardt validation applied with Matlab's feature pattern recognition toolbox. The resulting performance from the extensor muscles of the forearm for typical subject (consistent with the previous results), and during a typical test. The best validation performance is found at epoch 27 with a cross-entropy of 0.0122 .

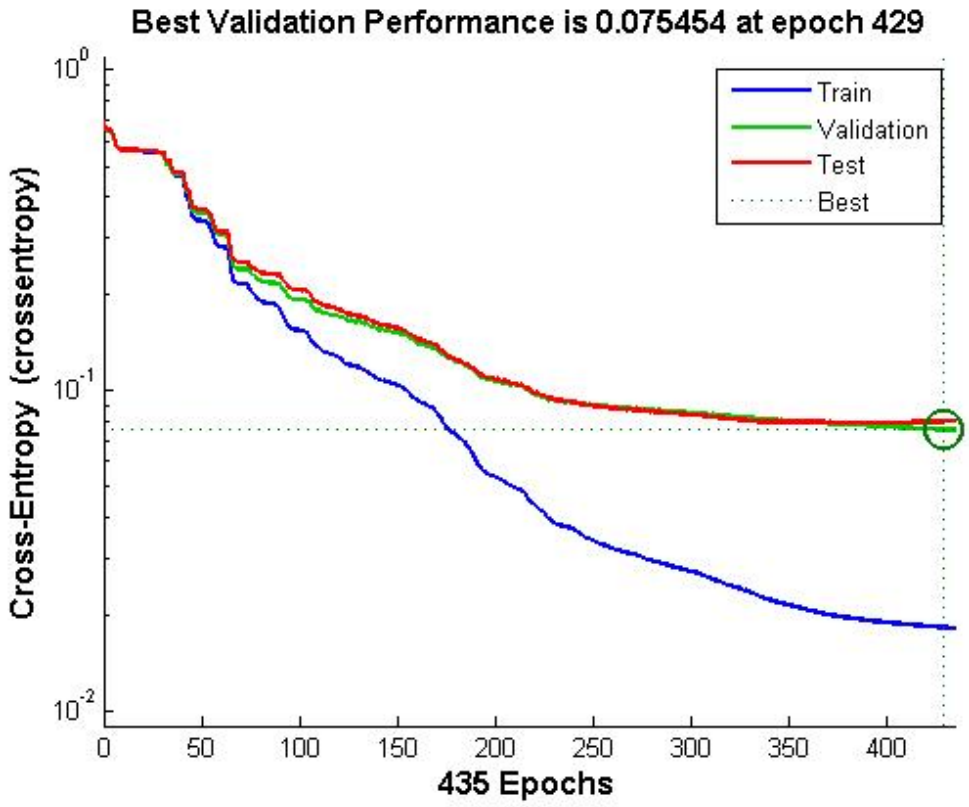

Figure 8.48: Best Validation Performance on the Anterior Compartment for S5 - Best validation performance found after the unsupervised Levenberg-Marquardt validation applied with Matlab's feature pattern recognition toolbox. The resulting performance from the flexor muscles of the forearm for randomly chosen subject (consistent with the previous results), and during a typical test. The best validation performance is found at epoch 429 with a cross-entropy of 0.0754

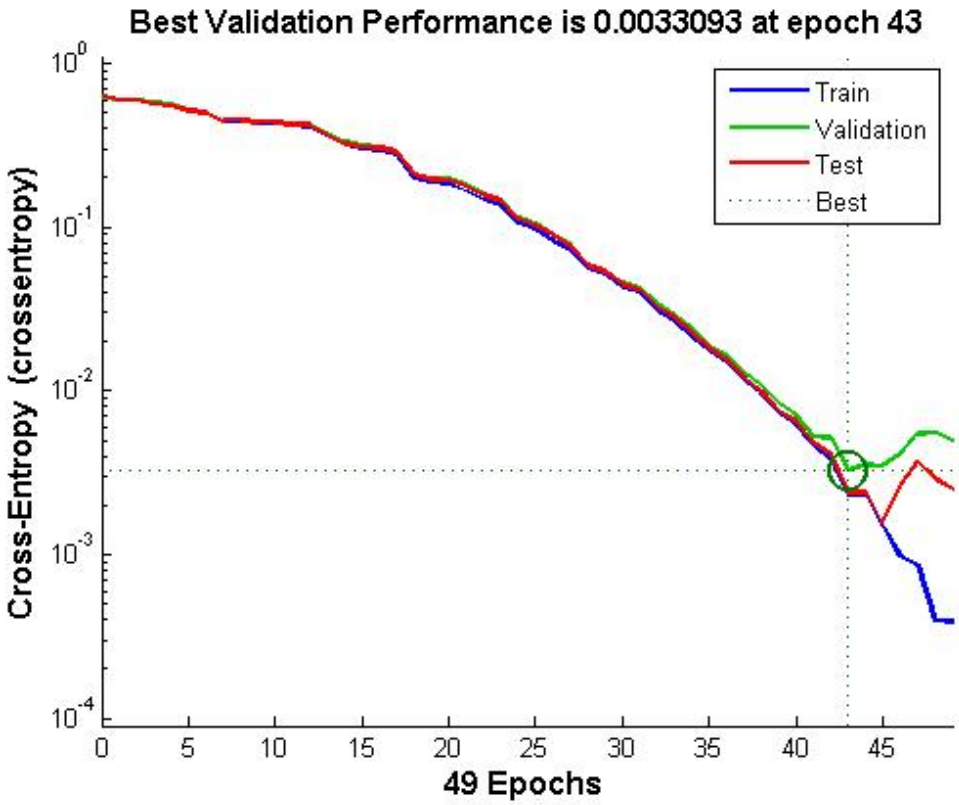

Figure 8.49: Best Validation Performance on the Posterior Compartment for S5 - Best validation performance found after the unsupervised Levenberg-Marquardt validation applied with Matlab's feature pattern recognition toolbox. The resulting performance from the extensor muscles of the forearm for typical subject (consistent with the previous results), and during a typical test. The best validation performance is found at epoch 43with a cross-entropy of 0.0033 .

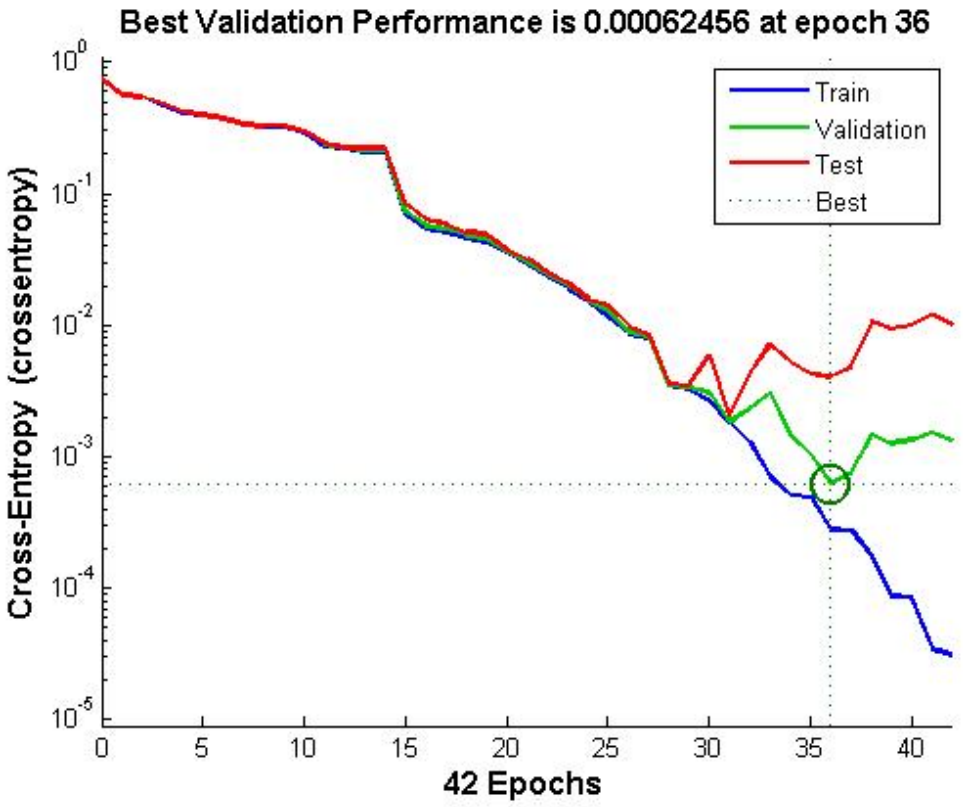

Figure 8.50: Best Validation Performance on the Anterior Compartment for S6 - Best validation performance found after the unsupervised Levenberg-Marquardt validation applied with Matlab's feature pattern recognition toolbox. The resulting performance from the flexor muscles of the forearm for randomly chosen subject (consistent with the previous results), and during a typical test. The best validation performance is found at epoch 36 with a cross-entropy of 0.00062 .

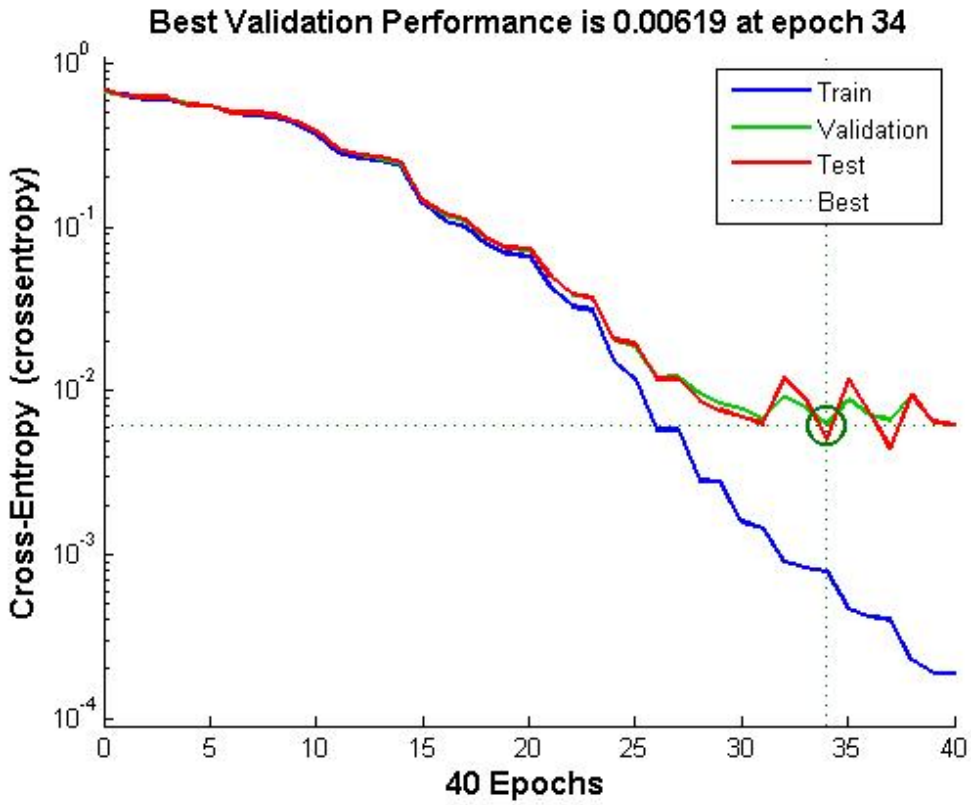

Figure 8.51: Best Validation Performance on the Posterior Compartment for S6 - Best validation performance found after the unsupervised Levenberg-Marquardt validation applied with Matlab's feature pattern recognition toolbox. The resulting performance from the extensor muscles of the forearm for typical subject (consistent with the previous results), and during a typical test. The best validation performance is found at epoch 34 with a cross-entropy of0.00619 .

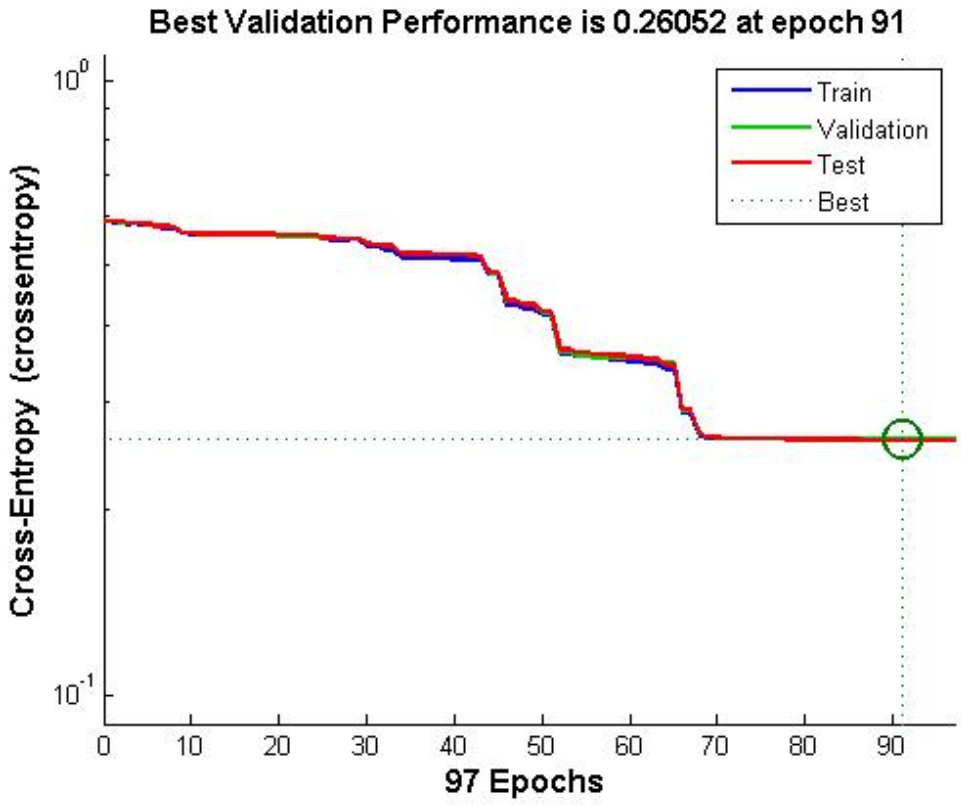

Figure 8.52: Best Validation Performance on the Anterior Compartment for S7 - Best validation performance found after the unsupervised Levenberg-Marquardt validation applied with Matlab's feature pattern recognition toolbox. The resulting performance from the flexor muscles of the forearm for randomly chosen subject (consistent with the previous results), and during a typical test. The best validation performance is found at epoch 91 with a cross-entropy of 0.2605.

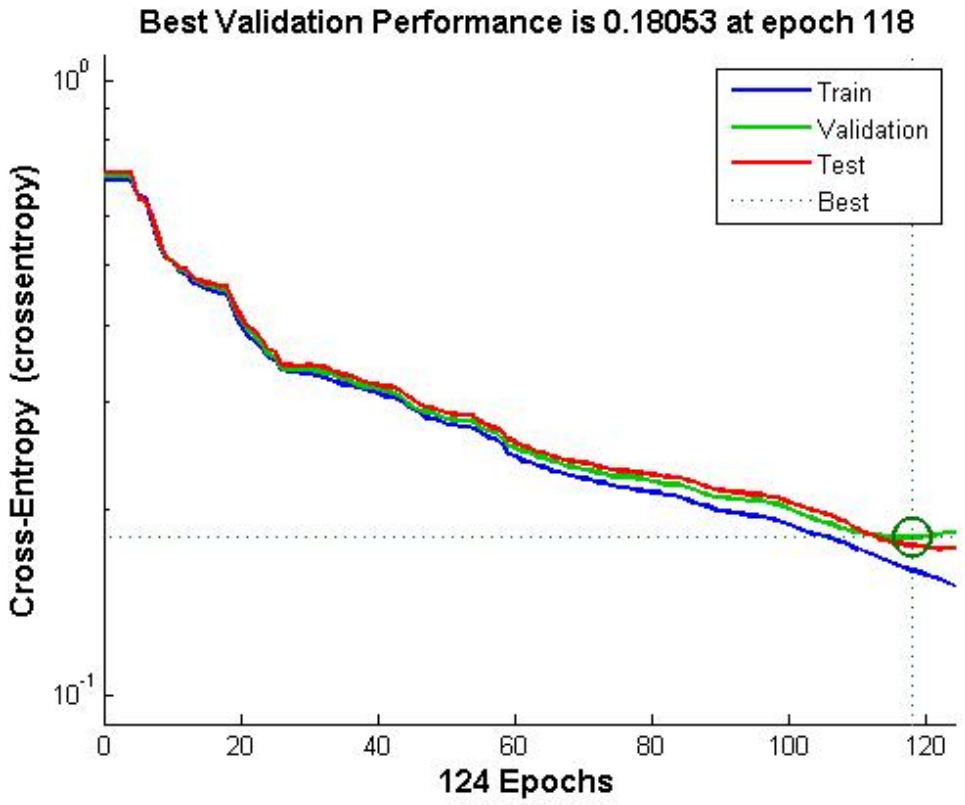

Figure 8.53: Best Validation Performance on the Posterior Compartment for S7 - Best validation performance found after the unsupervised Levenberg-Marquardt validation applied with Matlab's feature pattern recognition toolbox. The resulting performance from the extensor muscles of the forearm for typical subject (consistent with the previous results), and during a typical test. The best validation performance is found at epoch 118 with a cross-entropy of 0.18053 .

8.11.2 Confusion Matrix for All Subjects by Group Muscles

Confusion matrix from the different stages of the supervised machine learning, i.e. training; validation; testing; and the summation of all the previous. The accuracy of the classification is shown for each case. For the training classification, the accuracy was 93.1% with a 6.9% of misclassification; the validation accuracy is 90.6% with 9.4% misclassification; the test accuracy was 92% accuracy and 8% misclassification; and finally, the overall results for the extensor muscles of the forearm was 91.9% accuracy with 8.1% of misclassification.

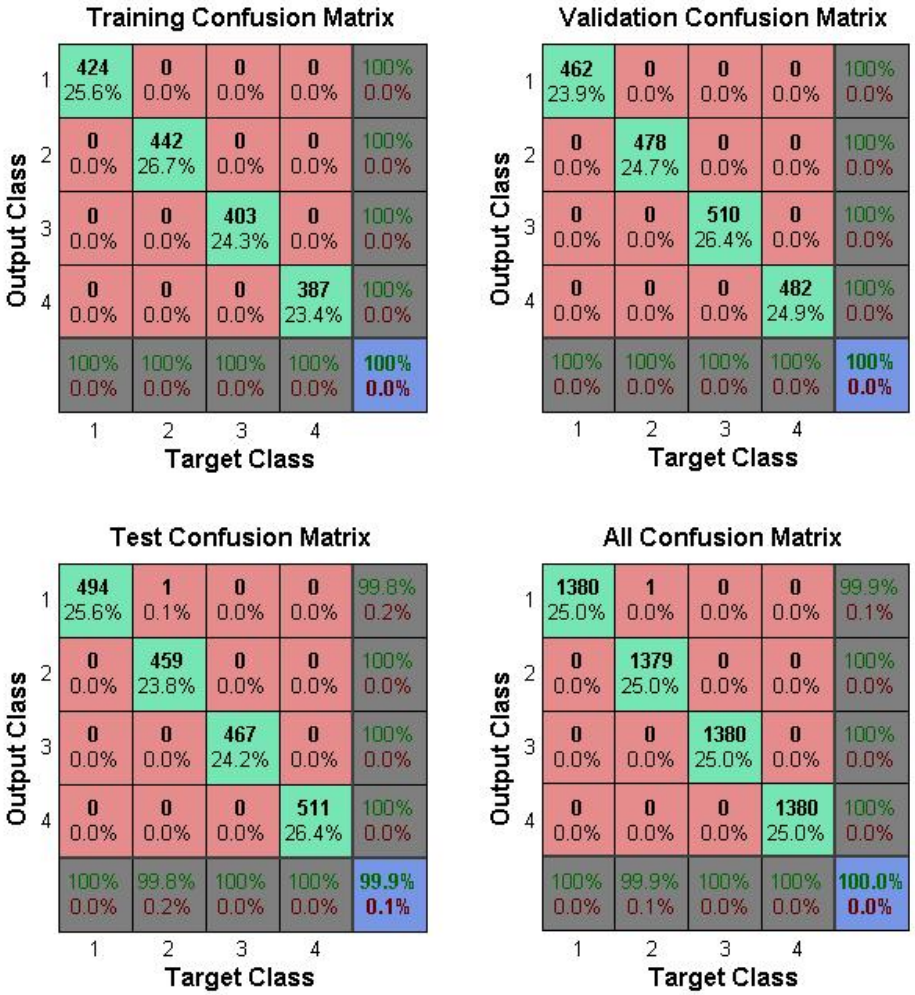

Figure 8.54: Resulting Confusion Matrix in the Flexor Muscles - S2 - Confusion matrix from the different stages of the supervised machine learning, i.e. training; validation; testing; and the summation of all the previous. The accuracy of the classification is shown for each case. For the testing, the accuracy was 99.9% with a 0.1% of classification error. For the flexor muscles, it is not clear which position is mostly a false classification.

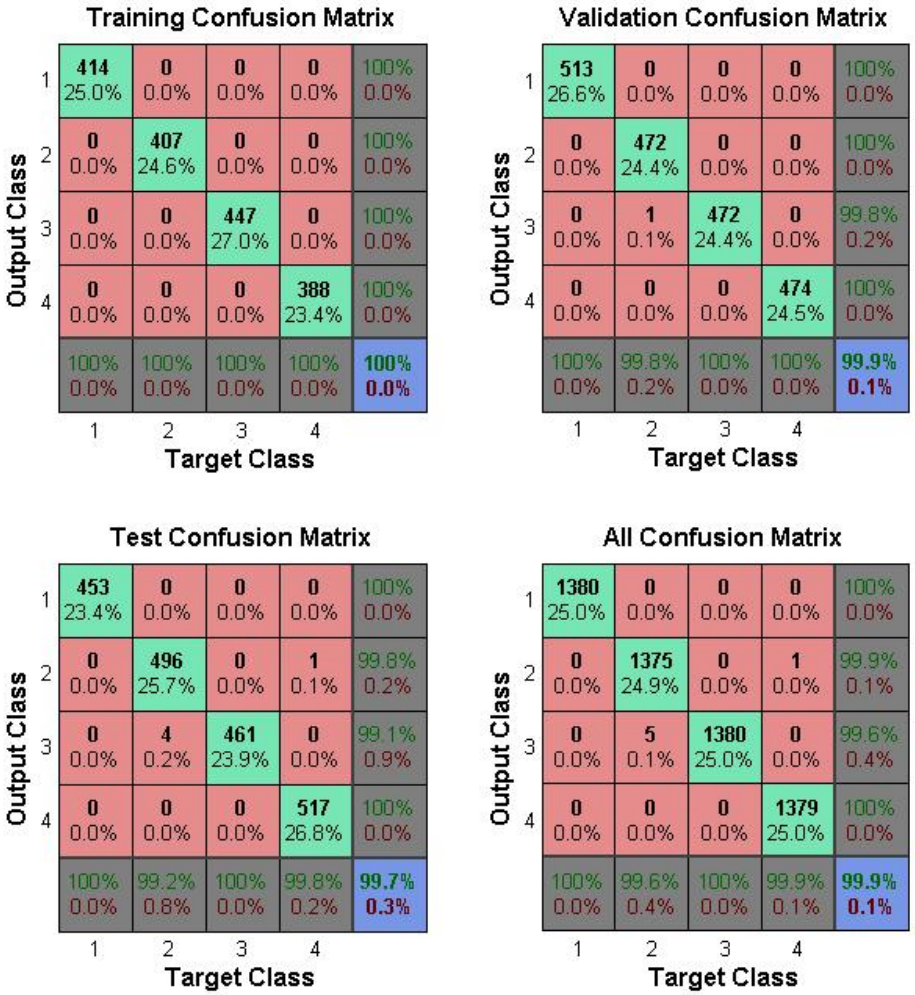

Figure 8.55: Resulting Confusion Matrix in the Extensor Muscles - S2 - Confusion matrix from the different stages of the supervised machine learning, i.e. training; validation; testing; and the summation of all the previous. The accuracy of the classification is shown for each case. For the validation, the accuracy was 99.9% with a 0.1% misclassification, for the training, it was 99.7% against 0.3%.

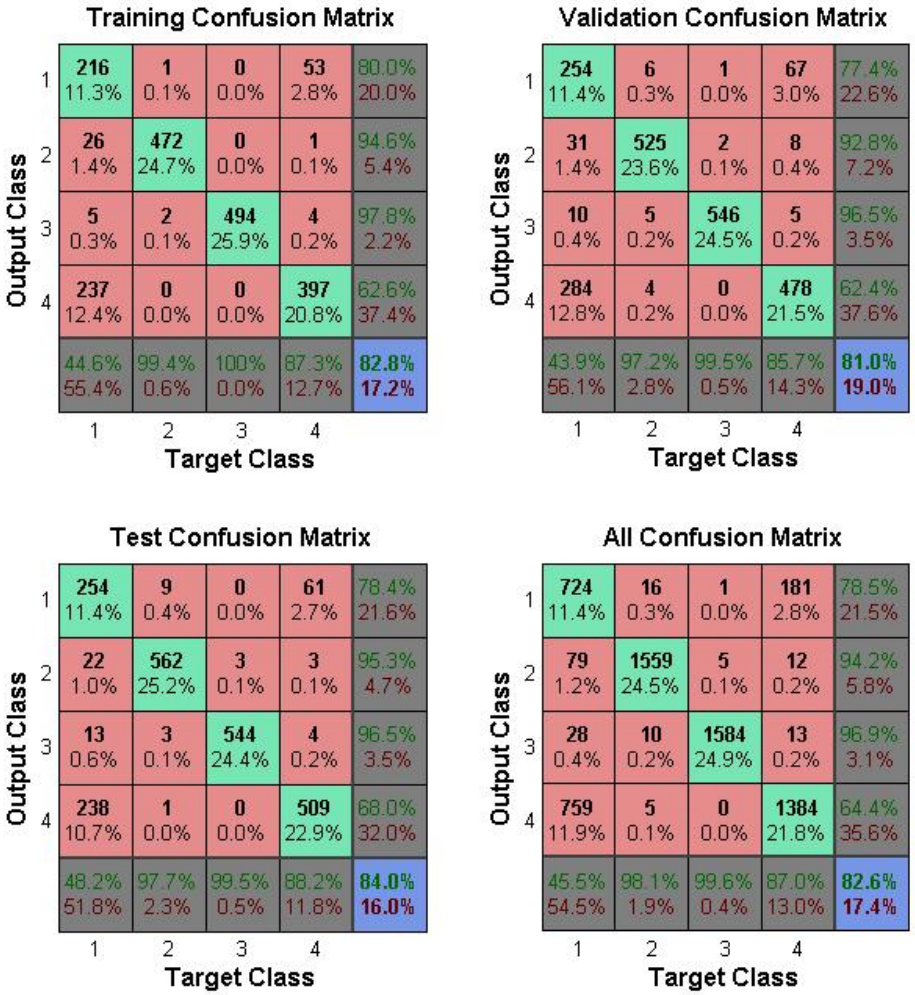

Figure 8.56: Resulting Confusion Matrix in the Flexor Muscles - S3 - Confusion matrix from the different stages of the supervised machine learning, i.e. training; validation; testing; and the summation of all the previous. The accuracy of the classification is shown for each case. For the training classification, the accuracy was 82.8% with a 17.2% of misclassification; the validation accuracy is 81% with 19% of misclassification; the test accuracy was 84% with 16% misclassification; and finally, the overall results for the flexor muscles of the forearm was 82.6% accuracy with 17.4% of misclassification.

Figure 8.57: Resulting Confusion Matrix in the Extensor Muscles - S3 - Confusion matrix from the different stages of the supervised machine learning, i.e. training; validation; testing; and the summation of all the previous. The accuracy of the classification is shown for each case. For the training classification, the accuracy was 97.9% with a 2.1% of misclassification; the validation accuracy is 95.7% with 4.3% of misclassification; the test accuracy was 94.8% with 5.2% misclassification; and finally, the overall results for the muscles of the forearm was 96% accuracy with 4% of misclassification.

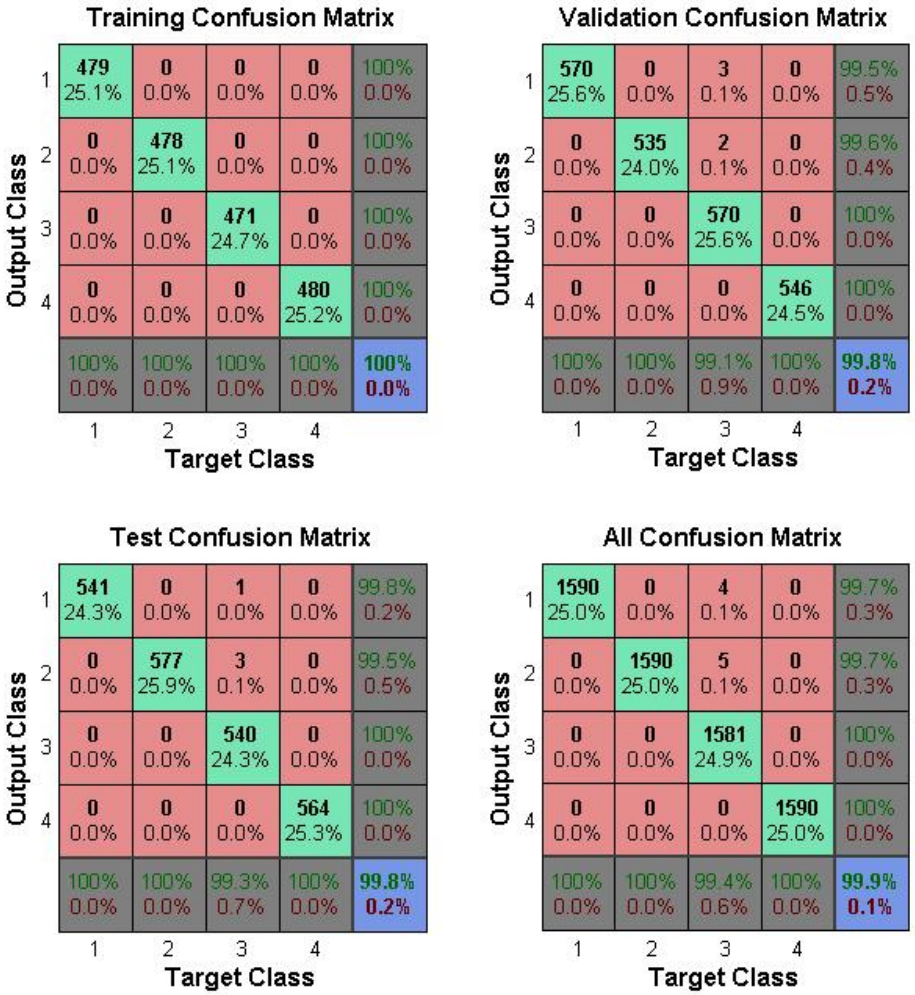

Figure 8.58: Resulting Confusion Matrix in the Flexor Muscles - S4 - Confusion matrix from the different stages of the supervised machine learning, i.e. training; validation; testing; and the summation of all the previous. The accuracy of the classification is shown for each case. The accuracy of the classification is shown for each case. For the training classification, the accuracy was 100% with no misclassification; the validation and test accuracy were 99.8% with 0.2% of misclassification; and finally, the overall results for the muscles of the forearm was 99.9% accuracy with 0.1% of misclassification.

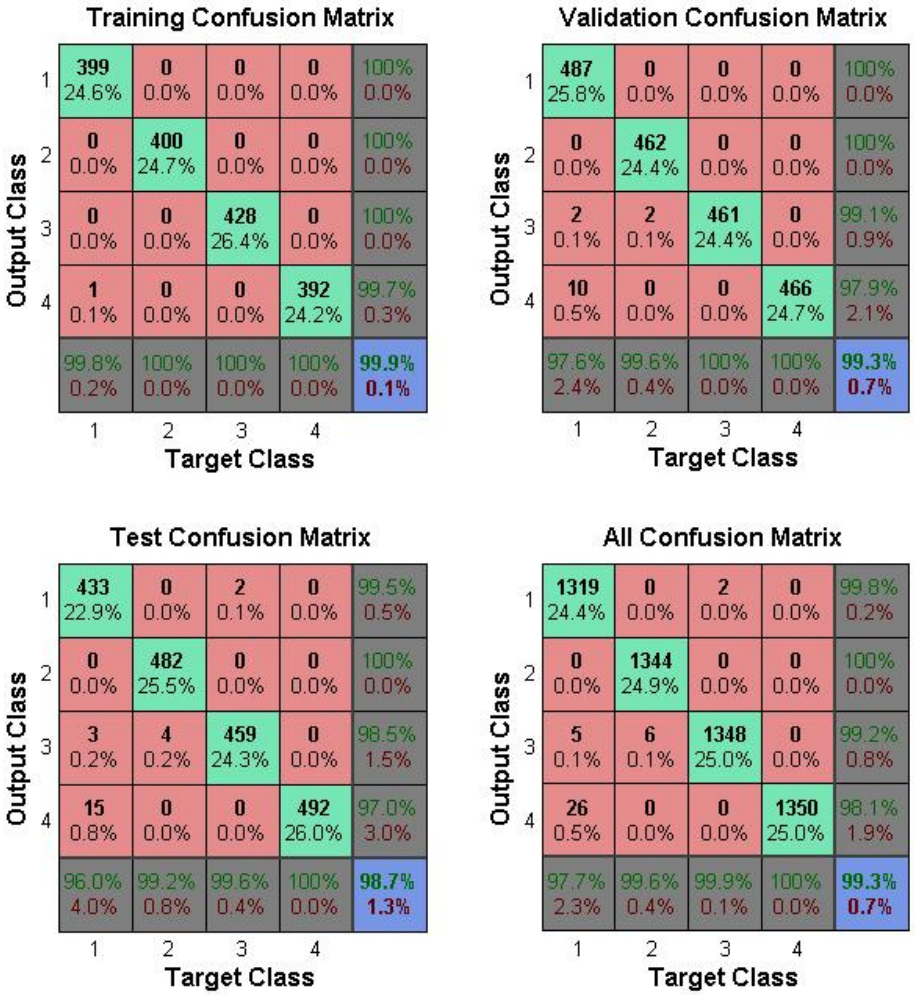

Figure 8.59: Resulting Confusion Matrix in the Extensor Muscles - S4 - Confusion matrix from the different stages of the supervised machine learning, i.e. training; validation; testing; and the summation of all the previous. The accuracy of the classification is shown for each case. For the training classification, the accuracy was 99.9% with a 0.1% of misclassification; the validation accuracy is 99.3% with 0.7% misclassification; the test accuracy was 98.7% accuracy and 1.3% misclassification; and finally, the overall results for the extensor muscles of the forearm was 99.3% accuracy with 0.7% of misclassification.

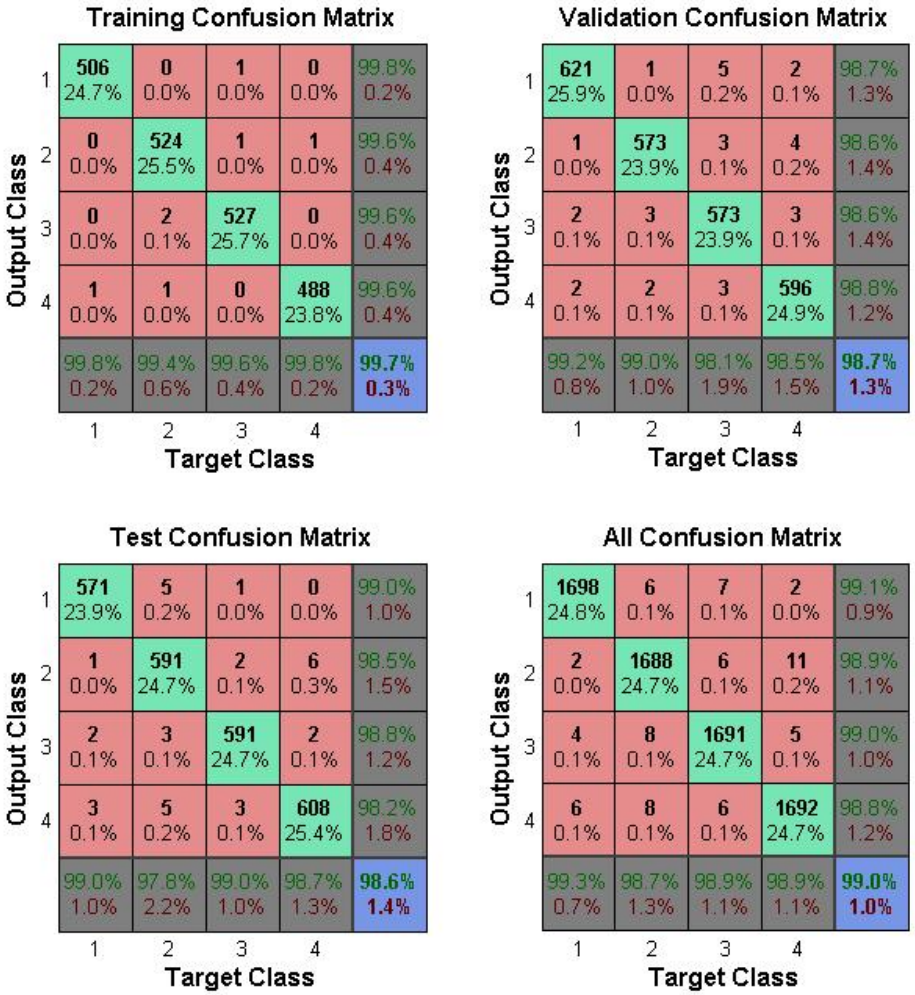

Figure 8.60: Resulting Confusion Matrix in the Flexor Muscles - S5 - Confusion matrix from the different stages of the supervised machine learning, i.e. training; validation; testing; and the summation of all the previous. The accuracy of the classification is shown for each case. For the training classification, the accuracy was 99.7% with a 0.3% of misclassification; the validation accuracy is 98.7% with 1.3% misclassification; the test accuracy was 98.6% accuracy and 1.4% misclassification; and finally, the overall results for the extensor muscles of the forearm was 99.0% accuracy with 1.0% of misclassification.

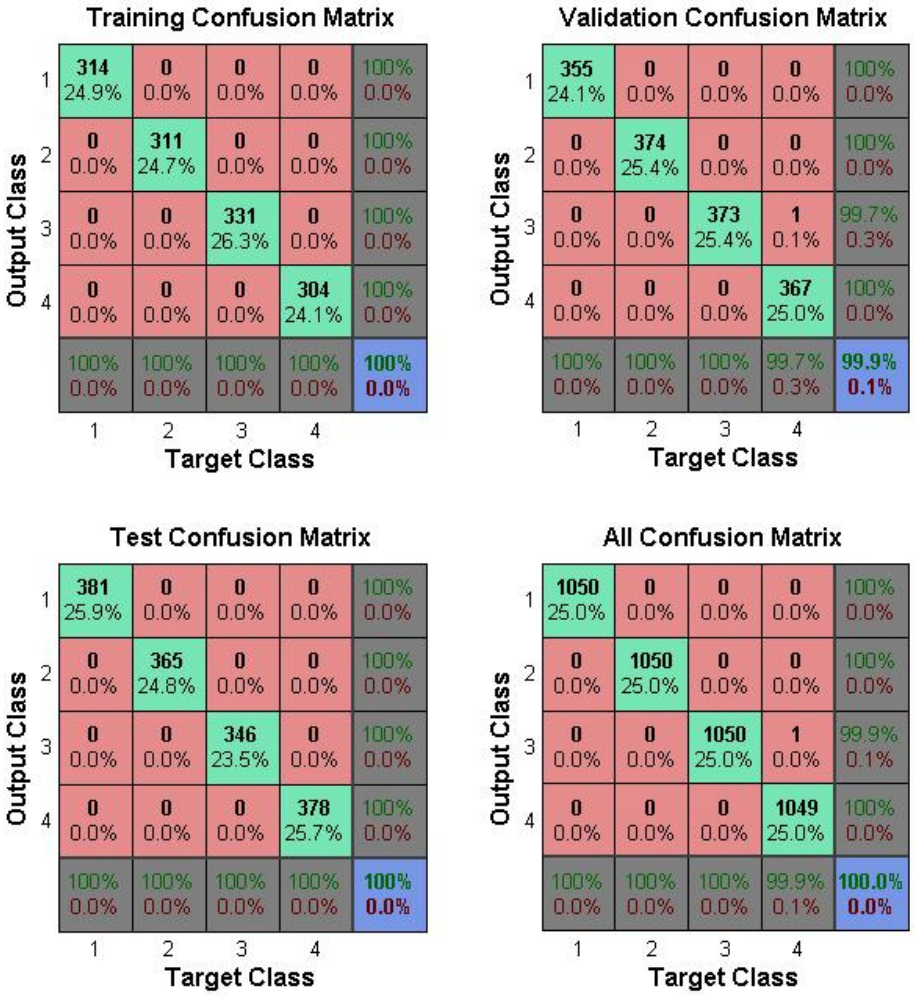

Figure 8.61: Resulting Confusion Matrix in the Extensor Muscles - S5 - Confusion matrix from the different stages of the supervised machine learning, i.e. training; validation; testing; and the summation of all the previous. The accuracy of the classification is shown for each case. For the training and testing, the classification accuracy was 100%; the validation accuracy is 99.9% with 0.1% misclassification.

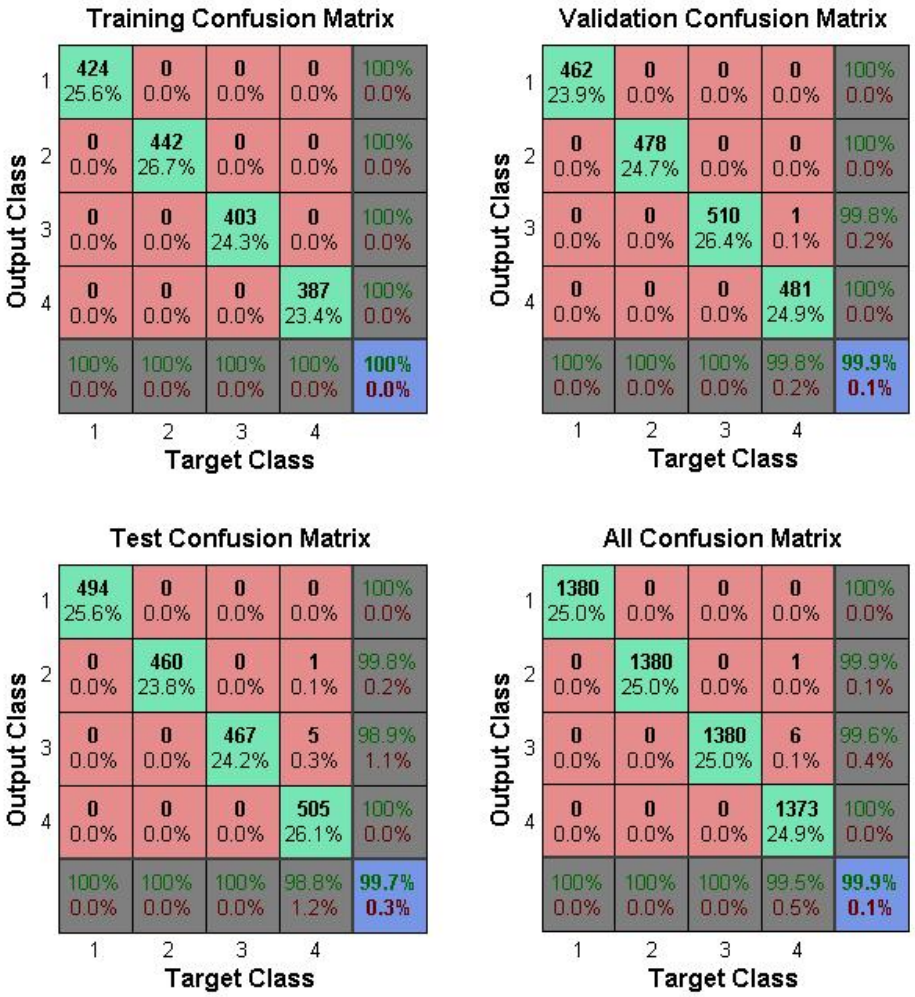

Figure 8.62: Resulting Confusion Matrix in the Flexor Muscles - S6 - Confusion matrix from the different stages of the supervised machine learning, i.e. training; validation; testing; and the summation of all the previous. For the training classification, the accuracy was 100%; the validation accuracy is 99.9% with 0.1% misclassification; the test accuracy was 99.7% accuracy and 0.3% misclassification; and finally, the overall results for the extensor muscles of the forearm was 99.9% accuracy with 0.1% of misclassification.

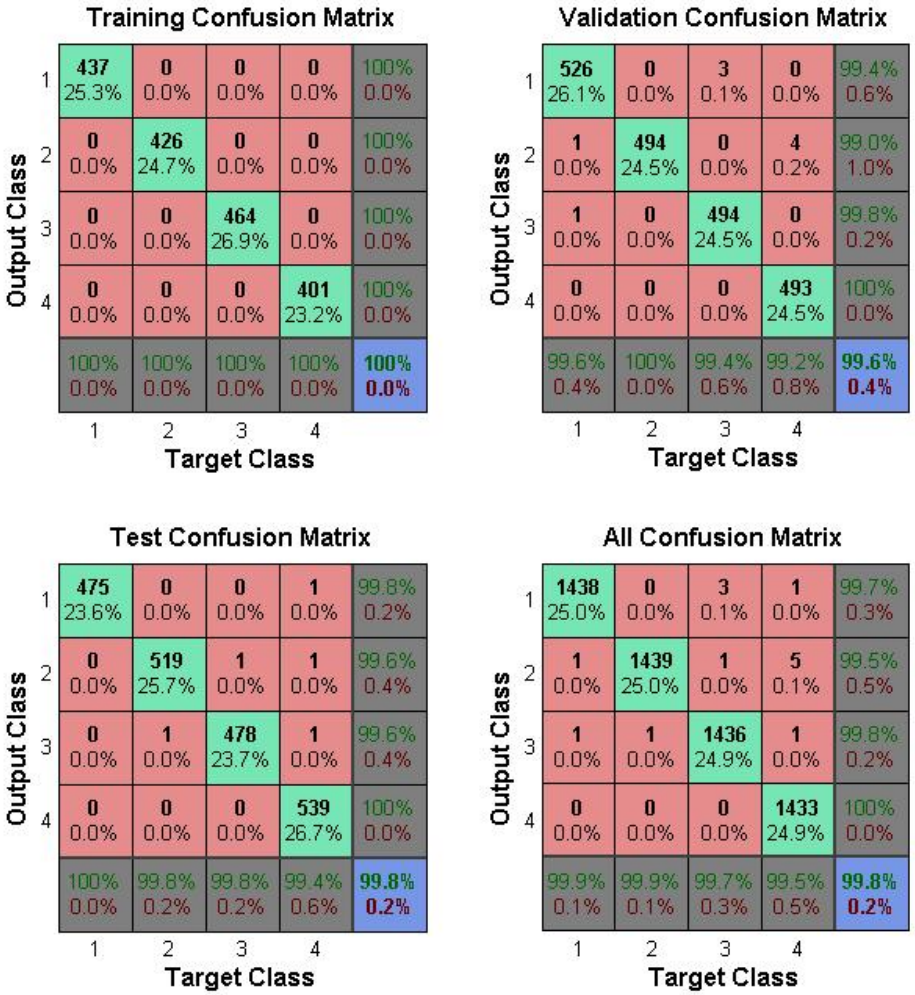

Figure 8.63: Resulting Confusion Matrix in the Extensor Muscles - S6 - Confusion matrix from the different stages of the supervised machine learning, i.e. training; validation; testing; and the summation of all the previous. The accuracy of the classification is shown for each case. For the training classification, the accuracy was 100%; the validation accuracy is 99.6% with 0.4% misclassification; the test accuracy was 99.8% accuracy and 0.2% misclassification; and finally, the overall results for the extensor muscles of the forearm was 99.8% accuracy with 0.2% of misclassification.

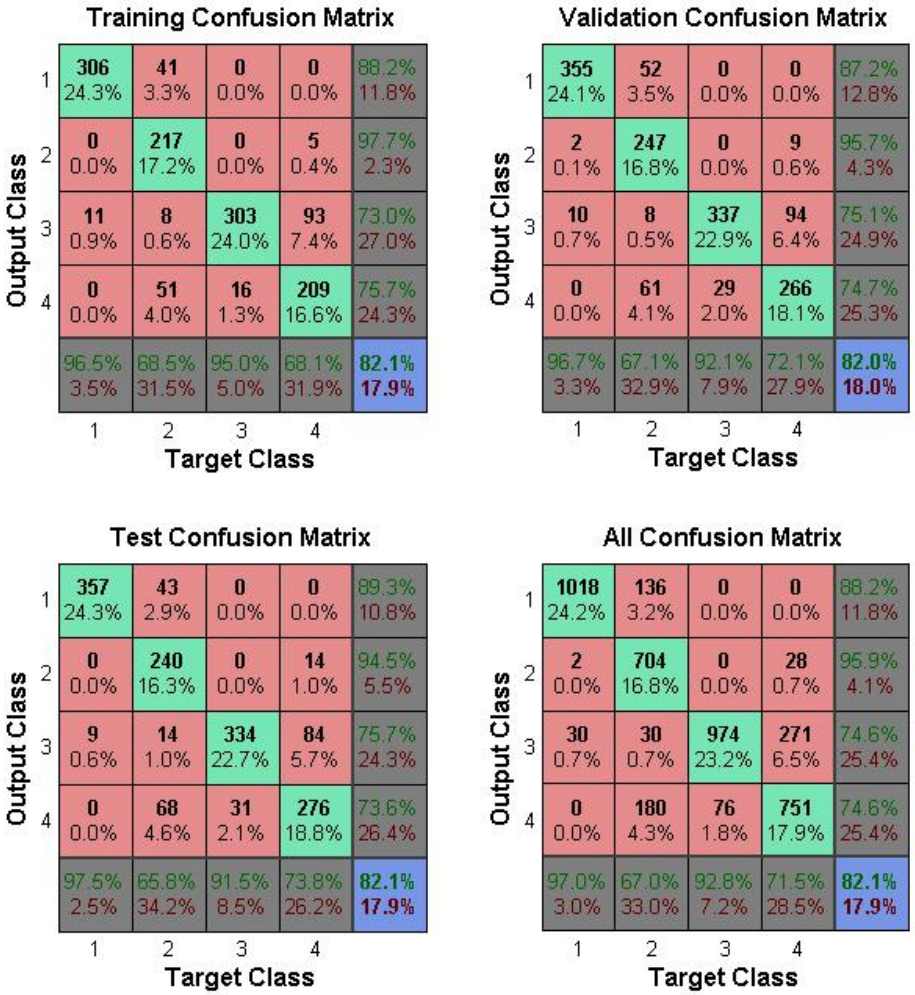

Figure 8.64: Resulting Confusion Matrix in the Flexor Muscles - S7 - Confusion matrix from the different stages of the supervised machine learning, i.e. training; validation; testing; and the summation of all the previous. For the training classification, the accuracy was 82.1% with a 17.9% of misclassification; the validation accuracy is 82% with 18% misclassification; the test accuracy was 82.1% accuracy and 17.9% misclassification; and finally, the overall results for the extensor muscles of the forearm was 82.1% accuracy with 17.9% of misclassification.

Figure 8.65: Resulting Confusion Matrix in the Extensor Muscles - S7 - Confusion Matrix Results in the Extensor Muscles - S7

8.12 Papers published

2013 IEEE International Conference on Systems, Man, and Cybernetics

An investigation into thumb rotation using high density surface electromyography of extrinsic hand muscles

A. Aranceta-Garza, H. Lakany, B. A. Conway
Department of Biomedical Engineering
University of Strathclyde
Glasgow, Scotland, UK
alejandra.aranceta-garza@strath.ac.uk

***Abstract*— Improving our understanding of mechanisms driving thumb rotation could potentially advance the design of current upper limb prosthesis to incorporate powered thumb control increasing the dexterity of the device.**

This study investigates thumb rotation using high density surface electromyography (HD-sEMG) of extrinsic hand muscles. An apparatus was designed and developed to test thumb rotation.

Relevant data were acquired during isometric voluntary contractions with a 20-40% of maximum voluntary contraction (MVC) performed by 7 healthy right-handed volunteers. Data were processed and analyzed. Analysis showed that, thumb position could be extracted using features extracted from the HD-sEMG data recorded with high statistical significance.

Keywords- high density surface electromyography; thumb rotation ; dexterous upper limb myoelectric prosthesis;

I. INTRODUCTION

According to a review by Biddis and Chau [1], prosthesis rejection rates in adult populations are 26% compared to pediatric populations, where the rejection rate increases up to 45% for body-powered and electric prostheses.

Using a prosthetic hand is a complex matter that involves different factors, e.g. type of prosthesis, rehabilitation training, time between the prosthetic fitting and amputation, among others and in an extensive literature review of the use of upper limb prosthetics with a focus on myoelectric hand conducted by C.W. Martin [2], it has revealed that these aforementioned factors are also related to prosthetic rejection.

In this research, we focus our attention on the muscle synergies of the forearm while a thumb rotation/opposition occurs. Different positions are considered (Figure 1) based on the position of the rest of the digits of the hand i.e. secundus digitus manus (index finger), digitus medius (middle finger), digitus annularis (ring finger) and the digitus minimus manus (pinky finger).

A. Aranceta-Garza is sponsored by CONACyT established in Mexico City, Mexico.

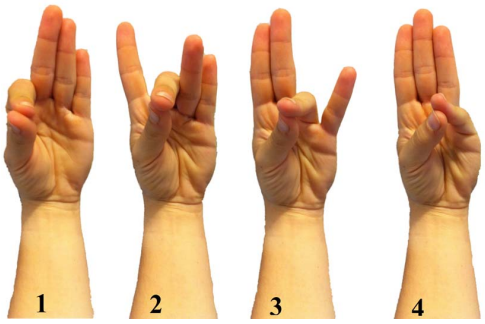

Figure 1. Different positions considered based on thumb opposition. 1) Opposition to the index finger, 2) opposition to the middle finger, 3) opposition to the ring finger, and 4) opposition to pinky finger.

Our hypothesis is that if we are able to extract information regarding the thumb rotation through the muscles of the forearm, then it will be possible to create mechanisms to improve amputees' experience using myoelectric upper limb prostheses. We, hence, in this paper focus on developing systems to extract signatures for thumb rotation at different positions to verify our hypothesis.

The paper is organized as follows:

In section II, we explain our experimental set up and the methodology in collecting and processing the recorded data. We also show the statistical analysis used to test our hypothesis. Section III depicts the results and our conclusions are summarized in Section IV.

II. METHODS

A. Experimental Setup

The experimental set up used in this study consisted of a high density surface EMG (HD-sEMG) system, a test rig and a GUI to present the cue to the subjects.

The HD-sEMG system we used to acquired surface EMG is the EMG-USB2 amplifier from OT-Bioelettronica, Italy. We recorded 129 channels (128 sEMG + 1 AUX). The device is optically isolated under the European Standards for biomedical instrumentation to assure patient safety.

978-1-4799-0652-9/13 $31.00 © 2013 IEEE
DOI 10.1109/SMC.2013.639

We designed and developed an apparatus to test thumb rotation. A test rig was designed to allow thumb rotation while preventing any movement from the muscles that control index, middle, ring and pinky finger, as well as preventing any muscle activity that might be produced by wrist and elbow movements. A detailed annotated illustration of the rig designed is shown in Figure 2.

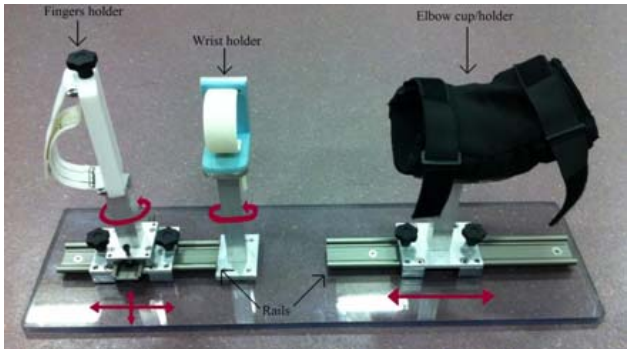

Figure 2. Test Rig used to test thumb rotation. The index, middle, ring and pinky fingers together with the wrist and elbow are fixed in the appropriate padded holder allowing the subject to be fixed while the hand is sitting in a resting position ensuring that no hand muscles are active while in rest. The finger holder has movement in the X and Y axis as well as holder rotation; the wrist holder has a rotation movement, and finally, the elbow cup is only allowed to move in the X axis. All the holders have an elastic band avoiding any harm and allowing constriction in the movement as desired.

The rig was designed to create a uniform contraction across the subjects. Load-sensor transducers (LSR) were attached to the fingers holder (Figure 3). Each sensor corresponds to one of the four digits in space, mimicking a thumb opposition with each of the remaining fingers. This allows the pollex (thumb) to be the only actuator in the movement, inducing muscle contraction only in those muscles related to thumb movement, specifically thumb rotation.

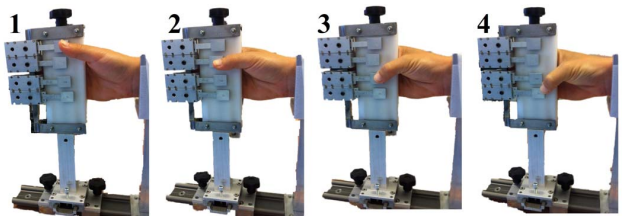

Figure 3. Load-sensor transducers (LSR) attached to the fingers holder. 1) First position where the LSR mimics an opposition of the index and the thumb, 2) second position where the LSR mimics an opposition of the middle finger and the thumb, 3) third position where the LSR mimics an opposition of the ring finger and the thumb and, 4) fourth position where the LSR mimics an opposition of the pinky finger and the thumb.

The load-sensor transducers were connected to a multichannel strain gauge amplifier built in-house (visible in Figure 4) and calibrated with a varying load from [0 - 581] g. Calibration curves for a typical transducer in a typical trial can be found in Table 1, alongside with its respective graph.

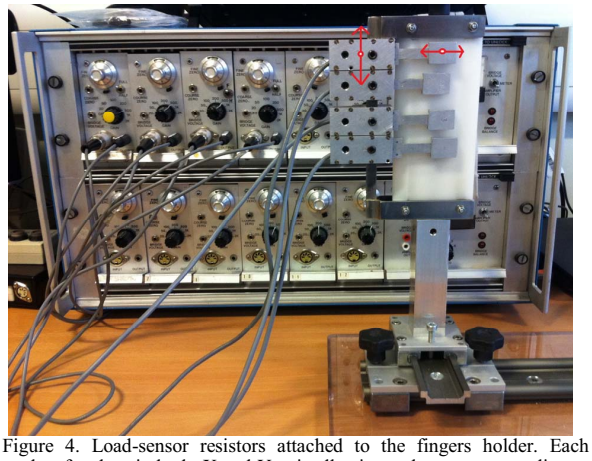

Figure 4. Load-sensor resistors attached to the fingers holder. Each resistor has freedom in both, X and Y axis allowing to be set up according to each subject's anatomical measurements. On the back of the fingers holder, the multichannel strain gauge amplifier built in-house.

TABLE 1. CALIBRATION VALUES FOR A TYPICAL LOAD-SENSOR TRANSDUCER

Transducer #1

Weight [g]	Rise [mV]	Fall [mV]	Rise [mV]	Fall [mV]	Rise [mV]	Fall [mV]	Rise [mV]	Fall [mV]
0	0	-0.7	0	3	0	-1	0	0
83	49	49	50	53	49	48	49	49
166	99	99	99	104	98	98	99	100
249	150	150	150	154	148	149	149	150
332	200	201	200	205	199	200	200	201
415	250	251	251	256	250	251	250	251
498	301	302	303	306	300	301	301	302
581	352	352	354	354	351	351	352	352

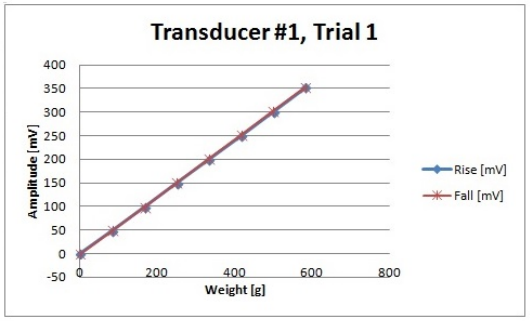

- Visual cue

A graphical user interface (GUI) incorporating visual feedback to display the percentage of MVC exerted was developed in LabVIEW. The GUI presented the subject with a cue to press on one of the transducers with a 20-40% of MVC as well as to hold until a relax cue was presented. The process only progressed when the relaxation or contraction stage time were reached. The order indicating which LSR to press was presented randomly by the program and to further ensure avoiding any predisposition from the subject towards the test, the relaxing stage time was also randomized. A timing diagram of the experiment block is shown in Figure 5. The press-relax phases were repeated 120 times (30 for each different position i.e. transducers).

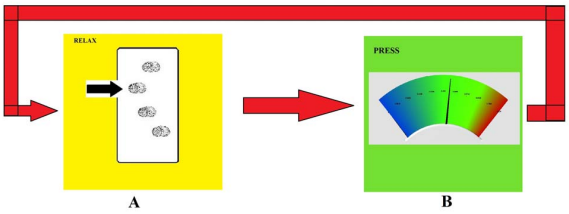

Figure 5. Timing diagram that shows the visual cues that the subject was exposed to. A) Relax stage, varied from 5 - 7 seconds, the arrow indicating the transducer to be pressed changed within each trial until a total of 120 was reached (30 for each position). B) Press stage, isometric contraction with a visual feedback was prompt. The subject was asked to contract for 5 seconds keeping an approximate of 20% of maximum voluntary contraction.

B. Subjects

Surface-EMG data were acquired from 7 healthy right-handed subjects [6 male, 1 female mean age 28.5 ± 3.7 yr (mean ± SD)]. Subjects had no history of nerve damage, prior hand surgery, existing neuromuscular pain, nor tremor; epilepsy or Parkinson disease.

Each subject was seated on an adjustable chair, set up accordingly to their height and comfort. Two 64-electrode array matrices were fixed on the posterior and anterior compartment, in addition to, a one 8-electrode for male subjects (or 4-electrode array for the female subject) placed on the dorsal interosseus muscle (DOI), and one disposable, low-density electrode on the flexor pollicis brevis muscle (FPB), finally, ground electrodes were fixed on the olecranon as depicted in figure 6. The electrodes were position based on palpation whilst thumb opposition-relaxation. Medical tape was used to secure the electrodes in place avoiding any motion.

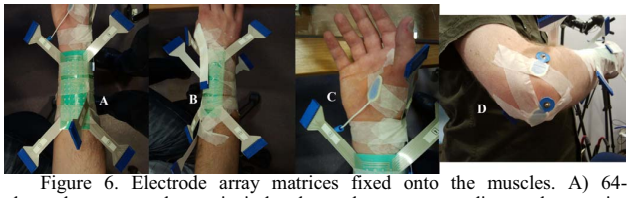

Figure 6. Electrode array matrices fixed onto the muscles. A) 64-electrode array on the extrinsic hand muscles, corresponding to the anterior compartment of the forearm. B) 64 - electrode array on the extrinsic hand muscles, posterior compartment of the forearm and 8-electrode array on the DOI muscle. C) Low-density electrode on FPB. D) Ground electrodes fixed onto the olecranon.

Once the electrodes were properly set, the right hand was fixed onto the rig (Figure 7), fixing the 4 digits and joints as described in the previous section.

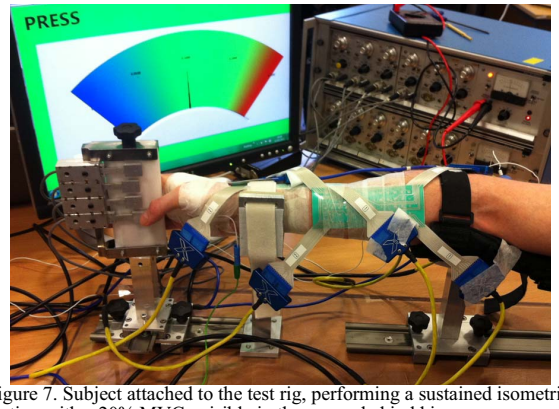

Figure 7. Subject attached to the test rig, performing a sustained isometric contraction with a 20% MVC, visible in the screen behind him.

C. Data

Surface-EMG was acquired using 128 channels with the setup previously described, plus one more channel corresponding to a trigger. This trigger was used to time-stamp the signal every time a transducer was pressed.

Raw sEMG signals were collected at a sample rate of 2048 Hz. The produced data files for each subject, before any processing, were ~ 0.43Gb.

Data were exported to MATLAB. A notch filter was applied to reduce the interference caused by the mains at 50Hz.

The processed EMG was visualized using a customized self coded toolbox and differences in the averaged EMG were analyzed with ANOVA, to compare and asses the significance of any differences within the recorded EMG across the four positions of the thumb.

III. RESULTS

A. Hd-sEMG Maps

Color maps of the EMG recorded in both compartments of the forearm, for each thumb position were created. These maps are an important visual aid to shed light and enhance our understanding regarding the distribution of activity and contribution of the extrinsic muscles of the hand.

For a detailed analysis, the mean of the sEMG amplitude values were obtained over 100ms window with a 50ms overlap of the sustained isometric contraction. These windows were applied to extract salient features according to the maximum amplitude within each electrode (Figure 8). The selection of different width of these windows have impact in the ANOVA analysis that will be explain in the next section.

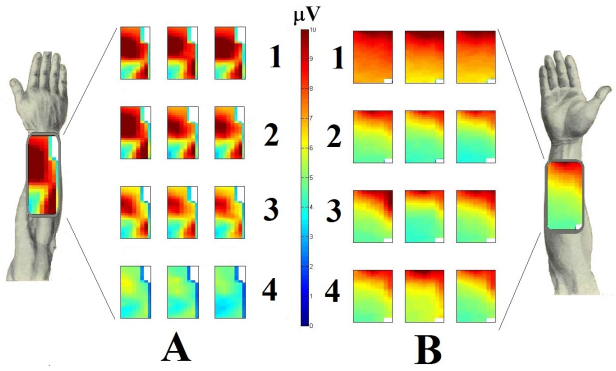

Figure 8. Resulting color plots of a typical subject over 3 windows [(0-100),(50-150),(100-150)]ms for each position of the thumb. A) Resulting windows from the posterior compartment. B) Resulting windows from the anterior compartment. The numbers: 1, 2, 3 and 4 correspond to the different positions of the thumb in relation to the index, middle, ring and pinky finger, respectively.

B. Statistical Analysis

The analysis of variance (ANOVA) of the EMG signal, revealed significant statistical differences in the p-values, across the means of the different positions of the thumb. The analysis was performed using the isometric sustained contraction at a 20-40% of the MVC across the different positions of the thumb. A typical result can be found in figure 9.

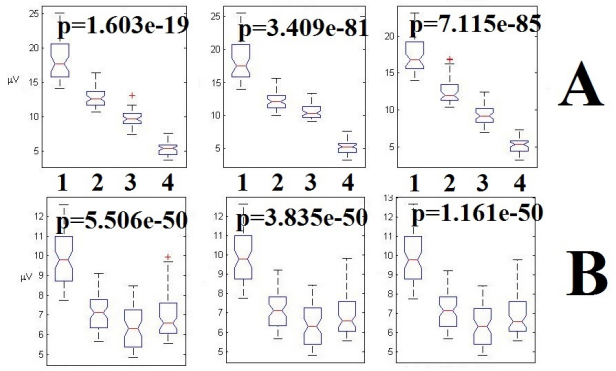

Figure 9. A typical result of a subject analyzed over 3 windows [(0-100),(50-150),(100-150)]ms. A) Posterior compartment statistical analysis with a 95% CI, p<<0.05. B) Anterior compartment statistical analysis with a 95% CI, p<<0.05. The numbers: 1, 2, 3 and 4 correspond to the different positions of the thumb in relation to the index, middle, ring and pinky finger, respectively.

IV. DISCUSSION

Visual inspection of the color maps showed visible differences across different thumb rotation positions. These differences lie in the muscle propagation of extrinsic muscles of the hand. Statistical analysis ascertained the significance of the differences.

These results indicate that it is potentially possible to extract different thumb rotation positions through sEMG analysis from the extrinsic muscles of the hand.

Our future work focuses on exploring various methods to extract salient features to classify different thumb positions. Furthermore, we will be investigating cross-correlation between the different muscle groups.

ACKNOWLEDGMENT

This research is funded by Consejo Nacional de Ciencia y Tecnología (CONACyT) under the student ID 214157.

Authors would like to thank Campbell Reid for interesting discussions; John Maclean, and Stephen Murray that helped with the development of the rig and all the subjects that took part of the experiment.

REFERENCES

[1] E.A. Biddiss, and T.T. Chau, "Upper limb prosthesis use and abandonment: a survey of the last 25 years", Prosthet Orthot Int, 31(3):236-57, September 2007.

[2] C.W. Martin , and D. Edeer, "Upper limb prostheses-A review of the literature with a focus on myoelectric hands", Richmond, BC: worksafeBC Evidence-Based Practice Grooup, February 2011. Available at: http://worksafebc.com/health_care_providers/Assets/PDF/UpperLimbProstheses2011.pdf

[3] M. Gazzoni, D. Farina, and R. Merletti, "A new method for the extraction and classification of single motor unit action pontentials from surface EMG signals", Journal of Neuroscience Methods 136(2004)165-177, January 2004.

[4] T. Masuda, and T. Sadoyama, "Topographical Map of Innervation Zones Within Single Motor Units Measured with a Grid Surface Electrode", IEEE Transactions on Biomedical Engineering, vol. 35, no. 8, August 1988.

[5] T. Masuda, and C. J. De Luca, "Technique for Detecting MUAP Propagation from High-Threshold Motor Units", Journal of Electromyography and Kinesiology, vol. 1, no. 1, pp 75-80, 1991.

[6] Z. C. Lateva, K. C. McGill, and M. E. Johanson, "The innervation and organizatino of motor units in a series-fibered human muscle: the brachioradialis", J. Appl. Physiol. 108(6): 1530-1541, June 2010.

[7] A. Kossev, N. Gantchev, Y. Gerasimenjo, and P. Christova, "The effect of muscle fiber length change on motor units potentials propagation velocity", Electromyogr. Clin. Neurophysiol., 32 (6): 287-94, June 1992.

[8] Z. C. Lateva, and K. C. McGill, "Estimating motor-unit architectural properties by analyzing motor-unit action potential morphology", Clinical Neurophysiology 112 (2001): 127-135, September 2000.

[9] A. Reffad, R. E. Bekka, K. Mebarkia, and D. Chikouche, "Efficient parameterization of MUAP signal for identification of MU and volume conductor characteristics using neural networks", J. Neuroscience Methods, 164 (2), 325-38, May 2007.

[10] T. Sadoyama, T. Masuda, and H. Miyano, "Relashionships between muscle fiber conduction velocity and frequency parameters of surface EMG during sustained contraction", Eur J. Appl. Physiol., 51:247-256, 1983.

[11] H. Broman, G. Bilotto, and C. J. De Luca, "A note on the noninvasive estimation of muscle fiber conduction velocity", IEEE Transactions on Biomedical Engineering, vol. 32 (5): 341- 344, October 1984.

[12] D. Farina, E. Fortunato, and R. Merletti, "Noninvasive estimation of motor unit conduction velocity distribution using linear electrode arrays", IEEE Transactions on Biomedical Engineering, 47 (3): 380-388, March 2000.

[13] D. Farina, W. Muhammad, E. Fortunato, O. Meste, R. Merletti, and H. Rix, "Estimation of single motor unit conduction velocity from surface electromyogram signals detected with linear electrode arrays", Med. Biol. Eng. Comput, vol. 39, 225-236, 2001.

[14] C. J. Houtman, D. F. Stegeman, J. P. Van Dijk, and M. J. Zwarts, "Changes in muscle fiber conduction velocity indicate rectruitment of

distinct motor unit populations", Journal of Applied Physiology, vol. 95 (3): 1045-1054, May 2003.

[15] L. M. Eaton, and E. H. Lambert, "Electromyography and electric stimulation of nerves in diseases of motor unit observations on myasthenic syndrome associated with malignant tumors", The Journal of the American Medical Association, Vol. 163 (13): 1117-1124, March 1957.

[16] A.A. Brownell, and M. B. Bromberg, "Comparison of three algorithms for multi-motor unit detection and waveform making", Muscle & Nerve, 33 (4):538-45, April 2006.

[17] J.L. McKay, T. D. J Welch, B. Vidakovic, and L. H. Ting, "Statistically-significant contrasts between EMG waveforms revealed using wavelet-based functional ANOVA", J. Neurophysiol 109(2):591-602, January 2013.

67223926722392A

References

[1] Hermie J Hermens, Bart Freriks, Catherine Disselhorst-Klug, and Gnter Rau. **Development of recommendations for {SEMG} sensors and sensor placement procedures**. *Journal of Electromyography and Kinesiology*, **10**(5):361 – 374, 2000. xix, 81, 82, 83

[2] De Luca CJ, Mikhail Gilmore LD FAU Kuznetsov, Serge H Kuznetsov M FAU Roy, and Roy SH. **Filtering the surface EMG signal: Movement artifact and baseline noise contamination.** xix, 85

[3] Stephen J Preece, John Y Goulermas, Laurence P J Kenney, Dave Howard, Kenneth Meijer, and Robin Crompton. **Activity identification using body-mounted sensorsa review of classification techniques**. *Physiological Measurement*, **30**(4):R1, 2009. xix, 90, 91

[4] Cosimo Urgesi, Valentina Moro, Matteo Candidi, and Salvatore M. Aglioti. **Mapping Implied Body Actions in the Human Motor System**. *The Journal of Neuroscience*, **26**(30):7942–7949, 2006. 16

[5] Ana Solodkin, Petr Hlustik, and Giovanni Buccino. **The Anatomy and Physiology of the Motor System in Humans**. In John T. Cacioppo, Louis G. Tassinary, and Gary Berntson, editors, *Handbook of Psychophysiology*, pages 507–539. Cambridge University Press, third edition, 2007. Cambridge Books Online. 16, 17, 21

[6] Purves Dale. *Neuroscience, 2nd edition.* Sinauer Associates Inc.,U.S., 2nd Revised edition edition (17 Jan 2001). 18

[7] Retrieved from http://www.britannica.com/EBchecked/topic/4491/action potential, editor. *Action Potential.* Encyclopaedia Britannica, 2014. 19

[8] McBee Tom. **ABE Advanced Level Physics**, Jan 23 2012. 19

[9] J. Malmivuo and R. Plonsey. *Bioelectromagnetism: Principles and Applications of Bioelectric and Biomagnetic Fields.* Oxford University Press, 1995. 20

[10] Johnson Alberts B. and Lewis A. *Molecular Biology of the Cell.* Garland Science, 2002. 21

[11] F. Mohd-Yasin M.B.I. Raez, M.S. Hussain. **Techniques of EMG signal analysis: detection, processing, classification and applications (Correction)**. *Biol Proced Online.*, 2006; 8: 163. 21, 84

[12] John V. Basmajian and Carlo J. De Luca. *Muscles Alive: Their Functions Revealed by Electromyography.* Williams & Wilkins, 1985. 23, 117

[13] Marco Barbero, Roberto Merletti, and Alberto Rainoldi. *Atlas of Muscle Innervation Zones: Understanding Surface Electromyography and Its Applications.* Springer, 2012. 26, 117

[14] Carlo De Luca. *Electromyography.* John Wiley & Sons, Inc., 2006. 27

[15] R. Merletti and H. J. Hermens. *Detection and Conditioning of the Surface EMG Signal*, pages 107–131. John Wiley & Sons, Inc., 2005. 27

[16] Dario Farina, Elena Fortunato, and Roberto Merletti. **Noninvasive estimation of motor unit conduction velocity distribution using linear electrode arrays**. *Biomedical Engineering, IEEE Transactions on*, **47**(3):380–388, 2000. 28

[17] Marco Barbero, Roberto Merletti, and Alberto Rainoldi. **Features of the Two-Dimensional sEMG Signal: EMG Feature Imaging**. In *Atlas of Muscle Innervation Zones*, pages 61–69. Springer Milan, 2012. 28

[18] Schack B, H Vath N FAU Petsche, H-G Petsche H FAU Geissler, E Geissler HG FAU Moller, and Moller E. **Phase-coupling of theta-gamma EEG rhythms during short-term memory processing.** 28

[19] J.T. Cacioppo, L.G. Tassinary, and G. Berntson. *Handbook of Psychophysiology.* Cambridge University Press, 2007. 29

[20] Farmer SF. **Rhythmicity, synchronization and binding in human and primate motor systems.** 29

[21] De Luca CJ and Erim Z. **Common drive of motor units in regulation of muscle force.** 29

[22] Baker SN, E M Kilner JM FAU Pinches, R N Pinches EM FAU Lemon, and Lemon RN. **The role of synchrony and oscillations in the motor output.** 29, 100, 101

[23] G HENNEMAN E FAU SOMJEN, D O SOMJEN G FAU CARPENTER, and CARPENTER DO. **Functional Significance of cell size in spinal motorneurons**. 29

[24] Dario Farina, Roberto Merletti, and Roger M. Enoka. **The extraction of neural strategies from the surface EMG: an update**. *Journal of Applied Physiology*, **117**(11):1215–1230, 2014. 30, 100

[25] Wang Hua, Ma Cuiqin, and Zhou Lijuan. **A Brief Review of Machine Learning and Its Application**. In *Information Engineering and Computer Science, 2009. ICIECS 2009. International Conference on*, pages 1–4, Dec 2009. 31

[26] John McCarthy. **Arthur Samuel: Pioneer in Machine Learning**. 31

[27] Thomas M. Mitchell. *Machine Learning.* McGraw Hill, 1997. 32

[28] Wee Meng Soon, Hwee Tou Ng, and Daniel Chung Yong Lim. **A Machine Learning Approach to Coreference Resolution of Noun Phrases**. *Computational Linguistics*, **27**(4):521–544, December 2001. 32

[29] Blake LeBaron. **Chapter 24 Agent-based Computational Finance**. **2** of *Handbook of Computational Economics*, pages 1187 – 1233. Elsevier, 2006. 32

[30] A Clifton, L Kilcher, J K Lundquist, and P Fleming. **Using machine learning to predict wind turbine power output**. *Environmental Research Letters*, **8**(2):024009, 2013. 32

[31] Yuan-Kang Wu, Chao-Rong Chen, and Hasimah Abdul Rahman. **A Novel Hybrid Model for Short-Term Forecasting in PV Power Generation**, 2014. 32

[32] Gentleman RC, Douglas M Carey VJ FAU Bates, Ben Bates DM FAU Bolstad, Marcel Bolstad B FAU Dettling, Sandrine Dettling M FAU Dudoit, Byron Dudoit S FAU Ellis, Laurent Ellis B FAU Gautier, Yongchao Gautier L FAU Ge, Jeff Ge Y FAU Gentry, Kurt Gentry J FAU Hornik, Torsten Hornik K FAU Hothorn, Wolfgang Hothorn T FAU Huber, Stefano Huber W FAU Iacus, Rafael Iacus S FAU Irizarry, Friedrich Irizarry R FAU Leisch, Cheng Leisch F FAU Li, Martin Li C FAU Maechler, Anthony J Maechler M FAU Rossini, Gunther Rossini AJ FAU Sawitzki, Colin Sawitzki G FAU Smith, Gordon Smith C FAU Smyth, Luke Smyth G FAU Tierney, Jean Y H Tierney L FAU Yang, Jianhua Yang JY FAU Zhang, and Zhang J. **Bioconductor: open software development for computational biology and bioinformatics.** 32

[33] Ben-Hur A, Soren Ong CS FAU Sonnenburg, Bernhard Sonnenburg S FAU Scholkopf, Gunnar Scholkopf B FAU Ratsch, and Ratsch G. **Support vector machines and kernels for computational biology.** 32

[34] Brown MP, D Grundy WN FAU Lin, N Lin D FAU Cristianini, C W Cristianini N FAU Sugnet, T S Sugnet CW FAU Furey, M Jr Furey TS FAU Ares, D Ares M Jr FAU Haussler, and Haussler D. **Knowledge-based analysis of microarray gene expression data by using support vector machines.** 32

[35] Ronan Collobert and Jason Weston. **A unified architecture for natural language processing: Deep neural networks with multitask learning**, 2008. 32

[36] Fabrizio Sebastiani. **Machine Learning in Automated Text Categorization**. *ACM COMPUTING SURVEYS*, **34**:1–47, 2002. 32

[37] Thomas A. Runkler. **Regression**. In *Data Analytics*, pages 63–78. Vieweg+Teubner Verlag, 2012. 34

[38] J.Tiago de Oliveira. **Regression and unbiased regression**. *Trabajos de Estadistica Y de Investigacion Operativa*, **29**(3):97–99, 1978. 34

[39] É. Davalo and P. Naïm. *Neural Networks*. Computer Science Series. Macmillan Education, 1991. 34

[40] *Complex-Valued Neural Networks*, **32** of *1860-949X*. Springer Berlin Heidelberg. 34

[41] J. F Magee. *Decision trees for decision making, a n d, how to use decision trees in capital investment.* Harvard business review, 1964. 34

[42] Igor Chikalov. *Average time complexity of decision trees [internet resource].* Berlin : Springer, c2011. 34

[43] Cha Zhang, Yunqian Ma, and Springerlink (Online service), editors. *Ensemble machine learning [internet resource] : methods and applications.* New York : Springer, c2012. 34

[44] Miguel A. L Nicolelis, editor. *Methods for neural ensemble recordings.* Boca Raton : Taylor & Francis, 2008. 34

[45] H. O. Hartley. **The Modified Gauss-Newton Method for the Fitting of Non-Linear Regression Functions by Least Squares**. *Technometrics*, **3**(2):269–280, 1961. 34

[46] China) ISICA 2012 (2012 : Wuhan. *Computational intelligence and intelligent systems [internet resource] : 6th International Symposium, ISICA 2012, Wuhan, China, October 27-28, 2012. Proceedings.* Berlin ; New York : Springer, c2012. 34

[47] 1953 James, M. (Mike). *Classification algorithms.* London : Collins Professional and Technical, 1985. 34

[48] Petteri Kaski. *Classification algorithms for codes and designs [internet resource].* Berlin : Springer, 2006. 34

[49] 1947 Abe, Shigeo. *Support vector machines for pattern classification [internet resource].* London : Springer, c2010. 34

[50] Lipo Wang and Springerlink (Online service), editors. *Support vector machines [internet resource] : theory and applications.* Berlin ; New York : Springer, c2005. 34

[51] Klecka William R. *Discriminant analysis.* Beverly Hills, Calif. : Sage Publications, c1980. 34

[52] 1934 Huberty, Carl J. *Applied discriminant analysis.* New York : Wiley, c1994. 34

[53] Daniel T Larose. *Data mining methods and models [internet resource].* Hoboken, NJ : Wiley-Interscience, c2006. 34

[54] author Lantz, Brett. *Machine learning with R [internet resource] : learn how to use R to apply powerful machine learning methods and gain an insight into real-world applications.* Birmingham, UK : Packt Publishing, 2013. 34

[55] Apostolos N Papadopoulos. *Nearest neighbor search [internet resource] : a database perspective.* New York, NY : Springer, c2005. 34

[56] Gregory Shakhnarovich, Trevor Darrell, Piotr Indyk, and IEEE Xplore, editors. *Nearest-neighbor methods in learning and vision [internet resource] : theory and practice.* Cambridge, Mass. : MIT Press, c2005. 34

[57] I. T. Jolliffe. *Principal Component Analysis.* Springer, 2002. 35, 124

[58] Harold Hotelling. **Analysis of a Complex of Statistical Variables into Principal Components**. *Journal of Educational Psychology*, **24**(6 and 7):417–441 and 498–520, 1933. 36

[59] Juha Vesanto, Johan Himberg, Esa Alhoniemi, and Juha Parhankangas. *SOM toolbox for Matlab 5.* Citeseer, 2000. 38, 123

[60] Teuvo Kohonen. **The self-organizing map**. *Neurocomputing*, **21**(1):1–6, 1998. 40

[61] Guanghao Sun, Yukiya Hakozaki, Shigeto Abe, Osamu Takei, and Takemi Matsui. **A neural network-based infection screening system that uses vital signs and percutaneous oxygen saturation for rapid screening of patients with influenza**. *Health*, **5**(8E):7–12, 2013. 41

[62] International Conference on Fuzzy Information and China) Engineering (5th : 2011 : Chengdu. *Fuzzy engineering and operations research [internet resource]*. Berlin ; New York : Springer, c2012. 40

[63] 1950 Miyamoto, Sadaaki. *Algorithms for fuzzy clustering [internet resource] : methods in c-means clustering with applications*. Berlin : Springer, c2008. 40

[64] Martin Pelikan. *Hierarchical Bayesian optimization algorithm [internet resource] : toward a new generation of evolutionary algorithms*. Berlin ; New York : Springer-Verlag, 2005. 40

[65] Z. Zivkovic. **Improved adaptive Gaussian mixture model for background subtraction**. In *Pattern Recognition, 2004. ICPR 2004. Proceedings of the 17th International Conference on*, **2**, pages 28–31 Vol.2, Aug 2004. 40

[66] 1969 Ching, Wai Ki. *Markov chains [internet resource] : models, algorithms and applications*. New York : Springer, c2006. 40

[67] 1947-author Ibe, Oliver C. (Oliver Chukwudi) and 1947 Ibe, Oliver C. (Oliver Chukwudi). *Markov processes for stochastic modeling [internet resource]*. London : Elsevier, 2013. 40

[68] National Health System-United Kingdom. **Amputation - How it's performed**, August 2014. 42

[69] National. **Amputation**, August 2014. 44

[70] United National Institute for Prosthetics & Orthotics Development. **Annual Report: A repository for quantitative information on the UK limbless population referred for prosthetics treatment**. Technical report. 46, 47, 49, 51, 53, 55

[71] Biddiss E and Chau T. **Upper-limb prosthetics: critical factors in device abandonment.** 56, 59, 61

[72] Elaine A Biddiss and Tom T Chau. **Upper limb prosthesis use and abandonment: A survey of the last 25 years**. *Prosthet. Orthot. Int.*, **31**(3):236–257, 2007. 56, 57

[73] Gear Patrol. **Life & Limb: The Evolution of Prosthetics**, 2014. 62

[74] **In memoriam Reinhold Reiter 17 November 192024 September 1998**. *International Journal of Biometeorology*, **43**(2):96–98, 1999. 66

[75] R. N. Scott. **Russian Hand**, March 1966. 68

[76] L. McLean and R.N. Scott. **The Early History of Myoelectric Control of Prosthetic Limbs (19451970)**. In Ashok Muzumdar, editor, *Powered Upper Limb Prostheses*, pages 1–15. Springer Berlin Heidelberg, 2004. 68

[77] Otto Bock Healthcare. [link]. 68

[78] Touch Bionics. **History of Touch Bionics**. 70

[79] Franceso Redi. *Esperienze intorno a diverse cose naturali e particolarmente a quelle che ci sono portare dalle indie*. 1671. 77

[80] L. Galvani. *Memorie ed esperimenti inediti di Luigi Galvani*. Cappelli, 1937. 77, 78

[81] Marco Bresadola. **Medicine and science in the life of Luigi Galvani (17371798)**. *Brain Research Bulletin*, **46**(5):367 – 380, 1998. 78

[82] Marco Piccolino. **Animal electricity and the birth of electrophysiology: the legacy of Luigi Galvani**. *Brain Research Bulletin*, **46**(5):381 – 407, 1998. 78, 79

[83] Francis Glisson. *Tractus de ventriculo et intestinis cui praemittitur alius de naturae eiusque tribus facultatibus*. London: Henry Broome, 1677. 78

[84] Haller Albrecht and. Victor Albrecht von. *Elementa physiologiae corporis humani.*, **1**. Lausannae,Sumptibus M. M. Bousquet et Sociorum,, 1757-1766. http://www.biodiversitylibrary.org/bibliography/3958. 78

[85] G. Aldini. *Essai théorique et expérimental sur le galvanisme,: avec une série d'expériences faites en présence des commissaires de l'Institut National de France, et en divers amphithéâtres anatomiques de Londres*. Number v. 1 in Essai théorique et expérimental sur le galvanisme,: avec une série d'expériences faites en présence des commissaires de l'Institut National de France, et en divers amphithéâtres anatomiques de Londres. De l'imprimerie de Fournier fils, chez Les Frères Piranesi, ..., Joseph Lucchesini, a Bologne, 1804. 78

[86] American Physical Society. **March 20,1800, Volta describes the Electric Battery**, 1995-2014. 79

[87] J. Muller. *Manuel de Physiologie*. Nabu Press, 1851. 79

[88] Moruzzi G. **The electrophysiological work of Carlo Matteucci. 1964.** 79

[89] Carlo Matteucci. **Deuxieme memoire sur le courant electrique propre de la grenouille et sur celui des animaux a sang chaud**. *Ann. Chim. Phys. (3eme serie) 6:301-39.*, 1842. 79

[90] G. Finkelstein. *Emil du Bois-Reymond: Neuroscience, Self, and Society in Nineteenth-Century Germany*. Transformations (M.I.T. Press). MIT Press, 2013. 80

[91] Emil Du Bois-Reymond. *Untersuchungen uber thierische elektricitat,*. G. Reimer, Berlin, 1848. 80

[92] F.H. Pratt. **The all-or-none principle in graded response of skeletal muscle**. *Americal Journal of Physiology, 44:517-42*, 1917. 80

[93] H. S. Gasser and H. S. Newcomer. **Physiological action currents in the phrenic nerve. An application of the thermionic vacuum tube to nerve physiology**. *American Journal of Physiology – Legacy Content*, **57**(1):1–26, 1921. 80

[94] M H PRICE JP FAU CLARE, F H CLARE MH FAU EWERHARDT, and EWERHARDT FH. **Studies in low backache with persistent muscle spasm.** 80

[95] W. F. Floyd and P. H. S. Silver. **The function of the erectores spinae muscles in certain movements and postures in man**. *J Physiol.*, 1955 September 28; 129(3): i3. 80

[96] BASMAJIAN JV. **Control and training of individual motor units.** 80

[97] Elmer E. Green, E. Dale Walters, Alyce M. Green, and Gardner Murphy. **Feedback technique for deep relaxation**. *Psychophysiology*, **6**(3):371–377, 1969. 80

[98] JaneE. Fowler, ThomasH. Budzynski, and RichardL. VandenBergh. **Effects of an EMG biofeedback relaxation program on the control of diabetes**. *Biofeedback and Self-regulation*, **1**(1):105–112, 1976. 80

[99] L F Hardyck CD FAU Petrinovich, D W Petrinovich LF FAU Ellsworth, and Ellsworth DW. **Feedback of speech muscle activity during silent reading: rapid extinction.** 80

[100] R T Booker HE FAU Rubow, P J Rubow RT FAU Coleman, and Coleman PJ. **Simplified feedback in neuromuscular retraining: an automated approach using electromyographic signals.** 80

[101] W H Johnson HE FAU Garton and Garton WH. **Muscle re-education in hemiplegia by use of electromyographic device.** 80

[102] JV Basmajian S. Wolf. **Assessment of paraspinal electromyographic activity in normal subjects and chronic back pain patients using a muscle biofeedback device.** *Asmussen E, Jorgensen K, eds. International Series on Biomechanics, VI-B. Baltimore, MD: University Press.*, 1978. 80

[103] J C Cram JR FAU Steger and Steger JC. **EMG scanning in the diagnosis of chronic pain.** 80

[104] W Taylor. **EMG biofeedback in assessment and treatment using a neuromuscular re-education model**. *Cram JR, ed. Clinical EMG for Surface Recordings, II. Nevada City, CA: Clinical Resources: 175-196.*, 1990. 80

[105] K. Lewit. *Manipulative Therapy in Rehabilitation of the Locomotor System.* Butterworth-Heinemann, 1999. 80

[106] JA Nicholson SJ Middaugh, WG Kee. **Muscle overuse and posture as factors in the development and maintainance of chronic musculoskeletal pain.** *Psychological Vulnerability to Chrronic Pain. New York, NY: Spingerl 55-89.*, 1994. 80

[107] Hermie J. Hermens. *European Recommendations for Surface Electromyography: Results of the Seniam Project (SENIAM).* Roessingh Research and Development, 1999. 81, 85

[108] Roberto Merletti and Philip Parker, editors. *Electromyography: Physiology, Engineering, and Noninvasive Application.* Wiley Online Library, 2005. 84, 85, 86

[109] De Luca CJ, Mikhail Gilmore LD FAU Kuznetsov, Serge H Kuznetsov M FAU Roy, and Roy SH. **Filtering the surface EMG signal: Movement artifact and baseline noise contamination.** 85

[110] J. Piskorowski. **Powerline interference rejection from sEMG signal using notch filter with transient suppression**. In *Instrumentation and Measurement Technology Conference (I2MTC), 2012 IEEE International*, pages 1447–1451, May 2012. 85

[111] Jacek Piskorowski. **Time-efficient removal of power-line noise from {EMG} signals using {IIR} notch filters with non-zero initial conditions**. *Biocybernetics and Biomedical Engineering*, **33**(3):171 – 178, 2013. 85

[112] Winter DA, Rau G, Kadefords R, Broman H, and DeLuca CJ. *Units, terms and standards in the reporting of EMG research.* 1980. 85

[113] Roberto Merletti and P Di Torino. **Standards for reporting EMG data**. *J Electromyogr Kinesiol*, **9**(1):3–4, 1999. 85

[114] van Boxtel A, A R Boelhouwer AJ FAU Bos, and Bos AR. **Optimal EMG signal bandwidth and interelectrode distance for the recording of acoustic, electrocutaneous, and photic blink reflexes.** 85

[115] van Boxtel A. **Optimal signal bandwidth for the recording of surface EMG activity of facial, jaw, oral, and neck muscles.** 85

[116] Hans Edmund Piper. *Electrophysiologie Menschlicher Muskeln.* Berlin. J. Springer, 1912. 86

[117] A J Muza SR FAU Young, M N Young AJ FAU Sawka, K B Sawka MN FAU Pandolf, J E Pandolf KB FAU Bogart, and Bogart JE. **Power spectral analysis of the surface electromyogram during shivering.** 86

[118] T. W. Schweitzer, J. W. Fitzgerald, J. A. Bowden, and P. Lynne-Davies. **Spectral analysis of human inspiratory diaphragmatic electromyograms**. *Journal of Applied Physiology*, **46**(1):152–165, 1979. 86

[119] Anne F. Mannion and Patricia Dolan. **Electromyographic Median Frequency Changes During Isometric Contraction of the Back Extensors to Fatigue.** *Spine*, **19**(11):–, 1994. 86

[120] H.J. Hermens, T.A.M.v. Bruggen, C.T.M. Baten, W.L.C. Rutten, and H.B.K. Boom. **The median frequency of the surface {EMG} power spectrum in relation to motor unit firing and action potential properties**. *Journal of Electromyography and Kinesiology*, **2**(1):15 – 25, 1992. 86

[121] A Gross D FAU Grassino, W R Grassino A FAU Ross, P T Ross WR FAU Macklem, and Macklem PT. **Electromyogram pattern of diaphragmatic fatigue.** 86

[122] Goran Hagg. **Electromyographic fatigue analysis based on the number of zero crossings**. *Pflgers Archiv*, **391**(1):78–80, 1981. 86

[123] G.F. Inbar, O. Paiss, J. Allin, and H. Kranz. **Monitoring surface EMG spectral changes by the zero crossing rate**. *Medical and Biological Engineering and Computing*, **24**(1):10–18, 1986. 86

[124] Gabriel DA. **Reliability of SEMG spike parameters during concentric contractions.** 86

[125] L.H. Lindstrom and R.I Magnusson. **Interpretation of myoelectric power spectra: A model and its applications**. *Proceedings of the IEEE*, **65**(5):653–662, May 1977. 86

[126] C.J. De Luca. **Physiology and Mathematics of Myoelectric Signals**. *Biomedical Engineering, IEEE Transactions on*, **BME-26**(6):313–325, June 1979. 86

[127] P. Lago and N.B. Jones. **Effect of motor-unit firing time statistics on e.m.g. spectra**. *Medical and Biological Engineering and Computing*, **15**(6):648–655, 1977. 86

[128] Foster B. Stulen and C.J. De Luca. **Frequency Parameters of the Myoelectric Signal as a Measure of Muscle Conduction Velocity**. *Biomedical Engineering, IEEE Transactions on*, **BME-28**(7):515–523, July 1981. 86

[129] Camata TV, Taufik Dantas JL FAU Abrao, Maria A C Abrao T FAU Brunetto, Antonio C Brunetto MA FAU Moraes, Leandro R Moraes AC FAU Altimari, and Altimari LR. **Fourier and wavelet spectral analysis of EMG signals in supramaximal constant load dynamic exercise.** 87

[130] Marcelo Bigliassi, Paulo Rogerio Scalassara, Thiago Ferreira Dias Kanthack, Taufik Abrao, Antonio Carlos de Moraes, and Leandro Ricardo Altimari. **Fourier and Wavelet Spectral Analysis of EMG Signals in 1-km Cycling Time-Trial**. *Applied Mathematics, 5, 1878-1886*, 2014. 87

[131] P.J. Sparto, M. Parnianpour, E.A Barria, and J.M. Jagadeesh. **Wavelet and short-time Fourier transform analysis of electromyography for detection of back muscle fatigue**. *Rehabilitation Engineering, IEEE Transactions on*, **8**(3):433–436, Sep 2000. 87

[132] MehmetRahmi Canal. **Comparison of Wavelet and Short Time Fourier Transform Methods in the Analysis of EMG Signals**. *Journal of Medical Systems*, **34**(1):91–94, 2010. 87

[133] Jun-Uk Chu, Inhyuk Moon, Yun-Jung Lee, Shin-Ki Kim, and Mu-Seong Mun. **A Supervised Feature-Projection-Based Real-Time EMG Pattern Recognition for Multifunction Myoelectric Hand Control**. *Mechatronics, IEEE/ASME Transactions on*, **12**(3):282–290, June 2007. 87

[134] Kuang Chua Chua, Vinod Chandran, U. Rajendra Acharya, and Choo Min Lim. **Application of higher order statistics/spectra in biomedical signals: A review**. *Medical Engineering & Physics*, **32**(7):679 – 689, 2010. 87

[135] Rubana H. Chowdhury, Mamun B. I. Reaz, Mohd Alauddin Bin Mohd Ali, Ashrif A. A. Bakar, Kalaivani Chellappan, and Tae G. Chang. **Surface Electromyography Signal Processing and Classification Techniques**. *Sensors*, 2013. 87

[136] Norden E. Huang, Zheng Shen, Steven R. Long, Manli C. Wu, Hsing H. Shih, Quanan Zheng, Nai-Chyuan Yen, Chi Chao Tung, and Henry H. Liu. **The empirical mode decomposition and the Hilbert spectrum for nonlinear and non-stationary time series analysis**. *Proceedings of The Royal Society*, 1998. 87

[137] Adriano O. Andrade, Slawomir Nasuto, Peter Kyberd, Catherine M. Sweeney-Reed, and F.R. Van Kanijn. **{EMG} signal filtering based on Empirical Mode Decomposition**. *Biomedical Signal Processing and Control*, **1**(1):44 – 55, 2006. 87

[138] Ling Bao and StephenS. Intille. **Activity Recognition from User-Annotated Acceleration Data**. In Alois Ferscha and Friedemann Mattern, editors, *Pervasive Computing*, **3001** of *Lecture Notes in Computer Science*, pages 1–17. Springer Berlin Heidelberg, 2004. 88, 89, 91

[139] Kiani K, E S Snijders CJ FAU Gelsema, and Gelsema ES. **Computerized analysis of daily life motor activity for ambulatory monitoring.** 88, 89

[140] J. Parkka, M. Ermes, P. Korpipaa, J. Mantyjarvi, J. Peltola, and I Korhonen. **Activity classification using realistic data from wearable sensors**. *Information Technology in Biomedicine, IEEE Transactions on*, **10**(1):119–128, Jan 2006. 88, 89, 91

[141] Uwe Maurer, Anthony Rowe, Asim Smailagic, and Daniel Siewiorek. **Location and Activity Recognition Using eWatch: A Wearable Sensor Platform**. In Yang Cai and Julio Abascal, editors, *Ambient Intelligence in Everyday Life*, **3864** of *Lecture Notes in Computer Science*, pages 86–102. Springer Berlin Heidelberg, 2006. 88, 89, 91

[142] Susanna Pirttikangas, Kaori Fujinami, and Tatsuo Nakajima. **Feature Selection and Activity Recognition from Wearable Sensors**. In HeeYong Youn, Minkoo Kim, and Hiroyuki Morikawa, editors, *Ubiquitous Computing Systems*, **4239** of *Lecture Notes in Computer Science*, pages 516–527. Springer Berlin Heidelberg, 2006. 88, 91

[143] Tâm Huynh and Bernt Schiele. **Analyzing Features for Activity Recognition**. In *Proceedings of the 2005 Joint Conference on Smart Objects and Ambient Intelligence: Innovative Context-aware Services: Usages and Technologies*, sOc-EUSAI '05, pages 159–163, New York, NY, USA, 2005. ACM. 88

[144] D. Peleg, E. Braiman, E. Yom-Tov, and G.F. Inbar. **Classification of finger activation for use in a robotic prosthesis arm**. *Neural Systems and Rehabilitation Engineering, IEEE Transactions on*, **10**(4):290–293, Dec 2002. 88

[145] K.A. Farry, I.D. Walker, and R.G. Baraniuk. **Myoelectric teleoperation of a complex robotic hand**. *Robotics and Automation, IEEE Transactions on*, **12**(5):775–788, Oct 1996. 88

[146] F.H.Y. Chan, Yong-Sheng Yang, F.K. Lam, Yuan-Ting Zhang, and P.A. Parker. **Fuzzy EMG classification for prosthesis control**. *Rehabilitation Engineering, IEEE Transactions on*, **8**(3):305 –311, sep 2000. 88

[147] K. Englehart and B. Hudgins. **A robust, real-time control scheme for multifunction myoelectric control**. *Biomedical Engineering, IEEE Transactions on*, **50**(7):848 –854, july 2003. 88

[148] Makikawa M and Iizumi H. **Development of an ambulatory physical activity memory device and its application for the categorization of actions in daily life.** 88

[149] Busser HJ, R C Ott J FAU van Lummel, M van Lummel RC FAU Uiterwaal, R Uiterwaal M FAU Blank, and Blank R. **Ambulatory monitoring of children's activity.** 88

[150] Bussmann JB, M P van de Laar YM FAU Neeleman, H J Neeleman MP FAU Stam, and Stam HJ. **Ambulatory accelerometry to quantify motor behaviour in patients after failed back surgery: a validation study.** 88

[151] Uiterwaal M, H J Glerum EB FAU Busser, R C Busser HJ FAU van Lummel, and van Lummel RC. **Ambulatory monitoring of physical activity in working situations, a validation study.** 88

[152] K. Aminian, Ph. Robert, E.E. Buchser, B. Rutschmann, D. Hayoz, and M. Depairon. **Physical activity monitoring based on accelerometry: validation and comparison with video observation**. *Medical & Biological Engineering & Computing*, **37**(3):304–308, 1999. 88

[153] J Fahrenberg, W Muller, F Foerster, and M Smeja. **A multi-channel investigation of physical activity**. *Journal of Psychophysiology (10) pp. 209217*, 1996. 89

[154] Fahrenberg J, M Foerster F FAU Smeja, W Smeja M FAU Muller, and Muller W. **Assessment of posture and motion by multichannel piezoresistive accelerometer recordings.** 89

[155] S. H. Lee, H. D. Park, S. Y. Hong, K.J. Lee, and Y. H. Kim. **A study on the activity classification using a triaxial accelerometer**. In *Engineering in Medicine and Biology Society, 2003. Proceedings of the 25th Annual International Conference of the IEEE*, **3**, pages 2941–2943 Vol.3, Sept 2003. 89

[156] F Foerster, M Smeja, and J Fahrenberg. **Detection of posture and motion by accelerometry: a validation study in ambulatory monitoring**. *Computers in Human Behavior*, **15**(5):571 – 583, 1999. 89

[157] Foerster F and Fahrenberg J. **Motion pattern and posture: correctly assessed by calibrated accelerometers.** 89

[158] Kristof Van Laerhoven and Hans Gellersen. **Spine versus Porcupine: A Study in Distributed Wearable Activity Recognition**. In *IEEE International Symposium on Wearable Computers (ISWC 2004)*. IEEE Computer Society, IEEE Computer Society, October 2004. 89

[159] Jonghun Baek, Geehyuk Lee, Wonbae Park, and Byoung-Ju Yun. **Accelerometer Signal Processing for User Activity Detection**. In MirceaGh. Negoita, RobertJ. Howlett, and LakhmiC. Jain, editors, *Knowledge-Based Intelligent Information and Engineering Systems*, **3215** of *Lecture Notes in Computer Science*, pages 610–617. Springer Berlin Heidelberg, 2004. 89

[160] T. Huynh and B. Schiele. **Towards Less Supervision in Activity Recognition from Wearable Sensors**. In *Wearable Computers, 2006 10th IEEE International Symposium on*, pages 3–10, Oct 2006. 89, 90

[161] Tong Zhang, Jue Wang, Ping Liu, and Jing Hou. **Fall Detection by Embedding an Accelerometer in Cellphone and Using KFD Algorithm**. *International Journal of Computer Science and Network Security*, 2006. 89

[162] Tong Zhang, Jue Wang, Liang Xu, and Ping Liu. **Fall Detection by Wearable Sensor and One-Class SVM Algorithm**. In De-Shuang Huang, Kang Li, and GeorgeWilliam Irwin, editors, *Intelligent Computing in Signal Processing and Pattern Recognition*, **345** of *Lecture Notes in Control and Information Sciences*, pages 858–863. Springer Berlin Heidelberg, 2006. 89

[163] C. Doukas and I Maglogiannis. **Advanced patient or elder fall detection based on movement and sound data**. In *Pervasive Computing Technologies for Healthcare, 2008. PervasiveHealth 2008. Second International Conference on*, pages 103–107, Jan 2008. 89

[164] Nicky Kern, Bernt Schiele, and Albrecht Schmidt. **Multi-sensor Activity Context Detection for Wearable Computing**. In Emile Aarts, RenW. Collier, Evert van Loenen, and Boris de Ruyter, editors, *Ambient Intelligence*, **2875** of *Lecture Notes in Computer Science*, pages 220–232. Springer Berlin Heidelberg, 2003. 90

[165] Nishkam Ravi, Nikhil D, Preetham Mysore, and Michael L. Littman. **Activity recognition from accelerometer data**. In *In Proceedings of the Seventeenth Conference on Innovative Applications of Artificial Intelligence(IAAI*, pages 1541–1546. AAAI Press, 2005. 90, 91

[166] Seon-Woo Lee and K. Mase. **Activity and location recognition using wearable sensors**. *Pervasive Computing, IEEE*, **1**(3):24–32, July 2002. 90

[167] Salarian A, Francois J G Russmann H FAU Vingerhoets, Pierre R Vingerhoets FJ FAU Burkhard, Kamiar Burkhard PR FAU Aminian, and Aminian K. **Ambulatory monitoring of physical activities in patients with Parkinson's disease.** 90

[168] K. Van Laerhoven and O. Cakmakci. **What shall we teach our pants?** In *Wearable Computers, The Fourth International Symposium on*, pages 77–83, Oct 2000. 90

[169] A Krause, D.P. Siewiorek, A Smailagic, and J. Farringdon. **Unsupervised, dynamic identification of physiological and activity context in wearable computing**. In *Wearable Computers, 2003. Proceedings. Seventh IEEE International Symposium on*, pages 88–97, Oct 2003. 90

[170] David G. Stork Richard O. Duda, Peter E. Hart. *Pattern Classification*. Wiley-Interscience Publication, 2000. 90, 124

[171] Keith D. Copsey Andrew R. Webb. *Statistical Pattern Recognition*. Wiley-Blackwell; 3rd Edition edition (21 Oct 2011), 2002. 90

[172] Sergios Theodoridis and Konstantinos Koutroumbas. **Chapter 1 - Introduction**. In Sergios Theodoridis and Konstantinos Koutroumbas, editors, *Pattern Recognition (Fourth Edition)*, pages 1 – 12. Academic Press, Boston, fourth edition edition, 2009. 90

[173] Ermes M, J Parkka J FAU Mantyjarvi, I Mantyjarvi J FAU Korhonen, and Korhonen I. **Detection of daily activities and sports with wearable sensors in controlled and uncontrolled conditions.** 91

[174] Jonathan Lester, Tanzeem Choudhury, Nicky Kern, Gaetano Borriello, and Blake Hannaford. **A Hybrid Discriminative/Generative Approach for Modeling Human Activities**. In *Proceedings of the 19th International Joint Conference on Artificial Intelligence*, IJCAI'05, pages 766–772, San Francisco, CA, USA, 2005. Morgan Kaufmann Publishers Inc. 91

[175] Allen FR, Nigel H Ambikairajah E FAU Lovell, Branko G Lovell NH FAU Celler, and Celler BG. **Classification of a known sequence of motions and postures from accelerometry data using adapted Gaussian mixture models.** 91

[176] Stegeman DF, H J Blok JH FAU Hermens, K Hermens HJ FAU Roeleveld, and Roeleveld K. **Surface EMG models: properties and applications.** 92

[177] A Mallik and A I Weir. **Nerve conduction studies: essentials and pitfalls in practice**. *Journal of Neurology, Neurosurgery & Psychiatry*, **76**(suppl 2):ii23–ii31, 2005. 92

[178] De Luca CJ. **Myoelectrical manifestations of localized muscular fatigue in humans.** 92

[179] Bystrom SE, C Mathiassen SE FAU Fransson-Hall, and Fransson-Hall C. **Physiological effects of micropauses in isometric handgrip exercise.** 93

[180] Hagg GM and Astrom A. **Load pattern and pressure pain threshold in the upper trapezius muscle and psychosocial factors in medical secretaries with and without shoulder/neck disorders.** 93

[181] Clarys JP and Cabri J. **Electromyography and the study of sports movements: a review.** 93

[182] Wakeling JM, H K Blake OM FAU Chan, and Chan HK. **Muscle coordination is key to the power output and mechanical efficiency of limb movements.** 93

[183] Clarys JP. **Electromyography in sports and occupational settings: an update of its limits and possibilities.** 93

[184] Mario Cifrek, Vladimir Medved, Stanko Tonkovi, and Saa Ostoji. **Surface {EMG} based muscle fatigue evaluation in biomechanics**. *Clinical Biomechanics*, **24**(4):327 – 340, 2009. 93

[185] George A Bekey, Chi-Wu Chang, J. Perry, and M.M. Hoffer. **Pattern recognition of multiple EMG signals applied to the description of human gait**. *Proceedings of the IEEE*, **65**(5):674–681, May 1977. 93

[186] Janice J. Eng and David A. Winter. **Kinetic analysis of the lower limbs during walking: What information can be gained from a three-dimensional model?** *Journal of Biomechanics*, **28**(6):753 – 758, 1995. 93

[187] P. Hodges A. Rainoldi, R. Casale and G. Jull. *Applications in Rehabilitation Medicine and Related Fields in : Electromyography: Physiology, Engineering, and Noninvasive Applications*. 28 JAN 2005: (p403433). 93, 95

[188] Hodges PW and Richardson CA. **Feedforward contraction of transversus abdominis is not influenced by the direction of arm movement.** 93, 94

[189] C. Richardson. *Therapeutic Exercise for Spinal Segmental Stabilization in Low Back Pain: Scientific Basis and Clinical Approach*. Churchill Livingstone, 1999. 93

[190] Huang HY, Yueliang Leon Lin JJ FAU Guo, Wendy Tzyy-Jiuan Guo YL FAU Wang, Yu-Jen Wang WT FAU Chen, and Chen YJ. **EMG biofeedback effectiveness to alter muscle activity pattern and scapular kinematics in subjects with and without shoulder impingement.** 95

[191] Nord S, D Ettare D FAU Drew, S Drew D FAU Hodge, and Hodge S. **Muscle learning therapy–efficacy of a biofeedback based protocol in treating work-related upper extremity disorders.** 95

[192] Fougner A, Peter J Stavdahl O FAU Kyberd, Yves G Kyberd PJ FAU Losier, Philip A Losier YG FAU Parker, and Parker PA. **Control of upper limb prostheses: terminology and proportional myoelectric control-a review.** 95, 96, 97, 98

[193] Yves Gilles Losier. *Shoulder Complex Motion Based Input Strategies for Prosthetic Limb Control*. PhD thesis, Fredericton, N.B., Canada, Canada, 2009. AAINR74351. 96

[194] R. W. Mann. **Efferent and Afferent Control of an Electromyographic, Proportional-Rate, Force Sensing Artificial Elbow with Cutaneous Display of Joint Angle**. *Proceedings of the Institution of Mechanical Engineers, Conference Proceedings*, **183**(10):86–92, 1968. 96

[195] B. Hudgins, P. Parker, and R.N. Scott. **A new strategy for multifunction myoelectric control**. *Biomedical Engineering, IEEE Transactions on*, **40**(1):82 –94, jan. 1993. 96

[196] Fougner A, Adrian D C Scheme E FAU Chan, Kevin Chan AD FAU Englehart, Oyvind Englehart K FAU Stavdahl, and Stavdahl O. **Resolving the limb position effect in myoelectric pattern recognition.** 96, 97

[197] C. Almstorm. **An electronic control system for a prosthetic hand with six degrees of freedom**. *Department of Applied Electronics, Chalmers, University of Technology, Gothenburg, Sweden, Tech. Report 1:77*, 1977. 97

[198] Farmer SF, D M Bremner FD FAU Halliday, J R Halliday DM FAU Rosenberg, J A Rosenberg JR FAU Stephens, and Stephens JA. **The frequency content of common synaptic inputs to motoneurones studied during voluntary isometric contraction in man.** 100, 119, 152, 222

[199] Halliday DM, A M Rosenberg JR FAU Amjad, P Amjad AM FAU Breeze, B A Breeze P FAU Conway, S F Conway BA FAU Farmer, and Farmer SF. **A framework for the analysis of mixed time series/point process data–theory and application to the study of physiological tremor, single motor unit discharges and electromyograms.** 100, 119

[200] Kilner JM, R Alonso-Alonso M FAU Fisher, R N Fisher R FAU Lemon, and Lemon RN. **Modulation of synchrony between single motor units during precision grip tasks in humans.** 100

[201] Semmler JG. **Motor unit synchronization and neuromuscular performance.** 100

[202] Farmer SF, David M Gibbs J FAU Halliday, Linda M Halliday DM FAU Harrison, Leon M Harrison LM FAU James, Margaret J James LM FAU Mayston, John A Mayston MJ FAU Stephens, and Stephens JA. **Changes in EMG coherence between long and short thumb abductor muscles during human development.** 100, 101, 222

[203] Saeid Mehrkanoon, Michael Breakspear, and Tjeerd W. Boonstra. **The reorganization of corticomuscular coherence during a transition between sensorimotor states**. *NeuroImage*, **100**(0):692 – 702, 2014. 100

[204] Halliday DM, S F Conway BA FAU Farmer, J R Farmer SF FAU Rosenberg, and Rosenberg JR. **Load-independent contributions from motor-unit synchronization to human physiological tremor.** 100, 101

[205] Kevin G. Keenan, Joseph D. Collins, William V. Massey, Tygh J. Walters, and Hillary D. Gruszka. **Coherence between surface electromyograms is influenced by electrode placement in hand muscles**. *J. Neurosci. Methods*, **195**(1):10 – 14, 2011. 100

[206] Beck TW, Joel T Housh TJ FAU Cramer, Michelle Cramer JT FAU Mielke, Russell Mielke M FAU Hendrix, and Hendrix R. **The influence of electrode shift over the innervation zone and normalization on the electromyographic amplitude and mean power frequency versus isometric torque relationships for the vastus medialis muscle.** 100

[207] Rainoldi A, I Melchiorri G FAU Caruso, and Caruso I. **A method for positioning electrodes during surface EMG recordings in lower limb muscles.** 100

[208] Yao B, Guang H Salenius S FAU Yue, Robert W Yue GH FAU Brown, Jing Z Brown RW FAU Liu, and Liu JZ. **Effects of surface EMG rectification on power and coherence analyses: an EEG and MEG study.** 100

[209] David M. Halliday and Simon F. Farmer. **On the Need for Rectification of Surface EMG**. *Journal of Neurophysiology*, **103**(6):3547–3547, 2010. 100

[210] Boonstra TW and Breakspear M. **Neural mechanisms of intermuscular coherence: implications for the rectification of surface electromyography.** 100

[211] Kakuda N, J Nagaoka M FAU Wessberg, and Wessberg J. **Common modulation of motor unit pairs during slow wrist movement in man.** 101

[212] J M Kilner, S N Baker, S Salenius, V Jousmki, R Hari, and R N Lemon. **Task-dependent modulation of 15-30 Hz coherence between rectified EMGs from human hand and forearm muscles**. *The Journal of Physiology*, **516**(2):559–570, 1999. 101

[213] Grosse P, M A J Edwards M FAU Tijssen, A Tijssen MA FAU Schrag, Andrew J Schrag A FAU Lees, K P Lees AJ FAU Bhatia, Peter Bhatia KP FAU Brown, and Brown P. **Patterns of EMG-EMG coherence in limb dystonia.** 101

[214] Danna-Dos Santos A, Mark Poston B FAU Jesunathadas, Lisa R Jesunathadas M FAU Bobich, Thomas M Bobich LR FAU Hamm, Marco Hamm TM FAU Santello, and Santello M. **Influence of fatigue on hand muscle coordination and EMG-EMG coherence during three-digit grasping.** 101

[215] Kisiel-Sajewicz K, Ken Fang Y FAU Hrovat, Guang H Hrovat K FAU Yue, Vlodek Yue GH FAU Siemionow, Chang-Kai Siemionow V FAU Sun, Anna Sun CK FAU Jaskolska, Artur Jaskolska A FAU Jaskolski, Vinod Jaskolski A FAU Sahgal, Janis J Sahgal V FAU Daly, and Daly JJ. **Weakening of synergist muscle coupling during reaching movement in stroke patients.** 101

[216] A. Aranceta-Garza, H. Lakany, and B.A. Conway. **An Investigation into Thumb Rotation Using High Density Surface Electromyography of Extrinsic Hand Muscles**. In *Systems, Man, and Cybernetics (SMC), 2013 IEEE International Conference on*, pages 3751–3755, Oct 2013. 106, 109, 110

[217] P V Viitasalo JT FAU Komi and Komi PV. **Interrelationships of EMG signal characteristics at different levels of muscle tension and during fatigue.** 117

[218] P V Viitasalo JH FAU Komi and Komi PV. **Signal characteristics of EMG during fatigue.** 117

[219] K. Englehart and B. Hudgins. **A robust, real-time control scheme for multifunction myoelectric control**. *Biomedical Engineering, IEEE Transactions on*, **50**(7):848–854, July 2003. 118

[220] Teuvo Kohonen. **Self-organized formation of topologically correct feature maps**. *Biol. Cybern.*, **43**(1):59–69, 1982. 123

[221] Tommi Vatanen. *Missing Value Imputation Using Subspace Methods with Applications on Survey Data.* Master's thesis, AALTO University, School of Science, Department of Information and Computer Science., April 2012. 123

[222] Mathworks. **Neural Network Toolbox**, 1994-2014. Last accessed 09th May 2014. 127

[223] Martin Fodslette Moller. **A scaled conjugate gradient algorithm for fast supervised learning**. *Neural Networks*, **6**(4):525 – 533, 1993. 126

[224] Christoph von der Malsburg, Werner von Seelen, Jan C. Vorbrüggen, and Bernhard Sendhoff, editors. *Artificial Neural Networks - ICANN 96, 1996 International Conference, Bochum, germany, July 16-19, 1996, Proceedings*, **1112** of *Lecture Notes in Computer Science*. Springer, 1996. 204

[225] Kevin G. Keenan, William V. Massey, Tygh J. Walters, and Joseph D. Collins. **Sensitivity of EMG-EMG coherence to detect the common oscillatory drive to hand muscles in young and older adults**. *Journal of Neurophysiology*, **107**(10):2866–2875, 2012. 220

[226] Mayston MJ, J A Harrison LM FAU Stephens, S F Stephens JA FAU Farmer, and Farmer SF. **Physiological tremor in human subjects with X-linked Kallmann's syndrome and mirror movements.** 222

[227] J Gibbs, L M Harrison, and J A Stephens. **Cross-correlation analysis of motor unit activity recorded from two separate thumb muscles during development in man.** *The Journal of Physiology*, **499**(Pt 1):255–266, 1997. 222

[228] Sebelius F, C Eriksson L FAU Balkenius, T Balkenius C FAU Laurell, and Laurell T. **Myoelectric control of a computer animated hand: a new concept based on the combined use of a tree-structured artificial neural network and a data glove.** 222, 225

[229] Nielsen JL, Ning Holmgaard S FAU Jiang, Kevin Jiang N FAU Englehart, Dario Englehart K FAU Farina, Philip Farina D FAU Parker, and Parker P. **Enhanced EMG signal processing for simultaneous and proportional myoelectric control.** 222, 225

[230] J.L.G. Nielsen, S. Holmgaard, Ning Jiang, K.B. Englehart, D. Farina, and P.A. Parker. **Simultaneous and Proportional Force Estimation for Multifunction Myoelectric Prostheses Using Mirrored Bilateral Training**. *Biomedical Engineering, IEEE Transactions on*, **58**(3):681–688, March 2011. 223, 225

[231] Amirreza Ziai and Carlo Menon. **Comparison of regression models for estimation of isometric wrist joint torques using surface electromyography**. *Journal of NeuroEngineering and Rehabilitation*, **8**(1):56, 2011. 223, 225

[232] Muceli S and Farina D. **Simultaneous and proportional estimation of hand kinematics from EMG during mirrored movements at multiple degrees-of-freedom.** 223, 225

[233] Christopher L Pulliam, Joris M Lambrecht, and Robert F Kirsch. **Continuous And Simultaneous Emg-Based Neural Network Control Of Transradial Prostheses**. Myoelectric Symposium, 2011. 223, 225

[234] Andrew Rutherford and Andrew Rutherford. *ANOVA and ANCOVA: A GLM Approach*. John Wiley & Sons Inc, August 2012. 247, 248